

SYNTHESIS AND CHARACTERIZATION OF CADMIUM ZINC SULPHIDE ($\text{Cd}_{1-x}\text{Zn}_x\text{S}$) THIN FILMS FROM ACIDIC CHEMICAL BATHS

By

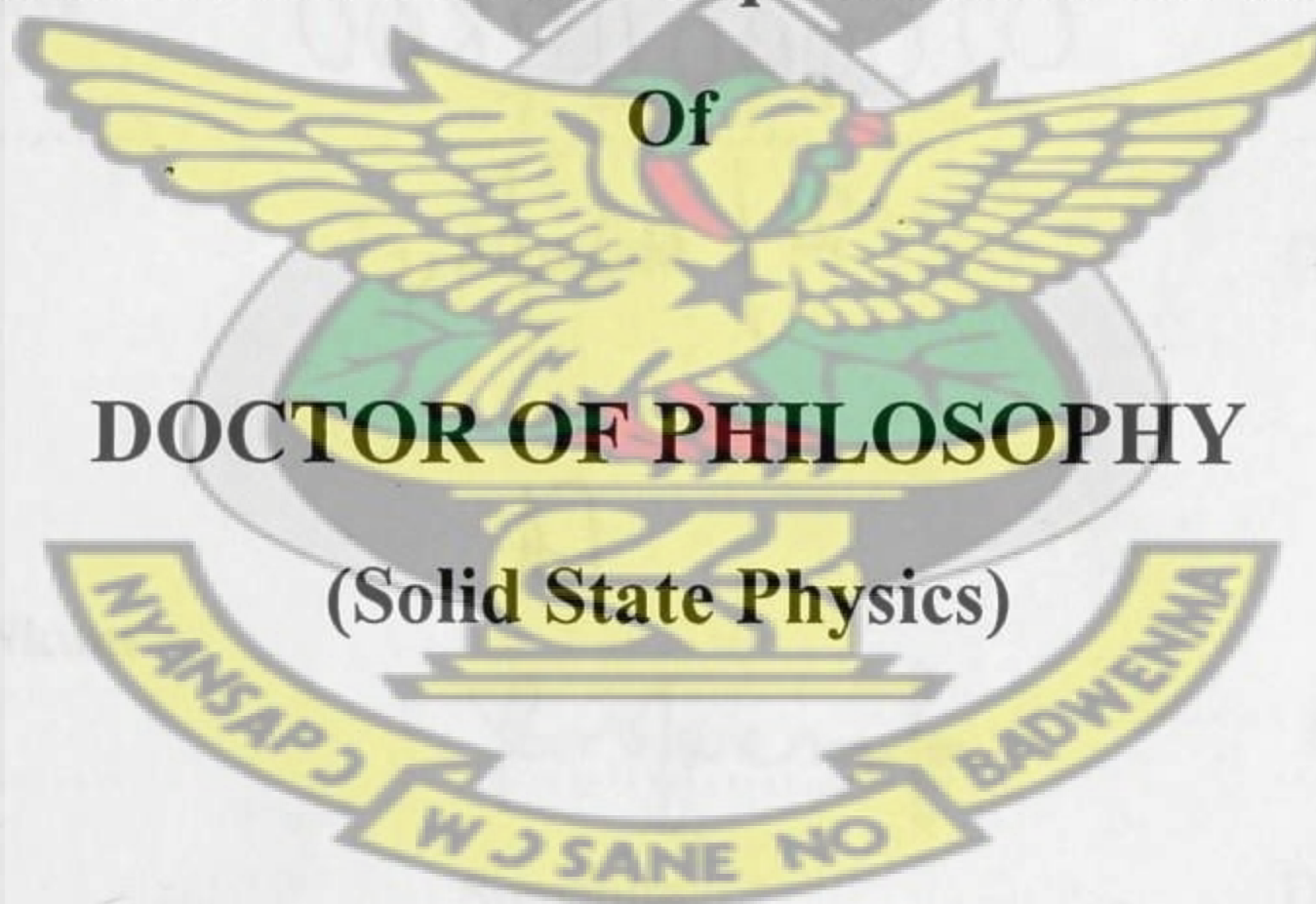
Francis Kofi Ampong, B.Sc(Hons.) M.Sc.

**A Thesis submitted to the Department of Physics,
Kwame Nkrumah University of Science and Technology
in partial fulfilment of the requirements for the degree**

Of

DOCTOR OF PHILOSOPHY

(Solid State Physics)



College of Science

©Department of Physics

May 2012

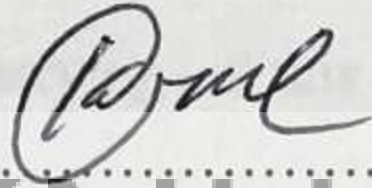
DECLARATION

I hereby declare that this submission is my own work towards the PhD and that, to the best of my knowledge, it contains no material previously published by any person nor material which has been accepted for the award of any other degree of the University, except where due acknowledgment has been made in the text.

Francis Kofi Ampong

.....

Student



Signature

13/12/12

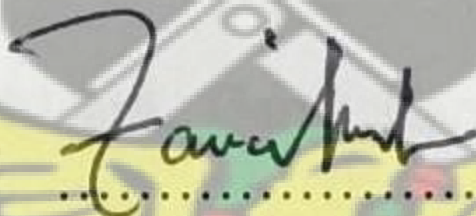
Date

Certified by:

Professor F. Boakye

.....

Supervisor



Signature

13/12/12

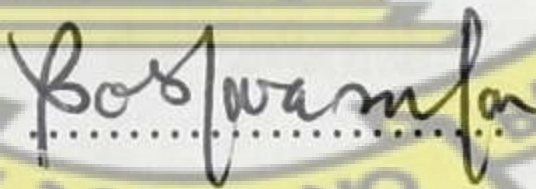
Date

Certified by:

Professor R. K. Nkum

.....

Supervisor



Signature

13/12/12

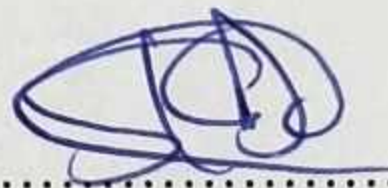
Date

Certified by:

Professor S. K. Danuor

.....

Head of Department



Signature

13/12/12

Date

ACKNOWLEDGEMENT

First of all, I render my gratitude to the ALMIGHTY who bestowed self-confidence, ability and strength in me to complete this work.

I express my sincere thanks to my esteemed and worthy supervisors, Professor Francis Boakye, and Professor Robert K. Nkum, for their valuable guidance, effective supervision, encouragement and enlightenment in carrying out this project.

I would never have succeeded in completing my task without the help and support provided me by various personalities. With a deep sense of gratitude, I express my sincere thanks to Dr. J. A. M. Awudza, of the Department of Chemistry, KNUST, Professor Paul O'Brien and Dr. John Thomas of the School of Chemistry, University of Manchester, UK.

My special thanks to Judith Shackleton, Garry Harrison, and Alexander Forrest of the Material Science Centre, University of Manchester, UK, for their help and support in carrying out X-ray diffraction and Scanning electron microscope measurements.

My heartfelt gratitude goes to my wife and children for their prayers and support.

And finally my sincere gratitude goes to the Leverhulme – Royal Society Africa Award, for funding this project.

ABSTRACT

Cadmium zinc sulphide thin films with the required composition were successfully deposited from chemical baths containing zinc chloride, cadmium chloride, urea and thioacetamide at modestly acid pH values. The $\text{Cd}_{1-x}\text{Zn}_x\text{S}$ films obtained by this method were smooth, uniform, adherent, pinhole free, bright yellow orange in colour and changed to pale yellow with increasing zinc content. ZnS films were white in colour and transparent. The films were annealed in air at 400°C for two hours. Both the as-deposited and annealed samples were characterized using a variety of techniques. Powder X-ray diffraction analysis of the thin films and precipitates of $\text{Cd}_{1-x}\text{Zn}_x\text{S}$, over the entire composition range, that is, $0 \leq x \leq 1$, showed that, all the compositions up to 75% Zn had the wurtzite structure, with preferred orientation along the (002) plane. Pure ZnS had the sphalerite structure with preferred orientation along the (111) plane. SEM micrographs of the as-deposited thin films showed the presence of uniform and crack-free surface morphologies characterized by well-interconnected globular crystallites. EDX analysis confirmed the film to be consistent with the formation of the ternary compound on silica glass slide. The crystal size measured from the XRD peak width varied from 12 nm (CdS) to 9 nm (ZnS). The variation of lattice parameters with increasing zinc ion content, showed a very good agreement with Vegard's law. The fundamental absorption edge of the as-deposited $\text{Cd}_{1-x}\text{Zn}_x\text{S}$ thin films, showed a blue shift with an increase in zinc ion content. The band gap, determined from optical absorption spectroscopy, varied almost linearly with composition between that of CdS (2.38 eV) and ZnS (3.70 eV) for the as-deposited samples while the annealed samples varied from CdS (2.40 eV) to ZnS (3.73 eV). This almost linear change in the band gap of CdS by addition of Zn shows formation of a continuous series of solid solutions. The as-deposited thin films possessed poor crystallinity compared to the annealed films.

Contents

Declaration	i
Acknowledgement	ii
Abstract	iii
List of Tables	viii
List of Figures	ix
List of Symbols and Acronyms	xvii
1. INTRODUCTION	1
1.1 Semiconductor Materials.....	4
1.2 Cadmium Zinc Sulphide.....	6
1.3 Synthesis of cadmium Zinc Sulphide Thin Films.....	8
1.3.1 Acidic Chemical baths.....	9
1.4 Characterization.....	10
1.5 Objectives of the Research.....	11
1.6 Justification of the Research.....	13
1.7 Structure of the Thesis.....	14
2. LITERATURE REVIEW	16
2.1 Thin Films.....	16
2.2 Thin film deposition techniques	17
2.2.1 Chemical Bath Deposition.....	18
2.2.1.1 A Brief Explanation of the CBD Process.....	21
2.3 Crystal Structure of some important II-VI Semiconductor Materials.....	23
2.3.1 Cadmium Sulphide.....	23
2.3.2 Zinc Sulphide.....	24
2.3.3 Cadmium Zinc sulphide.....	25

2.4	Review of Cadmium Zinc Sulfide thin films prepared by chemical bath deposition.....	26
3.	THEORY	39
3.1	Physics of Semiconductors.....	39
3.1.1	Energy Band Theory.....	39
3.1.1.1	The Free Electron Model.....	39
3.1.1.2	Particle in a Box.....	42
3.1.1.3	Electron Potential Energy and Energy States.....	46
3.1.1.4	From Discrete Energy States to energy bands.....	50
3.1.1.5	Energy Bands (an intuitive approach).....	52
3.1.2	Origin of the Band gaps in a Crystal.....	54
3.1.2.1	Electrons in a periodic potential of a crystal (Kronig-Penney Model).....	54
3.1.2.2	Effect of a periodic potential on the free electron model.....	59
3.1.2.3	Direct and Indirect band gap semiconductors.....	60
3.1.3	Electron and Hole distributions with energy.....	63
3.1.3.1	Density of States	63
3.1.3.2	Fermi Distribution Function	64
3.1.3.3	Concentration of electron and holes at equilibrium.....	67
3.2	Classification of solids	69
3.2.1	Crystalline Semiconductors.....	70
3.2.2	Polycrystalline Semiconductors.....	71
3.2.3	Amorphous Semiconductors	73
3.3	Basic Principles of Chemical Bath Deposition	78
3.3.1	Reaction mechanisms of chemical bath deposition	79
3.3.1.1	Ion-by-ion mechanism	80
3.3.1.2	Hydroxide cluster mechanism	80

3.3.1.3	Complex decomposition mechanism.....	81
3.3.1.3.1	Cluster mechanism.....	82
3.3.1.3.2	Ion-by-ion mechanism.....	82
3.3.2	Deposition of zinc sulphide.....	83
3.3.3	General considerations for precipitation and chemical deposition of Ternary compounds.....	84
3.3.3.1	Cadmium zinc sulphide.....	85
3.3.4	Basics of film formation and structure.....	86
4.	CHARACTERIZATION OF SEMICONDUCTOR MATERIALS	89
4.1	Optical Absorption Spectroscopy.....	89
4.1.1	Optical properties of Semiconductors	90
4.1.2	Fundamental Absorption in direct and indirect band gap semiconductors	92
4.1.3	Estimation of the band gap from absorbance measurements	95
4.2	Basics of x-ray diffraction	97
4.2.1	Bragg's law of diffraction	97
4.2.2	Powder Diffraction	99
4.2.3	Diffraction geometries	99
4.3	Energy Dispersion X-ray Spectroscopy	102
4.4	Scanning Electron microscopy	104
5.	EXPERIMENTAL DETAILS	107
5.1	Substrate Preparation	107
5.2	Synthesis of the thin films	108
5.3	Chemical equations for the deposition process	111
5.3.1	Decomposition of thioacetamide	111
5.3.2	Hydrolysis of Urea	112

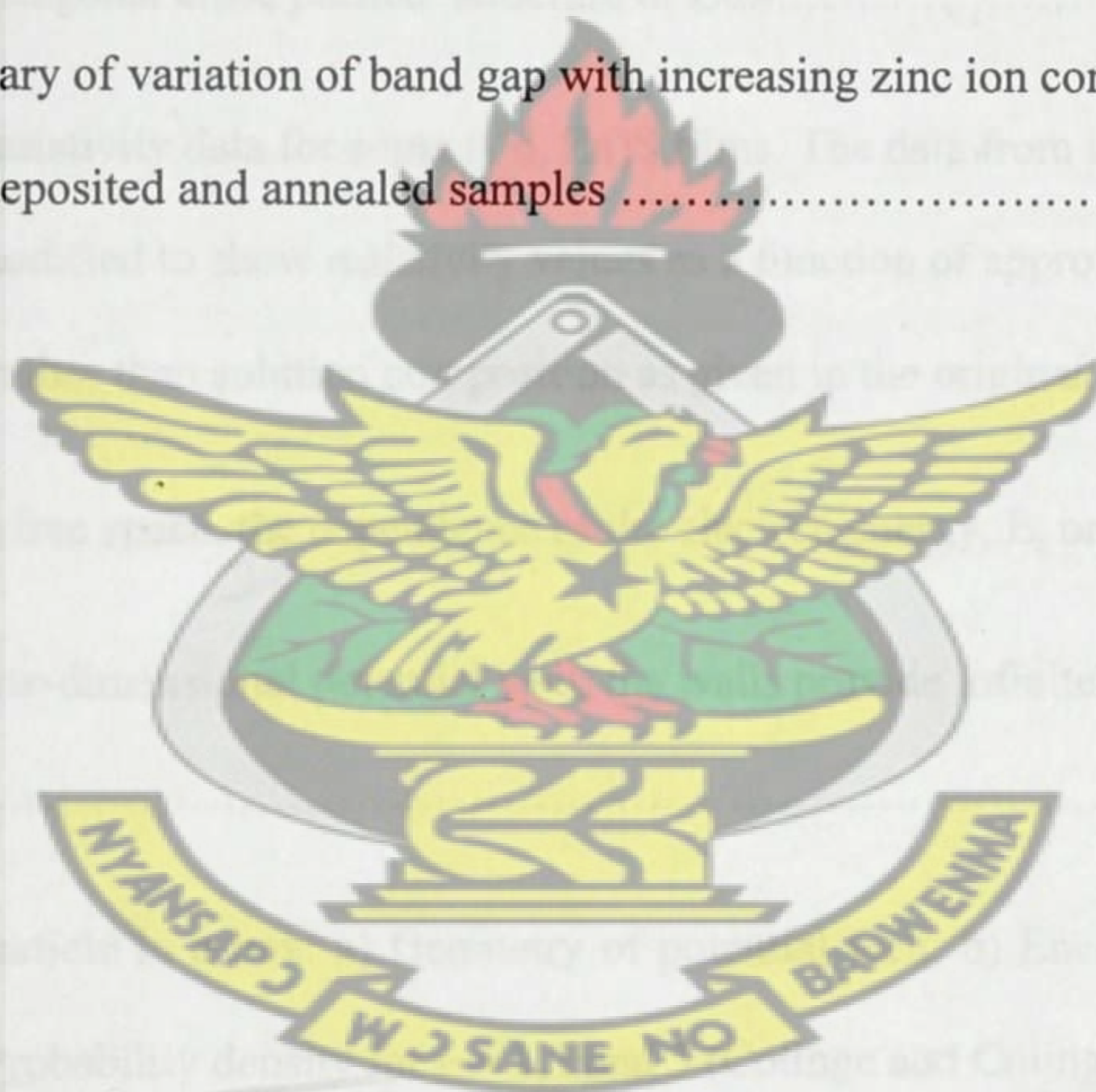
5.4	Measurement of Absorption Spectra	113
5.5	X-ray diffraction measurements	114
5.5.1	Important considerations for carrying out x-ray diffraction measurements	114
5.6	Scanning Electron Microscopy measurements	116
5.6.1	Sample preparation for SEM measurements	116
5.7	Energy dispersive x-ray analysis	118
5.8	Thermal Annealing	118
6.	RESULTS AND DISCUSSIONS	119
6.1	X-ray diffraction patterns of the thin films	119
6.2	X-ray diffraction patterns of the powder samples (precipitates)	127
6.3	Grain Size	137
6.4	Variation of lattice parameters with increasing zinc ion concentration	138
6.5	Results of scanning electron microscopy and energy dispersive x-ray analysis.....	145
6.6	Results of the Optical absorption spectra	157
6.7	Determination of the Optical band gap	158
6.8	Effect of thermal annealing on the optical properties	165
7.	CONCLUSIONS AND RECOMMENDATIONS	169
7.1	Conclusions.....	169
7.2	Recommendations.....	170
	REFERENCES	172

APPENDIX

1. JCPDS data file, reference code: 00-001-0780
2. JCPDS data file, reference code: 00-040-0834
3. JCPDS data file, reference code: 01-080-0020

LIST OF TABLES

Table 3.1: The first four Bohr energies and orbital radii for the hydrogen atom.....	49
Table 3.2: The four possible reaction mechanisms in CBD	79
Table 6.1: Summary of the EDX results for the as-deposited CdS thin film	146
Table 6.2: EDAX elemental analysis results for the as-deposited ZnS thin film	155
Table 6.3: Summary of variation of band gap with increasing zinc ion content for $Cd_{1-x}Zn_xS$ thin films for as-deposited and annealed samples	168



LIST OF FIGURES

Figure 2.1: Tetrahedral voids in the f.c.c structure, (b) Tetrahedral voids in the c.p.h. structure (Barrett and Massalski, 1980).....	24
Figure 2.2: Zinc blende Lattice: (a)The Cubic Unit Cell (b) Tetrahedral Bonding Configuration.....	25
Figure 2.3: hexagonal close packed structure of CdS.....	26
Figure 2.4: Resistivity data for some (Cd, Zn)S films. The data from the two yamaguchi papers were modified to show resistivity values as a function of approximate film composition, rather than solution composition as given in the original papers.....	29
Figure 3.1: In free space, the dependence of the electron energy, E, on k is parabolic..	41
Figure 3.2: One-dimensional potential well; the walls provide infinitely high-potential barriers.....	42
Figure 3.3: Particle in a box: a) Geometry of potential well; b) Energy levels; c) Wave functions; d) Probability density for $n = 1, 2$ and 3 (Colinge and Colinge, 2002).....	45
Figure 3.4: Potential Energy of an electron as a function of its distance from the atom nucleus, $V = 0$ when $x = \infty$ (Colinge and Colinge, 2002).....	47
Figure 3.5: The Coulomb, potential and the first three energy levels for a hydrogen atom (Shur, 1990).....	50
Figure 3.6: Energy band diagram for two non interacting hydrogen nuclei.....	50

Figure 3.7: As the nuclei are brought together, the upper energy levels merge and electrons in those levels are shared between atoms.....51

Figure 3.8: Permitted energy levels of an atom, a hypothetical molecule and a crystal of Lithium (Colinge and Colinge, 2002).....52

Figure 3.9a: One-Dimensional periodic potential distribution for a crystal.....54

Figure 3.9b: simplified one-dimensional periodic potential distribution used in the Kronig-Penney model.....54

Figure 3.10: The right-hand side of equation (3.45) for $P = 3\pi/2$ as a function of αa (Mahajan and Sree Harsha, 1998).....58

Figure 3.11: (a) The free-electron model of electrons as perturbed by a small periodic potential discontinuities in the energy at $k = n\pi/a$ in the extended representation. (b) the reduced representation in the first Brillouin zone achieved by translating band segments in (a) by $2\pi n/a$ to bring them into the basic zone. (c) Separate bands are indicated. (Mahajan and Sree Harsha, 1998).....60

Figure 3.12: Energy band diagram of (a) germanium, (b) silicon and (c) gallium arsenide.....61

Figure 3.13: General features of the energy-band structures for GaAs and Si showing allowed electron energies versus electron propagation vector k 62

Figure 3.14: Density of states as a function of Energy64

Figure 3.15: Fermi-Dirac function65

Figure 3.16: Schematics of the three general types of structural orders: (a) amorphous, (b) polycrystalline, (c) crystalline.	69
Figure 3.17: Two dimensional representation of the structure of (a) a crystalline solid and (b) an amorphous solid.	74
Figure 3.18: Schematic illustration of the free energy versus configuration curve.	75
Figure 3.19: (a) DOS of a crystalline semiconductor; (b) DOS models proposed by Mott (1967) (c) DOS models proposed by Cohen et. al. (1969) and (d) DOS models proposed by Marshall and Owen (1971). The hatched regions denote localized states. Note: the x-axis in all the 4 figures is logarithmic.	76
Figure 3.20: Basic modes of thin film growth	86
Figure 4.1: Absorption coefficient as a function of the photon energy in a typical semiconductor to illustrate various possible absorption processes.	91
Figure 4.2: A direct gap semiconductor	94
Figure 4.3: An indirect gap semiconductor	94
Figure 4.4: Diffraction of X-ray from a set of planes	97
Figure 4.5: Schematic for X-ray diffraction	98
Figure 4.6: Bragg-Brentano diffraction geometry	99
Figure 4.7: Illustration of Plane normal: the direction perpendicular to a plane of atoms. Diffraction vector: the vector that bisects the angle between the incident and diffracted beam	100
Figure 4.8: Illustration of the principle of EDX	102

Figure 4.9: Schematic diagram of a scanning electron microscope.	105
Figure 4.10: Signals produced by an electron beam incident on the specimen	105
Figure 5.1: schematic illustration of the experimental set up	109
Figure 5.2: Experimental set-up for the deposition process	110
Figure 5.3: Pictures of as-deposited thin films.	110
Figure 5.4: Schematic diagram of a single-beam spectrophotometer.	113
Figure 5.5: Samples loaded onto the diffractometer	115
Figure 5.6: Sample mounted on specimen stub for SEM	117
Figure 6.1a: X-ray diffraction pattern of CdS (as-deposited)	119
Figure 6.1b: X-ray diffraction pattern of CdS annealed at 400°C	120
Figure 6.2a: X-ray diffraction pattern of $\text{Cd}_{1-x}\text{Zn}_x\text{S}$, ($x=0.11$) as-deposited thin film ..	121
Figure 6.2b: X-ray diffraction pattern of $\text{Cd}_{1-x}\text{Zn}_x\text{S}$ ($x=0.11$), annealed at 400°C	121
Figure 6.3a: X-ray diffraction pattern of $\text{Cd}_{1-x}\text{Zn}_x\text{S}$ ($x=0.14$), as-deposited thin film ..	122
Figure 6.3b: X-ray diffraction pattern of $\text{Cd}_{1-x}\text{Zn}_x\text{S}$ ($x=0.14$), annealed at 400°C	122
Figure 6.4a: X-ray diffraction pattern of $\text{Cd}_{1-x}\text{Zn}_x\text{S}$ ($x=0.25$), as-deposited thin film ..	123
Figure 6.4b: X-ray diffraction pattern of $\text{Cd}_{1-x}\text{Zn}_x\text{S}$ ($x=0.25$), annealed at 400°C	123
Figure 6.5a: X-ray diffraction pattern of $\text{Cd}_{1-x}\text{Zn}_x\text{S}$ ($x=0.50$), as-deposited thin film ..	124
Figure 6.5b: X-ray diffraction pattern of $\text{Cd}_{1-x}\text{Zn}_x\text{S}$ ($x=0.50$), annealed at 400°C	124

Figure 6.6: X-ray diffraction pattern of $\text{Cd}_{1-x}\text{Zn}_x\text{S}$ ($x = 0.75$), annealed 400°C	125
Figure 6.7: X-ray diffraction pattern of ZnS annealed at 400°C	125
Figure 6.8a: X – ray diffraction pattern of CdS powder sample (as deposited)	127
Figure 6.8b: X – ray diffraction pattern of CdS powder sample (annealed at 400°C) .	128
Figure 6.9a: X – ray diffraction pattern of $\text{Cd}_{1-x}\text{Zn}_x\text{S}$ ($x = 0.06$) powder sample (as-deposited)	129
Figure 6.9b: X – ray diffraction pattern of $\text{Cd}_{1-x}\text{Zn}_x\text{S}$ ($x = 0.06$), powder sample (annealed at 400°C)	129
Figure 6.10a: X – ray diffraction pattern of $\text{Cd}_{1-x}\text{Zn}_x\text{S}$ ($x = 0.14$) powder sample (as-deposited)	130
Figure 6.10b: X – ray diffraction pattern of $\text{Cd}_{1-x}\text{Zn}_x\text{S}$ ($x = 0.14$), powder sample (annealed at 400°C)	130
Figure 6.11a: X – ray diffraction pattern of $\text{Cd}_{1-x}\text{Zn}_x\text{S}$ ($x = 0.20$), powder sample (as-deposited)	131
Figure 6.11b: X – ray diffraction pattern of $\text{Cd}_{1-x}\text{Zn}_x\text{S}$ ($x = 0.20$), powder sample (annealed at 400°C)	131
Figure 6.12a: X – ray diffraction pattern of $\text{Cd}_{1-x}\text{Zn}_x\text{S}$ ($x = 0.40$), powder sample (as-deposited)	132
Figure 6.12b: X – ray diffraction pattern of $\text{Cd}_{1-x}\text{Zn}_x\text{S}$ ($x = 0.40$), powder sample (annealed at 400°C)	132

Figure 6.13a: X – ray diffraction pattern of $\text{Cd}_{1-x}\text{Zn}_x\text{S}$ ($x = 0.60$), powder sample (as-deposited)	133
Figure 6.13b: X – ray diffraction pattern of $\text{Cd}_{1-x}\text{Zn}_x\text{S}$ ($x = 0.60$), powder sample (annealed at 400°C)	133
Figure 6.14a: X – ray diffraction pattern of $\text{Cd}_{1-x}\text{Zn}_x\text{S}$ ($x = 0.75$), powder sample (as-deposited)	134
Figure 6.14b: X – ray diffraction pattern of $\text{Cd}_{1-x}\text{Zn}_x\text{S}$ ($x = 0.75$), powder sample (annealed at 400°C)	134
Figure 6.15a: X – ray diffraction pattern of ZnS powder sample (as-deposited)	135
Figure 6.15b: X – ray diffraction pattern of ZnS powder sample (annealed at 400°C)	135
Figure 6.16: Variation of lattice parameter, d , with increasing zinc ion concentration	139
Figure 6.17: Variation of lattice parameter, d , with zinc ion concentration for thin films and powder samples	140
Figure 6.18: Variation of lattice parameters a and c with Zn ion content (annealed thin films).	141
Figure 6.19: Variation of lattice parameters a and c with Zn ion content (as-deposited powder samples).	142
Figure 6.20: Variation of lattice parameters a and c with Zn ion content (annealed powder samples).	142

Figure 6.21: Relation between $d_{002} \times 2$, $d_{004} \times 4$, and calculated value of c , for the annealed thin films143

Figure 6.22: Relation between $d_{002} \times 2$, $d_{004} \times 4$, and calculated value of c , for the as deposited powder samples144

Figure 6.23: Relation between $d_{002} \times 2$, $d_{004} \times 4$, and calculated value of c , for the annealed powder samples144

Figure 6.24: SEM micrograph of the as-deposited CdS thin film (magnification 40000x).....145

Figure 6.25: SEM micrograph of the as-deposited CdS thin film (magnification 16000x).....145

Figure 6.26: EDX spectrum of the as-deposited CdS thin film146

Figure 6.27: EDX elemental mapping of the as-deposited CdS Thin film147

Figure 6.28: SEM micrograph of the as-deposited $\text{Cd}_{0.86}\text{Zn}_{0.14}\text{S}$ thin film (magnification 12800x)148

Figure 6.29: SEM micrograph of the as-deposited $\text{Cd}_{0.86}\text{Zn}_{0.14}\text{S}$ thin film (magnification 3200x)149

Figure 6.30: SEM micrograph of the as-deposited $\text{Cd}_{0.86}\text{Zn}_{0.14}\text{S}$ thin film (magnification 25600x)149

Figure 6.31: EDX spectrum of the as-deposited $\text{Cd}_{0.86}\text{Zn}_{0.14}\text{S}$ thin film150

Figure 6.32: EDX line scan of the as-deposited $\text{Cd}_{0.86}\text{Zn}_{0.14}\text{S}$ thin film150

Figure 6.33: SEM micrographs of $\text{Cd}_{0.86}\text{Zn}_{0.14}\text{S}$ thin films annealed in air at 400°C for two hours (magnification 33000x)151

Figure 6.34: SEM micrographs of $\text{Cd}_{0.86}\text{Zn}_{0.14}\text{S}$ thin films annealed in air at 400°C for two hours (magnification 13000x)151

Figure 6.35: SEM micrograph of the as-deposited ZnS thin film (magnification 12708x).....152

Figure 6.36: SEM micrograph of as-deposited ZnS thin films (magnification 50830x).....152

Figure 6.37: SEM micrograph showing some nano size structures on the as-deposited ZnS thin film (magnification 4000x).153

Figure 6.38: EDX spectrum of the as-deposited ZnS thin films153

Figure 6.39: EDX line scan of the as-deposited ZnS thin films154

Figure 6.40: SEM micrograph of ZnS thin film annealed at 400°C (magnification 6354 x).....156

Figure 6.41: A plot of absorbance versus wavelength for $\text{Cd}_{1-x}\text{Zn}_x\text{S}$ ($0 \leq x \leq 1$) as deposited thin films.157

Figure 6.42: A graph of $(Ah\nu)^2$ plotted as a function of the photon energy, $h\nu$, for CdS thin film. Extrapolation of best fit line between $(Ah\nu)^2$ and $h\nu$ to intercept the $h\nu$ axis at $(Ah\nu)^2 = 0$ gives the band gap.159

Figure 6.43: A graph of $(Ah\nu)^2$ plotted as a function of the photon energy, $h\nu$, $\text{Cd}_{0.89}\text{Zn}_{0.11}\text{S}$ thin film. Extrapolation of best fit line between $(Ah\nu)^2$ and $h\nu$ to intercept

the $h\nu$ axis at $(A h\nu)^2 = 0$ gives the band gap. (Inset: band gap and defect state by Fan *et al.*, 2001)160

Figure 6.44: A graph of $(A h\nu)^2$ plotted as a function of the photon energy, $h\nu$, for $\text{Cd}_{0.86}\text{Zn}_{0.14}\text{S}$ thin film. Extrapolation of best fit line between $(A h\nu)^2$ and $h\nu$ to intercept the $h\nu$ axis at $(A h\nu)^2 = 0$ gives the band gap.162

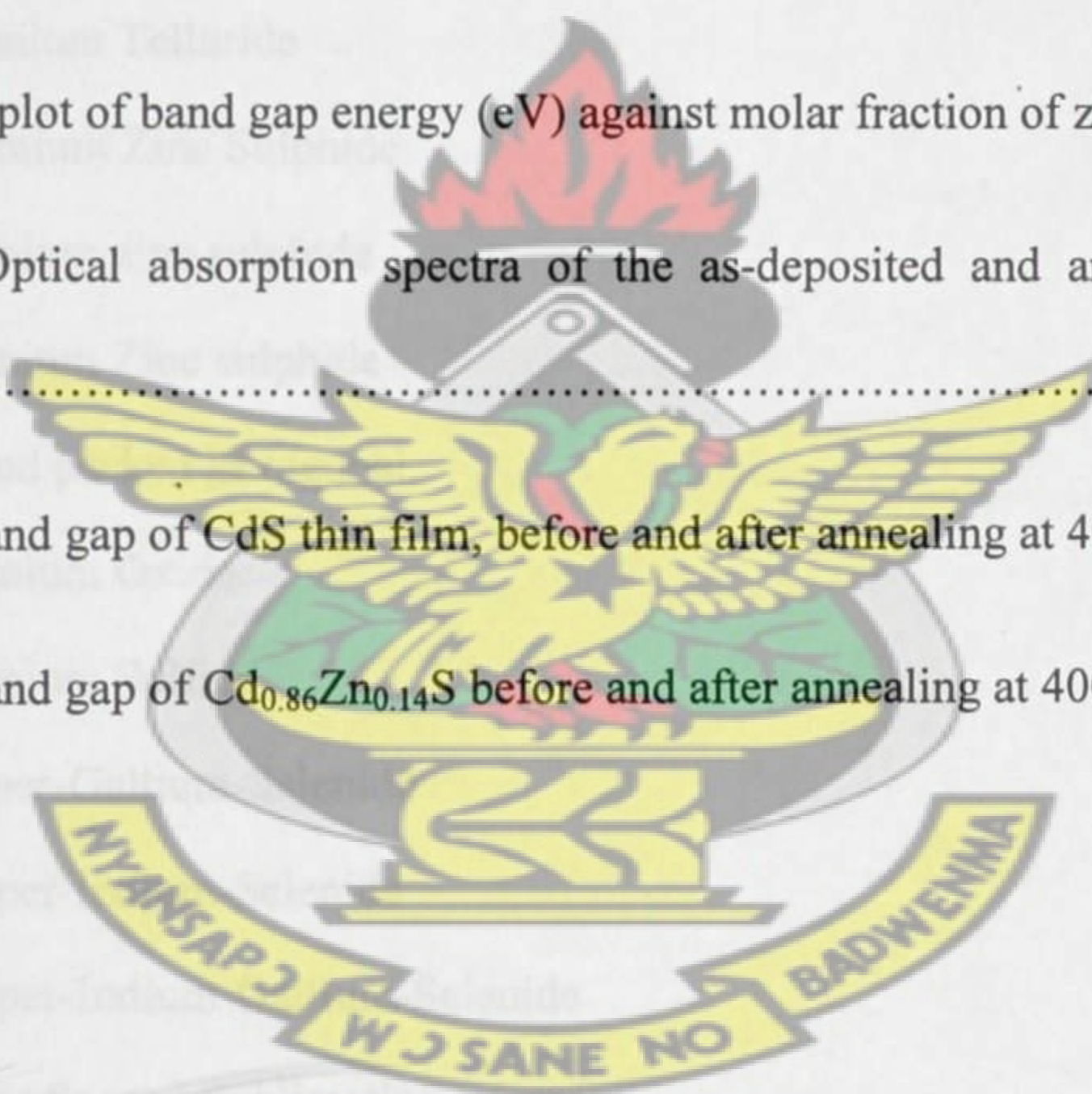
Figure 6.45: A graph of $(A h\nu)^2$ plotted as a function of the photon energy, $h\nu$, for ZnS thin film. Extrapolation of best fit line between $(A h\nu)^2$ and $h\nu$ to intercept the $h\nu$ axis at $(A h\nu)^2 = 0$ gives the band gap.163

Figure 6.46: A plot of band gap energy (eV) against molar fraction of zinc (x)164

Figure 6.47: Optical absorption spectra of the as-deposited and annealed CdS thin film.....165

Figure 6.48: Band gap of CdS thin film, before and after annealing at 400°C166

Figure 6.49: Band gap of $\text{Cd}_{0.86}\text{Zn}_{0.14}\text{S}$ before and after annealing at 400°C167



ABBREVIATIONS AND ACRONYMS

A	Absorbance
ACEE	American Council for an Energy-Efficient Economy
AFM	Atomic force microscopy
α	Absorption coefficient
ca	circa; Latin abbreviation for “approximately”
CBD	Chemical Bath Deposition
Cd	Cadmium
CdTe	Cadmium Telluride
(Cd, Zn)S	Cadmium Zinc Sulphide
CdZnS	Cadmium zinc sulphide
Cd_{1-x}Zn_xS	Cadmium Zinc sulphide
c.p.h	Closed packed hexagonal
CdO	Cadmium Oxide
CdS	Cadmium Sulfide
CGS	Copper-Gallium-Selenide
CIS	Copper-Indium-Selenide
CIGS	Copper-Indium-Gallium-Selenide
CSS	Close Spaced Sublimation
CSVT	Close space chemical vapour transport
CVD	Chemical Vapor Deposition
DI	De-ionized
DOS	Density of States
ED	Electron Diffraction
EDXRF	Energy Dispersive X-Ray Fluorescence

EDX	Energy Dispersive X-ray analysis
EDAX	Energy Dispersive X-ray analysis
E _g	Band gap
f.c.c	Face centred cubic
<i>h</i>	Planck constant
HP	Hewlett-Packard
In	Indium
IR	Infrared
JCPDS	Joint Committee for Powder Diffraction Standards
<i>k</i>	Wave vector, Extinction coefficient
λ	Wavelength
M	Molar concentration
MBE	Molecular Beam Epitaxy
NIR	Near Infrared
NREL	National Renewable Energy laboratory
P	Film Packing Factor
PV	Photovoltaic
<i>P(r)</i>	Radial distribution function
ρ	Resistivity
S	Sulphur
SEM	Scanning Electron Microscopy
SIA	Semiconductor Industry Association
T	Transmittance
TEA	Triethanolamine
τ_h	Heating time
τ_c	Cooling time

UV	Ultraviolet
ν	Photon frequency
VIS	Visible Spectrum
x, y	Compositional parameters/an integer number in polyacetylene
XRD	X-Ray Diffraction
Zn	Zinc
ZnS	Zinc Sulphide

KNUST



CHAPTER ONE

1. INTRODUCTION

Semiconductors have complex properties; many of these properties have been harnessed, and have been exploited in ingenious microelectronic devices. Over the years the devices have been rendered manufacturable by engineers and technologists (Korvink and Greiner, 2002). Discovery begun in 1821, when the German physicist Tomas Seebeck first noticed unusual properties of semiconductor materials, such as lead sulphide (PbS). The temperature dependence of the conductivity for a new class of materials – semiconductors - was reported by the English physicist Michael Faraday, in 1833. This dependence was very unusual. The resistance of these materials decreases as temperature increases whereas in metals, resistance always increases with temperature. The British engineer W. Smith discovered in 1873 that the resistivity of selenium, a semiconductor material, is very sensitive to light (Shur, 1996). The first practical application of semiconductors dates back to 1875, when Werner von Siemens invented a selenium photometer, and to 1878, when Alexander Graham Bell used this device for a wireless telephone communication system, and culminating most impressively with the invention of the transistor at Bell Laboratory in 1947 by Bardeen, Brattain, and Shockley. Semiconductors have since moulded and shaped the world of electronics and optoelectronics, and with this paradigm shift has come huge progress that has made life easier and technology more accessible to more and more people. From semiconductors to microelectronic and optoelectronic devices for information applications, these advances and applications were catalyzed by an improved understanding of the interrelationship

between different aspects (i.e., structure, properties, synthesis and processing, performance, and characterization of materials) of this multidisciplinary field (Yacobi, 2004).

In the field of renewable energy, semiconductor materials have made significant contribution to the development of alternative energy sources. A study conducted by the Washington DC-based American Council for an Energy-Efficient Economy (ACEEE) commissioned by the Semiconductor Industry Association (SIA), under the heading: "Semiconductor Technologies: The Potential to Revolutionize the United States of America (USA) Energy Productivity," in May 2009, found that, compared to the technologies available in 1976, the entire family of semiconductor-enabled technologies generated a net savings of about 775 billion kilowatt-hours (kWh) of electricity in the year 2006 alone, and but for these technologies, the USA might have had to build another 184 large electric power plants to satisfy the demand for goods and services. The study concluded that if new policies accelerated adoption of these technologies by just one percentage point per year, by 2030, the USA could decrease the amount of electricity used annually.

The most spectacular and most important application of semiconductors is the development of information technology. These developments have only been possible because of the miniaturization of the logic elements allowing the construction of compact systems with great computing power or memory. Miniaturization has become possible through the perfection of "planar" fabrication techniques. These allow "integration" of

circuits and thereby the production of devices containing thousands of elements on a few mm^2 . These integrated circuits operate from a power supply where nonelectrical forces, such as, chemical or mechanical forces, separate positive and negative electric charges. These separated charges create electric fields, and those electric fields make charge carriers, such as free electrons, to carry electric current. Such a supply can operate a computer, in which semiconductor devices perform many millions or even billions of operations per second (Shur, 1996). All this industrial development has come into existence only because physics allows us to understand the specific properties of semiconductors, and then use this understanding to create “electron machines” in the form of semiconductor devices (Sapoval and Herman, 1993). Semiconductor devices have penetrated into large parts of our lives. The modern desktop or laptop computer would be unthinkable without microelectronic semiconductor devices, and so would a myriad of other devices (Petterson and Bailey, 2005). More and more, these devices determine the competitiveness of our economy and the strength of our defense. Just recall the role of smart munitions and night vision devices in the Gulf war. Both sides used the same explosives and their shells were made from the same metal. However, the Allied forces had superior semiconductor electronics (Shur, 1996). New ideas in economics in 1990s (often linked to Paul Romer of Berkeley) emphasize the role of innovation (such as invention of a computer chip) in creating wealth (Shur, 1996). Semiconductors are and will be in the foreseeable future, the key elements for the majority of electronic systems, serving communications, signal processing, computing, and control applications in both the consumer and industrial markets (Encyclopedia Britannica, 2010).

In addition to being very important for materials science, the study of semiconductors is of great interest for fundamental research as well, as a great number of new phenomena can be observed in them. For example, the discovery of the quantum Hall effect arose from the possibility of creating semiconductor heterojunctions in which the electron gas is practically confined to a two-dimensional region next to the interface. This opened the way to the study of the properties rooted in the two-dimensional character of the system. Besides, very high purity materials can be fabricated from a semiconductor, which is a prerequisite to studying certain physical phenomena (Sólyom, 2008).

1.1 SEMICONDUCTOR MATERIALS

Essential physical properties of semiconductors are:

- their resistivities decrease as the temperature rises, at least for a certain temperature range, unlike metals;
- semiconductors are sensitive to visible light but transparent in the infrared. When irradiated, their resistivity decreases. If they are inhomogeneous, an induced electric field may appear;
- they often give rise to rectifying or non-ohmic contacts;
- they exhibit a strong thermoelectric effect, i.e., an electric field induced by a temperature gradient;
- their resistivity lies between 10^{-5} and 10^6 ohm-cm.

The materials possessing such properties are the elements of column IV of the periodic table, silicon and germanium, III – V compounds of the type GaAs, GaSb, InSb, InP and so forth, II – VI compounds such as CdSe, CdTe, and ZnS. In addition to these elemental

and binary semiconductors, materials such as ternary (e.g., $\text{Al}_x\text{Ga}_{1-x}\text{As}$, $\text{GaAs}_{1-x}\text{P}_x$, and $\text{Hg}_{1-x}\text{Cd}_x\text{Te}$) and quaternary (e.g., $\text{Ga}_x\text{In}_{1-x}\text{As}_y\text{P}_{1-y}$) alloys with “tunable” properties are also used in specific device applications. The subscript x and y are composition parameters. Organic compounds which are semiconductors include anthracene, $\text{C}_{14}\text{H}_{10}$, and polyacetylene $(\text{CH})_x$ (Yacobi, 2004; Balkanski and Wallis, 2000). It should be noted, however, that for semiconductors the boundaries for both the resistivity (between about 10^{-5} and $10^6 \Omega\text{-cm}$) and the upper limit of the energy gap (of about 4 eV) are only approximate. For example, diamond, having the energy gap of about 5.5 eV also exhibits semiconducting properties if properly processed (e.g., doped) for applications in semiconductor devices (Yacobi, 2004).

During the early 1950s germanium was the major semiconductor material. However, it proved unsuitable for many applications, because devices made of the material exhibited high leakage currents at only moderately elevated temperatures. Since the early 1960s silicon has become by far the most widely used semiconductor, virtually supplanting germanium as a material for device fabrication. The main reasons for this are twofold: (1) silicon devices exhibit much lower leakage currents, and (2) silicon dioxide (SiO_2), which is a high-quality insulator, is easy to incorporate as part of a silicon-based device. Thus, silicon technology has become very advanced and invasive, with silicon devices constituting more than 95 percent of all semiconductor products sold worldwide.

Compound semiconductors have been a subject of semiconductor research for nearly as long as elemental semiconductors such as silicon and germanium. Compound

semiconductors, whose merit of superior transport was recognized as early as 1952 by Welker, have continued to be of interest although their success has been narrower in scope. The areas of significant applications include light sources (light emitting diodes and light amplification by stimulated emission of radiation), microwave sources (Gunn diodes, Impatt diodes, etc.), microwave detectors (metal-semiconductor diodes, etc.), and infrared detectors. All of these applications have been areas of the semiconductor endeavour to which compound semiconductors are uniquely suited. Compound semiconductors have also made significant contributions to the generation of electricity from solar radiation. Today's most efficient technology for the generation of electricity from solar radiation is the use of multijunction solar cells made of III-V compound semiconductors. Efficiencies up to 39 % have already been reported under concentrated sunlight. These solar cells have initially been developed for powering satellites in space and are now starting to explore the terrestrial energy market through the use of photovoltaic concentrator systems. This opens a huge potential market for the application of compound semiconductor materials due to the large areas that are necessary to harvest sufficient amounts of energy from the sun. Concentrator systems using III-V solar cells have shown to be ecological and could play an important role for the sustainable energy generation of the future (Dimroth, 2005).

1.2 CADMIUM ZINC SULPHIDE

Interest in the preparation and study of the physical properties of ternary chalcogenide compounds for their possible application in solar cells, light emitting diodes and non-linear optical devices has been increasing in recent years (Ortega-Lopez *et al.*, 2003).

Ternary compounds are found to be promising materials for optoelectronic device applications such as green emitting devices and are suggested to be possible material for window layer of solar cells. These compounds are increasingly being studied for efficient solar energy conversion through photo-electrochemical solar cells and have become potential candidate for such applications (Woon-Jo and Gye-Choon, 2003; Padam and Rao, 1986; Pawar *et al.*, 1986). Cadmium zinc sulphide (Cd, Zn)S ternary alloy is one of the promising materials in this respect (Kumar *et al.*, 1998).

Cadmium zinc sulphide (Cd, Zn)S has the hexagonal wurtzite structure and a wider band gap than cadmium sulphide (Boyle *et al.*, 2000). Interest in (Cd, Zn)S has been driven by the expected improvement in performance of thin film photovoltaic cells CdTe- and CIS(CuInSe₂-based cells) using (Cd, Zn)S rather than the presently used CdS. This expectation arises mainly from the increased band gap of the Zn-containing solid solution, resulting in increased transparency to shorter wavelength of light. Cd_{1-x}Zn_xS ternary compounds can form a continuous series of solid solution allowing systematic variation of the band gap from 2.43 eV for CdS to 3.7 eV for ZnS by adjusting the composition (Yokogawa *et al.*, 1994). The use of the Cd_{1-x}Zn_xS window layer instead of CdS is suitable to circumvent window absorption losses as well as lattice mismatch problems associated with a quaternary solar absorber layer (Yamaguchi *et al.*, 1996).

Keeping these aspects in view, more attention is being given in producing good quality (Cd, Zn)S thin films for comprehensive optical studies and their various applications (Sanap and Pawar, 2011).

1.3 SYNTHESIS OF CADMIUM ZINC SULPHIDE THIN FILMS

There exist a huge variety of deposition processes and technologies for the preparation of (Cd, Zn)S thin films, which originate from purely physical or purely chemical processes. These include; electrodeposition (Al Bassan, 1999), chemical bath deposition (Yamaguchi *et al.*, 1996), successive ionic layer adsorption and reaction (SILAR) (Laukaitish, 2000) and metal organic chemical vapor deposition (Chu *et al.*, 1991). One driver for such research is to develop cheap reproducible and relatively simple routes for applications where low capital cost is important for successful commercialization e.g. thin film photovoltaic technologies (Boyle *et al.*, 2000). A method which may meet the above criteria is Chemical Bath Deposition (Lincot *et al.*, 1999; Fröment and Lincot, 1995).

Chemical bath deposition (CBD) is becoming an important deposition technique for thin films of compound materials like chalcogenides (Hodes, 2002). A major success can be found in the recent period with the deposition of semiconducting cadmium sulphide, or zinc sulphide buffer or window layers, in efficient copper indium diselenide or cadmium telluride thin film solar cells. CBD takes advantage of the use of a reaction from a solution where different precursors can be dissolved easily either in the ionic or molecular form and react chemically on the substrates leading to film formation. The key advantages are low cost, large area and low temperature atmospheric processing (Lincot *et al.*, 1999).

1.3.1 Acidic Chemical baths

Typical CBD processes for sulphides employ an alkaline medium containing the chalcogenide source, the metal ion and added base. A chelating agent is used to limit the hydrolysis of the metal ion and impart some stability to the bath, which would otherwise undergo rapid hydrolysis and precipitation. The technique under these conditions relies on the slow release of sulphide ions into an alkaline solution in which the free metal ion is buffered at a low concentration (Boyle *et al.*, 1999). There are few reports of the CBD of the ternary $\text{Cd}_{1-x}\text{Zn}_x\text{S}$; the most convincing studies demonstrate that the production of good quality thin films is very difficult by conventional chemical bath system (Doña and Herrero, 1995). The deposition of ternary materials such as $\text{Cd}_{1-x}\text{Zn}_x\text{S}$ by CBD methods is a problem due to differing hydrolytic stabilities of the two metals. O'Brien and McAleese (1998), have reviewed some of the chemistry underlying such processes with some emphasis on the incompatibility between the conditions for the deposition of zinc and cadmium sulphide. In fact, the most important difference between CBD of CdS and ZnS is related to the solubility products of the hydroxide and sulphide of the two metals. The solubility product of zinc sulphide ($K_{sp} = 3 \times 10^{-25}$) is much closer to that of zinc hydroxide ($K_{sp} = 10^{-16}$) compared to cadmium sulphide ($K_{sp} = 10^{-28}$), and cadmium hydroxide ($K_{sp} = 10^{-14}$) compounds. This difference indicates that metal hydroxide insertion in CBD-ZnS layers is much more likely than for CdS. Many of the films reported as ZnS which have not been rigorously characterized are probably at best heavily contaminated with zinc oxide or hydroxide (O'Brien and McAleese, 1998). The obvious solution to this problem is to deposit (Cd, Zn)S at a lower pH where the

hydroxide concentration will be lower. This has led to development of a more favorable medium for the formation of $\text{Cd}_{1-x}\text{Zn}_x\text{S}$ thin films.

Boyle *et al.* (2000), developed a novel approach for the deposition of such films, based on the use of low solution pH, and have reported the first definitive evidence for the successful preparation of polycrystalline thin films of cadmium zinc sulphide by chemical bath deposition from acidic solutions. This acidic CBD route provides films of a well defined ternary composition, in contrast to those reported from basic solution (Boyle *et al.*, 2000).

This thesis reports on the synthesis and characterization of cadmium zinc sulphide thin films deposited from chemical baths containing zinc chloride, cadmium chloride, urea and thioacetamide at modestly acid values of pH.

1.4 CHARACTERIZATION

Properties exhibited by thin films are diverse and the ability to tailor numerous properties of thin-films required for an efficient device such as a solar cell, demands good understanding of the material produced, with the help of a range of monitoring and analytic facilities. Only then can the material be suitably tailored to suit the application.

Characterization, when used in materials science, refers to the use of external techniques to probe into the internal structure and properties of a material. This involves investigating the relationship between the structure of materials at atomic or molecular scales and their macroscopic properties.

In this study, the composition of the deposit, crystal structure and morphology were studied using Powder X-Ray diffraction (XRD) and Scanning electron microscopy (SEM). Elemental analysis was carried out using Energy Dispersive X-ray analysis (EDAX). Optical Absorption spectroscopy was used to investigate the optical properties.

1.5 OBJECTIVES OF THE RESEARCH

The research presented in this thesis has the following objectives:

- I. **To deposit $\text{Cd}_{1-x}\text{Zn}_x\text{S}$ thin films from acidic chemical baths;** Physical properties of thin films are highly sensitive to the deposition parameters and if these parameters are not carefully chosen, they can produce a multitude of undesired results. The synthesis method, would require a good knowledge of the deposition mechanism and carefully select deposition parameters such as pH, temperature, and precursor concentrations, and finally deposit a true ternary compound of cadmium zinc sulphide.
- II. **To investigate the composition, structure, morphology, and optical properties of $\text{Cd}_{1-x}\text{Zn}_x\text{S}$ thin films prepared under the deposition conditions used in I;** The method used to prepare or deposit a material can profoundly affect the phase, composition, thermal stability, and morphology, which in turn can influence the functional behaviour of the material (Ramasamy *et al.*, 2011). Investigating the composition of the deposit, crystal phase, orientation and morphology helps to describe those features of composition and structure (including defects) of a material that are significant for a particular preparation, study of properties, or

use, and suffice for reproduction of the material. The effect of increasing zinc content (x value) on structural, morphological and some optical properties would also be studied.

III. **To investigate the effect of thermal annealing on the optical properties, structure and morphology of the films;** Annealing is heat treatment of materials at elevated temperatures aimed at investigating or improving their properties. The results of annealing depend significantly on its kinetics: the rate of heating and cooling and the time of exposure at a given temperature. Being able to tune the properties of $\text{Cd}_{1-x}\text{Zn}_x\text{S}$ thin film by thermally annealing it or varying the relative ratio of cadmium and zinc may make it fit buffer layer material with enhanced performance.

All these investigations are necessary for determining the right conditions for deposition of a material, which provide for optimum device performance and also help tailor the physical properties of the material to suit the application for which it is intended.

Although a lot of work has been done on the deposition of CdZnS for photovoltaic applications, there are very few reports on the preparation of CdZnS thin films from acidic chemical baths. The few reports available on the deposition of CdZnS from acidic chemical baths, investigate the physical properties of single compositions, most of the time with low zinc content. For the first time, this investigation looks at the crystal structure, morphology and optical properties of CdZnS deposited from acidic chemical baths, over the entire compositional range (that is, $\text{Cd}_{1-x}\text{Zn}_x\text{S}$, $0 \leq x \leq 1$).

1.6 JUSTIFICATION OF THE RESEARCH

There is a growing need for energy in the world and since the traditional energy sources based on fossil fuels are limited and will be exhausted in future, PV solar energy is considered a promising energy source candidate. Large-scale application of PV solar energy will also contribute to the diversification of energy sources resulting in more equal distribution of energy sources in the world (NREL Report, 2001 - 2002). The most widely used commercial solar cells are made from single crystalline silicon and efficiencies up to 26.5 % are reported for commercial products. However, such single crystalline solar cells are relatively expensive with the silicon itself making up 20 to 40 % of the final cost (Afzaal and O'Brien, 2006). Amorphous silicon solar cells can be produced at lower temperatures and deposited on low-cost flexible substrates such as plastics or metal foils. Ultimately, the amorphous cells tend to degrade when exposed to sunlight and their efficiency decreases by 10 to 20 % (Afzaal and O'Brien, 2006). Therefore, a large-scale application of renewable energy sources as electricity power sources is not yet economically attractive in the industrialized countries. One of the most promising strategies for lowering PV costs is the use of thin film technologies in which the PV materials are deposited onto inexpensive large area substrates such as window glass and flexible substrates. Benefiting from the inherent advantages to thin film PV will require breakthroughs in reducing manufacturing costs, primarily by improving yields and increasing throughput (NREL Report, 2001 - 2002). CIGS-based thin-film solar cell modules currently represent the highest-efficiency alternative for large-scale, commercial thin-film solar cells. Several companies have confirmed module efficiencies exceeding 13 %. CIGS thin film solar cells were typically fabricated using a high-resistivity

cadmium sulfide (CdS) buffer layer deposited by (CBD) in order to avoid the formation of undesirable shunt paths (Liu and Mao, 2009).

The reported efficiencies of CuInGaSe₂ and CdTe based solar cells (using CdS buffer layer) have reached 19.9 and 16.5 %, respectively (Repins *et al.*, 2008; Wu *et al.*, 2001). However, CdS window layer absorbs the blue portion of the solar spectrum for its relatively low band gap and it has lattice mismatch problems associated with a quaternary solar absorber layer, which inhibit the higher performance of the solar cell devices (Meng *et al.*, 2010). These issues have prompted much research in developing a better buffer layer. Cadmium Zinc Sulphide ternary material with wurtzite structure fits this application (AbuShama *et al.*, 2005). Cd_{1-x}Zn_xS has a larger band gap than CdS and it is suitable to circumvent the problems mentioned above (Borse *et al.*, 2007). Thus, tailoring the opto-electronic properties of CdZnS buffer layers to improve the performance of thin film photovoltaics is currently an active area of research. (McPeak, 2010)

1.7 STRUCTURE OF THE THESIS

The thesis is organized into seven chapters. The first chapter gives an introduction to the impact of semiconductor research over the years, and how new semiconductor materials including ternary and quaternary alloys are being developed and used. Interests in cadmium zinc sulphide as well as the reasons for using acidic chemical baths instead of the conventional alkali baths for the deposition of this material are explained. The reasons for characterization are also given. The chapter also states the justification of the research and finally describes how the thesis is structured.

The second Chapter introduces thin film materials, chemical bath deposition, which is followed by a description of the structure of some important II-VI semiconductor materials, and finally a review of cadmium zinc sulphide thin films prepared by chemical bath deposition.

The third chapter treats the relevant theory; The physics of semiconductors, classification of semiconductors and the basic principles of chemical bath deposition.

The theories behind the main techniques used for characterizing the thin films are presented in chapter four.

Characterization of the thin films and the precipitates forms the basis for chapter six. Data obtained from analytical techniques such as X-ray diffraction, Optical absorption, scanning electron microscopy and energy dispersive x-ray analysis are presented in graphical format and discussed.

The seventh chapter presents conclusions that can be made from the results presented in the preceding chapters. Recommendations relating to possible future work are also made.

Lastly, references cited in this thesis and appendices are presented.

CHAPTER TWO

2. LITERATURE REVIEW

This chapter begins with an introduction to thin films, explains their importance to the study of semiconductor materials and mentions the various techniques used in the deposition of thin films. This is followed by a brief history of chemical bath deposition as well as an explanation of the CBD process. A description of the structure of some important II- VI semiconductor materials, and a review of cadmium zinc sulphide thin films prepared by chemical bath deposition are presented.

2.1 THIN FILMS

In recent times, the study of semiconductors in the bulk has been replaced with that of thin films. Thin film technique is one of the most fully-fledged technologies that greatly contribute to developing the study of semiconductors by giving a clear indication of their chemical and physical properties (Chopra, 1969). According to Chopra *et al.* (2004), a thin film is a material created *ab initio* by the random nucleation and growth processes of individually condensing (or reacting) atomic (or ionic or molecular) species on a substrate. The structural, chemical, metallurgical and physical properties of such a material are strongly dependent on a large number of deposition parameters and may also be thickness dependent. Thin-films may encompass a considerable thickness range, varying from a few nanometers to tens of micrometers and thus are best defined in terms of the birth processes rather than by thickness. The atomistic, random nucleation and growth processes bestow new and exotic properties to thin-film materials (Chopra, 1969). These properties can be controlled and reproduced, provided a range of deposition parameters are monitored and controlled

precisely. In addition to major contributions to a variety of new and future scientifically based technology, thin film studies have directly and indirectly advanced many new areas of research in solid state physics and chemistry which are based on phenomena uniquely characteristic of thickness, geometry and structure of films (Nadeem *et al.*, 2005). Semiconductor thin film technology has attracted much attention, because of its matchless size dependent properties and applications in optoelectronics devices such as, solar cells, sensors and laser materials. As thin film deposition processes have developed very rapidly over the past 25 years, particularly in the context of semiconductor devices, processes have become highly specialized (Ohring, 1992; Venables, 2003). Presently, rapidly changing needs for thin film materials and devices are creating new opportunities for the development of new processes, materials and technologies.

2.2: THIN FILM DEPOSITION TECHNIQUES

There exists a huge variety of thin film deposition processes and technologies which originate from purely physical or purely chemical processes. These include, vacuum evaporating, screen printing, sintering, chemical deposition, physical vapour deposition, spray pyrolysis, dip technique, electrodeposition etc. Despite the existence of these large variety of deposition techniques, searching for the most reliable and economic deposition technique has always been the main goal. Chemical bath deposition (CBD) offers a simple and inexpensive route to deposit semiconductor nanostructures and thin films, but lack of fundamental understanding and control of the underlying chemistry has limited its versatility (McPeak 2010). CBD is traditionally performed in a batch reactor, requiring only a substrate to be immersed in a supersaturated solution of aqueous precursors such as metal salts, complexing agents, and pH buffers. Highlights of CBD include low cost, operation at low temperature and atmospheric pressure, and scalability to large area substrates (McPeak, 2010). Chemical bath deposition is

becoming an important deposition technique for thin films of compound materials like chalcogenides (Hodes, 2002).

2.2.1: Chemical Bath Deposition

Chemical bath deposition of films is not a new technique. Liebig (1835) reported the first deposition of silver—the silver mirror deposition—using a chemical solution technique. The first reported chemical bath deposition of a compound semiconductor film appears to be formation of “lusterfarben” (lustrous colours) on various metals from thiosulphate solutions of lead acetate, copper sulphate, and antimony tartrate, giving films of PbS, Cu-S or Sb-S, which possessed “splendid” colours (interference colours resulting from various thicknesses of the deposited films) (Pusher, 1869). Emerson-Reynolds (1884) reported deposition of PbS films by reaction between thiourea (thiocarbamide) and alkaline lead tartrate, where the metallic sulphide became firmly attached as a specular layer to the sides of the vessel. A wide range of substrates (apart from a glass beaker), was successfully used for this deposition; porcelain, ebonite, iron, steel, and brass were specifically mentioned. Even more important, the deposits were very adherent, as quantified by their ability to withstand considerable friction with a ‘wash’ leather, and under this treatment take a fine polish (Hodes, 2002). Rosenheim *et al.* (1906) reported infrared photoconductivity in CBD PbS, and this application has been a central driving force for subsequent investigations in CBD lead chalcogenide films. The early literature invariably mentions the pioneering work of Kutscher in Germany, during World War II, in developing CBD PbS and PbSe films for infrared detectors. However, the apparent lack, in all these references to Kutscher’s studies, of any published papers might suggest (to the overly suspicious reader) a possible military involvement in these studies (Hodes, 2002). These (and subsequent) studies succeeded to the

extent that CBD was, and apparently still is, the main technique used in making commercial PbS and PbSe infrared detectors. Vacuum evaporation was the only competing technology (Bube, 1960; Bode, 1966). For a long time, CBD was then essentially limited to PbS and PbSe. It was not until 1961 that deposition of CdS, now the most widely studied material in CBD, was explicitly reported by Mokrushin and Tkachev (1961). Over the past decade CBD has experienced an increased level of interest. A simple literature search in the Web of Science for chemical bath deposition shows a steady increase in publications over the past decade from 53 publications in the year 2000 to 211 publications in 2009. This renaissance in CBD has been primarily fuelled by a need to deposit large area semiconductor films and nanowire arrays for inexpensive photovoltaic devices (McPeak, 2010).

The range of materials deposited by CBD was gradually extended, particularly in the 1980s, to include sulphides and selenides of many metals, some oxides, and also many ternary compounds. Chemical deposition received a major impetus after CdS films, chemically deposited onto CdTe (and, later, onto CuInSe₂) films, were shown to give superior photovoltaic (PV) cells compared with the previously evaporated CdS. The CBD method is presently attracting considerable attention, as these do not require sophisticated instrumentation like vacuum system and other expensive equipments. Simple equipments like hot plate with magnetic stirrer are needed. The starting chemicals are commonly available and cheap. Thiourea, thioacetamide, thiosulphate and sodium sulphide are generally used as sulphide precursors. Metallic precursors are metal complexed ions with ammonia ligands, for instance (Chopra, 1982). The reaction takes place between the dissolved precursors generally in aqueous solution at low temperature (300 to 353 K). With CBD methods, a large number of substrates can be coated in a single run with a proper jig design (Pawar *et al.*, 2011).

Chemical bath deposition (CBD) which is also known as solution growth, controlled precipitation, or simply chemical deposition, recently has emerged as the method for the deposition of metal chalcogenide thin films (Hodes, 2002). Another cause of interest in this technique is due to the fact that the crystals in most as-deposited CBD films are very small. Considering the current interest in nanoparticles, CBD is an excellent technique to deposit nanocrystalline films. More specifically, if the nanocrystals are small enough, they exhibit size quantization, the most obvious manifestation of which is an increase in the optical band gap with decrease in crystal size, as was shown for CBD CdSe (Hodes *et al.*, 1987) and later for CBD PbSe (Hodes and Albu-Yaron, 1988; Gorer *et al.*, 1995). In fact, the changes in optical spectra that occurred in these films as a function of nanocrystal size were exploited to provide information on the different mechanisms of the deposition process (Gorer and Hodes, 1994). Chemical bath deposition has also been emphasized as a technique to form solar control coatings. Solar control coatings are envisaged for use on windows in hot climates and possess the (ideal) characteristic of moderate to high visible transmission to provide adequate lighting, together with high infrared (0.7 to 2.5 μm) reflectance to minimize heating by solar energy. CBD is a potentially suitable method to prepare these coatings on the large areas of glass that would be needed. Most of the work in this field has been carried out by Nair and Nair (1990) in Mexico using various semiconductor films, mainly PbS and Cu_xS .

2.2.1.1. A Brief Explanation of the CBD Process

Chemical bath deposition refers to the deposition of films on a solid substrate from a reaction occurring in a solution (almost always aqueous) (Hodes, 2002). Using the prototypical CdS as an example, a Cd salt in solution can be converted to CdS by adding sulphide ions (e.g., as H_2S or Na_2S); CdS immediately precipitates (unless the solution is very dilute—a few millimolar or less, in which case CdS often forms as a colloidal sol). In CBD, this process is modified such that precipitation is controlled to eliminate or reduce spontaneous precipitation. This allows the metal ion to diffuse and form gradually on the substrate (at the early stages of deposition), rather than aggregate into larger particles in solution and precipitate out. The first method of controlling the reaction is by complexing the metal ions such that only a controlled number of free ions are available. The second method of controlling the reaction is by the slow and uniform generation of the chalcogen ions in solution. The rate of generation of sulphide, and therefore reaction rate, can be controlled through a number of parameters, in particular the concentration of sulphide-forming precursor, solution temperature, and pH. Although CBD can be carried out in both acidic and alkaline solutions, most CBD reactions have been carried out in alkaline solutions. The chalcogenide precursor must not be too stable under all conditions, otherwise they will not work.

In principle, CBD can be used to deposit any compound that satisfies four basic requirements.

- i. The compound can be made by simple precipitation. This generally, although not exclusively, refers to the formation of a stoichiometric compound formed by ionic reaction.
- ii. The compound should be relatively (and preferably highly) insoluble in the solution used (except in a very few cases, this has been water).

- iii. The compound should be chemically stable in the solution. If the reaction proceeds via the free anion, then this anion should be relatively slowly generated (to prevent sudden precipitation).
- iv. If the reaction is of the complex-decomposition type, then decomposition of the metal complex should similarly occur relatively slowly

Of course there are other specific factors that need to be taken into account, particularly whether the compound will form an adherent film on the substrate or not. However, the preceding four factors are general requirements. Despite the advances that have been made using CBD, the full development of the technology has been hampered by poor understanding of the relationships between process chemistry and film structure, factors that are dependent on the properties of the bath and deposition precursors. The process is sensitive to precursor concentrations and to the substrate used (Shandalov *et al.*, 2004; Shandalov *et al.*, 2003). The optimal deposition parameters are generally different for each compound deposited. Although there have been numerous papers published, reporting the preparation of chalcogenide thin films using CBD, Kaur *et al.* (1980), point out that the process has remained recipe oriented with little understanding of the kinetics of the process. With a few exceptions, this is also true regarding the mechanistic understanding of the process. There is, therefore, a need for careful investigation of the CBD process and identification of the conditions that favour high quality coherent deposits.

The basic principles of CBD will be explained in chapter three.

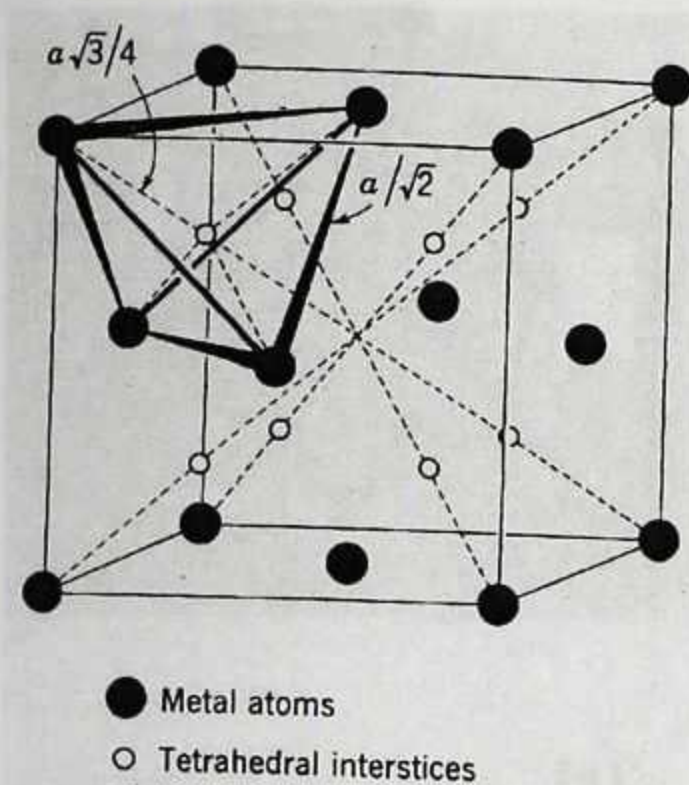
2.3. CRYSTAL STRUCTURE OF SOME IMPORTANT II – VI CHALCOGENIDE SEMICONDUCTOR MATERIALS

II–VI chalcogenide semiconductor materials show structural duality, and can be formed as either sphalerite (cubic, zinc blend type) or wurtzite (hexagonal type) (Bouroushian *et al.*, 1997). This section examines the crystal structure of some important II – VI chalcogenide semiconductor materials namely; cadmium sulphide, zinc sulphide, and cadmium zinc sulphide

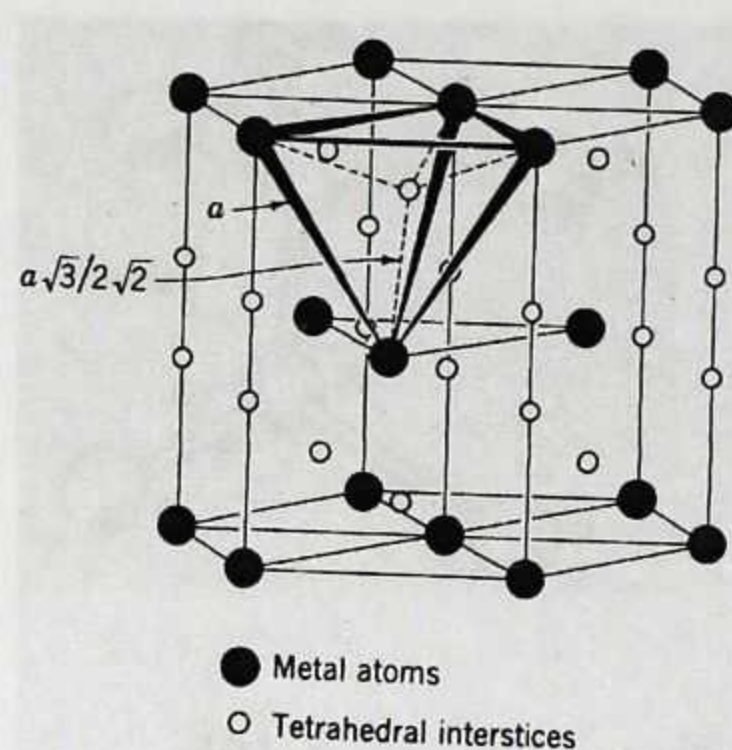
KNUST

2.3.1. Cadmium Sulphide

CdS is an important semiconductor with a direct band gap of 2.42 eV, which falls in the visible spectrum at room temperature. The melting point of CdS is 1475 °C. It exists in two crystallographic phases namely, the α - and β -phases. The α -phase of CdS is a wurtzite structure. This structure is hexagonal with $a = 4.1348 \text{ \AA}$ and $b = 6.77490 \text{ \AA}$. The β -phase is zinc blende with an f.c.c. structure with $a = 5.818 \text{ \AA}$ (Boakye and Nusenu, 1996). This structure may be regarded as two interpenetrating face centred lattices of the elements, with the corner of one located at the position $\frac{1}{4} \frac{1}{4} \frac{1}{4}$ of the other, as in the diamond structure. The zinc blende structure is related to the wurtzite structure which has one kind of atom on c.p.h. positions and the other at intermediate positions, corresponding to tetrahedral voids, where each atom is surrounded symmetrically by four atoms of the other kind (Barrett and Massalski, 1966). The hexagonal layers are stacked in one sequence in the wurtzite and in another in zinc blende and stacking faults are frequent (Jagodzinski, 1949). The wurtzite phase is thermodynamically slightly more stable (Hodes, 2002). The wurtzite-zinc blende transformation occurs at a temperature of 1000 °C (Wyckoff, 1963).



(a)



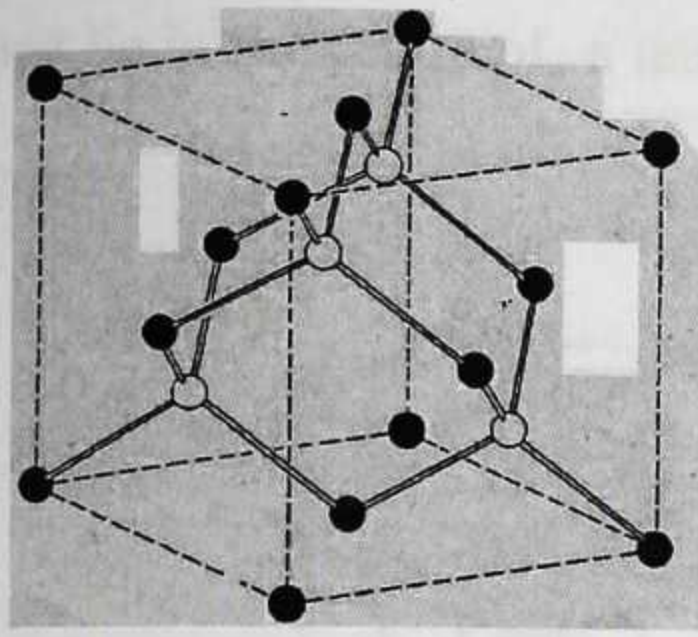
(b)

Figure 2.1: Tetrahedral voids in the f.c.c structure, (b) Tetrahedral voids in the c.p.h. structure (Barrett and Massalski, 1980)

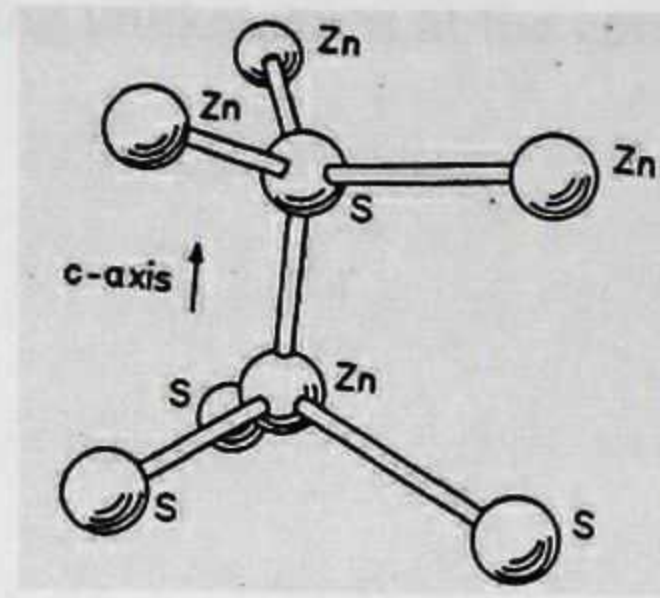
Figure 2.1(a) and (b) shows the lattice sites occupied by metal ions and the tetrahedral interstices in the f.c.c and c.p.h structures. The tetrahedral holes of the c.p.h. structure are partially occupied in the structure of wurtzite, as are the tetrahedral holes in the f.c.c. structure partially occupied in the case of zinc blende (Barrett and Massalski, 1980).

2.3.2. Zinc Sulphide

ZnS is an important group II-VI semiconductor with a large direct band gap which lies between 3.5 to 3.7 eV in the UV range (Vipin *et al.*, 2008). Zinc sulphide is a white to yellow-coloured powder or crystal with molecular mass of 97.474 gmol^{-1} and density of 4.090 gcm^{-3} . It is typically encountered in the more stable cubic form, known also as zinc blende or sphalerite.



(a)



(b)

Figure 2.2: Zinc blende Lattice: (a) The Cubic Unit Cell (b) Tetrahedral Bonding Configuration

Figure 2.2 (a) and (b) shows the cubic unit cell of zinc blende lattice (ZnS), and the tetrahedral coordination. ZnS can also exist in the hexagonal form which is known, both as a synthetic material and as the mineral wurtzite. Both sphalerite and wurtzite are intrinsic, wide-band gap semiconductors. The cubic form has a band gap of 3.54 eV at 300 K whereas the hexagonal form has a band gap of 3.91 eV (Wells, 1984). The cubic form is stable at room temperature, while the less dense hexagonal form (wurtzite) is stable above 1020 °C at atmospheric pressure (Gilbert *et al.*, 2002).

2.3.3. Cadmium Zinc Sulphide

Thin films of $\text{Cd}_{1-x}\text{Zn}_x\text{S}$ have properties between those of ZnS and CdS (Ramasamy *et al.*, 2011). As mentioned earlier, cadmium sulphide and zinc sulphide can crystallize in two polymorphic modifications, either in a cubic sphalerite structure or as a hexagonal wurtzite structure. Throughout most of the composition range of $\text{Cd}_{1-x}\text{Zn}_x\text{S}$, the wurtzite structure is the stable one. Only when the concentration of zinc sulphide nears 100 % does the sphalerite form predominate (Cherin *et al.*, 1970). The wurtzite phase can be considered as two interpenetrating hexagonal structures, one composed of cations and the other of anions. All

the atoms lie in the centre of a tetrahedra containing unlike atoms at the corners (Cherin *et al.*, 1970).

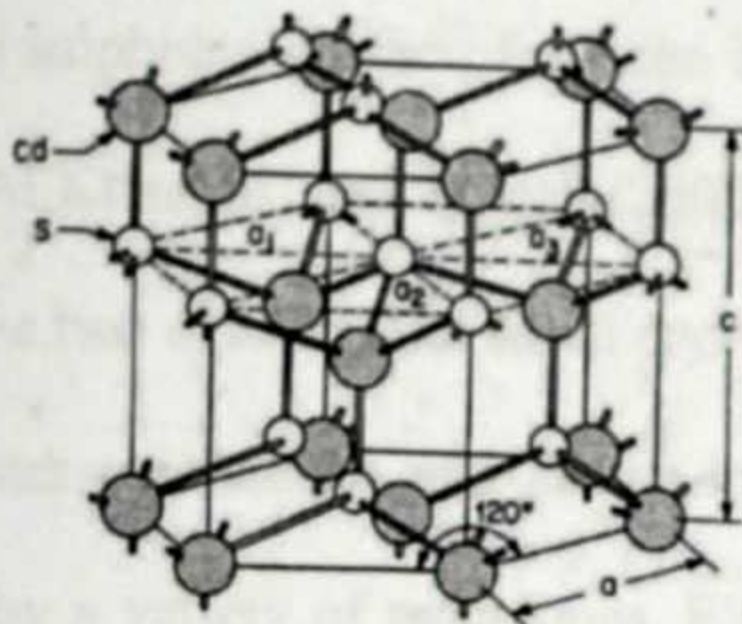


Figure 2.3: hexagonal close packed structure of CdS

Figure 2.3 shows the hexagonal structure of CdS. It is considered that during formation of $\text{Cd}_{1-x}\text{Zn}_x\text{S}$, the Zn^{2+} ions are incorporated in the CdS lattice or entered in its interstitial sites because the radii of Zn^{2+} ion (0.74 \AA) is smaller than that of Cd^{2+} (0.97 \AA) (Prem Kumar *et al.*, 2010).

2.4. REVIEW OF CADMIUM ZINC SULPHIDE THIN FILMS PREPARED BY CHEMICAL BATH DEPOSITION

By far the greatest interest and effort in the CBD of ternary semiconductors has been focused on cadmium zinc sulphide (Cd, ZnS). This literature review summarizes some of the various techniques used in the preparation of chemical bath deposited Cadmium zinc sulphide thin films and the results of their characterization.

The first well-characterized deposition of a true $(\text{Cd, Zn})\text{S}$ alloy film prepared by chemical bath deposition was described by Padam *et al.* (1988). In their work, Cd and Zn acetates were used in various ratios complexed with ammonia, TEA and thiourea. The deposition temperature was between 90 and $95 \text{ }^\circ\text{C}$. $\text{Cd}_{1-x}\text{Zn}_x\text{S}$, (for $0 \leq x \leq 1$) were deposited onto a

glass substrate. Interestingly, the Zn was more heavily complexed than the Cd in this solution, which shows that the mechanism of deposition is not one based solely on solubility product of the sulphides. In fact, from the crystal size measurement of a similar deposition described by Al Kuhaimi and Tulbah (2000), it is possible that the deposition mechanism is different for the two cations. The small crystals of pure ZnS and the larger ones of pure CdS suggest a cluster mechanism and an ion-by-ion mechanism, respectively. The films were characterized by a variety of techniques. Elemental analysis using electron diffraction (ED) showed that the Zn:Cd ratio in the film was almost equal. X-ray diffraction (XRD) and ED were used for phase and compositional analysis. All the compositions up to 80 % Zn were wurtzite structure, while pure ZnS was sphalerite. Interestingly, while most of the films gave ring ED patterns showing nonoriented growth, some showed a degree of orientation, in spite of the glass substrate. The band gap, calculated from optical absorption spectroscopy, varied almost linearly with composition between that of CdS (2.4 eV) and ZnS (3.6 eV). The films were all n-type (hot probe) with resistivity, ρ that varied linearly on a log ρ scale from $10^9 \Omega\text{-cm}$ (CdS) to $10^{12} \Omega\text{-cm}$ (ZnS). Doping by Indium (as InCl_3 in the deposition solution) reduced ρ ; e.g., for a $\text{Cd}_{0.8}\text{Zn}_{0.2}\text{S}$ film, ρ dropped linearly on a log ρ scale with indium content from about $10^{10} \Omega\text{-cm}$ (undoped) to around $10^5 \Omega\text{-cm}$ (1.5 % Indium - the indium ratio in the film was similar to that in the solution). At high indium ratios, ρ increased, explained by a decrease in mobility due to scattering by In. Annealing in H_2 at 200°C also decreased ρ . For example, a $\text{Cd}_{0.8}\text{Zn}_{0.2}\text{S}$: 1.5 % indium film, showed a minimum value for ρ of approximately $10 \Omega\text{-cm}$, presumably due to loss of S.

This same method was more recently repeated with very similar results by Al Kuhaimi and Tulbah, (2000). It was additionally found that the films were strongly textured, with only one

XRD peak—either (001) wurtzite or (111) sphalerite, although this texture was lost if a subsequent layer was deposited to produce thicker films. The crystal size measured from XRD peak width varied from 20 nm (CdS) to 9 nm (ZnS). The band gap varied between the same limits as found in the previous study, but changed more rapidly for high Zn content. The resistivity of the films varied linearly on a log ρ scale from $10^9 \Omega\text{-cm}$ (CdS) to $10^{14} \Omega\text{-cm}$ (ZnS), the latter, higher than the value measured by Padam *et al.* (1988), as evidenced in Figure 2.4.

KNUST

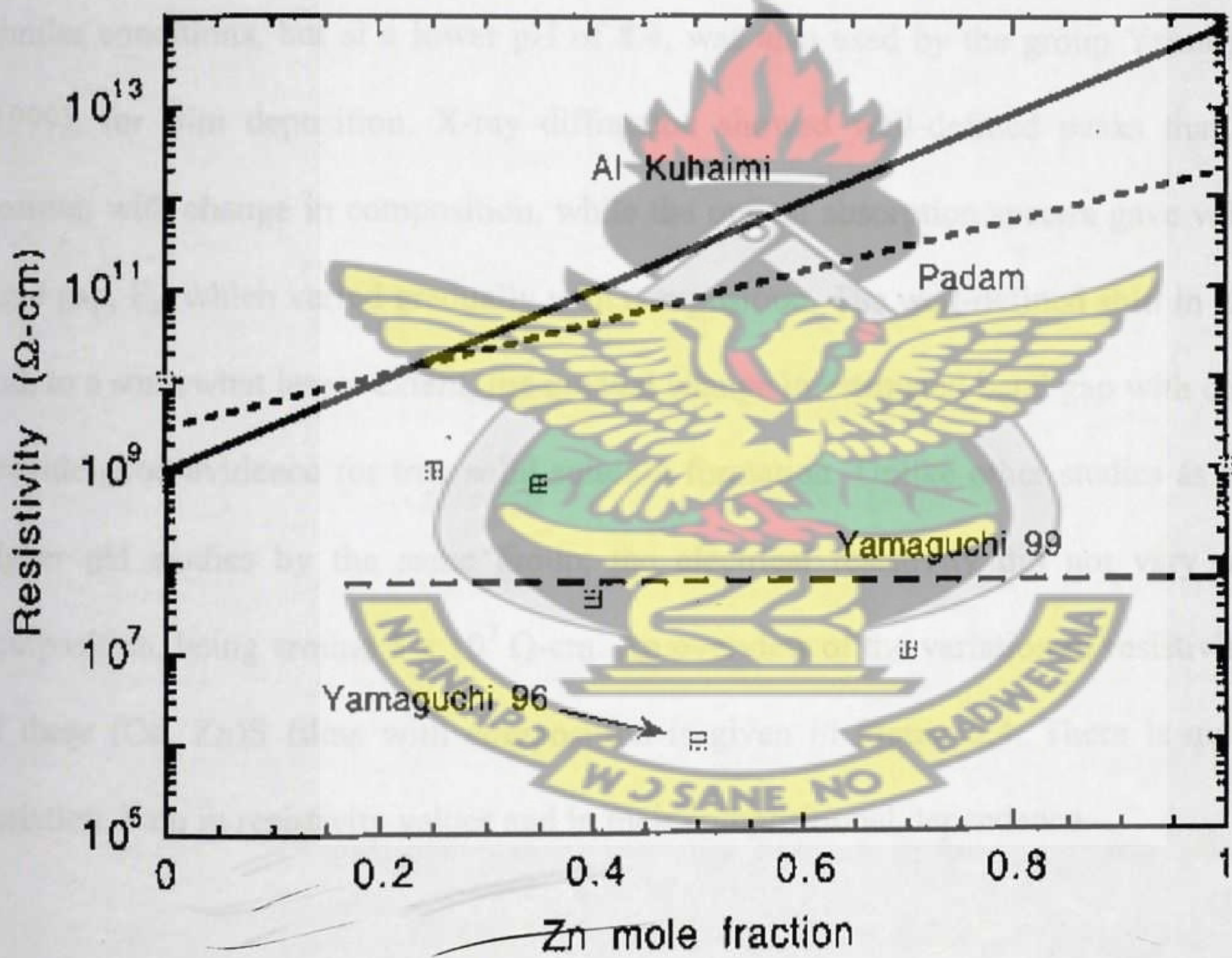


Figure 2.4: Resistivity data for some (Cd, Zn)S films. The data from the two Yamaguchi papers were modified to show resistivity values as a function of approximate film composition, rather than solution composition as given in the original papers.

Using ammonia-complexed metal iodide and thiourea at a pH of 10, Yamaguchi *et al.* (1996), formed films whose properties depended on the temperature. The resistivity of the films decreased with increase in Zn content from 10^{10} Ω -cm for CdS (a very high value for CdS) to about 10^6 Ω -cm for 90 % (solution concentration) Zn and then increased to approximately 10^9 Ω -cm for pure ZnS. No explanation for this effect was given. The films were photoconductive, with the resistivity decreasing in a somewhat sporadic manner as a function of composition, up to a maximum dark: light ratio of 5×10^3 for the 90 % Zn films.

KNUST

Similar conditions, but at a lower pH of 8.4, was also used by the group Yamaguchi *et al.* (1999), for film deposition. X-ray diffraction showed well-defined peaks that shifted in position with change in composition, while the optical absorption spectra gave values of the band gap, E_g , which varied gradually with composition. The well-defined shift in XRD peaks and, to a somewhat lesser extent, the gradual change in estimated band gap with composition provide good evidence for true solid solution formation. Unlike other studies as well as the higher pH studies by the same group, the electrical resistivity did not vary much with composition, being around 5×10^7 Ω -cm. An overview of the variation of resistivity of some of these (Cd, Zn)S films with composition is given in Figure 2.4. There is quite a large variation, both in resistivity values and in their compositional dependence.

Boyle *et al.* (2000), developed a novel method for the synthesis of cadmium zinc sulphide thin films from acidic chemical baths. In a typical experiment, thin films (about 30 to 50 nm diameter) of the ternary $\text{Cd}_{0.9}\text{Zn}_{0.1}\text{S}$ were grown on tin oxide glass substrates from acidic baths (pH between 5.5 and 4.9) containing cadmium chloride ($0.005 \text{ mol dm}^{-3}$), zinc chloride

(0.015 mol dm⁻³), urea (0.5 mol dm⁻³) and thioacetamide (0.2 mol dm⁻³). The reaction mixture was maintained at 353 K and stirred for deposition. Substrates were removed from the bath after 1 to 2 hours, washed with de-ionised water and any adherent particulate matter removed by ultrasonic agitation. The substrates were allowed to dry under ambient conditions. The as-deposited films were yellow-orange in colour and adherent. Annealing in air at 500 °C for 30 minutes produced adherent and pale yellow films. Glancing angle X-ray diffraction (XRD) measurements were recorded and the diffractograms compared with data in the JCPDS data files. Air annealed films were optically transparent and highly crystalline, the pattern of prominent peak positions was consistent with a hexagonal "wurzite-type" structure. The band gaps of the films were determined from electronic absorption spectra before and after annealing by the direct band gap method (from plots of α^2 vs. photon energy). Annealing produced a shift in the band gap from 2.55 eV to 2.50 eV. The surface morphology of films was assessed by scanning electron microscopy. Films were dense, homogeneous and composed of large grains (~500 nm diameter) with preferential growth on the tin oxide coated side of the TO glass substrate. Energy dispersive analytical X-ray analysis (EDAX) profiles were consistent with formation of the ternary compound. The approximate elemental ratios were estimated (from peak area analysis) as 8 : 2 : 10 Cd : Zn : S. Transmission electron microscopy (TEM) and selected area electron diffraction (SAED) measurements presented further evidence of increasing crystallinity with thermal treatment. X-Ray photoelectron spectroscopy (XPS) was utilized to gain information on the elemental composition and electronic state of the surface of the films. The binding energies of the major peaks were consistent with the formation of ternary material. Minor features were assigned to carbon (C 1s 284.8 eV) and oxygen (O 1s 531.8 eV) which were tentatively attributed to incorporation into films during CBD. This report concluded that this was the first definitive evidence for the successful preparation of polycrystalline thin films of cadmium zinc sulfide by Chemical

Bath Deposition (CBD) from acidic solutions. According to Boyle *et al.* (2000), the success of this approach is rationalized in terms of overcoming the fundamental differences between CdS and ZnS CBD systems and driving the process towards a surface controlled ion-by-ion deposition.

Khelifachaa *et al.* (2003), studied the Electrical and optical properties of $\text{Cd}_{1-x}\text{Zn}_x\text{S}$ ($0 < x < 0.18$) grown by chemical bath deposition technique on glass substrates. The thin films of $\text{Cd}_{1-x}\text{Zn}_x\text{S}$ were grown on glass substrates from alkaline bath (pH 11.7) containing cadmium sulphate ($2.8 \times 10^{-3} - 1.19 \times 10^{-2}$ mol/l), zinc sulphate ($2.1 \times 10^{-3} - 1.4 \times 10^{-3}$ mol/l), thiourea (0.028 mol/l) and ammonia (1.74 mol/l). Deposition took place on commercial glass slides, which were cleaned by means of a mixture of chloride and nitric acids (1:2), degreased by methanol and finally etched in a 5 % HF solution just before use for the deposition. The glass slides were placed vertically in a 100 ml closed beaker and together were introduced in a water bath kept at a constant temperature. Microstructural features, obtained from X-ray diffraction and scanning electron microscopy (SEM) measurements, revealed a predominance of Wurtzite structure and a homogenous microstructure formed by densely microcrystallines for all the samples studied. $\text{Cd}_{1-x}\text{Zn}_x\text{S}$ semiconductor was found to be resistive and of n-type. Also, the electron density decreased with increasing x and the mobility reached a maximum around $x = 0.12$, which means that the $\text{Cd}_{1-x}\text{Zn}_x\text{S}$ films at this composition were of high crystallinity, i.e. having reduced intrinsic defect concentrations.

Zhou *et al.* (2004), studied the composition, optical properties, structure properties, and surface morphology of thin films of $\text{Cd}_{1-x}\text{Zn}_x\text{S}$ ($x \leq 10\%$) prepared by chemical bath

deposition (CBD). $\text{Cd}_{1-x}\text{Zn}_x\text{S}$ film with zinc concentration $x \leq 10\%$ was prepared from a solution of 4.6 ml NH_4Ac (1 M), 15.2 ml NH_4OH (15 M), (0–16) ml $\text{Zn}(\text{Ac})_2$ (0.033 M), 4 ml $\text{Cd}(\text{Ac})_2$ (0.033 M) and 8 ml thiourea (0.067 M) solution in 550 ml of DI water. The growth was carried out at 90°C in a stirred solution. This group of films was used for material characterization and CdTe cell preparation. The absorption started at a wavelength of 520 nm. The optical band gap of the CdS thin film was 2.42 eV, suggesting a pure phase of CdS. XRD data also confirmed this. The peak at $2\theta = 26.9^\circ$ of the (111) planes of cubic CdS or the (002) plane of hexagonal CdS was detected in the XRD. The surface roughness and grain size of the films were compared between $\text{Cd}_{0.92}\text{Zn}_{0.08}\text{S}$ and CdS samples. AFM analysis was performed on two films deposited on SnO_2 substrates with thickness around 1000 Å, which showed that the films had similar surface roughness. The mean square roughness was 7.50 and 7.97 nm for $\text{Cd}_{0.92}\text{Zn}_{0.08}\text{S}$ and CdS films, respectively. The average grain size of CdS (~25 nm) was smaller than that of $\text{Cd}_{0.92}\text{Zn}_{0.08}\text{S}$ (~50 nm). The grains of $\text{Cd}_{0.92}\text{Zn}_{0.08}\text{S}$ appeared to be more randomly distributed on the surface, whereas the surface of CdS was composed of coalescence of a number of small grains.

Song *et al.* (2005), studied (Cd, Zn)S thin films grown on the soda-lime glass substrates by (CBD) process, for buffer layer applications in CuGaSe_2 (CIGS) solar cells. The structural, surface morphology, optical and electrical properties of the as deposited films were investigated by XRD, SEM, spectrophotometer and four probes resistivity measurements as a function of Zn- composition in the solution. The films had hexagonal structures and the grain size increased with increasing Zn- content in the solution. The resistivity of the CdZnS films were reported to increase as the Zn content increased. Optical absorbance and transmittance spectra of the films were measured using an HP 8453 UV-Visible spectrophotometer over the

wavelength range of 300 to 1100 nm. The film with 30 % of Zn in the solution showed a better than 80 % transmittance for wavelengths longer than 600 nm and film thickness less than 50nm. The values of energy band gaps obtained were 2.40, 2.55 and 2.70 eV for Zn-content of 0, 30 and 50 %, respectively.

Gaewdang and Wongcharoen (2007), investigated the optical and electrical properties of chemical bath co-deposited CdS-ZnS thin films. The deposition was carried out at a temperature of 80 °C for 60 min, on glass slide substrates cleaned with trichloroethylene, acetone, ethanol and distilled water in an ultrasonic cleaner. The aqueous solution used for CdS-ZnS co-deposition contained 0.01 M $[\text{CdSO}_4 + \text{ZnSO}_4]$, 0.05 M $\text{SC}(\text{NH}_2)_2$, 1.5 M NH_3 and 3.0 M $\text{N}_2\text{H}_4 \cdot \text{H}_2\text{O}$ in deionized water with a total volume of 150 ml. The films obtained by this method, after ultrasonic cleaning, were smooth, uniform, adherent, bright yellow orange in colour and the yellowness increased with increasing zinc content. Crystal structure of the films was checked by XRD measurements.

The SEM and AFM micrographs showed that the grain size decreased as the Zn content increased. The optical transmission spectra were obtained by means of a spectrophotometer. Ohmic contacts were made with silver paste on the surface of a $\text{Cd}_{1-x}\text{Zn}_x\text{S}$ film with the contact separation about 3 mm. The current passed through the contacts by applying dc voltage source was measured by using a Keithley 614 electrometer. $\text{Cd}_{1-x}\text{Zn}_x\text{S}$ films deposited on glass slide substrates showed only one diffraction peak located around $2\theta = 28^\circ$. The peak could be probably associated with (111) reflection of the zincblende structure. Increasing Zn content gave rise to rapid decrease in the peak intensity and it disappeared

when the Zn atomic ratio, $x > 0.7$ corresponding to amorphous characteristics. From SEM micrograph, grain size decreases rapidly as Zn atomic ratio, x increased. AFM surface images and roughness of the as-deposited $\text{Cd}_{1-x}\text{Zn}_x\text{S}$ films as a function of x was determined. The as-deposited films had a globular surface morphology, which agrees with the growth mechanism; homogeneous and heterogeneous reactions. The mean size of individual agglomerated grains was around 50 to 150 nm for the as-deposited films, which was in good agreement with SEM and AFM images. The optical transmission spectra of the as-deposited $\text{Cd}_{1-x}\text{Zn}_x\text{S}$ films were recorded. The shift of absorption edge towards shorter wavelengths indicates that, increasing Zn atomic ratio gives rise to an increase in energy gap (E_g). The energy band gap varied from 3.1 to 3.9 eV when the Zn atomic ratio increased from 0.2 to 0.9.

Chavhan *et al.* (2008), carried out a study on the effect of annealing on the structural and optical properties of $\text{Cd}_{1-x}\text{Zn}_x\text{S}$ thin films for photovoltaic applications. The $\text{Cd}_{1-x}\text{Zn}_x\text{S}$ thin films were grown on an ITO substrate using a chemical bath deposition technique. CdCl_2 , $\text{Zn}(\text{NO}_3)_2$ and $\text{NH}_2\text{--CS--NH}_2$ were used as source materials for Cd^{2+} , Zn^{2+} and S^{2-} ions, respectively. All the chemicals used in the investigation were of analytical reagent grade. For the preparation of good quality films, the concentration of (0.1 M) CdCl_2 , (0.175 M) $\text{Zn}(\text{NO}_3)_2$ and (1 M) $\text{NH}_2\text{--CS--NH}_2$ were optimized and used as stock solutions. The as-deposited films were annealed in air at 400 °C for 30 min. The composition, surface morphology and structural properties of the as-deposited and annealed $\text{Cd}_{1-x}\text{Zn}_x\text{S}$ thin films were studied using EDX, SEM and X-ray diffraction techniques. The annealed films were observed to possess a crystalline nature with a hexagonal structure. The optical absorption spectra were recorded within the wavelength range of 350 to 800 nm. The band gap of the as-

deposited thin films varied from 2.46 to 2.62 eV, whereas in the annealed films these varied from 2.42 to 2.59 eV. The decreased band gap of the films after annealing was due to the improved crystalline nature of the material.

Kumar *et al.* (2009), studied the Growth and Optical Properties of Chemical Bath Deposited $\text{Cd}_{0.7}\text{Zn}_{0.3}\text{S}$ Nanoparticles. Nanocrystalline thin films of $\text{Cd}_{0.7}\text{Zn}_{0.3}\text{S}$ were deposited on optically plane glass substrates by CBD technique. Analytical grade cadmium sulphate ($3\text{CdSO}_4 \cdot 7\text{H}_2\text{O}$) having molecular mass 769.51 gm/mole, zinc sulphate (ZnSO_4) having molecular mass of 287.54 gm/mole and thiourea ($\text{CN}_2\text{H}_4\text{S}$) having molecular mass of 76.12 gm/mole are used as the source of Cadmium, Zinc and Sulphur respectively. The XRD traces were taken using X-Ray powder diffractogram (Seifert XRD 3003 T/T) operated at 40 kV and 30 mA with Cu $\text{K}\alpha$ radiation (1.5405 Å). The peak positions suggest that the as-deposited films have the hexagonal wurtzite structure corresponding to orientations along (100), (002), (101), (102), (110), (103), (200), (112) and (201) planes. Photoluminescence (PL) spectrum of the films exhibit four emission bands at 470 nm, 485 nm, 490 nm and 503 nm in blue-green region. The PL intensity at 490 nm was expected due to the band edge luminescence of as deposited $\text{Cd}_{0.7}\text{Zn}_{0.3}\text{S}$. It showed the narrow spectral width that indicates the homogeneous composition of nanocrystals. TEM studies were done using Transmission Electron Microscope JEOL (Japan), JEM 100 CX-II operating in the accelerating voltage of 100 kV at room temperature. SEM images revealed that the nanoparticles deposited were uniform, adherent and pinhole free with hexagonal shape in structure. The average particle size was found to be about 65 nm.

Meng *et al.* (2010), reported on the Acidic chemical bath deposition of $\text{Cd}_{1-x}\text{Zn}_x\text{S}$ thin films. CdS thin films were grown on commercial $\text{SnO}_2:\text{F}$ (FTO) conducting transparent glass, before the CBD process. FTO substrates were cleaned in acetone, alcohol and de-ionized water, respectively. The substrates were dried at 90°C in an oven. CdS thin films were prepared using a reactant solution at 80°C controlled by a water bath. $\text{CdCl}_2 \cdot 2\text{H}_2\text{O}$, $\text{Zn}(\text{NO}_3)_2 \cdot 6\text{H}_2\text{O}$ and $\text{C}_2\text{H}_5\text{NS}$ were used as source materials for Cd^{2+} , Zn^{2+} and S^{2-} ions, respectively. Urea was added into the reaction solution to adjust the balance of the hydrolyzation and deposition. A 200 ml reaction solution was prepared at room temperature, in which the concentration of cadmium ions, zinc ions, urea and thioacetamide were 0.019, 0.001, 0.5, 0.02 M, respectively. The pH value of the solution was adjusted to 4.0~4.1 by a diluted HCl solution. The mixture was stirred for homogeneous solution. After deposition, the substrates were taken out of the bath, rinsed with deionized water, dried under a stream of nitrogen. Finally, $\text{Cd}_{1-x}\text{Zn}_x\text{S}$ thin films were annealed in air at 400°C for 30 minutes.

Strong peaks at 2.31 and 3.14 eV for S and Cd respectively, were found in the EDX spectrum of the as-deposited $\text{Cd}_{0.95}\text{Zn}_{0.05}\text{S}$ thin films. The peaks at 0.5, 1.75, 3.45 and 3.69 keV showed the presence of oxygen, silicon, stannum and calcium, respectively, which appeared due to the FTO substrate. The percentage concentrations of Cd and Zn were 7.72 % and 0.42 % in the film. The elemental composition of the film and the initial values in the reaction bath were similar. The deposited $\text{Cd}_{0.95}\text{Zn}_{0.05}\text{S}$ thin films were smooth, homogenous and densely packed with particles of about 200 to 250 nm in diameter. The SEM images showed the nanocrystalline nature of the $\text{Cd}_{0.95}\text{Zn}_{0.05}\text{S}$ thin films. After thermal annealing, the particles tried to coalesce and/or diffuse together to form relatively bigger grains which enhanced the crystallinity of the material. X-ray diffraction patterns were studied to determine the crystal

structure of the $\text{Cd}_{0.95}\text{Zn}_{0.05}\text{S}$ thin films, before and after annealing. The as-deposited thin films possessed poor crystallinity compared to the annealed films. The reflection peaks at 24.8° , 26.5° and 28.2° over a broad hump correspond to reflections from (100), (002) and (101) planes of hexagonal (wurtzite) structured $\text{Cd}_{0.95}\text{Zn}_{0.05}\text{S}$ thin films. After annealing, the intensities of the (100) and (101) plane increased, indicating the increased crystallinity of the films. The plane (002) gives lattice matching to CuInGaSe_2 and $\text{Cu}_2\text{ZnSnS}_4$ chalcogenide absorber layers used in photovoltaic devices. The band gaps of the as-deposited and the annealed films were 2.46 and 2.44 eV.

KNUST

Asogwa (2010), synthesized thin films of CdZnS on glass substrates by chemical bath deposition at room temperature. The bath constituents for deposition of cadmium zinc sulphide (CdZnS) thin films were cadmium chloride (CdCl_2) as a source of Cd^{2+} , Zinc sulphate (ZnSO_4) as a source of Zn^{2+} , thiourea $[(\text{NH}_2)_2\text{CS}]$ as a source of sulphide ions (S^{2-}) in the presence of ammonia (NH_3) as the complexing agent. In a typical deposition set up, the bath was composed of 3 ml of 1 M CdCl_2 , 2 ml of 1 M ZnSO_4 , 5 ml of 1 M thiourea and 35 ml of distilled water put in that order into a 50 ml beaker. The solution was made alkaline by addition of NH_3 . The mixture was stirred well to form a homogeneous solution. Microscope glass slide substrates were cleaned using a standard procedure and placed vertically inside the beaker for 5 hours at room temperature. After deposition, the substrates were removed from the bath, rinsed with distilled water and allowed to drip dry in air. Two of the as-grown films were then annealed in the oven for one hour. XRD analysis revealed that thin films of CdZnS (as-deposited and annealed in air), have preferred orientation along (101) and (002) planes. From the absorption spectra, the band gap energy for CdZnS thin films were found to lie within the range of 2.10 to 2.30 eV. The transmittance of the films increases steadily with

wavelength and with the annealing temperature to maximum values in the NIR region of the solar spectrum. The film annealed at 300 °C exhibited the highest transmittance of 69 % at a wavelength of 700 nm.

Sanap and Pawar (2011), studied chemical bath deposited nanocrystalline CdZnS thin films.

The $\text{Cd}_{1-x}\text{Zn}_x\text{S}$ thin films were prepared by CBD technique on commercial glass slide for various zinc concentration ($0 \leq x \leq 0.8$). The starting materials used were CdSO_4 (0.06 M) as a Cd^{2+} ion source, ZnSO_4 (0.2 M) as Zn^{2+} ion source, thiourea (0.6 M) as a S^{2-} ion source and triethenolamine (TEA) complexing to control the Cd^{2+} and Zn^{2+} ion concentrations. An alkaline solution of ammonia was used to adjust the pH of the reaction mixture. The pH value of the working solution was adjusted by a pH meter and kept between 9 and 9.5 for different deposition times (10 to 60 minutes) at a temperature of 72 ± 2 °C. The effect of zinc content (x value) on structural, morphological and some optical properties were also studied. All the films showed nanocrystallinity with both cubic and hexagonal structure. The average grain size changed from 8.75 nm to 3.57 nm with increase in zinc content. It was found that as the zinc content increased, the peak intensity decreased and for $x \geq 0.8$ the films had near amorphous character. The values of energy band gap obtained were between 2.48 eV and 3.62 eV, for Zn content between 0 and 0.8 respectively. The SEM micrograph showed smoother and more uniform films with fibre like structure as Zn content increased.

CHAPTER THREE

3. THEORY

3.1 PHYSICS OF SEMICONDUCTORS

3.1.1 Energy band theory

This Section describes the behaviour of an electron in a crystal. It will be demonstrated that the electron can have only discrete values of energy. The concept of "energy bands" will also be introduced. This concept is a key element for understanding the electrical properties of semiconductors.

In semiconductor devices, the primary interest lies in the behavior of electrons in semiconductor crystals, and consequently, it will be necessary to develop this gradually by first examining the properties of free electrons, and progressively add more realism to this model so that it represents a semiconductor.

3.1.1.1 The Free Electron Model

The free electron model can be applied to an electron which does not interact with its environment. In other words, the electron is not submitted to the attraction of the atoms in a crystal; it travels in a medium where the potential is constant. Such an electron is called a free electron. For a one-dimensional crystal, which is the simplest possible structure imaginable, the time-independent Schrödinger equation can be written for a constant potential V using the relationship:

$$\frac{d^2\psi}{dx^2} + \frac{2m}{\hbar^2}(E - V)\psi = 0 \text{ ----- (3.1)}$$

where, Ψ is the wave function associated with an electron, E is the electronic allowed energy or eigenvalue.

In free space, the potential energy $V = 0$ and the Schrödinger equation becomes

$$\frac{d^2\psi}{dx^2} + \frac{2m}{\hbar^2} E\psi = 0 \quad (3.2)$$

The solution to equation 3.2 is

$$\psi(x) = Ae^{ikx} \quad (3.3)$$

where

$$k = \sqrt{\frac{2mE}{\hbar^2}} \quad (3.4)$$

or

$$E = \frac{\hbar^2 k^2}{2m} \quad (3.5)$$

The momentum operator, p_x , of the electron, is given by the relation:

$$p_x = \frac{\hbar}{j} \frac{\partial}{\partial x}$$

Consider an electron moving along the $+x$ direction in a one-dimensional sample and applying the momentum operator to the wave function

$$\psi(x) = C_1 \exp(jkx)$$

we obtain

$$p_x \psi(x) = \frac{\hbar}{j} \frac{d\psi(x)}{dx} = C_1 \hbar k \exp(jkx) = \hbar k \psi(x)$$

The eigenvalues of the operator p_x are thus given by:

$$p_x = \hbar k$$

Hence, the number, k , called the wave number, is equal to the momentum of the electron, within a multiplication factor \hbar

From equation 3.5, the energy of the free electron is a parabolic function of its momentum, k , as shown in Figure 3.1. This is identical to what is expected from classical mechanics considerations: the 'free' electron can take any value of energy in a continuous manner. It is worth noting that electrons with momentum k or $-k$ have the same energy. These electrons have the same momentum but travel in opposite directions

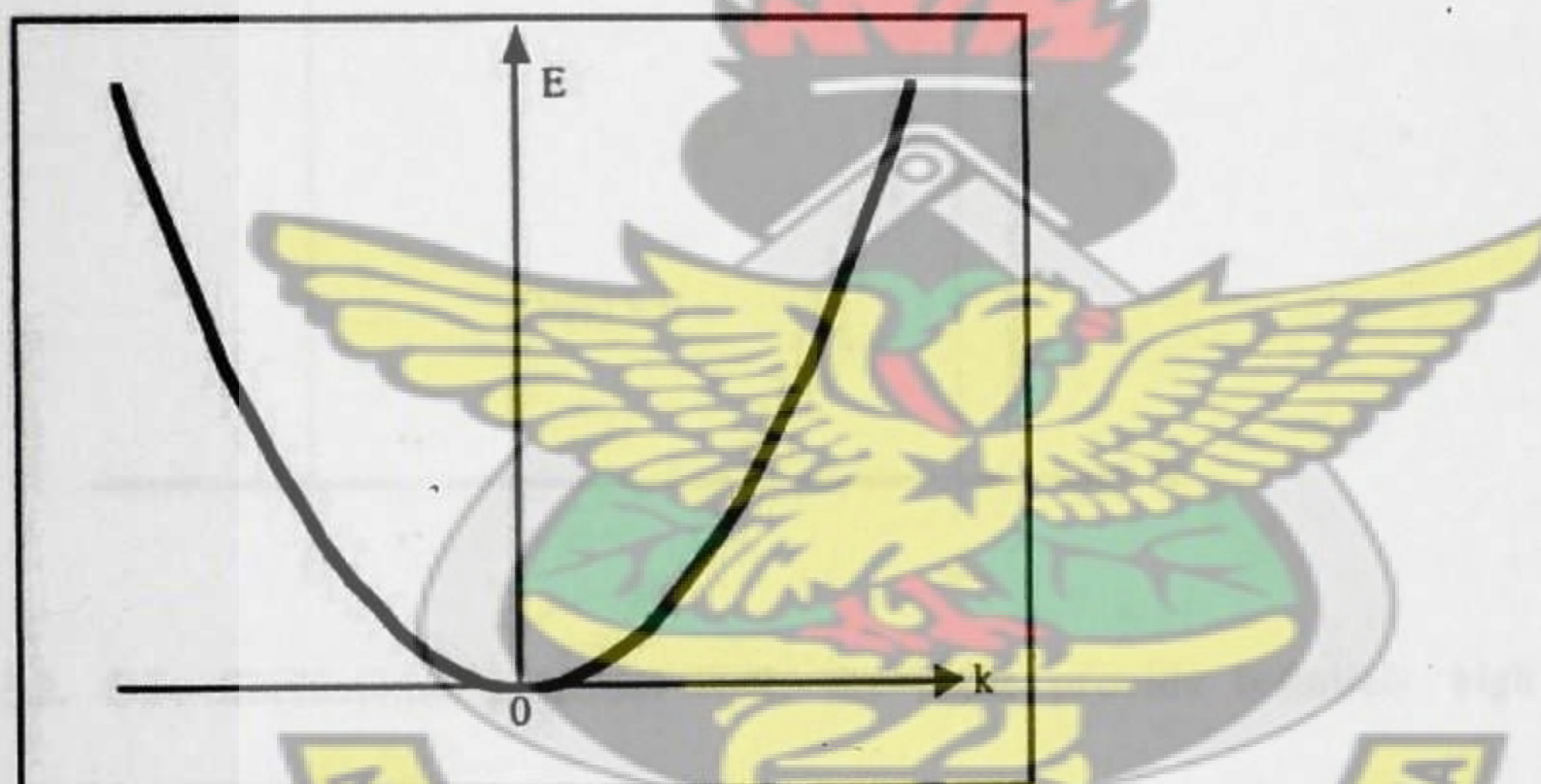


Figure 3.1. In free space, the dependence of the electron energy, E , on k is parabolic

Although the free electron model is sometimes used for metals because of its simplicity, it is not appropriate for semiconductors because it doesn't predict the existence of discrete energy bands. More realistic models that do predict multiple bands do so because they take into account the periodicity of the potential energy for an electron in a crystal lattice.

3.1.1.2 Particle in a box

The simple model shown below describes this scenario in which a particle is confined to a restricted region of space from which it cannot escape. To some limited extent, the particle in-a-box problem resembles that of electrons in an atom, where the attraction from the positively charged nucleus creates a potential well that "traps" the electrons. The Schrödinger equation is used to determine the possible energy levels and the corresponding wave functions associated with this system.

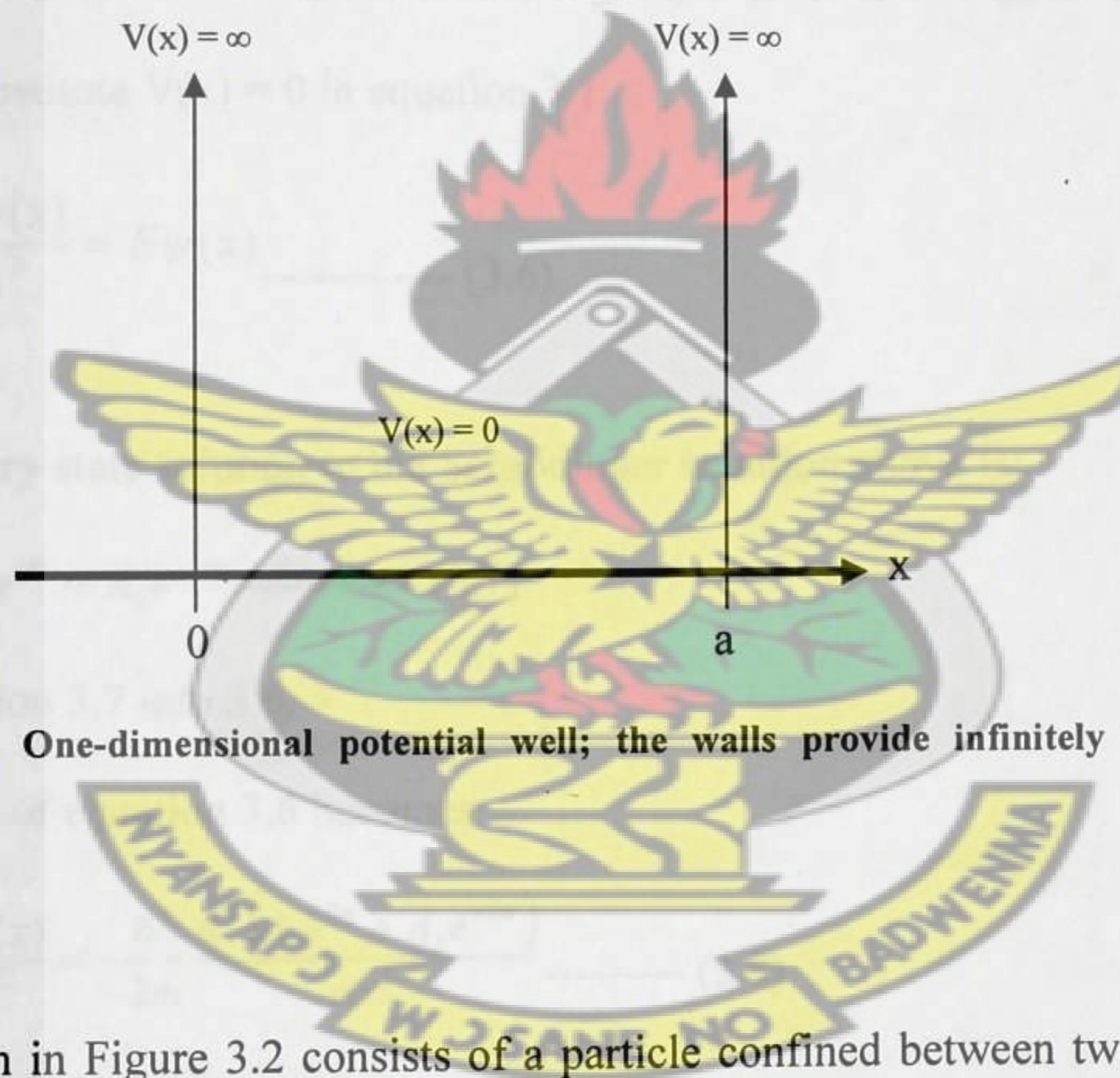


Figure 3.2. One-dimensional potential well; the walls provide infinitely high-potential barriers.

The above system in Figure 3.2 consists of a particle confined between two rigid walls separated by a distance 'a'. The motion is one dimensional, with the particle moving only along the x-axis and between the walls $x = 0$ and $x = a$. The potential energy corresponding to the rigid walls is infinite, so the particle cannot escape. The potential energy is zero between the walls (since the particle experiences no force). To solve the Schrödinger equation for this system, we consider the restrictions on the particles wave function.

Because the particle is confined to the region, $0 \leq x \leq a$, we expect $\psi(x) = 0$ outside that region. This agrees with the Schrödinger equation, if the term $V(x)\psi(x)$ in equation 3.1 is to be finite, $\psi(x)$ must be zero where $V(x)$ is infinite. Furthermore $\psi(x)$ must be a continuous function to be mathematically well behaved solution to the Schrödinger equation; if it is, then $\psi(x)$ must be zero at the boundary, $x = 0$ and $x = a$. These two conditions serve as boundary conditions for the problem.

KNUST

Thus, to solve for the wave function in the region, $0 \leq x \leq a$, subject to the above conditions, we substitute $V(x) = 0$ in equation 3.1.

$$-\frac{\hbar^2}{2m} \frac{d^2\psi(x)}{dx^2} = E\psi(x) \quad \text{-----} (3.6)$$

A general stationary state solution to the Schrödinger equation above is:

$$\psi(x) = A_1 e^{ikx} + A_2 e^{-ikx} \quad \text{-----} (3.7)$$

substituting equation 3.7 into 3.6,

The left hand side of equation 3.6 becomes

$$-\frac{\hbar^2}{2m} \frac{d^2\psi(x)}{dx^2} = -\frac{\hbar^2}{2m} \frac{d^2(A_1 e^{ikx} + A_2 e^{-ikx})}{dx^2} \quad \text{-----} (3.8)$$

$$= \frac{-\hbar^2}{2m} \left[(ik)^2 A_1 e^{ikx} + (-ik)^2 A_2 e^{-ikx} \right] \quad \text{-----} (3.9)$$

$$= \frac{-\hbar^2 k^2}{2m} [A_1 e^{ikx} + A_2 e^{-ikx}] = \frac{\hbar^2 k^2}{2m} \psi(x) \quad \text{-----} (3.10)$$

Substituting equation 3.10 into 3.6 yields;

$$E = \frac{\hbar^2 k^2}{2m} \text{----- (3.11)}$$

The possible energy levels are given by equation 3.11 as;

$$E = \frac{\hbar^2 k^2}{2m} = \frac{p^2}{2m}$$

where

$$p = \hbar k = \left(\frac{h}{2\pi} \right) \left(\frac{2\pi}{\lambda} \right) = \frac{h}{\lambda}$$

KNUST

is the momentum of a free particle with wave number k and wavelength λ .

For each value of n there are corresponding values of p , λ and E , which we denote as p_n , λ_n and E_n . Hence we get;

$$p_n = \frac{h}{\lambda_n} = \frac{nh}{2a}$$

And

$$E_n = \frac{p_n^2}{2m} = \frac{n^2 h^2}{8ma^2} = \frac{n^2 \pi^2 \hbar^2}{2ma^2}, \text{ where } (n=1,2,3,\dots) \text{----- (3.12)}$$

The above equation 3.13, gives the possible energy levels for a particle in a box. Each energy level has its own value of the quantum number n and a corresponding wave function ψ_n . When we substitute $k = n\pi/a$ into equation 3.12 we find

$$\psi_n(x) = C \sin \frac{n\pi x}{a} \text{----- (3.13)}$$

Where $n = 1, 2, 3, \dots$

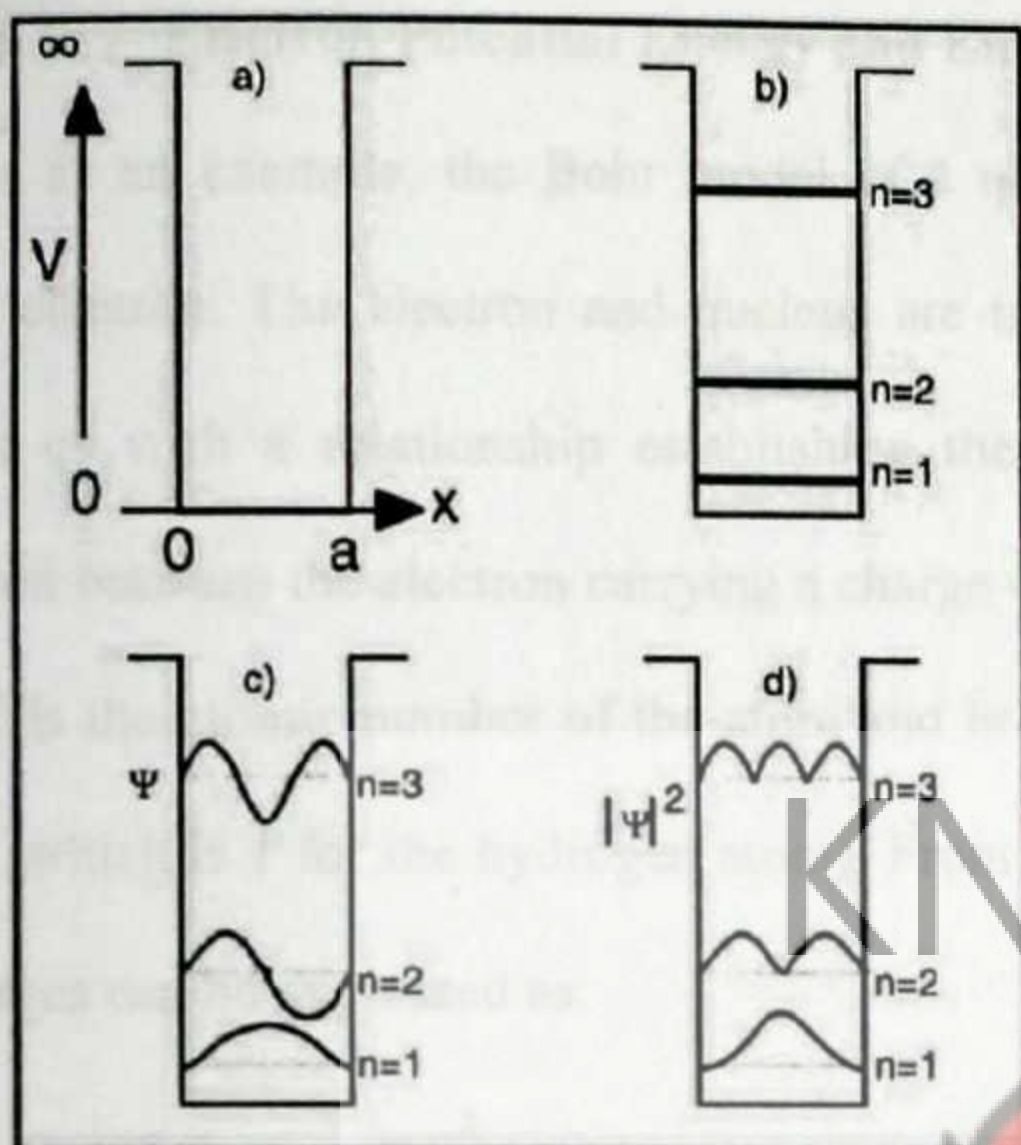


Figure 3.3: Particle in a box: a) Geometry of potential well; b) Energy levels; c) Wave functions; d) Probability density for $n = 1, 2$ and 3 (Colinge and Colinge, 2002)

This result is quite similar to that obtained for a free electron, in both cases the energy is a function of the squared momentum. The difference resides in the fact that in the case of a free electron, the wave number k and the energy E can take any value, while in the case of the particle-in-a-box problem, k and E can only take discrete values (replacing k by $n\pi/a$ in equation 3.5 yields equation 3.12. These values are fixed by the geometry of the potential well. Intuitively, it is interesting to note that if the width of the potential well becomes very large, the different values of k become very close to one another, such that they are no longer discrete values but rather form a continuum, as in the case for the free electron.

3.1.1.3. Electron Potential Energy and Energy States

Consider as an example, the Bohr model of a neutral hydrogen atom, which has one orbiting electron. The electron and nucleus are treated as point charges. Electrostatics provides us with a relationship establishing the potential energy resulting from the interaction between the electron carrying a charge $-q$ and a nucleus bearing a charge $+qZ$, where Z is the atomic number of the atom and is equal to the number of protons in the nucleus (which is 1 for the hydrogen atom). From Coulomb's law the force between the two charges can be expressed as:

$$F = \frac{q_1 q_2}{4\pi\epsilon_0 x^2} = \frac{-q^2}{4\pi\epsilon_0 x^2} \text{-----} (3.14)$$

where x , is the distance between the two charges and ϵ_0 is 8.85×10^{-12} farads/meter, is the permittivity of free space. The resulting negative sign in equation 3.14, indicates that the force is attractive.

From classical mechanics, the force on a particle is equal to the negative gradient of the potential energy, that is;

$$F = -\nabla E_p = -\frac{dE_p}{dx} \text{-----} (3.15)$$

The gradient is taken in the x direction and E_p is the potential energy of the electron at position x . From equation 3.14 and 3.15;

$$dE_p = dE_p(x) = -Fdx = \frac{q^2 dx}{4\pi\epsilon_0 x^2} \text{-----} (3.16)$$

Integrating both sides to obtain E_p , there will be a constant of integration. The actual value of the potential energy is arbitrary (as is the choice of the constant), since the value of the potential energy depends entirely on one's choice of reference. A convenient

reference is chosen, by noting that the Coulomb force at infinite distance is zero. It makes sense for this case, then to choose $x = \infty$ as a reference point, so we define the potential energy at $x = \infty$ as the vacuum level, E_{vac} :

$$E_p(x = \infty) = E_{vac} \text{ ----- (3.17)}$$

This is the energy required to free the electron from the influence of the nucleus, essentially by moving the electron infinitely far away from it. If the electron is infinitely far away from the nucleus, it cannot really be considered part of the atom – it is now a free electron in vacuum. Solving equation 3.16, for a given value of x :

$$\int_{E_p}^{E_{vac}} dE_p = \int_x^{\infty} \frac{q^2 dx}{4\pi\epsilon_0 x^2} \text{ ----- (3.18)}$$

Where, E_p is the electron potential energy at a distance x , from the nucleus. Integrating both sides and rearranging, we obtain

$$E_p = E_{vac} - \frac{q^2}{4\pi\epsilon_0 x} \text{ ----- (3.19)}$$

The potential energy of the electron as a function of its distance from the nucleus is sketched in Figure 3.4

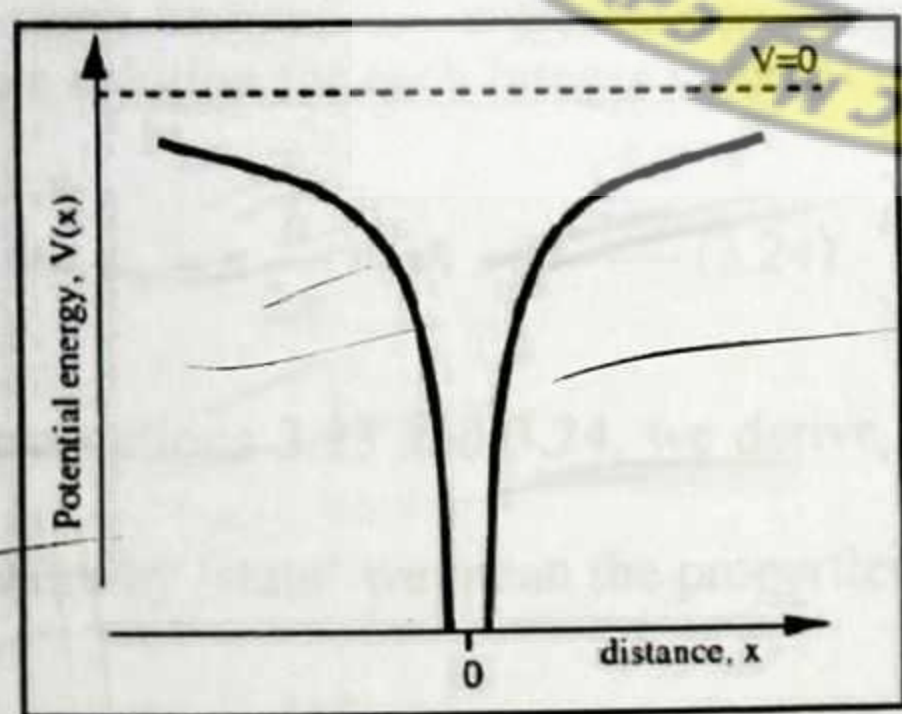


Figure 3.4: Potential Energy of an electron as a function of its distance from the atom nucleus, $V = 0$ when $x = \infty$ (Colinge and Colinge, 2002)

From Newtonian mechanics, the centrifugal force of an electron revolving in a circle of radius x , round the nucleus is expressed as;

$$F = \frac{mv^2}{x} \text{ ----- (3.20)}$$

For the atom to be stable, the net force on the electron must be zero. Equating our previous expression for the centripetal force due to the coulomb attraction, equation 3.14, to the centrifugal force, equation 3.20, we can write

$$\frac{mv^2}{x} - \frac{q^2}{4\pi\epsilon_0 x^2} = 0 \text{ ----- (3.21)}$$

Bohr also postulated that the integral of the angular momentum around one complete orbit is an integer multiple of Plank's constant h :

$$\oint P_\theta d\theta = \int_0^{2\pi} mvxd\theta = nh \text{ ----- (3.22)}$$

Where n is an integer. Since the orbit is assumed to be circular in the Bohr model, x is a constant, and so are the potential energy E_p and the speed, v . Therefore, the integral becomes

$$2\pi mxv = nh \text{ ----- (3.23)}$$

There is a solution for each integer value of n , thus, we write

$$mv_n x_n = n \frac{h}{2\pi} = n\hbar \text{ ----- (3.24)}$$

Solving equations 3.23 and 3.24, we derive an expression for the Bohr radius of the n^{th} state, where by 'state' we mean the properties associated with a particular value of n :

$$x_n = \frac{4\pi\epsilon_0 n^2 \hbar^2}{mq^2} \text{ ----- (3.25)}$$

And the speed of the electron in that particular state is

$$v_n = \frac{q^2}{4\pi\epsilon_0 n\hbar} \text{-----} (3.26)$$

Our primary goal, however, is to find the energies associated with these states. The total energy of a system is equal to the kinetic energy plus the potential energy. The kinetic energy of the n^{th} energy level is

$$E_{Kn} = \frac{1}{2}mv_n^2 = \frac{mq^4}{2(4\pi\epsilon_0)^2 n^2\hbar^2} \text{-----} (3.27)$$

For the potential energy we can write, substituting the value for x_n from equation 3.25 into 3.19,

$$E_{pn} = E_{vac} - \frac{mq^4}{(4\pi\epsilon_0)^2 n^2\hbar^2} \text{-----} (3.28)$$

Thus, the total energy E_n is

$$E_n = E_{Kn} + E_{pn} = E_{vac} - \frac{mq^4}{2(4\pi\epsilon_0)^2 n^2\hbar^2} \text{-----} (3.29)$$

From equation 3.29, we say that the energy is quantized. It can have only discrete values associated with the quantum number n .

Table 3.1: The first four Bohr energies and orbital radii for the hydrogen atom

E_n	x_n
$E_1 = E_{vac} - 1.36 \text{ eV}$	$x_1 = 0.053 \text{ mm}$
$E_2 = E_{vac} - 3.4 \text{ eV}$	$x_2 = 0.212 \text{ mm}$
$E_3 = E_{vac} - 1.51 \text{ eV}$	$x_3 = 0.477 \text{ mm}$
$E_4 = E_{vac} - 0.85 \text{ eV}$	$x_4 = 0.848 \text{ mm}$

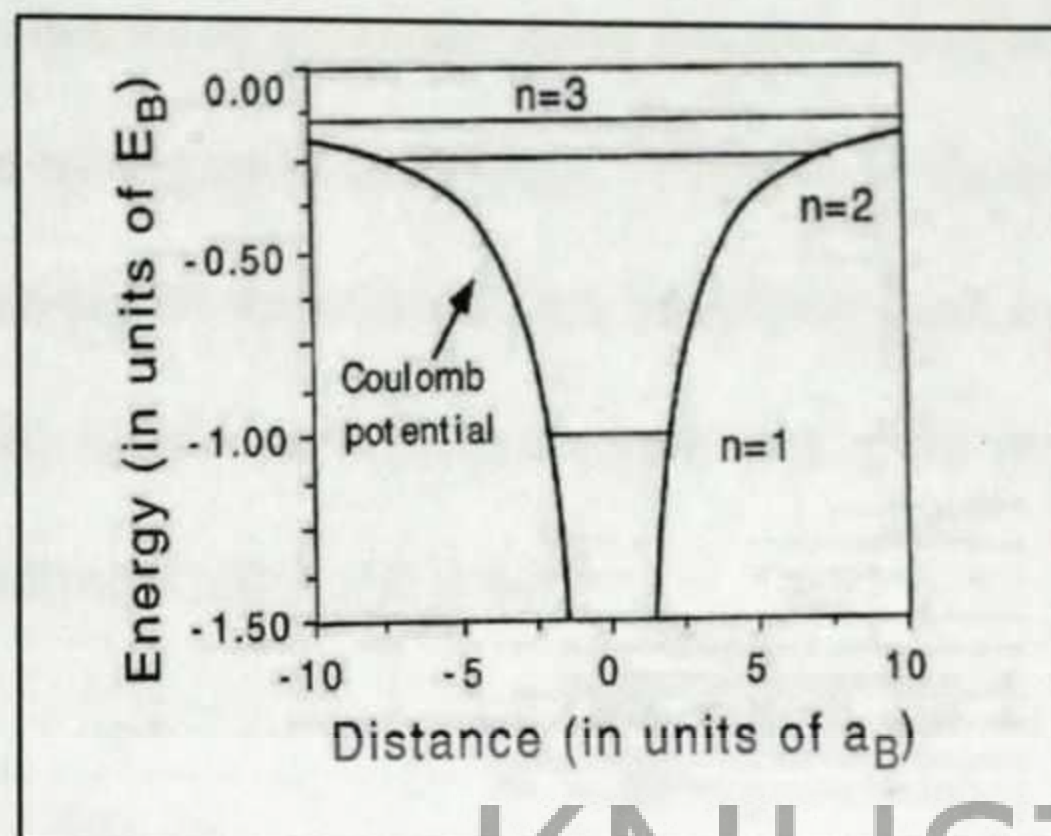


Figure 3.5: The Coulomb, potential and the first three energy levels for a hydrogen atom (Shur, 1990).

3.1.1.4. From Discrete Energy States to Energy Bands

Consider the electron energy diagrams for two isolated hydrogen nuclei shown in Figure 3.6. By isolated, we mean that the nuclei are sufficiently far apart that they do not influence each other.

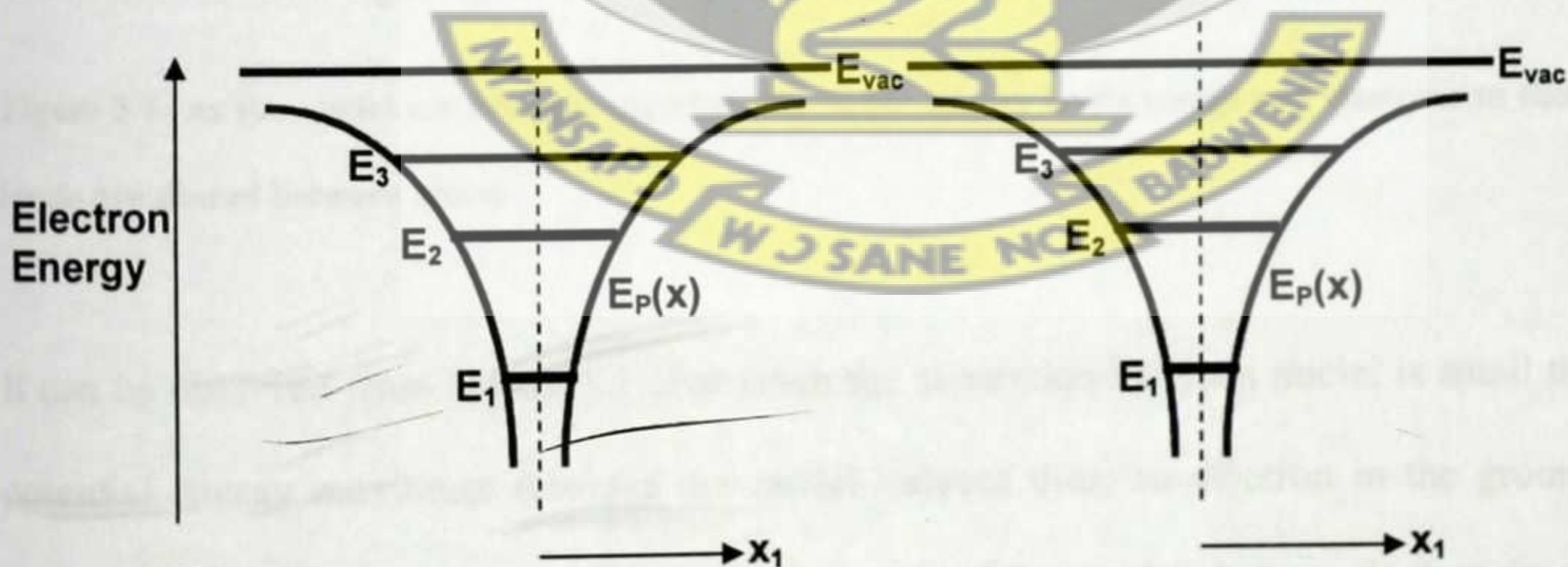


Figure 3.6: Energy band diagram for two non interacting hydrogen nuclei (not drawn to scale)

The energy levels for the electron are the same for each other and are quantized. When the nuclei are allowed to approach each other, as shown in Figure 3.7, the upper energy levels merge and electrons in those levels are shared between atoms. Thus, an electron would be influenced by both nuclei. According to coulomb's law, the electron potential energy of a single electron at any point is now

$$E_P = E_{vac} - \frac{q^2}{4\pi\epsilon_0 x_1} - \frac{q^2}{4\pi\epsilon_0 x_2} \quad (3.30)$$

Where x_1 and x_2 are the distances between the electron and each of the two nuclei respectively.

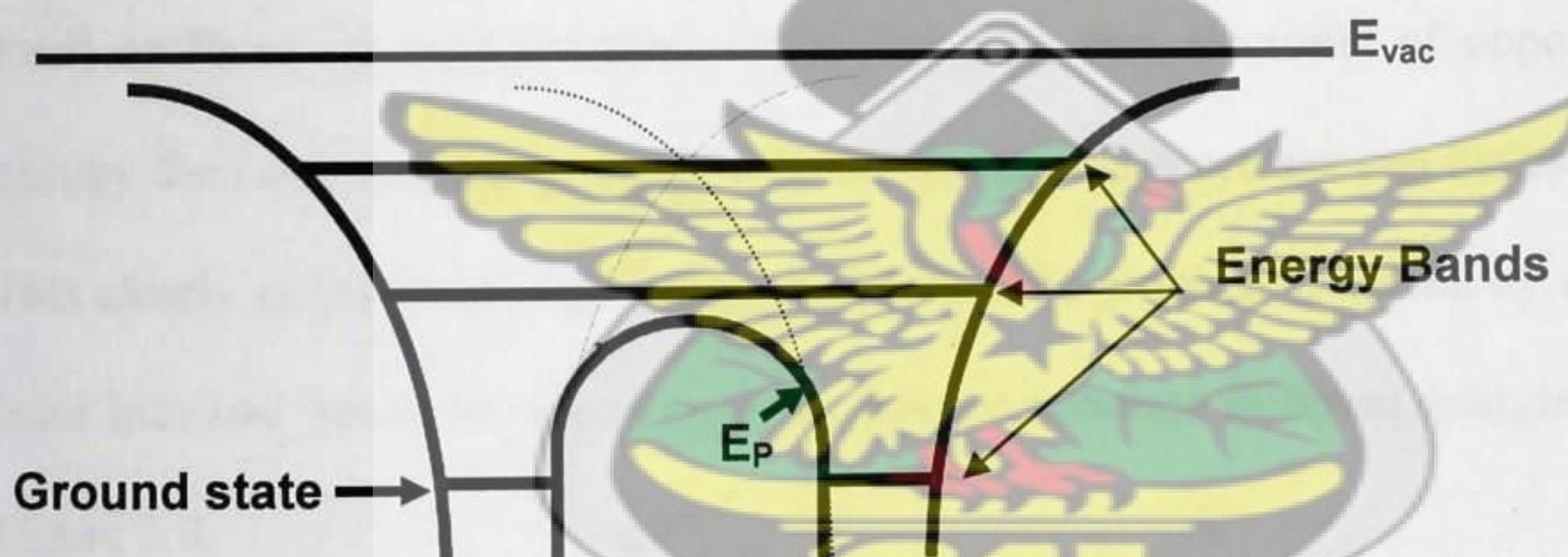


Figure 3.7: As the nuclei are brought together, the upper energy levels merge and electrons in those levels are shared between atoms

It can be observed from Figure 3.7, that when the separation between nuclei is small the potential energy maximum between the nuclei reduces thus, an electron in the ground state (lowest energy state) would be bound to one of the nuclei, but an electron in an excited state could travel back and forth between the nuclei, in effect shared by the two atoms, that is they are delocalized: they belong to all atoms in the crystal.

3.1.1.5. Energy Bands (An Intuitive Approach)

To understand the nature of semiconductors one must consider what happens when similar atoms are brought together to form a solid such as a crystal. Let us take the example of a relatively simple element with low atomic number, such as lithium ($Z=3$). In a lithium atom, two electrons of opposite spin occupy the lowest energy level (1s level), and the remaining third electron occupies the second energy level (2s level). The electronic configuration is thus $1s^2 2s^1$. All lithium atoms have exactly the same electronic configuration with identical energy levels. If a hypothetical molecule containing two lithium atoms is formed, we are now in the presence of a system in which four electrons "wish" to have an energy equal to that of the 1s level. But because of the Pauli exclusion principle, which states that only two electrons of opposite spins can occupy the same energy level, only two of the four 1s electrons can occupy the 1s level. This clearly poses a problem for the molecule. The problem is solved by splitting the 1s level into two levels having very close, but nevertheless different energies as shown in Figure 3.8.

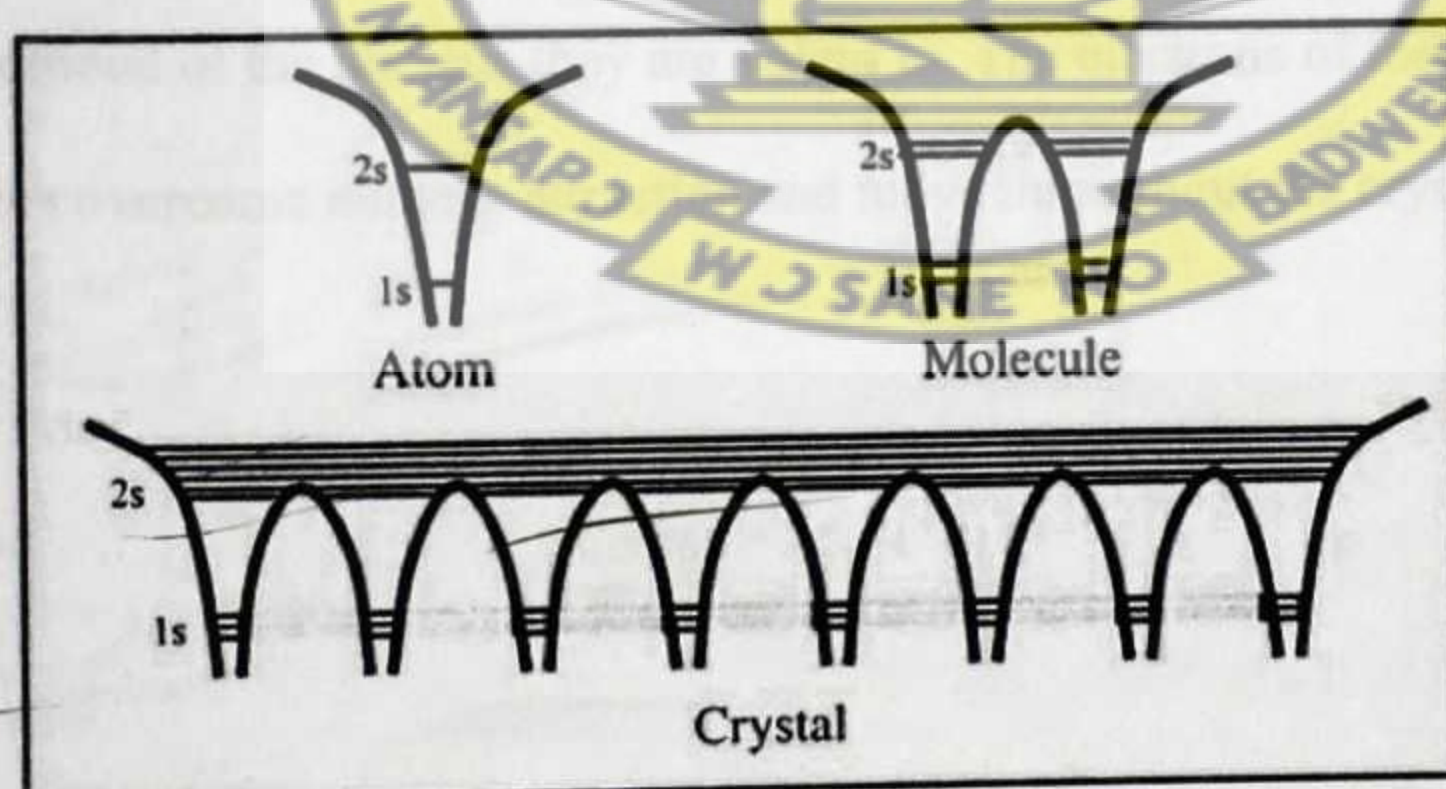


Figure 3.8: Permitted energy levels of an atom, a hypothetical molecule and a crystal of Lithium (Colinge and Colinge, 2002)

In practice, the energy difference between the highest and the lowest energy value resulting from this process of splitting an energy level is on the order of a few electronvolts; the energy difference between two neighboring energy levels is on the order of 10^{-22} eV (Colinge and Colinge, 2002). This value is so small that one can consider that the energy levels are no longer discrete, but form a continuum of permitted energy values for the electron. An important feature of Figure 3.7, is that the discrete states associated with the isolated atoms are now broadened into energy bands in the crystal. For a crystal with N atoms, each state originating from a single atom splits into a band of N discrete states. In a crystal containing billions of atoms, these states are infinitesimally close to each other in energy and each band is considered to be continuous. Between the energy bands (between the 1s and the 2s energy bands in Figure 3.7), there may be a range of energy values which are not permitted. In that case, a forbidden energy gap is produced between permitted energy bands. The energy levels and the energy bands extend throughout the entire crystal. Because of the potential wells generated by the atom nuclei, however, some electrons (those occupying the 1s levels) are confined to the immediate neighborhood of the nucleus they are bound to. The electrons of the 2s band, on the other hand, can overcome nucleus attraction and move throughout the crystal.

3.1.2. Origin of the Band Gaps in a Crystal

3.1.2.1. Electron in a Periodic Potential of a Crystal (Kronig-Penney Model)

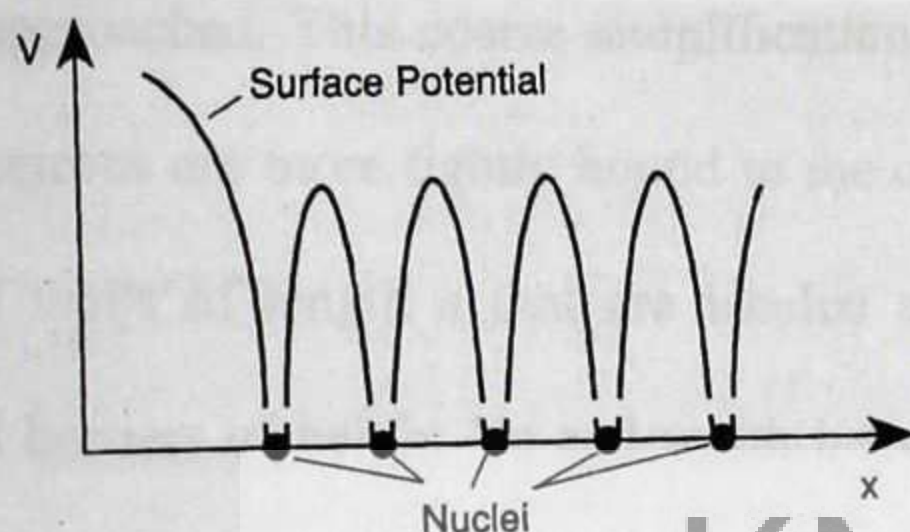


Figure 3.9a: One-Dimensional periodic potential distribution for a crystal

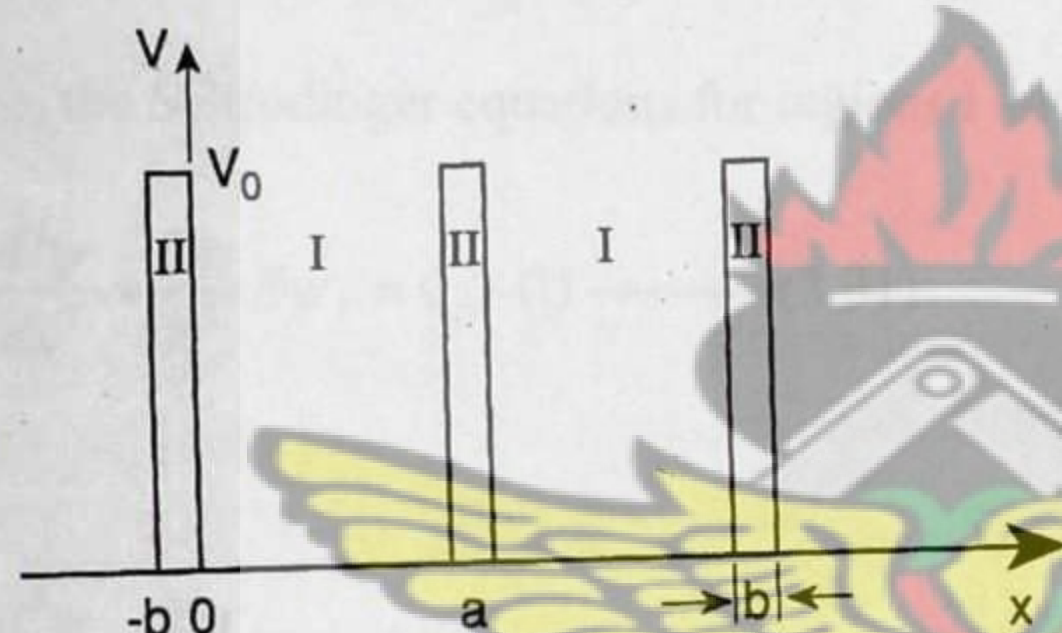


Figure 3.9b: simplified one-dimensional periodic potential distribution used in the Kronig-Penney model.

The potential energy function in a one-dimensional crystal may vary as shown in Figure 3.9a. The positively charged nuclei provide the attractive potential for the negatively charged electrons. To evaluate the movement of an electron in such a potential, Kronig and Penney (1931), simplified it into the situation depicted in Figure 3.9b (Mahajan and Sree Harsha, 1998). This model is historically the first, and is concerned with the solution of Schrodinger's equation, assuming a certain potential distribution inside the solid. The basis of the free electron model is the fact that the constant potential due to the ions and all other electrons (i.e. core electrons) may be ignored (i. e. set to zero). The Kronig-Penney model goes one step further by taking into account the variation of potential due

to the presence of immobile lattice ions. Considering Figure 3.9a, the highest potential is halfway between the ions and the potential tends to minus infinity as the position of the ions is approached. This coarse simplification does not take into consideration that the inner electrons are more tightly bound to the core, but it is adequate. Figure 3.8b shows potential wells of length a that are labeled as region I. these wells are separated by potential barriers of height V_0 and width b (region II); V_0 is assumed to be larger than the energy E of the electron. This situation is very similar to the finite potential barrier discussed in section 3.1.1.2 except that the arrangement repeats forever.

As before, the Schrodinger equations for regions I and II are:

$$\frac{d^2\psi}{dx^2} + \frac{2m}{\hbar^2} E \psi_I = 0 \quad \text{(I) ----- (3.31)}$$

and

$$\frac{d^2\psi}{dx^2} + \frac{2m}{\hbar^2} (E - V_0) \psi_{II} = 0 \quad \text{(II) ----- (3.32)}$$

where

$$\alpha^2 = \frac{2m}{\hbar^2} E \quad \text{----- (3.33)}$$

and

$$\beta^2 = \frac{2m(V_0 - E)}{\hbar^2} \quad \text{----- (3.34)}$$

The complexity of the present case in comparison to the finite potential barrier is obvious.

$\psi_I, \psi_{II}, \frac{d\psi_I}{dx}, \frac{d\psi_{II}}{dx}$ not only have to be continuous at $x = 0$

In Figure 3.9b; they are assumed to be continuous at $x = a+b$ and at other equivalent positions; that is the existence of a periodic potential imposes a periodicity on wave functions in the crystal. Bloch (1930), mathematically showed that in a one-dimensional potential the simultaneous solution of equations 3.31 and 3.32 has the following form:

$$\psi(x) = U(x)e^{ikx} \text{ ----- (3.35)}$$

The amplitude $U(x)$ is no longer a constant, but changes periodically with x , which has a period equal to the lattice constant. Calculating the value of $d^2\psi/dx^2$ from equation 3.35 and substituting it into equation 3.31 and 3.32, we obtain the following equations for u :

$$\frac{d^2u}{dx^2} + 2ik \frac{du}{dx} - (k^2 - \alpha^2)u = 0 \quad \text{(I) ----- (3.36)}$$

and

$$\frac{d^2u}{dx^2} + 2ik \frac{du}{dx} - (k^2 + \beta^2)u = 0 \quad \text{(II) ----- (3.37)}$$

The solutions for equations 3.36 and 3.37 are:

$$u = e^{-ikx} (Ae^{i\alpha x} + Be^{-i\alpha x}) \quad \text{(I) ----- (3.38)}$$

and

$$u = e^{-ikx} (Ce^{-i\beta x} + De^{i\beta x}) \quad \text{(II) ----- (3.39)}$$

The constants A , B , C , and D can be determined from the boundary conditions. The functions $\psi(x)$ and $d\psi/dx$, and therefore $U(x)$ and du/dx , pass over continuously from region I to region II at $x = 0$. These boundary conditions yield

$$A + B = C + D \text{ ----- (3.40)}$$

and

$$A(i\alpha - ik) + B(-i\alpha - ik) = C(-\beta - ik) + D(\beta - ik) \text{ ----- (3.41)}$$

Imposing the periodic boundary condition that $U(x)$ from equation 3.38 at $x = 0$ must be equal to $U(x)$ from equation 3.39 at $x = a + b$, and equivalently from Figure 3.8b, equation 3.38 at $x = a$ is equal to equation 3.39 at $x = -b$, we have

$$Ae^{(i\alpha - ik)a} + Be^{(-i\alpha - ik)a} = Ce^{(ik + \beta)b} + De^{(ik - \beta)b} \text{ ----- (3.42)}$$

Finally du/dx is periodic in $(a + b)$:

$$Ai(\alpha - k)e^{ia(\alpha - k)} - Bi(\alpha + k)e^{-ia(\alpha + k)} = -C(\beta + ik)e^{(ik + \beta)b} + D(\beta - ik)e^{(ik - \beta)b} \text{ --- (3.43)}$$

To determine the values of $U(x)$, equations 3.40 through 3.43 have to be solved simultaneously. The solutions exist if the determinant of the coefficients A , B , C , and D vanishes. Using this criterion, the energy-restricting condition after extensive simplification is

$$\frac{\beta^2 - \alpha^2}{2\alpha\beta} \sinh \beta b \sin \alpha a + \cosh \beta b \cos \alpha a = \cos k(a + b) \text{ ----- (3.44)}$$

Assuming that the potential barriers in Figure 3.8b are such that b is very small and V_0 is very large, equation 3.44 can be simplified to

$$P \frac{\sin \alpha a}{\alpha a} + \cos \alpha a = \cos ka \text{ ----- (3.45)}$$

where

$$P = \frac{maV_0b}{\hbar^2} \text{ ----- (3.46)}$$

P represents the strength of the barrier, and from equation (3.33) α is a function of the energy. In order to find the E - k curve we plot the right-hand side of equation 3.45 as a function of αa .

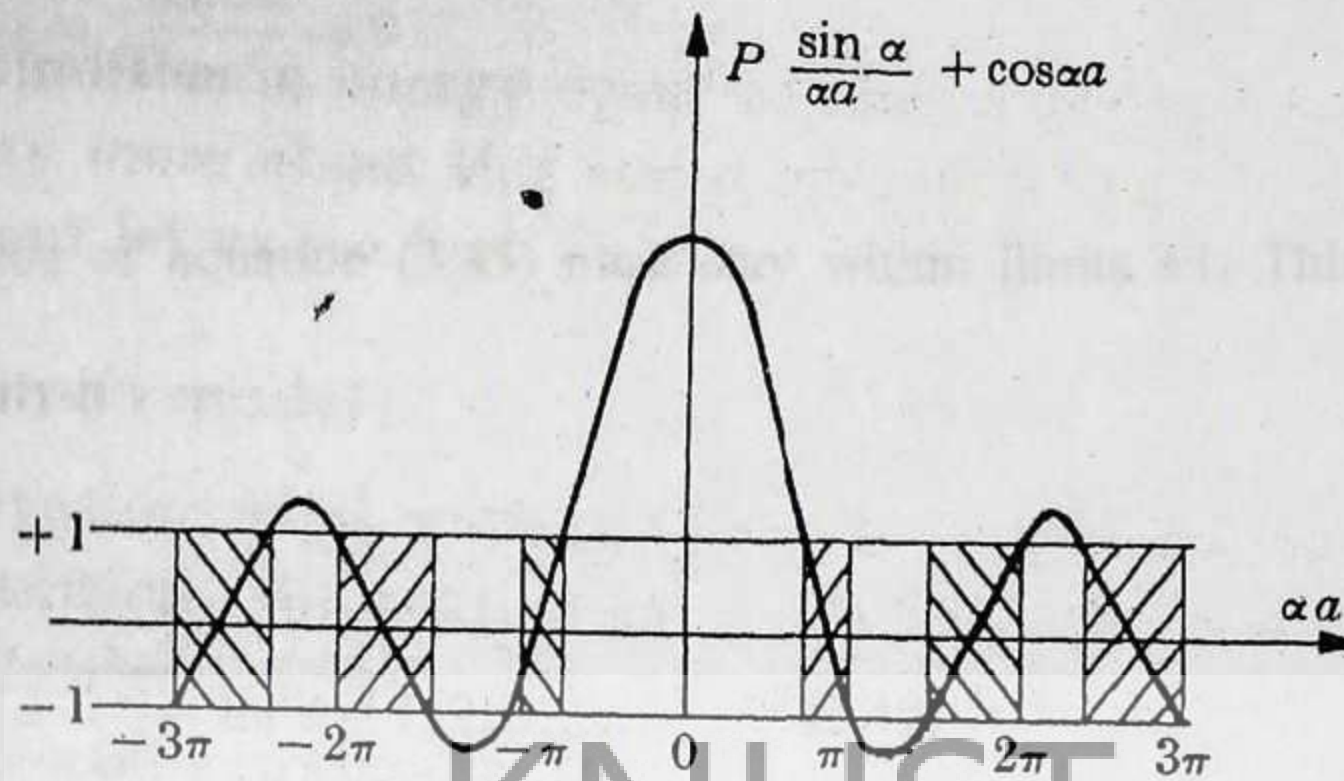


Figure 3.10: The right-hand side of equation (3.45) for $P = 3\pi/2$ as a function of αa (Mahajan and Sree Harsha, 1998)

Since the left-hand side of equation 3.45 must be between +1 and -1, a solution exists only for those values of E for which the right-hand side is between the same limits; that is there is a solution for the shaded region. Since α is related to E , this means that the electron may possess energies within certain bands but not outside them. Expressed in another way: there are allowed and forbidden bands of energy.

Consider two special cases:

- (i) The potential barrier strength becomes smaller and smaller and finally disappears completely, that is, in the limit $P \rightarrow 0$, we get

$$\cos \alpha a = \cos k a \quad \text{-----} (3.47)$$

or $\alpha = k$

It follows from equation (3.33) that

$$E = \frac{\hbar^2 k^2}{2m} \quad \text{-----} (3.48)$$

Which is the well-known equation for free electrons developed in section 3.1.1.1.

(ii) When $P \rightarrow \infty$, $\frac{\sin \alpha a}{\alpha a} \rightarrow 0$

The left side of equation (3.45) must stay within limits ± 1 . This condition is possible only if

$$\alpha a = n\pi \text{ or}$$

$$\alpha^2 = \frac{n^2 \pi^2}{a^2} \text{ for } n = 1, 2, 3, \dots \quad (3.49)$$

Substituting for α^2 from 3.49 into 3.33, we obtain

$$E = \frac{n^2 \pi^2 \hbar^2}{2ma^2} \quad \text{-----} (3.50)$$

which is the result for an electron confined in an infinite barrier.

Thus by varying P from zero to infinity, we cover the whole range from the completely free electron to the completely bound electron.

3.1.2.2. Effect of a periodic potential on the free electron model

From Figure (3.10), at the boundary of an allowed band

$$\cos k\alpha = \pm 1$$

That is,

$$k = \frac{n\pi}{a} \quad n = 1, 2, 3, \dots$$

For values of k other than $n\pi/a$, we treat electrons as free. However, discontinuities in energy occur at the values of k specified above. Thus the energy versus k plot in Figure 3.1 is modified in the vicinity of $k = n\pi/a$ as illustrated in Figure 3.11a.

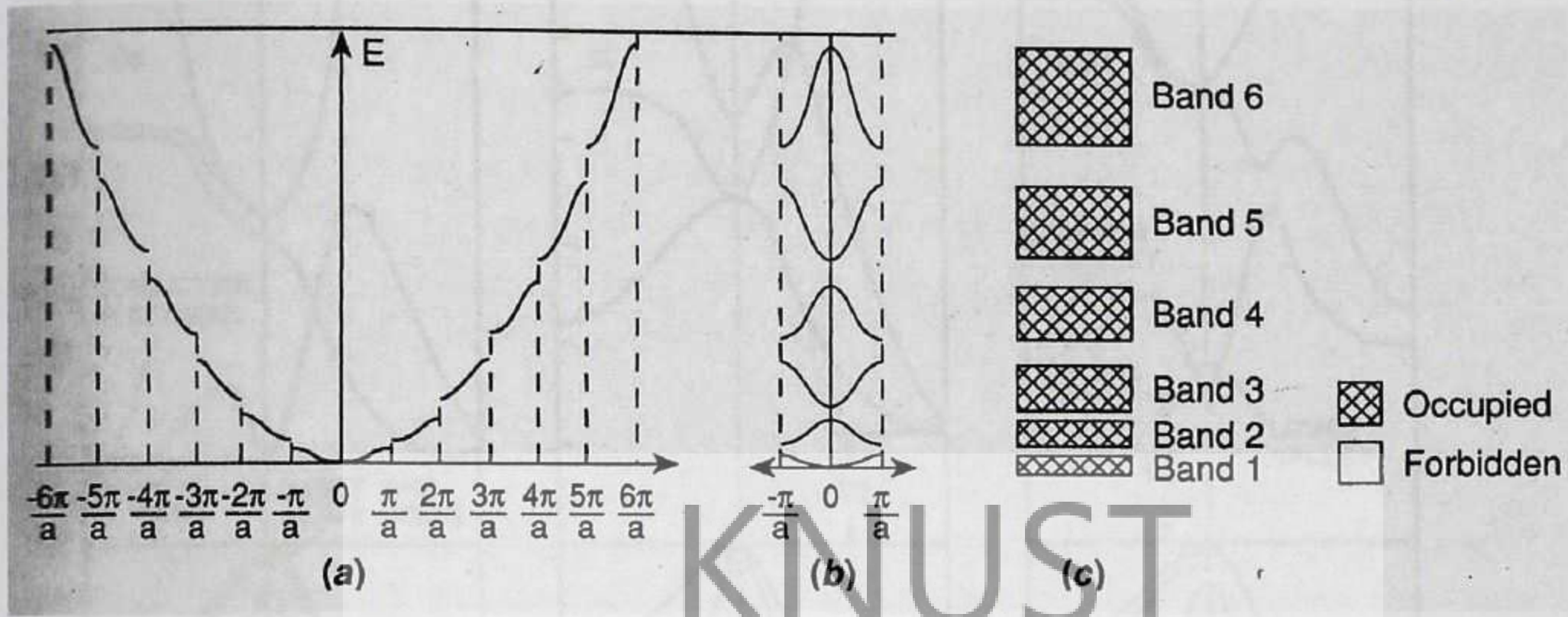


Figure 3.11: (a) The free-electron model of electrons as perturbed by a small periodic potential discontinuities in the energy at $k = n\pi/a$ in the extended representation. (b) the reduced representation in the first Brillouin zone achieved by translating band segments in (a) by $2\pi n/a$ to bring them into the basic zone. (c) Separate bands are indicated. (Mahajan and Sree Harsha, 1998)

The emergence of energy bands and forbidden gaps in the spectrum of electron energies in a periodic crystal has most important consequences for electron transport in semiconductors.

3.1.2.3. Direct and Indirect Band gap semiconductors

The energy band diagrams of semiconductors are rather complex. The energy bands of solids have been studied theoretically using a variety of numerical methods. For semiconductors the three methods most frequently used are the orthogonalized plane-wave method, the pseudo potential method, and the $k.p$ method. Figure 3.12 shows recent results of studies of the energy band structure of Ge, Si and GaAs. Notice that for any semiconductor there is a forbidden energy region in which allowed states cannot exist. Energy regions or energy bands are permitted above and below this energy gap.

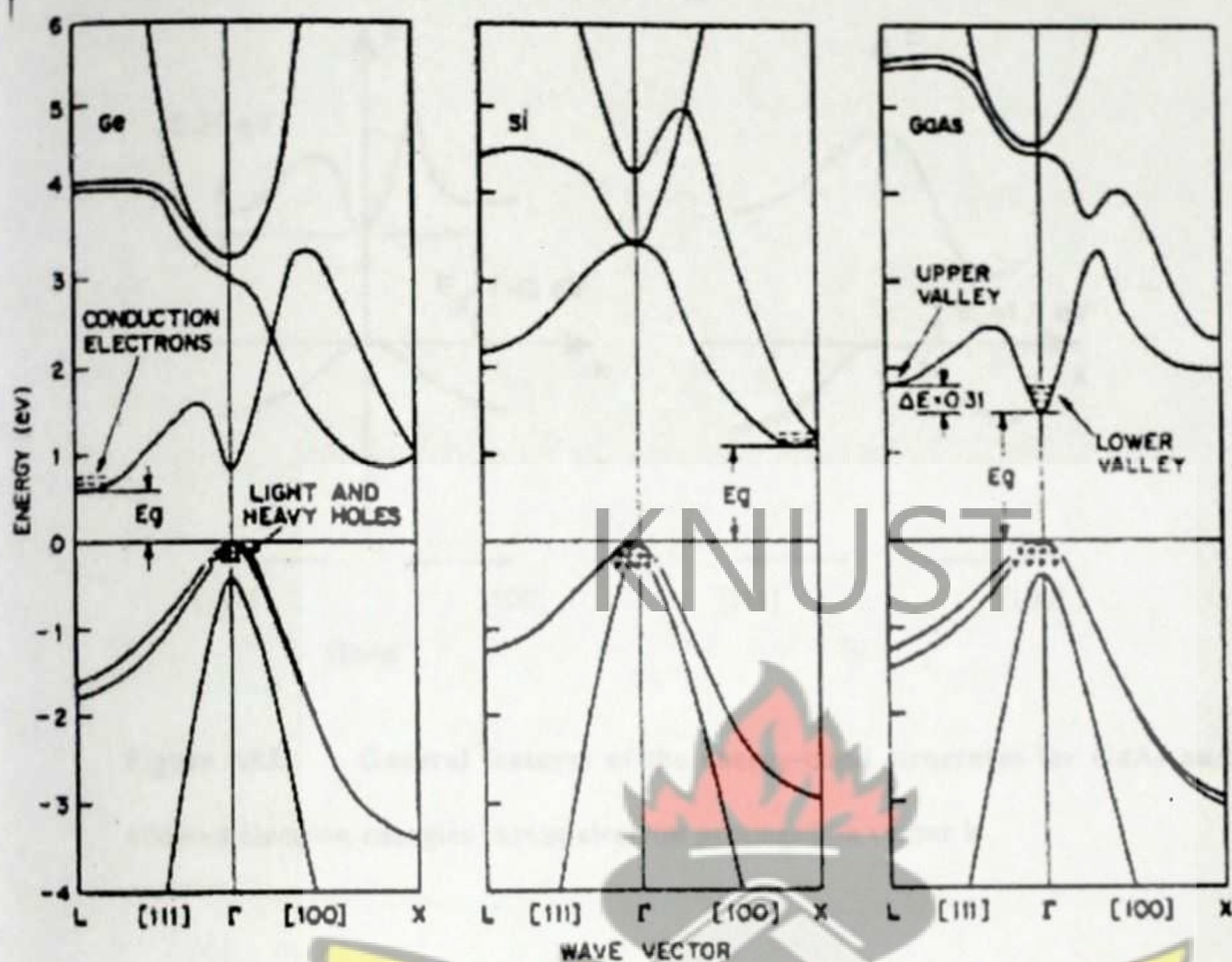


Figure 3.12: Energy band diagram of (a) germanium, (b) silicon and (c) gallium arsenide

The upper bands are called the **conduction band**; the lower bands, the **valence bands**. The separation between the energy of the **lowest conduction band** and that of the **highest valence band** is called the **band gap**, E_g , which is the most important parameter in semiconductor physics. However, to explain the concept of **direct and indirect band gaps** we shall use the simplified model shown in Figure 3.13.

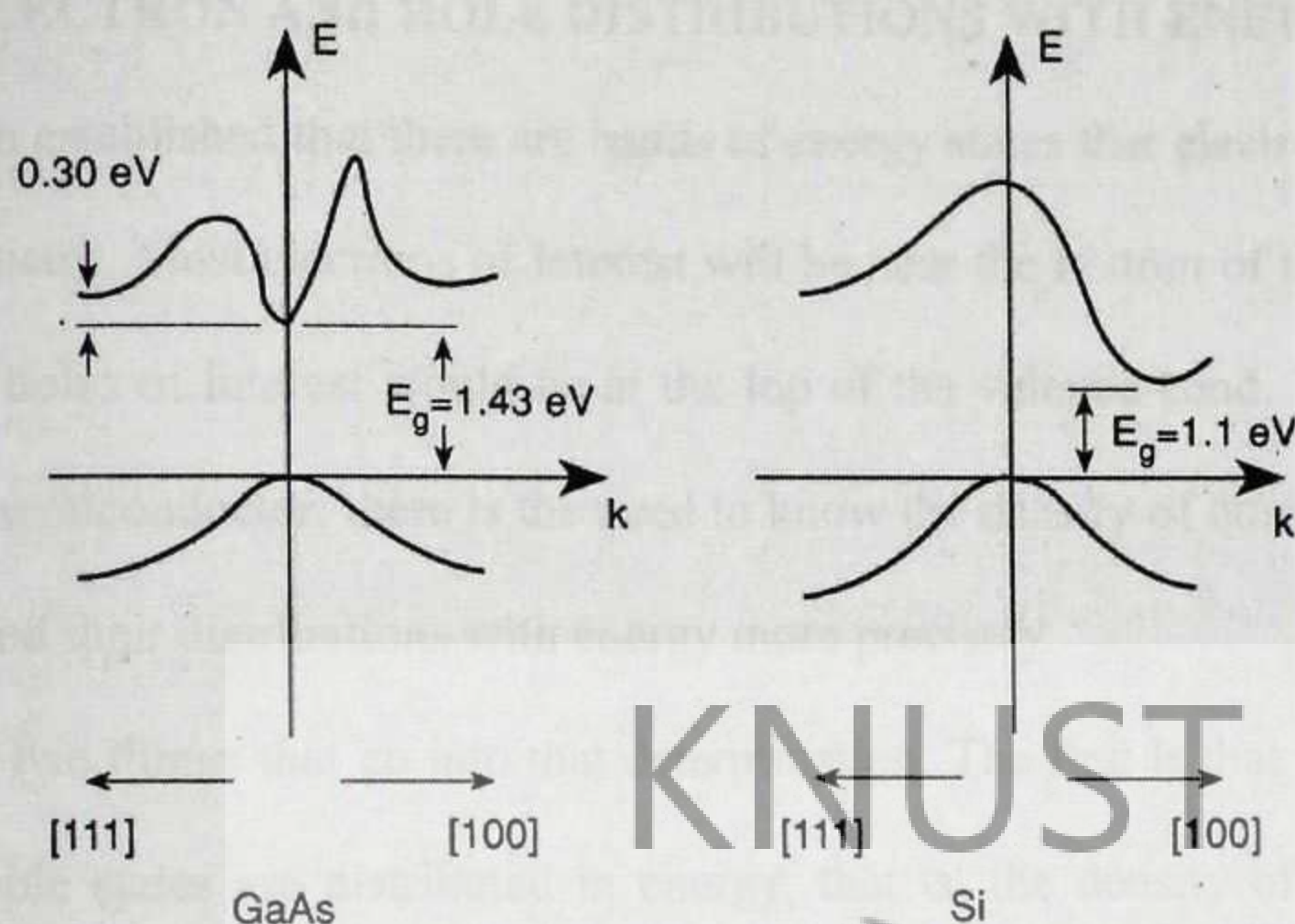


Figure 3.13: General features of the energy-band structures for GaAs and Si showing allowed electron energies versus electron propagation vector k

Direct band gap semiconductors, are semiconductors for which the minimum of the conduction band occurs at the same wave vector, k , as the maximum of the valence band example, gallium arsenide (GaAs). These semiconductors have a stronger absorption of light as characterized by a larger absorption coefficient. They are also the favoured semiconductors when fabricating light emitting devices. Indirect band gap semiconductors, are semiconductors for which the minimum of the conduction band does not occur at the same wave vector as the maximum of the valence band, such as silicon (Si). They are known to have a smaller absorption coefficient and are rarely used in light emitting devices.

3.1.3 ELECTRON AND HOLE DISTRIBUTIONS WITH ENERGY

It has been established that there are bands of energy states that electrons can occupy in a semiconductor. Most electrons of interest will be near the bottom of the conduction band and most holes of interest would be at the top of the valence band. To describe current flow in a semiconductor, there is the need to know the density of quasi-free electrons and of holes and their distributions with energy more precisely.

There are two things that go into that determination. The first is that we must know how the available states are distributed in energy, that is, the density of states. The second factor we need to know is the probability that a state at a given energy is occupied.

3.1.3.1 Density of states

The density of states function for an electron near the bottom of the conduction band in a semiconductor can be stated mathematically as:

$$g(E) = \frac{1}{2\pi^2} \left(\frac{2m_{dse}^*}{\hbar^2} \right)^{3/2} \sqrt{E - E_C} \quad \text{--- 3.51}$$

$$= \frac{1}{2\pi^2} \left(\frac{2m_{dse}^*}{\hbar^2} \right)^{3/2} \sqrt{E_K} \quad \text{--- 3.52}$$

where m_{dse}^* is referred to as the density of states effective mass for electrons. The kinetic energy E_K is the difference between the total energy and the potential energy E_C for an electron in the parabolic region near the bottom of the conduction band.

This represents the number of electron states per unit volume per unit energy at energy E . This energy density is a factor in many of the electrical properties of solids. The density of states as a function of energy is shown in Figure 3. 14.

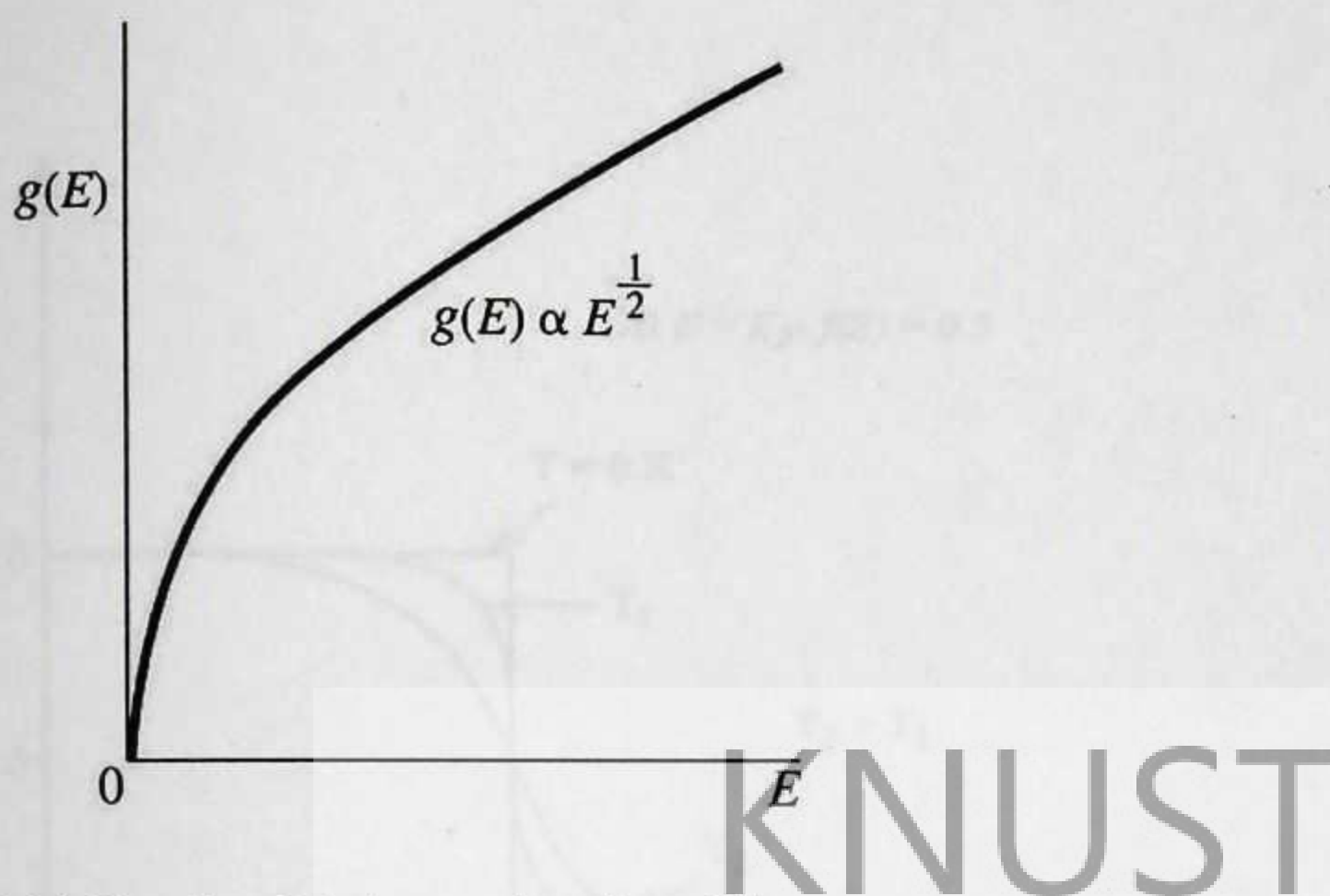


Figure 3.14: Density of states as a function of Energy

3.1.3.2 Fermi Distribution Function

The Fermi function $f(E)$ gives the probability that a given available electron energy state will be occupied at a given temperature. The Fermi function comes from Fermi-Dirac statistics and has a different form depending on whether the electrons under consideration are free to move through the crystal (as within a band) or bound to localized states (as for impurities).

The probability that an electron occupies a given state at energy E in an allowed band is given by:

$$f(E) = \frac{1}{1 + e^{(E-E_f)/kT}} \text{-----3.53}$$

where the energy E_f is a reference energy called the Fermi energy or Fermi level.

Equation 3.53 is known as the Fermi-Dirac probability function. The Fermi level is chosen to be that particular energy level for which $f(E) = 1/2$, or the probability of occupancy of a state at that energy (if the state exists) is fifty percent.

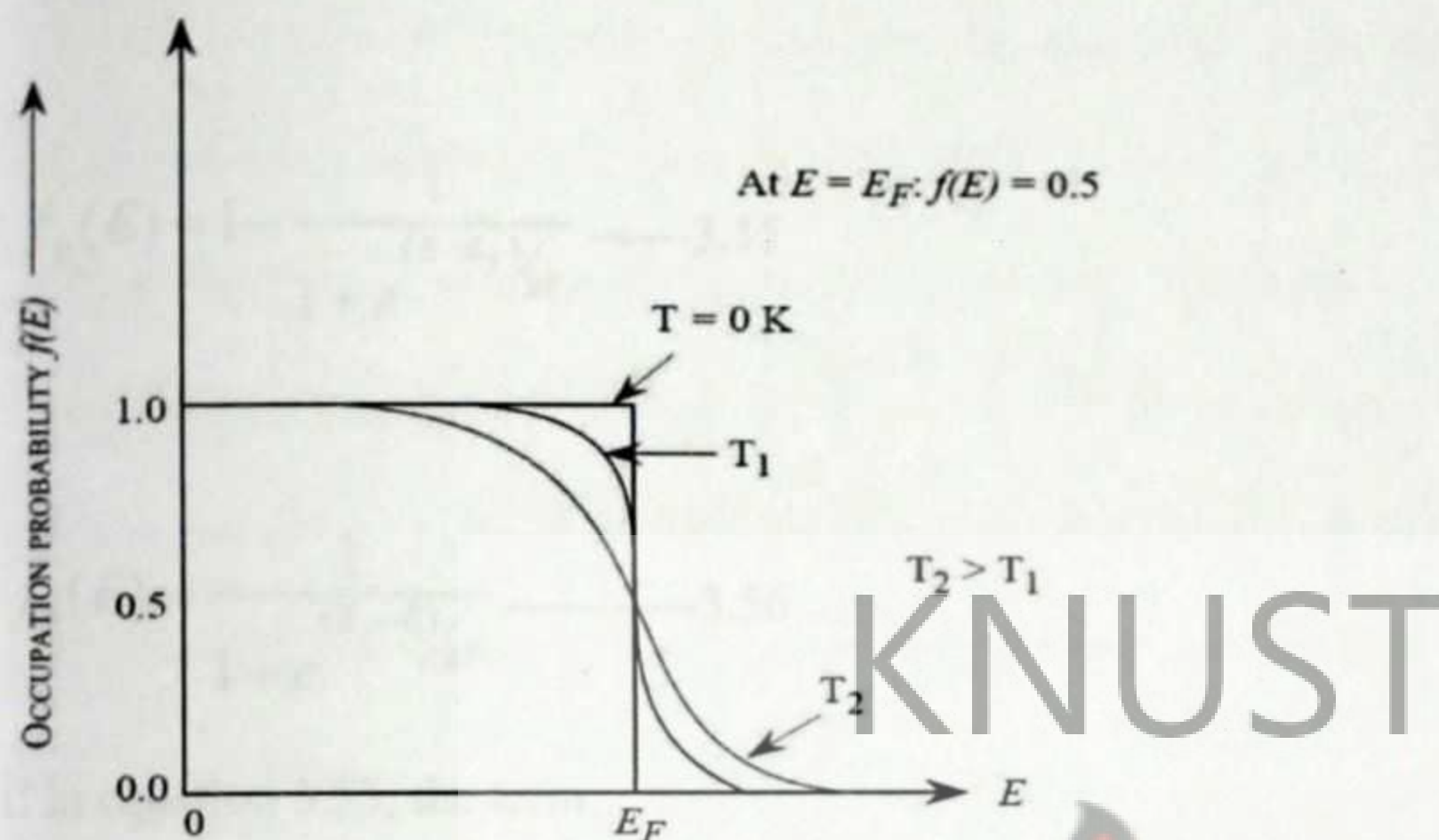


Figure 3.15: Fermi-Dirac probability function

Figure 3.15, shows the Fermi-Dirac probability function for several different temperatures. At absolute zero, every electron is at its lowest possible energy. That is every state in the valence band is occupied. The probability of occupancy of any state in the valence band is then unity, and the probability of occupancy of any state in the conduction band is then zero. At higher temperatures some electrons have enough energy to be in the conduction band. The probability of occupancy of a state near the bottom of the conduction band is less than $\frac{1}{2}$, but is not zero either. Similarly some states near the top of the valence band will be empty, indicating that there are some holes. With increasing temperature, the probability of occupancy in the conduction band increases. Likewise the probability of occupancy of a given state in the valence band decreases. This means that at higher temperatures there are more electrons and holes available to carry current. The probability of a state being occupied by a hole is:

$$f_p(E) = 1 - f(E) \text{-----3.54}$$

$$f_p(E) = 1 - \frac{1}{1 + e^{\frac{(E-E_f)}{kT}}} \text{-----3.55}$$

$$f_p(E) = \frac{1}{1 + e^{\frac{(E_f-E)}{kT}}} \text{-----3.56}$$

KNUST

If in equation 3.53, the term

$$e^{\frac{(E-E_f)}{kT}} \gg 1, \text{ then } f(E) \ll 1 \text{-----3.57}$$

Thus,

$$f(E) \approx e^{-\frac{(E-E_f)}{kT}} \text{-----3.58}$$

Similarly from equation 3.56, for $f_p(E) \ll 1$

$$f_p(E) \approx e^{-\frac{(E_f-E)}{kT}} \text{-----3.59}$$

Equations 3.58 and 3.59 are referred to as the Boltzmann approximations to the Fermi-Dirac probability function, or simply the Boltzmann probability function.

3.1.3.3 Concentrations of electrons and holes at equilibrium

The concentration of majority carriers can be estimated from doping levels, but the concentration of minority carriers is more difficult to compute. Therefore we need to develop expressions that can adequately describe these situations.

Now that we know how the available states are distributed in energy, and the probability that a given energy state is occupied by electrons, we can figure out how many electrons jump from the filled valence band, across the band gap, and into the conduction band at a given temperature.

The number of electrons per unit volume per unit energy, in a small energy range dE , is given by;

$$n(E)dE = g(E)f(E)dE \quad \text{-----} (3.60)$$

In a given band, then, at equilibrium, the total number of electrons per unit volume, n_o , in the entire energy band is

$$n_o = \int_{\text{band}} g(E)f(E)dE \quad \text{-----} (3.61)$$

where the integration is taken over the total band of allowed energies.

$$n_o = \int_{E_c}^{\text{top of conduction band}} g_c(E)f(E)dE$$

The energy at the top of the conduction band is not known, however, since $f(E)$ is so small deep in conduction band, we can replace top of conduction band with ∞ . Thus, by using the Boltzmann approximation, and extending the integration limit to ∞ , we obtain

$$n_o = N_c e^{-(E_c - E_F)/kT} \quad \text{where } N_c = 2 \left(\frac{2\pi m_{dse}^* kT}{h^2} \right)^{3/2} \quad \text{-----} 3.62$$

There are three ways of classifying solids, the most useful of these is into

where, N_c is called the effective density of state at conduction band edge.

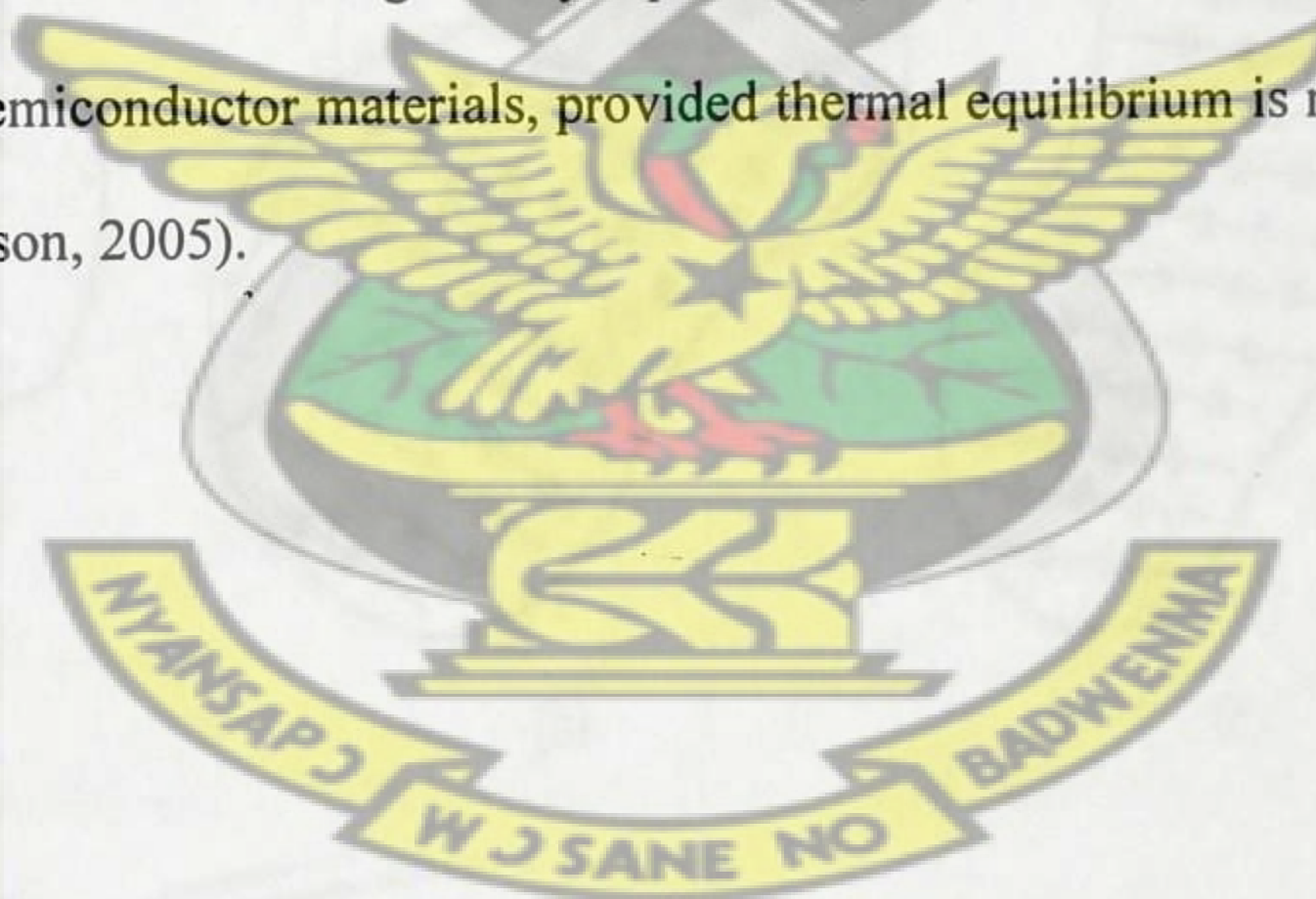
And similarly for holes

$$p_o = \int_{\text{bottom of valence band}}^{E_v} g_v(E)[1 - f(E)]dE$$

By using the Boltzmann approximation, and extending the integration limit to $-\infty$, we obtain

$$p_o = N_v e^{-(E_F - E_v)/kT} \quad \text{where } N_v = 2 \left(\frac{2\pi m_{dsh}^* kT}{h^2} \right)^{3/2} \quad \text{----- 3.63}$$

The electron and hole concentrations given by equations (3.62) and (3.63) are valid for doped and undoped semiconductor materials, provided thermal equilibrium is maintained (Anderson and Anderson, 2005).



3.2. CLASSIFICATION OF SOLIDS

There are diverse ways of classifying solids, but perhaps the most useful division is into *crystalline*, *polycrystalline* and *amorphous*. Each type is characterized by the size of an ordered region within the material. An ordered region is a spatial volume in which atoms or molecules have a regular geometric arrangement or periodicity. Figure 3.16 shows the three structural orders (Neamen, 2003). It should be noted that the majority of semiconductors used in electronic applications are crystalline materials, although some polycrystalline and amorphous semiconductors have found a wide range of applications in various electronic devices, (Yacobi, 2004).

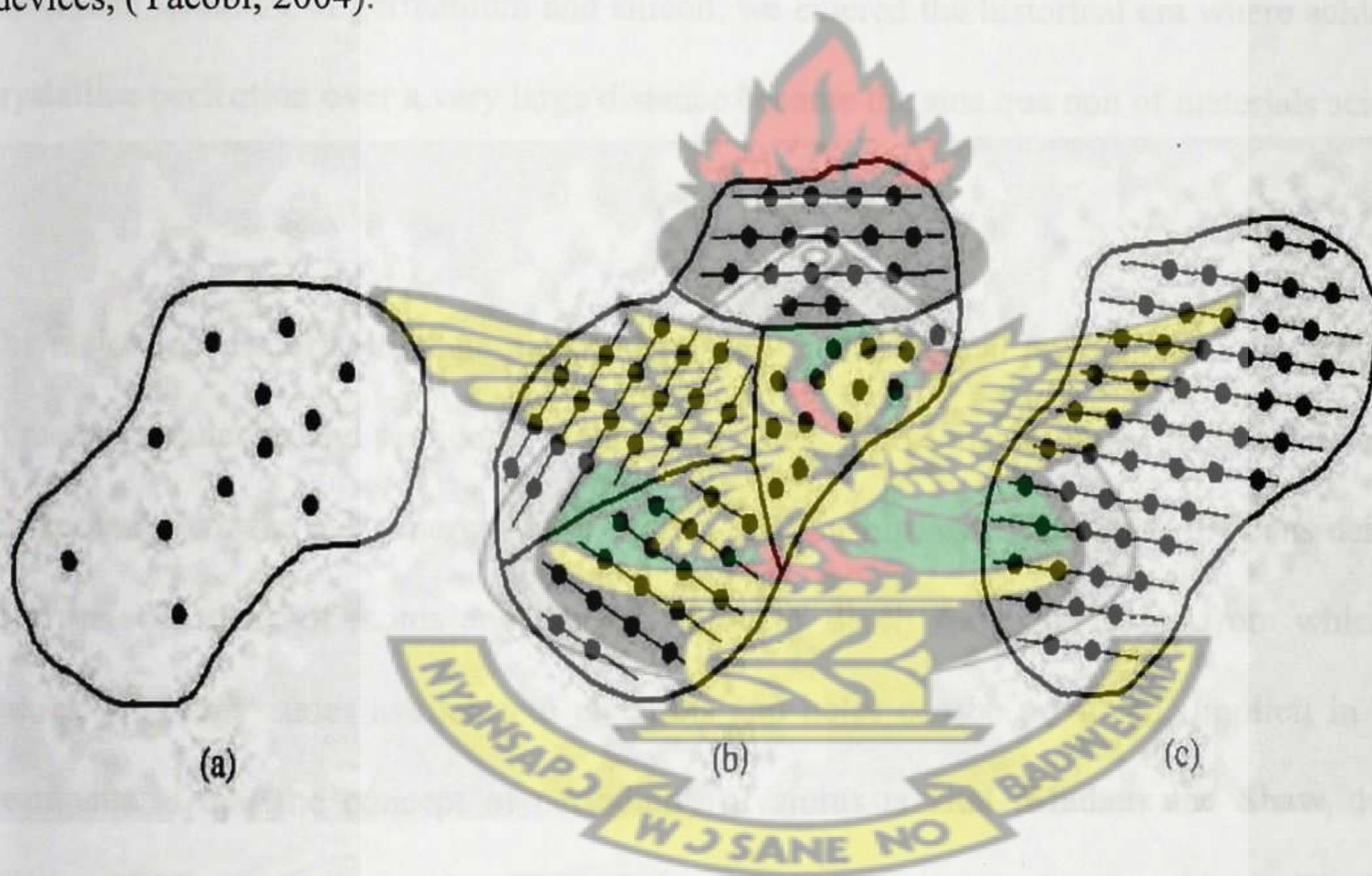


Figure 3.16: Schematics of the three general types of structural orders: (a) amorphous, (b) polycrystalline, (c) crystalline.

3.2.1 CRYSTALLINE SEMICONDUCTORS

A crystal is a solid composed of atoms or other microscopic particles arranged in an orderly repetitive array. That is about the shortest definition of a crystal. It may not be a complete definition, yet it is a true description (Pillai, 2005). Single crystals have long range order. Many important properties of materials are found to depend on the structure of crystals and on the electron states within the crystals (Pillai, 2005). It is well known that the great success of the 20th century, the transistor, is based upon the periodicity of materials with particular emphasis on one element, silicon. Indeed, with the great success of the transistor based upon the crystal structure of germanium and silicon, we entered the historical era where achieving crystalline perfection over a very large distance became the sine qua non of materials science.

The major success of solid state physics has been the theoretical prediction of the behaviour of metals, insulators and semiconductors. The success of the energy band theory has relied on the derivation of the E-k (energy-wave vector) relationship, which involves the consideration of a periodic array of atoms and the derivation of Bloch wave functions, from which the classes of energy states available to electrons and holes can be predicted. Implicit in these treatments is that the concept of periodicity of atoms is vital (Madam and Shaw, 1988). Wilson (1931), showed how the electronic band theory of crystals developed by F. Bloch can be applied to understanding semiconductors. Properties such as the negative temperature coefficient of electrical resistivity, follow naturally from Wilson's theory. The key ingredients are the *Bloch states* which are the eigenstates of an electron moving in the periodic potential of a crystal. The energies of the Bloch states cannot take on all possible values, but are restricted to certain allowed regions or *bands* separated from one another by forbidden regions called *band gaps* or *energy gaps*. Band theory and its outcome effective

mass theory, has allowed us to understand the difference between metals, insulators and semiconductors and how electrons respond to external forces in solids (Balkanski and Wallis, 2000; Singh, 2003).

The advantage of crystalline material is that, in general, its electrical properties are superior to those of a polycrystalline material, since grain boundaries tend to degrade the electrical characteristics (Neamen, 2003).

3.2.2. POLYCRYSTALLINE SEMICONDUCTORS

In polycrystalline materials, numerous crystalline regions called *grains*, have different orientation and are separated by a *grain boundary*. These ordered regions or single-crystal regions, have a high degree of order over many atomic or molecular dimensions. They only vary in size and orientation with respect to one another (Neamen, 2003). Polycrystalline semiconductors can be further classified as (i) microcrystalline and nanocrystalline materials that are usually prepared as thin films and (ii) large grain materials in the form of sliced ingots and sheets. The grain size in polycrystalline thin film materials depends on the substrate temperature during thin film growth, the thickness of the film and also on post-growth annealing treatment of the film. It is important to note here that many solids are incorrectly described as being amorphous, but are in fact microcrystalline or nanocrystalline with small crystallite sizes which fail to give crystalline X-ray diffraction patterns. However, often these materials can be confirmed as crystalline using electron diffractions, with lattice images routinely obtained from particles in the range of 5 nm. The grain boundaries generally have an associated space-charge region controlled by the defect structure of the material.

These grain boundaries are paths for the rapid diffusion of impurities affecting various properties of polycrystalline materials.

An important consequence of the presence of potential barriers on grain boundaries in a polycrystalline semiconductor is the increase of its electrical resistivity. One of the important processes is the “decoration” of grain boundaries, that is, the process in which precipitates of impurity elements segregate to the boundaries. In general, the grain boundaries introduce allowed levels in the energy gap of a semiconductor and act as efficient recombination centres for the minority carriers. This effect is important in minority-carrier devices, such as photovoltaic solar cells, where it is expected that some of the photo generated carriers will be lost through recombination on the grain boundaries. Typically, the efficiency of the device will improve with increasing grain size. In this context, the *columnar grain structure*, that is, where grains in a polycrystalline material extend across the wafer thickness, is more desirable as compared to the material containing fine grains that do not extend from back to front of a device structure. In order to prevent significant grain boundary recombination of the minority carriers, it is also desirable that the lateral grain sizes in the material be larger than the minority carrier diffusion length. It should also be mentioned that the possible preferential diffusion of dopants along the grain boundaries and or precipitates of impurity elements segregated at the boundaries may provide shunting paths for current flow across the device junction. It should also be noted that hydrogen passivation of grain boundaries in polycrystalline silicon devices, such as photovoltaic cells, is an effective method of improving their photovoltaic performance efficiency. This improvement is associated with the mechanism similar to that of the passivation of dangling bonds in amorphous silicon (Yacobi, 2004; Gellings and Bouwmeester, 1997)

3.2.3. AMORPHOUS SEMICONDUCTORS

Amorphous solids have been used as so-called glasses with various modifications in our lives since more than 2000 B.C. The earliest glasses were beads made in Egypt and earlier Mesopotamia. Scientific investigations on amorphous solids however began in the 20th century (Morigaki, 1999). Recent years have seen an upsurge in interest in the electronic properties of non-crystalline materials; these materials, lack the simple structures and long range order that make crystals relatively easy to understand. The first reason for this is their potential industrial applications as suitable materials for fabricating electronic devices such as photo-, X-ray and electron beam lithography, thin film solar cells, thin film transistors, memory storage discs, holographic optical elements, switching devices, optical waveguides, coatings, ultra-sensitive photoconductors for use in flat panel x-ray image detectors and high definition digital and video cameras (Tan, 2006; Gaga, 1981; Wolf, 1971; Shwartz, 1993). Secondly, there is a lack of understanding of many properties of these materials compared with that of crystalline materials. (Tan, 2006).

Over the years it has been discovered that an amorphous solid is a solid whose atomic structure is random such that long range atomic order is absent. Amorphous solids, nevertheless, retain the short range order due to valence bonding of atoms, which is also characteristic of crystalline solids. However, bonding angles and bonding lengths vary from that of their crystalline counterparts thus, the lack of long range atomic order, resulting in the general irregular appearance of the amorphous atomic structure. This type of disorder is termed translational disorder. The disorder in amorphous solids, brings certain atoms closer together resulting in extra bonds. This is termed overcoordination. Undercoordination occurs when there is a lack of atomic bonds where they are usually present in crystalline solids. Thus

amorphous solids tend to deviate from the 8-N rule of coordination (Morigaki, 1999). Figure 3.17 compares the atomic structures of crystalline and amorphous solids.

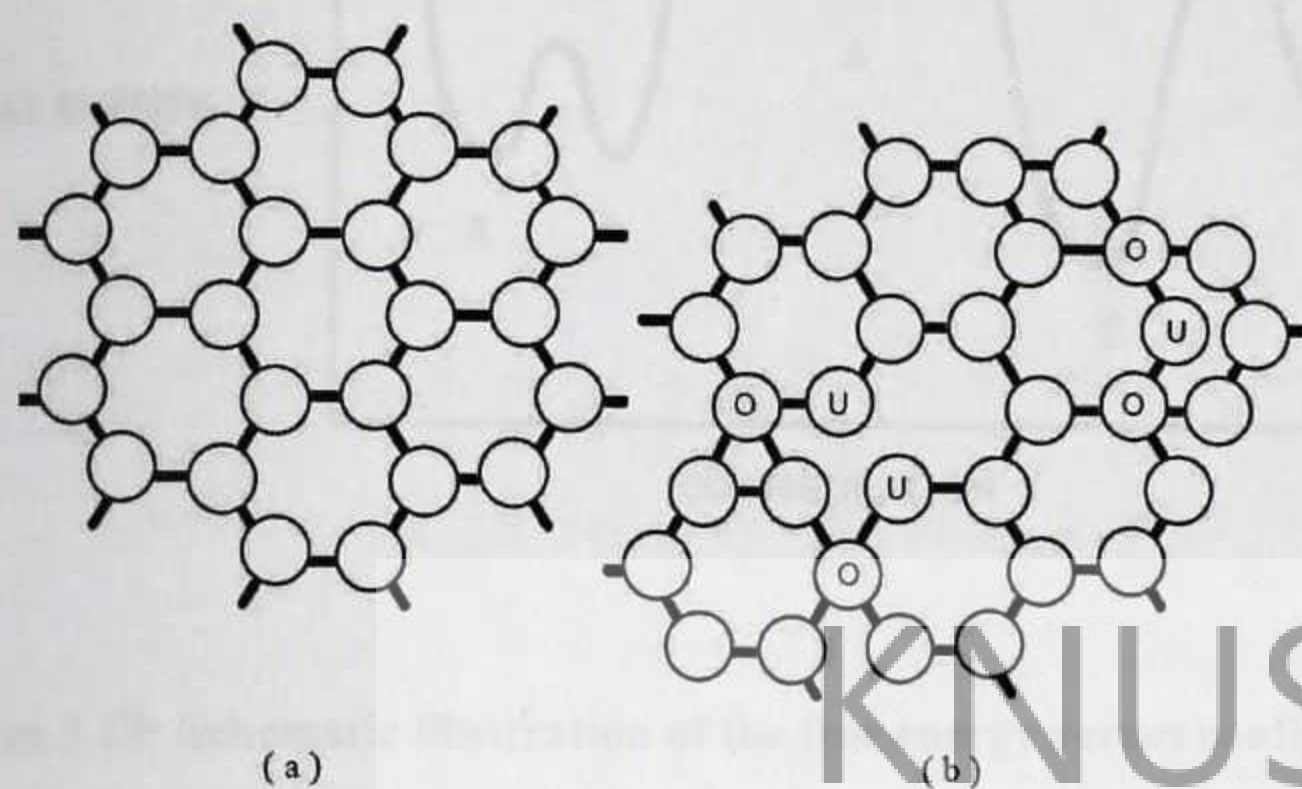


Figure 3.17: Two dimensional representation of the structure of (a) a crystalline solid and (b) an amorphous solid.

Figure 3.16 (a) and (b), shows a two dimensional representation of the structure of a crystalline and an amorphous solid. Atoms marked "O" represent over-coordinated atoms with more than usual numbers of bonding with adjacent atoms and "U" represent under-coordinated atoms, having less than the usual number of bonds with adjacent atoms (Tan, 2006). Due to the permanent displacement of constituent atoms from lattice sites, amorphous solids are said to be in metastable states, i.e. in non equilibrium states. The metastable states are separated from the minimum energy level corresponding to a crystalline state. External perturbations such as thermal, optical, electrical and mechanical agitations can cause the metastable states to be brought to the crystalline state.

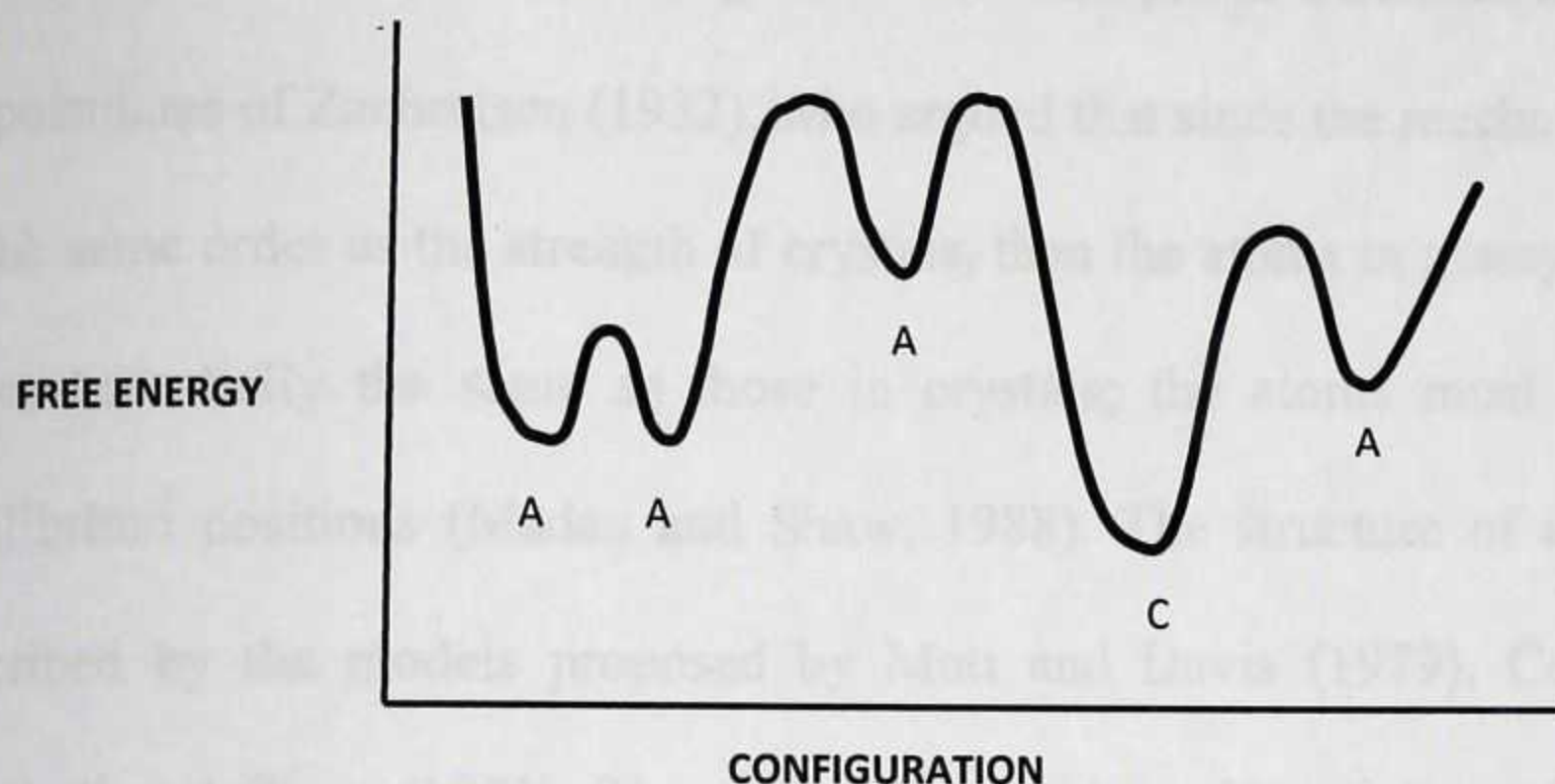


Figure 3.18: Schematic illustration of the free energy versus configuration curve (Morigaki, 1999).

From Figure 3.18, local minimum states are separated from the state C with some barriers. External perturbations such as thermal, optical, electrical and mechanical agitations etc., cause the metastable state, e.g., A, to be brought to the crystalline state C. (Morigaki, 1999).

The term glassy and/or non-crystalline material has been used synonymously with the term amorphous material. It is important to understand that amorphous semiconductors are metastable thin solid film materials (Madam and Shaw, 1988). Glasses, on the other hand, are formed when solids are heated above their melting point and then cooled rapidly so that constituent atoms are unable to acquire the necessary energy to return to their regular lattice positions. Thus crystallization is prevented and the solids become supercooled liquids (Morigaki, 1999). Glass transition occurs at a certain temperature T_g , below which solids become glasses (Morigaki, 1999). However not all supercooled liquids have a transition temperature T_g and so not all amorphous solids can be called glasses. T_g depends on the speed of liquefaction and is therefore not a phase transition in the usual sense (Morigaki, 1999).

Present views of the structure of glasses and amorphous materials are derived largely from the postulates of Zachreisen (1932), who argued that since the mechanical strength of glass is on the same order as the strength of crystals, then the atoms in glassy materials are linked by forces essentially the same as those in crystals; the atoms must oscillate about definite equilibrium positions (Madan and Shaw, 1988). The structure of amorphous solid can be described by the models proposed by Mott and Davis (1979), Cohen *et al.* (1969), and Marshall and Owen (1971). These models provide a clear picture of the density distribution of states in the energy gap of amorphous semiconductors (Hoff and Ruzyllo, 2006).

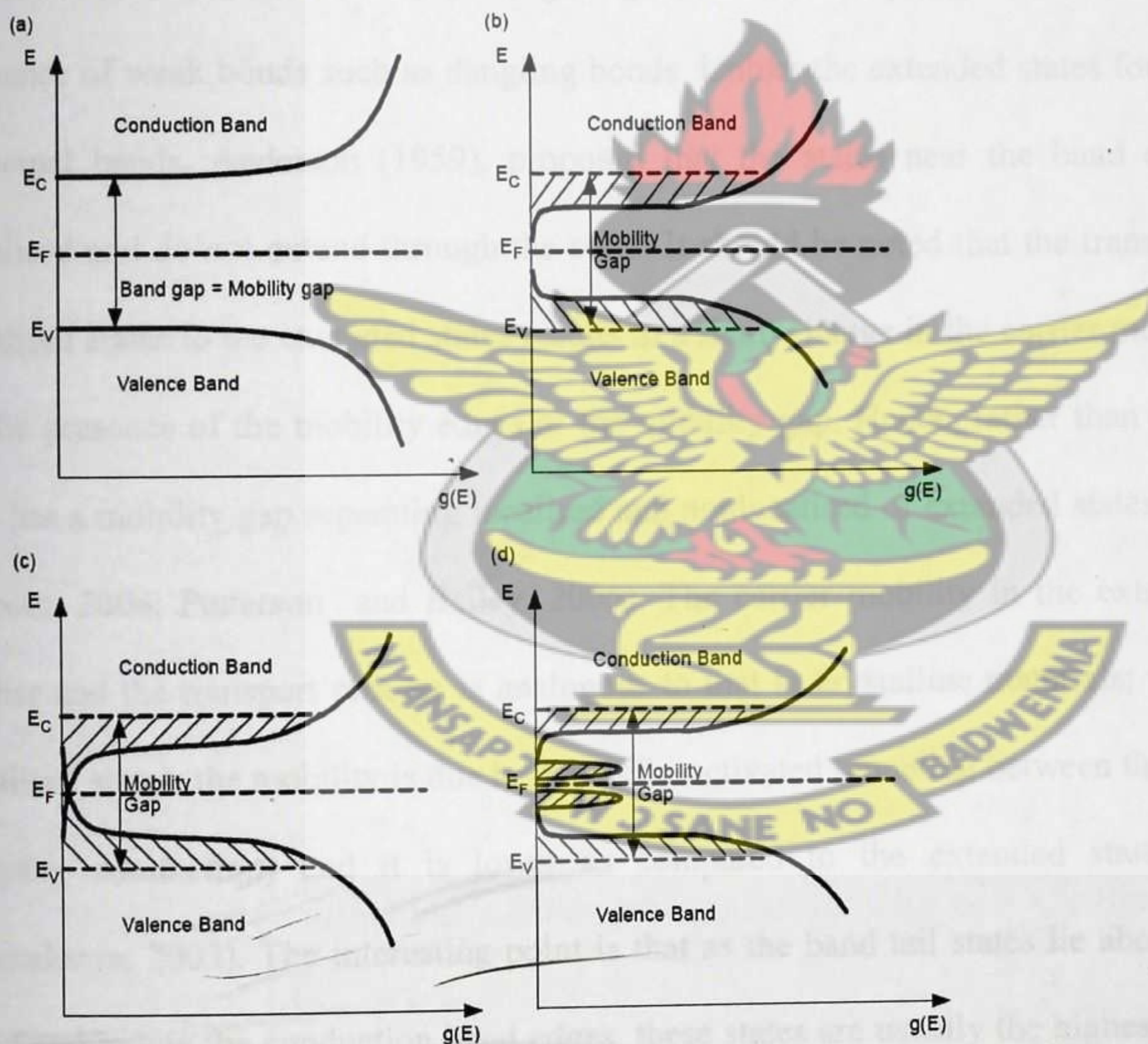


Figure 3.19: (a) DOS of a crystalline semiconductor; (b) DOS models proposed by Mott (1967) (c) DOS models proposed by Cohen *et al.* (1969) and (d) DOS models proposed by Marshall and Owen (1971). The hatched regions denote localized states. Note: the x-axis in all the 4 Figures is logarithmic.

Figures 3.19(a) and (b) show schematically, typical features of density of states (DOS) of a crystalline semiconductor and an amorphous semiconductor, respectively. In a crystalline semiconductor, there is no DOS within the free electron energy gap, E_g , whereas in the amorphous semiconductor, there exists a non-zero DOS within the mobility gap. It is now well established that these distinct features of the DOS of amorphous semiconductors arise due to the presence of tail states and gap states, which are localized states, and which do not exist in crystalline semiconductors (Mott and Davis, 1979; Cody, 1984; Overhof and Thomas, 1989; Adachi, 1999; Morigaki, 1999). It is also well established that the origin of tail states is due to the absence of long range order in amorphous semiconductors, and the presence of weak bonds such as dangling bonds. Unlike the extended states found in the two principal bands, Anderson (1959), proposed that the states near the band edges may be localised and do not extend through the solid. It should be noted that the transition from the localised states to the extended states results in a sharp change in the carrier mobility, leading to the presence of the mobility edges or the mobility gap. Hence, rather than an energy gap one has a mobility gap separating localised and nonlocalised or extended states (Kittel, 2005; Yacobi, 2004; Petterson and Bailey, 2005). The carrier mobility in the extended states is higher and the transport process is analogous to that in crystalline materials; whereas in the localised states, the mobility is due to thermally-activated tunneling between those states (i.e., *hopping conduction*) and it is lower as compared to the extended states (Singh and Shimakawa, 2003). The interesting point is that as the band tail states lie above the valence band and below the conduction band edges, these states are usually the highest occupied and the lowest empty energy states in any amorphous semiconductor. Therefore, band tail states play the dominant role in most optical and electronic properties of amorphous semiconductors, particularly in the low temperature region (Singh and Shimakawa, 2003). From observations and measurements we find that it is the regular crystalline structure that

leads to certain special properties and behaviour of the associated materials (Korvink and Greiner, 2002).

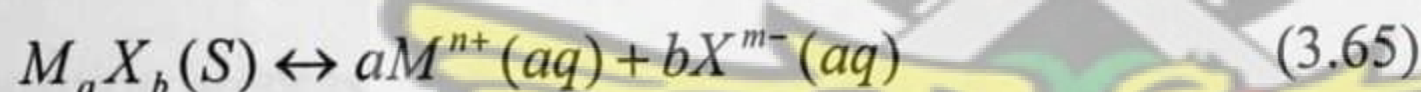
3.3. BASIC PRINCIPLES OF CHEMICAL BATH DEPOSITION

The basic principles behind the CBD process are similar to those for all precipitation reactions, and are based on the relative solubility product. The equilibrium concentration of ions in solution is defined by the solubility product expression (equation 3.64):

$$K_{sp} = [M^{n+}]^a [X^{m-}]^b \quad (3.64)$$

Where K_{sp} is the solubility constant and $[M^{n+}]^a [X^{m-}]^b$ is the ionic product IP.

aM^{n+} ions and bX^{m-} ions are formed from the solid as in equation (3.65).



The preparation of sulphides by introducing S^{2-} ions into an aqueous solution of a metal salt to effect chemical precipitation is well established. Precipitation occurs when $IP > K_{sp}$. In CBD, this process is modified such that precipitation is controlled to eliminate or reduce spontaneous precipitation. The first method of controlling the reaction is by complexing the metal ions such that only a controlled number of free ions are available. As the complex dissociates, the following equation applies (assuming a metal ion with a charge of $2+$):



At any given temperature, the concentration of free metal ions is given by equation 3.67.

$$K_i = \frac{[M^{2+}][A]}{[M(A)^{2+}]} \quad (3.67)$$

In this equation, K_i is the stability constant of the complex ion. A complex with a small K value is most stable, and will therefore have a lower concentration of metal ions in solution than one with a higher constant. By controlling the concentration and temperature of the complexing reagent, the concentration of metal ions in solution can also be controlled. If these ions can be generated at the surface of a substrate, it results in the formation of a film. The second method of controlling the reaction is by the slow and uniform generation of the chalcogen ions in solution. This rate control can be accomplished through a number of parameters, in particular, the concentration of sulphide-forming precursor, solution temperature and pH (Hodes, 2002). CBD has been shown to be particularly successful in preparing high quality cadmium sulphide films, with the mechanisms and kinetics extensively investigated. Cadmium sulphide thus provides a good reference position for understanding the general principles of CBD. Thus, CdS would be used for explaining most of the theory on the deposition process.

3.3.1. REACTION MECHANISMS OF CHEMICAL BATH DEPOSITION

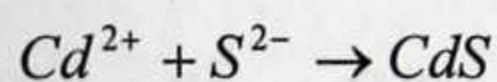
Table 3.2 shows the four possible reaction steps proposed by O'Brien and McAleese (1998), leading to the formation of high quality thin films.

Table 3.2: The four possible reaction mechanisms in CBD

$M^{2+} + S^{2-} \text{ films} \rightarrow \text{'MS' nuclei} \rightarrow \text{'MS' particulate}$	Ion by ion growth, nucleation and growth
$M^{2+} + OH^- \rightarrow \text{'M(OH)}_2 \text{ nuclei} \rightarrow \text{'M(OH)}_2 \text{ particulate}$	Ion by ion growth in solution nucleation and growth of hydroxide
$\text{M(OH)}_2 \text{ nuclei} + (\text{NH}_2)_2\text{CS} \rightarrow \text{'MS' nuclei} \rightarrow \text{MS}$	Thiourea 'metathesis' at surface of hydroxide
$\text{MS' nuclei} + (\text{NH}_2)_2\text{CS} \rightarrow M^{2+} \text{ nuclei} \rightarrow \text{MS particulate}$	Thiourea 'metathesis' at surface of sulphide

3.3.1.1. Ion-by-Ion Mechanism

The simplest mechanism, often assumed to be the operative one in general, is commonly called the ion-by-ion mechanism, since it occurs by sequential ionic reactions. The basis of this mechanism, illustrated for CdS, is given by;

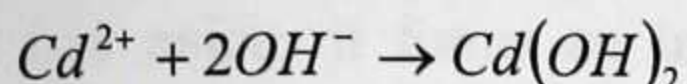


If the ion product $[\text{Cd}^{2+}][\text{S}^{2-}]$ exceeds the solubility product, K_{sp} , of CdS (10^{-28}), then, neglecting kinetic problems of nucleation, CdS will form as a solid phase. If the reaction is carried out in alkaline solution (by far the most common case), then a complex is needed to keep the metal ion in solution and to prevent the hydroxide from precipitating out. Since the decomposition of the chalcogenide precursor can be controlled over a very wide range (by temperature, pH, concentration), the rate of CdS formation can likewise be well controlled. The CdS should form a film on the substrate and (at least ideally) not precipitate in the solution.

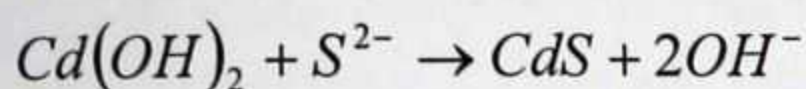
3.3.1.2. Hydroxide cluster mechanism

It was stated earlier that complexation of the Cd was necessary to prevent $\text{Cd}(\text{OH})_2$ precipitation. However, very often (more often than realized), $\text{Cd}(\text{OH})_2$ (or metal hydroxides in general) are important reaction intermediates in the CBD process (Hodes, 2002). If the complex concentration is not high enough to prevent completely the formation of $\text{Cd}(\text{OH})_2$, then a relatively small amount of $\text{Cd}(\text{OH})_2$ may be formed, not as a visible precipitate, but as a colloid. Since $\text{Cd}(\text{OH})_2$ is colourless and colloids typically do not scatter light, unless they aggregate to a large extent (in which case a suspension is the result), this means that the

Cd(OH)₂ colloid may not be visible to the eye. The CdS is then formed by reaction of slowly generated S²⁻ ion with the Cd(OH)₂:



Followed by



The reaction above occurs because K_{sp} for CdS (10⁻²⁸) is much smaller than that for Cd(OH)₂ (2 x 10⁻¹⁴). The role of metal hydroxide groups has been shown to play a key role in the deposition process (Chopra *et al.*, 1982; Rieke and Bentjen, 1993; Kainthla *et al.*, 1980; Froment and Lincot, 1995; Yu and Yoshimura, 2002). High quality films have been reported when there has been visible hydroxide observed in the chemical bath (Chopra *et al.*, 1982; Kaur *et al.*, 1980). It should be borne in mind that the mechanism may change in the course of the deposition. As the metal is depleted from solution, the complex:metal ratio will increase and may pass the point where no solid hydroxide phase is present in the solution. In this case, the ion-by-ion process will occur (initially in parallel with the hydroxide mechanism, later may be exclusively) if the conditions are suitable (Hodes, 2002).

3.3.1.3. Complex-Decomposition Mechanism

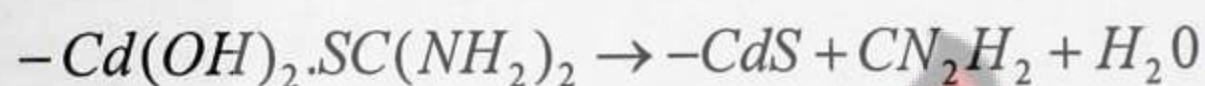
CBD processes can also proceed through a pathway involving decomposition of a metal/chalcogen-containing complex without the formation of a free sulphide ion. The complex-decomposition mechanism can, as with the free-anion mechanisms, be divided into ion-by-ion and cluster pathways.

3.3.1.3.1. Cluster Mechanism

The basis of this mechanism is that a solid phase is formed but, instead of reacting directly with a free anion, it forms an intermediate complex with the "anion forming" reagent. Continuing with CdS deposited from a thiourea bath as our example, this would be given as;



where $-Cd(OH)_2$ is one molecule in the solid-phase cluster. This complex, or a similar one containing also ammine ligands, then decomposes to CdS:



i.e., the S - C bond of the thiourea breaks, leaving the S bound to Cd.

3.3.1.3.2. Ion-by-Ion Mechanism

Consider the complexation of free Cd^{2+} by thiourea to give a Cadmium-thiourea complex ion:



This ion could, in principle, hydrolyze by breaking the S - C bond to form CdS:

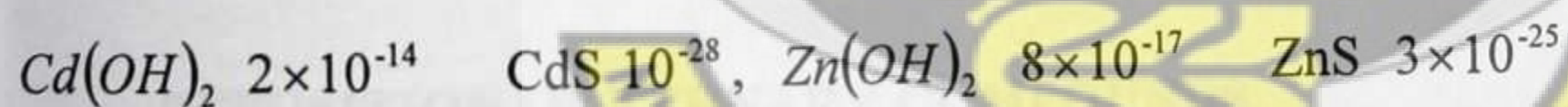


This would lead to CdS formation in solution. If the Cd^{2+} is adsorbed on the substrate (either directly or indirectly through a hydroxide linkage) or on previously deposited CdS, then the same reaction would occur. If the CdS so formed remained bound to the substrate (it is assumed that CdS generated on previously deposited CdS would remain bound), the result

would be film growth by an ion-by-ion, complex-decomposition mechanism. As with the cluster mechanism, it is difficult to distinguish experimentally between the complex-decomposition mechanism and the free-anion pathway (Hodes, 2002). Some studies have involved deposition (or precipitation) from acidic solutions. It is reasonable to assume that no hydroxide is present under these conditions for most metal ions commonly used in CBD and that deposition occurs via an ion-by-ion mechanism (Hodes, 2002).

3.3.2 DEPOSITION OF ZINC SULPHIDE

Since the chemistries of Zn and Cd are similar in many ways, it might be expected that deposition of their chalcogenides is also similar. However, there is a dominant difference in their properties that results in the fact that ZnS is considerably more difficult to deposit by CBD than CdS. This difference is manifested by the difference in solubility products between the respective hydroxides and chalcogenides. Considering, for example, the sulphides, the relevant values of K_{sp} are:



The deposition mechanisms proceeding through hydroxide clusters is dependent on a large difference between the solubility products of the hydroxide and sulphide, since the sulphide exchanges the hydroxide. The situation for ZnS is therefore much less favourable than that for CdS. The interesting consequence is that layers prominently containing CdS are more easily formed, while the deposition in the ZnS system tends to involve more significant quantities of hydroxide and finally zinc oxide. Many of the films reported as ZnS which have not been rigorously characterized are probably at best heavily contaminated with zinc oxide or hydroxide (O'Brien and McAleese, 1998). A report by Nasr et al (2005), on the effect of

pH on the properties of ZnS thin films grown by chemical bath deposition, suggests that an increase of pH leads to more OH^- ions in the solution, which tend to combine readily with Zinc without leaving enough zinc for ZnS growth on the substrate. For this reason, hydroxide formation needs to be minimized in order to form quality CBD zinc sulphide thin films (Edelson, 2007). The obvious solution to this problem is to deposit ZnS at a lower pH where the OH^- concentration will be lower. Lincot and co-workers developed the deposition of ZnS from acidic solutions in which urea hydrolysis was used to control the pH and produced among the best ZnS films reported to date (Boyle *et al.*, 2000).

KNUST

The successful deposition of ZnS from acidic chemical baths was one of the factors that informed the choice of using an acidic medium for the deposition of CdZnS for this project, instead of an alkaline medium associated with the conventional CBD process.

3.3.3 GENERAL CONSIDERATIONS FOR PRECIPITATION AND CHEMICAL DEPOSITION OF TERNARY COMPOUNDS

Mixed compositions are of interest mainly because they allow tuning of the semiconductor properties (most commonly band gap and, therefore, spectral sensitivity). This is useful for various device applications. Photoconductive detectors, where a certain spectral sensitivity range is desired, is probably the main application that drove many studies on CBD of ternary semiconductors (Hodes, 2002). Mixed metal chalcogenides have been deposited by CBD. According to simple fundamental considerations, the deposition should proceed according to the solubility products (K_{sp}) of the two separate metal chalcogenides; the one with a smaller K_{sp} should precipitate first, and only after, when the concentration of free (first) metal ion

was low enough, would the other chalcogenide precipitate, assuming a sufficient supply of chalcogenide ions. If the difference in K_{sp} was large, then the solution would be almost entirely depleted of the low- K_{sp} chalcogenide before precipitation of the second would start. Note that this discussion relates to CBD where deposition is slow; for rapid precipitation, kinetic factors might be more important, and differences in concentrations of the two cations are likely to play a more dominant role. This picture is in many (probably most) cases oversimplified. There are other factors that may become important in such mixed products (Hodes, 2002).

KNUST

3.3.3.1 Cadmium Zinc Sulphide

By far the greatest interest and effort in the CBD of ternary semiconductors has been focused on cadmium zinc sulphide. In spite of the overall chemical similarity of Cd and Zn, however, it has not proven simple to deposit true solid solutions of the sulphides. There are a number of reasons for this, some of which have been treated in detail in section 3.3.2, in the discussion on ZnS deposition. We sum them up here. While CdS is less soluble than ZnS, $\text{Cd}(\text{OH})_2$ is more soluble than $\text{Zn}(\text{OH})_2$. For this reason, ZnS is more difficult to deposit than CdS, since $\text{Zn}(\text{OH})_2$ tends to form instead of, or together with, ZnS. Although the solubility product of ZnS is lower than that of $\text{Zn}(\text{OH})_2$, the concentration of hydroxide in any typical aqueous solution will be much higher than that of sulphide. In an alkaline solution (the most common medium for CBD), CdS deposition will be preferred over ZnS. The concentration of free Cd^{2+} should be much lower than that of Zn^{2+} in order for ZnS to deposit according to simple solubility product considerations.

3.3.4. BASICS OF FILM FORMATION AND STRUCTURE

Film growth, by whatever technique is used, can typically be described in terms of three main events: (1) nucleation, (2) crystal growth, and (3) grain growth. *Nucleation* is the process of the vapor-phase atoms or molecules coming together to form a condense unit. Soon after exposure of the substrate to the incident vapor, a uniform distribution of small but highly mobile clusters or islands is observed. The next stage involves merging of the islands by a coalescence phenomenon that is liquid like in character especially at high substrate temperatures. Crystallographic facets and orientations are frequently preserved on islands and at interfaces between initially disoriented, coalesced particles. Coalescence continues until a connected network with unfilled channels in between develops. With further deposition, the channels fill in and shrink, leaving isolated voids behind. Finally, even the voids fill in completely, and the film is said to be continuous. This collective set of events occurs during the early stages of deposition, typically accounting for the first few hundred angstroms of film thickness. The many observations of films formation have pointed to three basic growth modes: (1) island (or Volmer-Weber), (2) layer (or Frank-van der Merwe) and (3) Stranski-Krastanov, which are illustrated schematically in Figure 3.20.

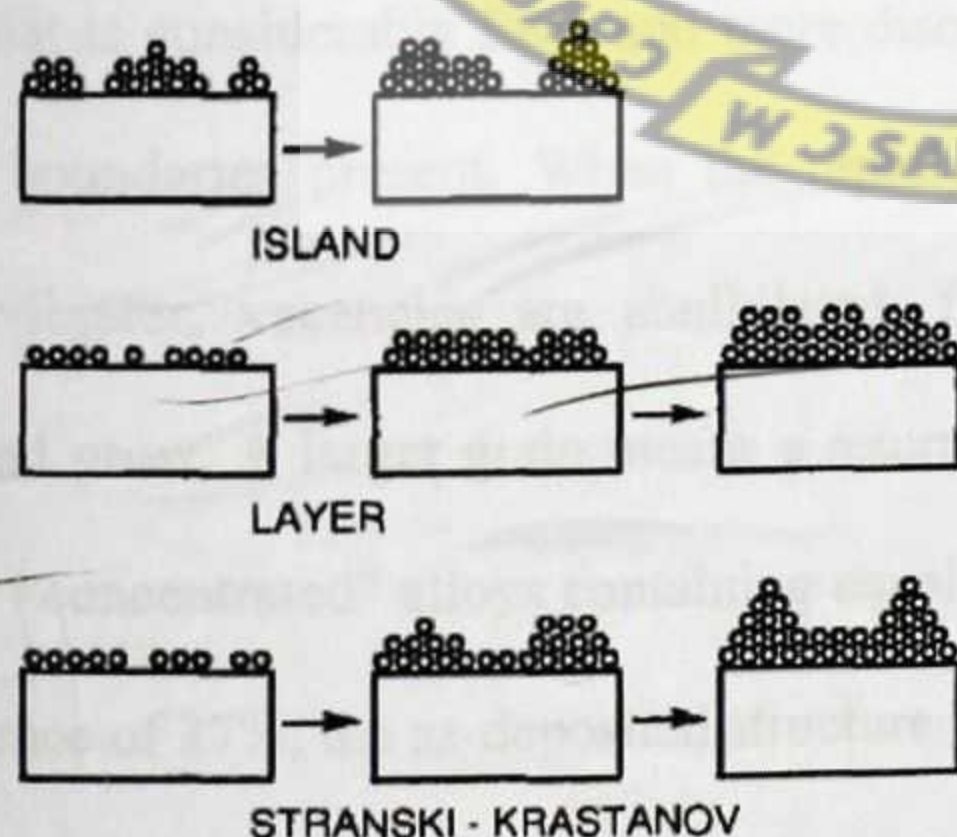


Figure 3.20: Basic modes of thin film growth

Island growth occurs when the smallest stable clusters nucleate on the substrate and grow in three dimensions to form islands. This happens when atoms or molecules in the deposit are more strongly bound to each other than to the substrate. The opposite characteristics are displayed during layer growth. Here the extension of the smallest stable nucleus occurs overwhelmingly in two dimensions resulting in the formation of planar sheets. The assumption is that the adsorbed atoms have a stronger attraction for the substrate than they do for one another, which is why each layer is completed before the next layer is started (Ohring, 1992; Lalena *et al.*, 2008).

KNUST

The layer plus island or Stranski-Krastanov growth mechanism is an intermediate combination of the aforementioned modes. In this case, after forming one or more monolayers, subsequent layer growth becomes unfavorable and islands form. The transition from two- to three-dimensional growth is not completely understood, but any factor that disturbs the monotonic decrease in binding energy characteristic of layer growth (e.g., lattice mismatch and strain energy) may be the cause. When a film is deposited "slowly," there are grains, vacancies and stacking faults present. Films deposited at "high" rate have grain structure that is considerably finer and more disordered with numerous point defects, voids and grain boundaries present. When the rapidly deposited films are annealed through a magnetic vibrator, vacancies are annihilated, faults are eliminated and grains reorient, coalesce and grow. A larger grain means a return to the spotted diffraction pattern (Ohring, 1992). For "concentrated" alloys containing equal numbers of large and small spheres with a size difference of 27%, the as-deposited structure is amorphous.

All of the foregoing results were for films deposited on the smooth substrate. The “crystalline substrate” affords the opportunity to model epitaxy phenomena. Pure films deposit in almost perfect alignment with the substrate when deposited slowly. Imperfect regions are readily eliminated upon annealing and nearly perfect singly crystals are obtained. Rapidly deposited films are less influenced by the underlying substrate and remain polycrystalline after annealing. Clearly epitaxial growth is favoured by low deposition rates. The presence of alloying elements impeded epitaxy from occurring in accord with experience (Ohring, 1992).

KNUST

The main interaction that determines whether and to what extent particles will adhere to each other and also (if there is no specific chemical interaction) to a substrate is, in most cases, the Van der Waals interaction (Hodes, 2002). The Van der Waals force of attraction is a universal interaction that operates between all particles, whether atoms, molecules, clusters, charged, or non charged. In the initial stages of growth, there may be specific chemical interactions between the deposit and substrate. For example, if gold is used as a substrate, S, Se, and many of their compounds interact chemically with the gold to form S(Se)-Au bonds. This would promote good adhesion of the deposit to the gold. There could also be chemical and electrostatic interactions between surfaces of the individual crystals. However, the Van der Waals interaction between the crystals in the strongly ionic solution is enough in most cases to ensure adhesion of the crystals to one another. The fact that reasonably adherent films can be grown on apparently unreactive substrates, such as plastics, and even on such an inert and hydrophobic material as Teflon suggests that while such specific interactions between the semiconductor and substrate may improve adhesion to the substrate, they are not essential for film formation (Hodes, 2002).

CHAPTER FOUR

4. CHARACTERIZATION OF SEMICONDUCTOR MATERIALS

Characterization, when used in materials science, refers to the use of external techniques to probe into the internal structure and properties of a material (Wikipedia.org /wiki/ Characterization). The purpose of characterization is to investigate the relationship between the structure of materials at atomic or molecular scales and their macroscopic properties. Characterization describes those features of composition and structure (including defects) of a material that are significant for a particular preparation, study of properties, or use, and suffice for reproduction of the material (wikipedia.org/wiki/materials_science). Many techniques have been used to characterize CBD films. Three common techniques used are scanning electron microscopy together with electron diffraction, powder X-ray diffraction, and optical absorption (or transmission) spectroscopy.

4.1. OPTICAL ABSORPTION SPECTROSCOPY

Experimental investigations on the optical behaviour of thin films deal primarily with optical reflection, transmission and absorption properties, and their relation to the optical constants. Optical properties are directly related to structural and electronic properties of solids, and hence very important in device applications. A detailed knowledge of optical properties can provide a huge amount of information about their structure, optoelectronic behaviour, transport of charged carriers, etc. (Singh and Shimakawa, 2003). These are important parameters for scientists and technocrats to decide its end use.

The most direct and perhaps the simplest method for probing the band structure of semiconductors is to measure the absorption spectrum (Pankove, 1975). In the absorption

process, a photon of known energy excites an electron from a lower to a higher energy state. In a semiconductor there exist allowed energy bands. Thus, there will be a range of photon energies that can be absorbed. By inserting a slab of semiconductor material at the output of a monochromator and studying the changes in the transmitted radiation, one can discover all possible transitions an electron can make and learn much about the distribution of states (Pankove, 1975). Optical absorption spectroscopy is often carried out on CBD films to verify that the films have a band gap expected from the deposited semiconductor. Additionally, since CBD films are often nanocrystalline and the most apparent effect of very small crystal size is the increasing bandgap due to size quantization (the effect is visible to the eye if the bandgap is in the visible region of the spectrum), absorption (or transmission) optical spectroscopy is clearly a fast and simple pointer to crystal size, since bandgap-size correlations have been made for a number of semiconductor colloids and films (Hodes, 2002).

4.1.1. Optical Properties of Semiconductors

The unifying concept that embraces all optical properties is the interaction of electromagnetic radiation with the electrons of the material. On this basis, optical properties are interpretable from what we know of the electronic structure and how it is affected by atomic structure, bonding, impurities, and defects (Ohring, 1992).

Optical properties of semiconductors typically consist of their refractive index n and extinction coefficient k or absorption coefficient α (or equivalently the real and imaginary parts of the relative permittivity) and their dispersion relations, that is, their dependence on

the wavelength, λ , of the electromagnetic radiation or photon energy $h\nu$, and the changes in the dispersion relations with temperature, pressure, alloying, impurities, etc. A typical relationship between the absorption coefficient, α , and photon energy, $h\nu$, observed in a crystalline semiconductor is shown in Figure 4.1, where various possible absorption processes are illustrated (Singh, 2006).

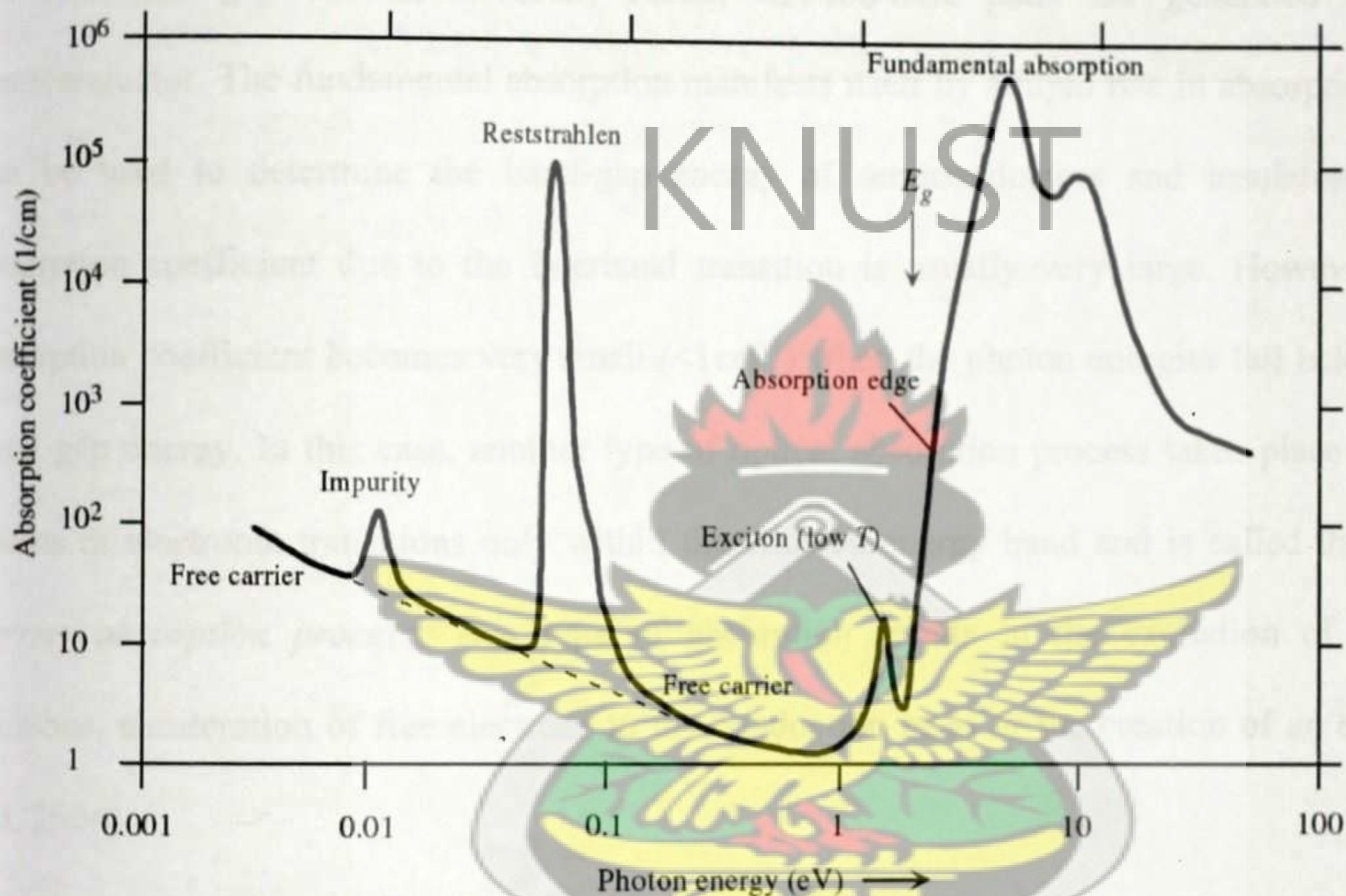


Figure 4.1: Absorption coefficient as a function of the photon energy in a typical semiconductor to illustrate various possible absorption processes.

The important features in the α vs. $h\nu$ behaviour as the photon energy increases, can be classified in the following types of absorptions: (a) *Reststrahlen* or *lattice absorption* in which the radiation is absorbed by vibrations of the crystal ions, (b) *free-carrier absorption* due to the presence of free electrons and holes, an effect that decreases with increasing photon energy, (c) *an impurity absorption* band (usually narrow) due the various dopants, (d) *exciton absorption* peaks that are usually observed at low temperatures and are close to the

fundamental absorption edge and (e) *band-to-band or fundamental absorption* of photons, which excites an electron from the valence to the conduction band (Singh, 2006).

The *fundamental absorption process*, probably the most important absorption effect, involves the absorption of photons, which have energies equal to or greater than the band gap energy. The fundamental absorption process is usually accompanied by an electronic transition across the forbidden gap and as a result, excess electron-hole pairs are generated in the semiconductor. The fundamental absorption manifests itself by a rapid rise in absorption and can be used to determine the band-gap energy of semiconductors and insulators. The absorption coefficient due to the interband transition is usually very large. However, the absorption coefficient becomes very small ($<1\text{cm}^{-1}$) when the photon energies fall below the band gap energy. In this case, another type of optical absorption process takes place which results in electronic transitions only within the allowed energy band and is called the *free-carrier absorption process*. This type of absorption results in the excitation of lattice phonons, acceleration of free electrons in the conduction band or the creation of an exciton (Li, 2006).

4.1.2. Fundamental Absorption in Direct and Indirect Band Gap Semiconductors

The fundamental absorption which manifests itself by a rapid rise in absorption can be used to determine the energy gap of the semiconductor. However, because the transitions are subject to certain selection rules (i.e. there are some restrictions based on the E-k diagrams), the estimation of the energy gap from the “absorption edge” is not a straightforward process – even if competing absorption processes can be accounted for (Pankove, 1975). Absorption at the band edge depends on whether the material is a direct or indirect semiconductor. If a

photon is to be absorbed, by conservation of energy, the energy of the system must be the same before and after the absorption event. Before the collision, of the electron and the photon, their combined energy is

$$E_{\text{electron+photon}} = E_o + h\nu$$

where E_o is the initial electron energy. When the photon collides with an electron, it is possible that the electron will absorb the energy of the photon. When the photon energy is transferred to the electron, the photon annihilates. Therefore, after the event, the electron, by conservation of energy, now has energy, E_1

$$E_1 = E_o + h\nu, \text{ where } E_1 > E_c$$

E_c is the energy at the bottom of the conduction band.

If a photon of energy less than the band gap is incident on the semiconductor, that photon cannot be absorbed. For such a photon to be absorbed, the electron would have to end up at an energy state inside the forbidden gap. Except through the help of traps or impurities that might provide the occasional state within the forbidden gap, this is not possible. Therefore, light of photon energy less than the band gap is not absorbed and the semiconductor appears transparent to that radiation (Anderson and Anderson, 2005). Aside from the conservation of energy, there is also the law of conservation of wave vector k (analogous to conservation of momentum in classical mechanics). Photons of interest in semiconductor electronics have wave vectors that are small and in most cases can be considered to be essentially zero. Therefore, when the electron makes an energy transition, it must do so at virtually constant k , which is to say it must make a vertical transition on the E - k diagrams this is shown in Figure 4.2.

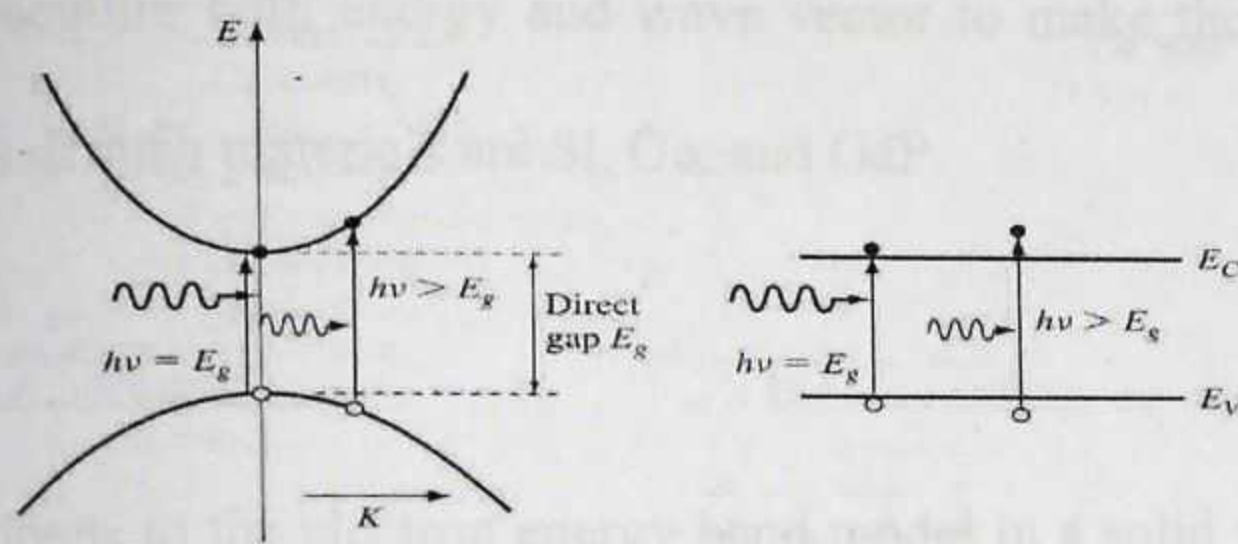


Figure 4.2: A direct gap semiconductor

The particular semiconductor whose E-k diagram is shown in Figure 4.2 is called a direct gap material. Direct means that the minimum in the conduction band is at the same value of k as the maximum in the valence band, here at $k = 0$. Thus, the transition results from the direct interaction of a photon with an electron. Direct gap materials are generally efficient emitters and absorbers of optical energy because it is easy for electrons to move between the conduction and valence band without having to acquire or give off k . GaAs and InP are good examples of direct gap materials. An indirect gap material, on the other hand, has an E-k diagram as shown in Figure 4.3. In an indirect gap material, the minimum in the conduction band is not at the same value of k as the top of the valence band.

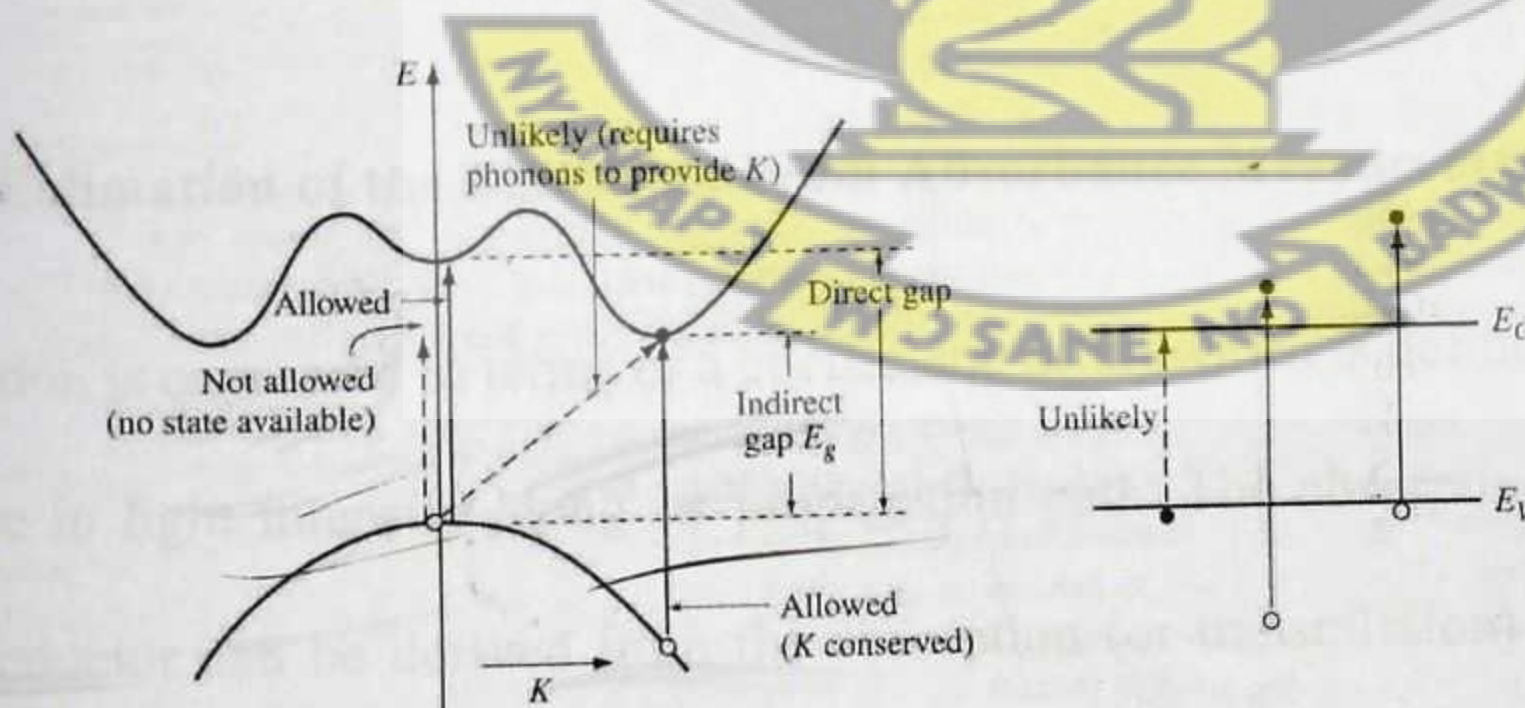


Figure 4.3: An indirect gap semiconductor

An electron cannot go from one band to another simply by absorbing a photon of energy close to the band gap, because the photon cannot supply adequate wave vector. The electron

needs to acquire both energy and wave vector to make the transition in indirect materials.

Examples of such materials are Si, Ge, and GaP.

What happens to the electron energy band model in a solid without regular crystalline order?

The Bloch theorem is not applicable when the structure is not periodic, so that the electron states cannot be described by well-defined k values. Thus, the momentum selection rule for optical transitions is relaxed; hence all infrared and Raman modes contribute to the absorption spectra (Anderson and Anderson, 2005). The optical absorption edge is rather featureless. And since momentum conservation rules for direct and indirect optical transitions no longer apply, in the case of amorphous silicon, for example, this results in very high absorption coefficient, allowing the use of only micrometer scale thin films for absorption of solar energy. As previously noted, allowed bands and energy gaps still occur because the form of the density of states (DOS) versus energy is determined most strongly by local electron bonding configurations.

4.1.3. Estimation of the Band Gap From Absorbance Measurements

Absorption is expressed in terms of a coefficient, $\alpha(h\nu)$ which is defined as the relative rate of decrease in light intensity along its propagation path. The absorption coefficient, α , of the semiconductor can be derived from the absorption (or transmission) spectrum according to the Beer – Lambert equation applied to solids: $I = I_0 e^{-\alpha t}$, where I is the intensity of the transmitted light and I_0 that of the incident light. t is the film thickness

Mott, Davis and Tauc (1979), have proposed a mathematical equation to represent the relationship between optical energy gap and the energy of the incident photon, which is given as:

$$\alpha h\nu = B[h\nu - E_g]^n$$

where α , is the optical absorption coefficient, B is a constant that depends on the films material, $h\nu$ is the energy of the incident photon, E_g is the energy gap, and n is an index which could take different values according to the electronic transition. In a direct transition n is equal to 0.5 and 1.5 for allowed and forbidden transitions respectively. For indirect transition, n is equal to 2 for allowed transitions and 3 for forbidden transitions. The band gap energy is obtained by extrapolating the linear portion of $(\alpha h\nu)^2$ versus $h\nu$ to the energy axis at $(\alpha h\nu)^2 = 0$. The intercepts of these plots on the energy axis gives the energy band gaps

Alternatively, Band gap energy and transition type can be derived from mathematical treatment of data obtained from optical absorbance versus wavelength with the Stern (1963), relationship of near-edge absorption

$$A = \frac{[k(h\nu - E_g)]^{n/2}}{h\nu}$$

where ν is the frequency, h is the Planck's constant, k equals a constant while n carries the value of either 1 or 4. The value of n is 1 and 4 for the direct transition and indirect transition, respectively. The band gap energy is obtained by extrapolating the linear portion of $(Ah\nu)^2$ versus $h\nu$ to the energy axis at $(Ah\nu)^2 = 0$.

4.2. BASICS OF X-RAY DIFFRACTION

Max von Laue, in 1912, discovered that crystalline substances act as three-dimensional diffraction gratings for X-rays of wavelengths similar to the spacing of planes in a crystal lattice. Shortly after this, W.L. Bragg showed that wavelength of the X-ray undergoing diffraction by a crystal is related to the interplanar distances by the famous Bragg's equation.

4.2.1. Bragg's Law of Diffraction

Figure 4.4 shows a set of crystal planes consisting of an array of atoms. The X-ray beam incident on a plane at angle θ will be reflected from the plane such that the angle of reflection is also θ and part of the intensity will pass through the crystal undeviated from its path. Reflection is caused by the interaction of the electromagnetic radiation with the electrons of the atoms in the lattice. In order that the intensity of the reflection is sufficiently strong, reflected waves from the successive planes separated by the distance, d_{hkl} , should be in phase.

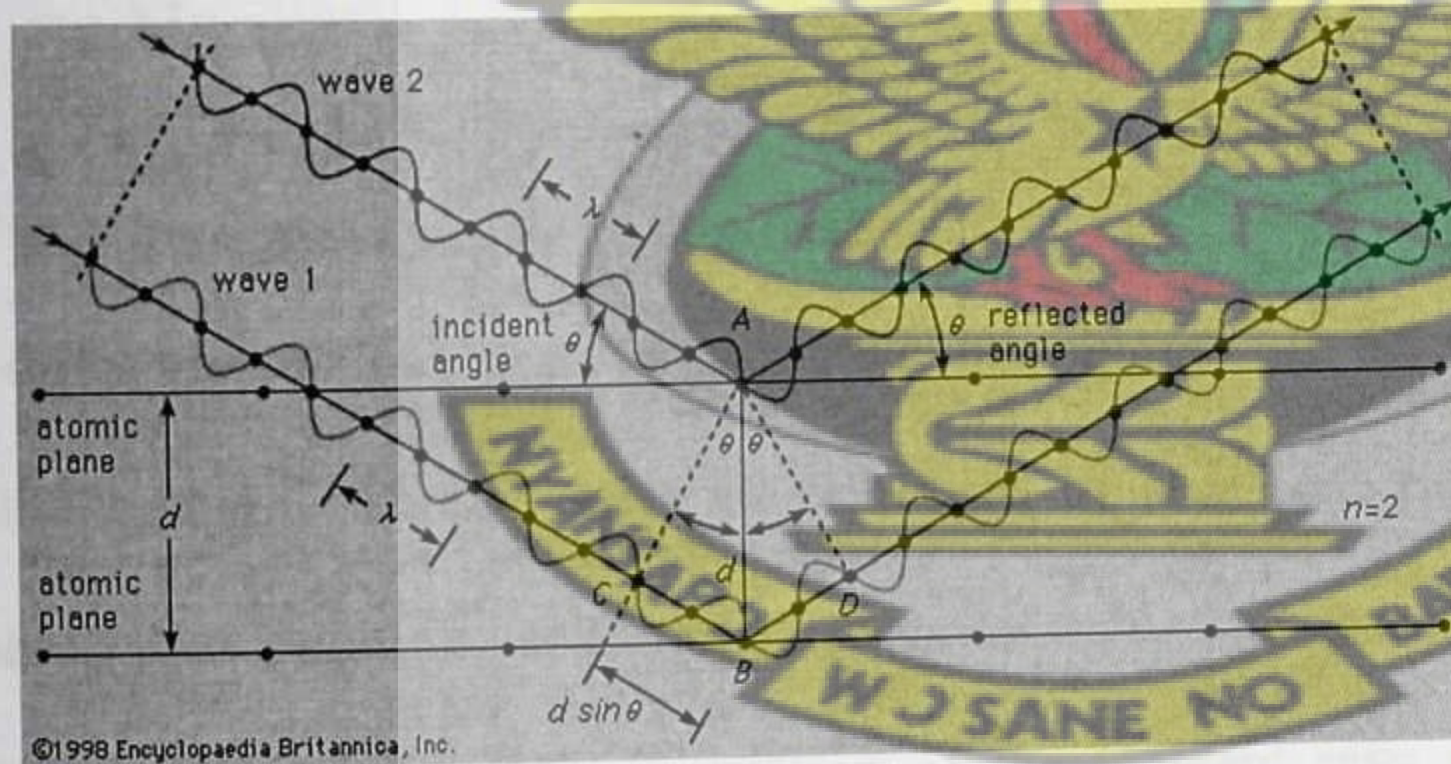


Figure 4.4: Diffraction of X-ray from a set of planes

From Figure 4.4, it can be seen that the path difference of the waves from successive planes is $2d \sin\theta$. In order that the waves travelling from successive planes are in phase the condition

$$n\lambda = 2d_{hkl} \sin\theta$$

should be satisfied. This is Bragg's condition of reflection and is known as Bragg's law.

where the integer n is the order of the diffracted beam, λ is the wavelength of the incident X-ray beam, d_{hkl} is the distance between adjacent planes of atoms (the d -spacings), and θ is the angle of incidence of the X-ray beam. Since λ is known and θ can be measured, the d -spacing can be calculated.

X-ray diffraction is now a common technique for the study of crystal structures and atomic spacing.

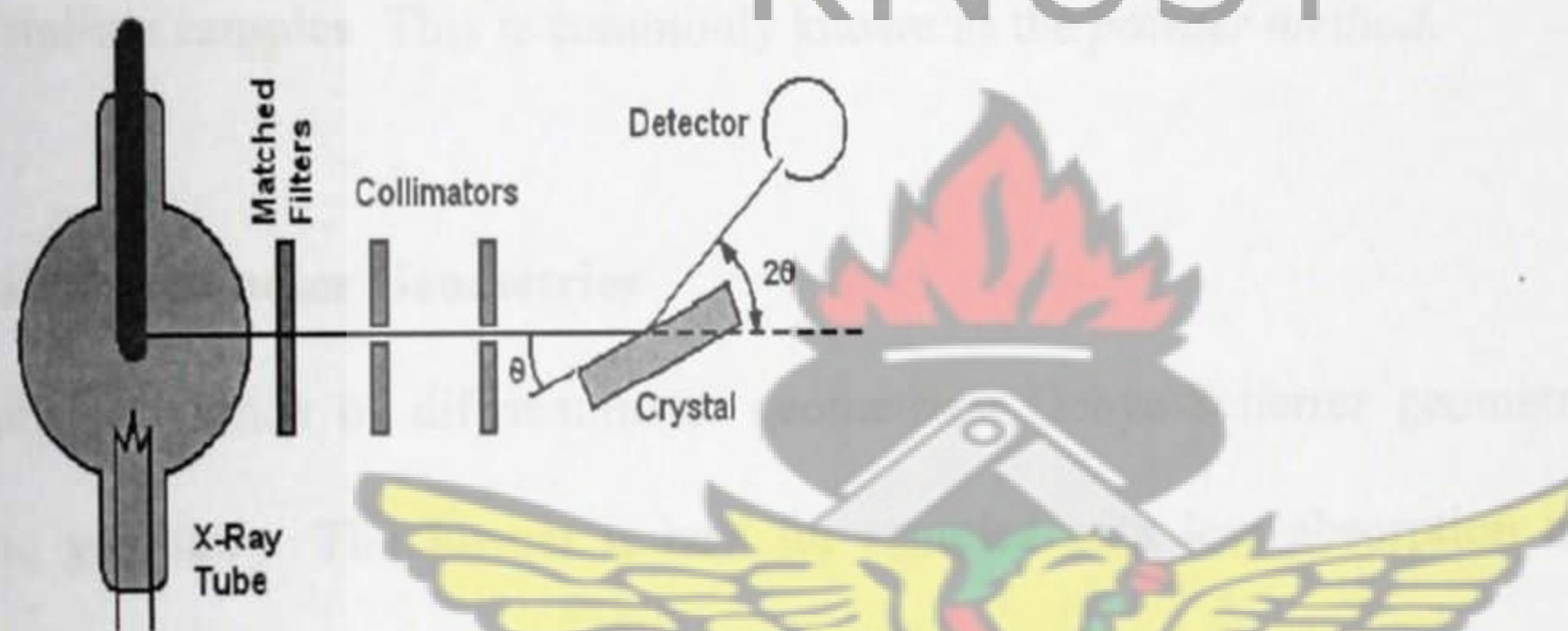


Figure 4.5: Schematic for X-ray diffraction

X-ray diffraction is based on constructive interference of monochromatic X-rays and a crystalline material. These X-rays are generated by a cathode ray tube, filtered to produce monochromatic radiation, collimated to concentrate, and directed toward the sample as illustrated in Figure 4.5. The interaction of the incident rays with the sample produces constructive interference (and a diffracted ray) when conditions satisfy Bragg's Law. A detector records and processes this X-ray signal and converts the signal to a count rate which is then output to a device such as a printer or computer monitor.

4.2.2. Powder Diffraction

The most common method for determining the structure of a crystalline solid is X-ray diffraction. There are many experimental variations. Complete determination of the crystal structure by locating the coordinates of all the atoms requires a good single crystal of, at least, about 1 mm size. But most substances crystallize as polycrystalline solids which means that each particle is made of a number of randomly oriented tiny crystals. Growing a single crystal needs some special techniques and is not always easy. However, it is possible to get important structural information by recording the X-ray diffraction pattern of the powdered polycrystalline samples. This is commonly known as the *powder method*.

4.2.3. Diffractometer Geometries

There are two kinds of diffractometer geometries: Debye-Scherrer geometry, and Bragg-Brentano geometry. The former is best for samples with low absorption and is used for measurement of air sensitive samples/suspensions. Whilst the later is best for strongly absorbing samples and easily adapted for in situ investigations. The Bragg-Brentano geometry is used for investigating the crystal structure of thin films.

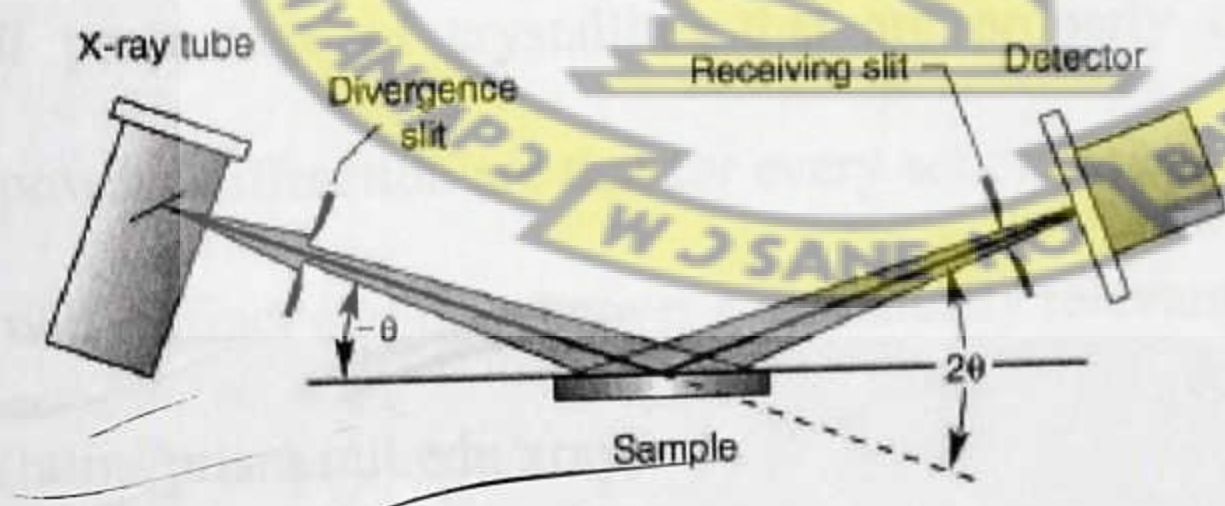


Figure 4.6: Bragg-Brentano diffraction geometry

The Brucker D8 powder diffractometer uses the Bragg-Brentano geometry illustrated in Figure 4.6. The incident angle, θ , is defined between the X-ray source and the sample. The diffracted angle, 2θ , is defined between the incident beam and the detector angle. The

incident angle, θ , is always $\frac{1}{2}$ of the detector angle 2θ . In this diffractometer, the X-ray wavelength, λ is fixed, consequently, a family of planes produces a diffraction peak only at a specific angle, θ . Additionally, the plane normal must be parallel to the diffraction vector as illustrated in Figure 4.7.

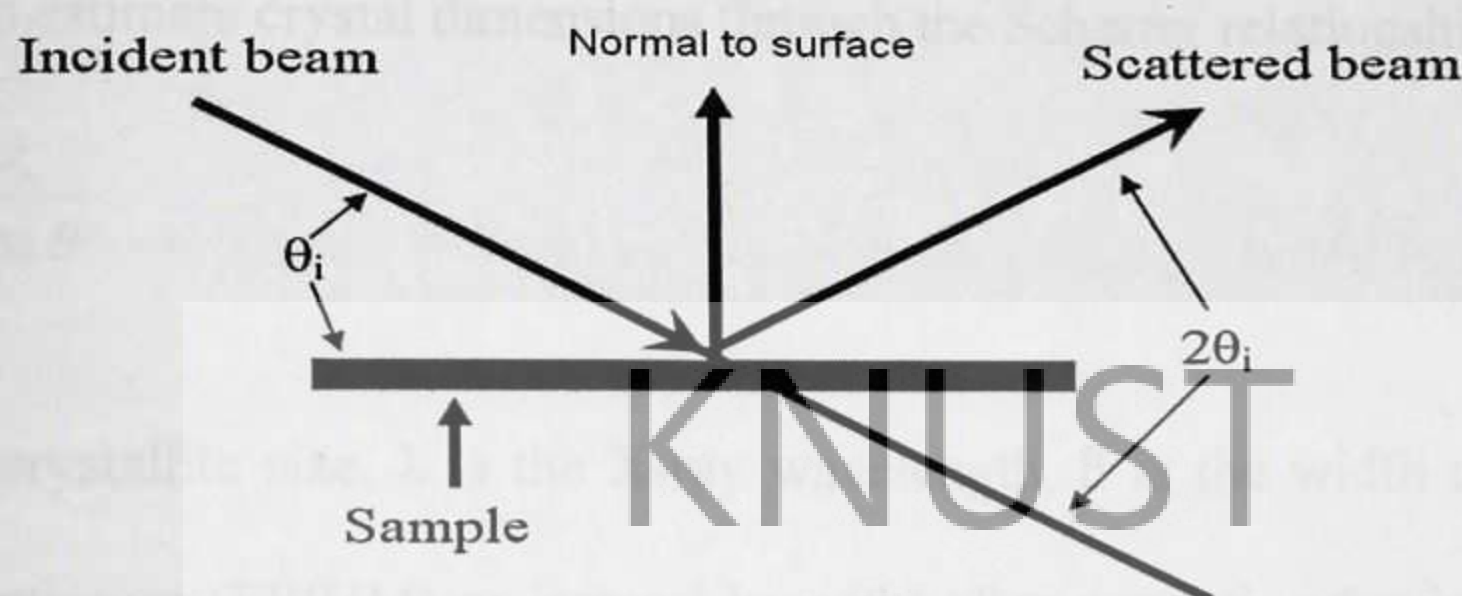


Figure 4.7: Illustration of Plane normal: the direction perpendicular to a plane of atoms. Diffraction vector: the vector that bisects the angle between the incident and diffracted beam

Only planes of atoms that share this normal will be seen in the $\theta - 2\theta$ scan. A single crystal specimen in a Bragg-Brentano diffractometer would produce only one family of peaks in the diffraction pattern. A polycrystalline sample should contain thousands of crystallites. Therefore, all possible diffraction peaks should be observed. For every set of planes, there will be a small percentage of crystallites that are properly oriented to diffract. Basic assumptions of powder diffraction are that for every set of planes there is an equal number of crystallites that will diffract and that there is a statistically relevant number of crystallites, not just one or two (<http://prism.mit.edu/xray>).

The characteristic set of d -spacing and their intensity generated in a typical X-ray scan provides a unique "fingerprint" of the phases present in the sample. When properly

interpreted, by comparison with standard reference patterns and measurements, this "fingerprint" allows for identification of the material.

CBD films are often nanocrystalline. One very important use of XRD when dealing with nanocrystals is to estimate crystal dimensions through the Scherrer relationship:

$$D = \frac{K\lambda}{\beta \cos \theta}$$

where D is the crystallite size, λ is the X-ray wavelength, β is the width of the peak (full width at half maximum (FWHM) or integral breadth) after correcting for instrumental peak broadening (β expressed in radians), θ is the Bragg angle and K is the Scherrer constant. The Scherrer equation gives volume-weighted mean column length. The D value calculated for (hkl) peak should be understood as mean crystallite size in the direction that is perpendicular to the (hkl) plane (Hodes, 2002).

XRD methods for crystallite size determination are applicable to crystallites in the range of 2-100 nm (Hodes, 2002). The diffraction peaks are very broad for crystallites below 2-3 nm, while for particles with size above 100 nm the peak broadening is too small. If analyzed crystals are free from microstrains and defects, peak broadening depends only on the crystallite size and diffractometer characteristics. It is useful to remember that except for compounds that are commonly amorphous, CBD semiconductor films are rarely truly amorphous (Hodes, 2002).

4.3. ENERGY DISPERSION X-RAY SPECTROSCOPY (EDX)

Energy dispersive X-ray spectroscopy (EDS, EDX or EDAX) is an analytical technique used for the elemental analysis or chemical characterization of a sample. As a type of spectroscopy, it relies on the investigation of a sample through interactions between electromagnetic radiation and matter, analyzing X-rays emitted by the matter in response to being hit with charged particles. Its characterization capabilities are due in large part to the fundamental principle that each element has a unique atomic structure allowing X-rays that are characteristic of an element's atomic structure to be identified uniquely from each other.

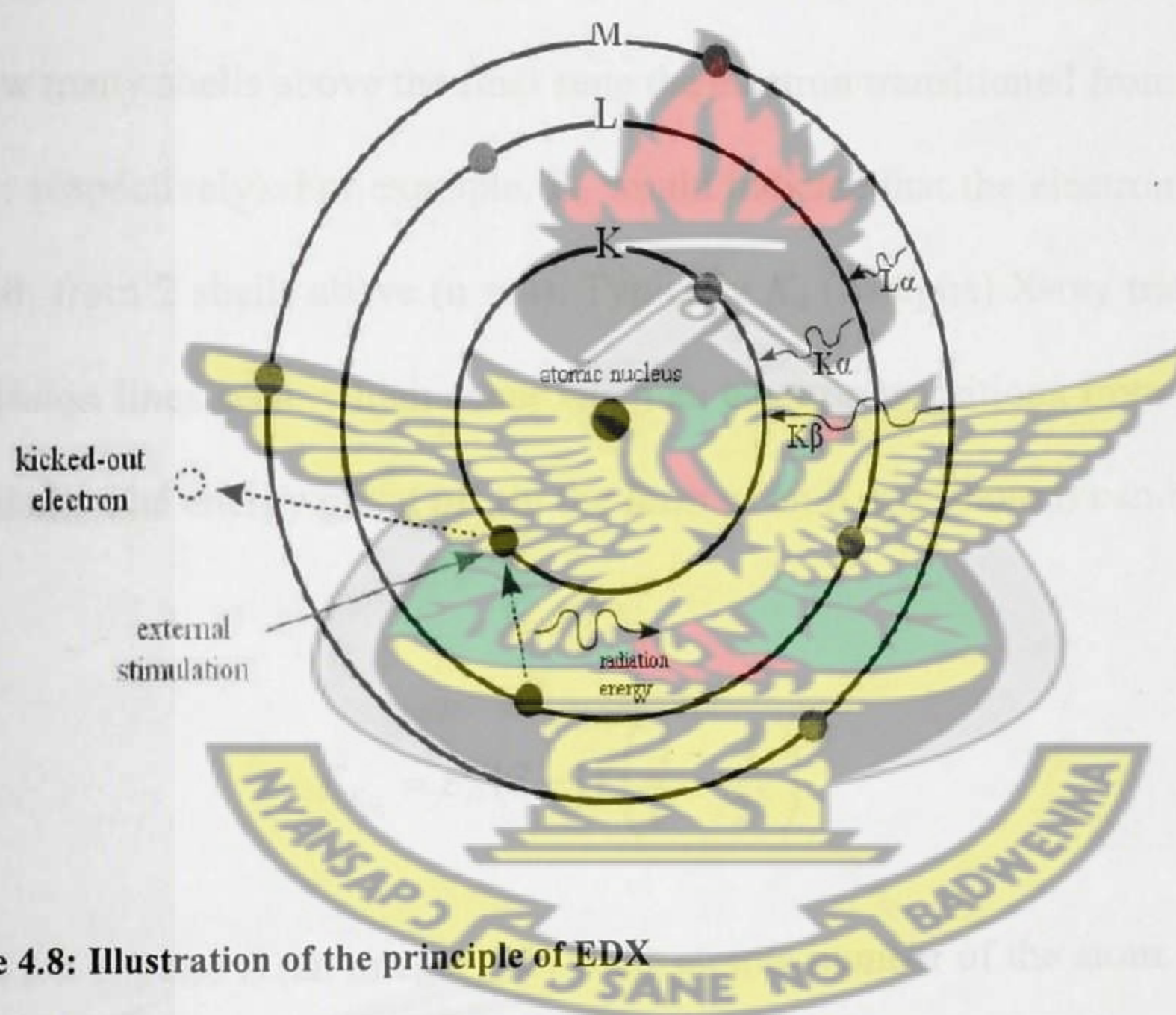
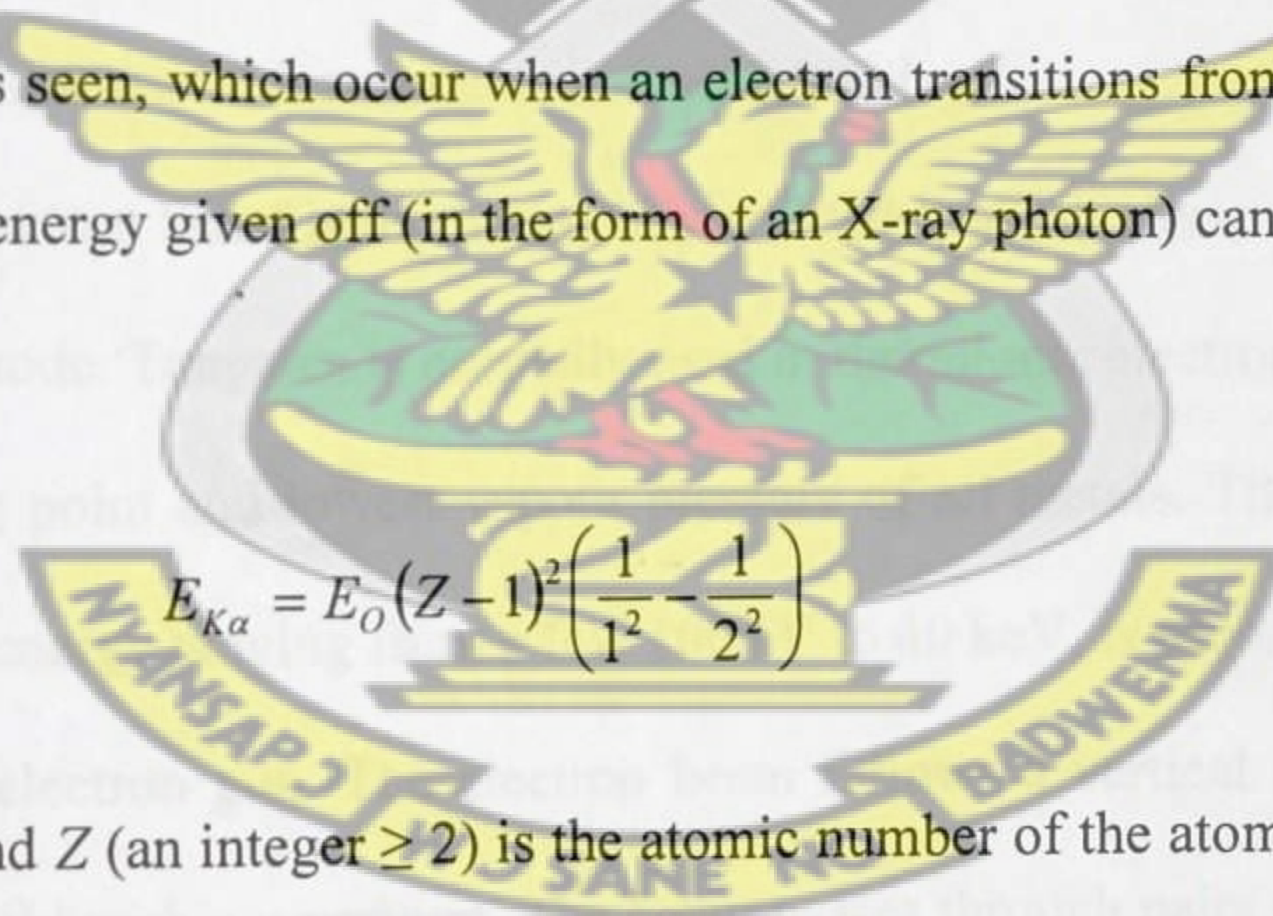


Figure 4.8: Illustration of the principle of EDX

Figure 4.8, illustrates the principle of EDX. To stimulate the emission of characteristic X-rays from a specimen, a high energy beam of charged particles such as electrons or protons, or a beam of X-rays, is focused into the sample being studied. At rest, an atom within the sample contains ground state (or unexcited) electrons in discrete energy levels or electron shells bound to the nucleus. The incident beam may excite an electron in an inner shell, ejecting it from the shell while creating an electron hole where the electron was. An electron from an

outer, higher-energy shell then fills the hole, and the difference in energy between the higher-energy shell and the lower energy shell may be released in the form of an X-ray. The number and energy of the X-rays emitted from a specimen can be measured by an energy dispersive spectrometer. This allows the elemental composition of the specimen to be measured. The energy of the X-ray photon depends on the element of which the electron was part, as well as the initial and final states of the electron making the transition. These energies are predictable. X-ray producing transitions are commonly grouped into categories based on the initial and final states of the electron. These transitions are labeled as X_J , with X denoting the final state shell of the electron (K for $n = 1$, L for $n = 2$, M for $n = 3$, and so on), and J indicating how many shells above the final state the electron transitioned from ($J = \alpha, \beta, \gamma, \dots$ for 1, 2, 3, ... respectively). For example, L_β would indicate that the electron transitioned to the $n = 2$ shell, from 2 shells above ($n = 4$). Typically K_α (K-alpha) X-ray transitions are the strongest emission lines seen, which occur when an electron transitions from the $n = 2$ shell to the $n = 1$ shell. The energy given off (in the form of an X-ray photon) can be calculated as follows;



$$E_{K\alpha} = E_0 (Z-1)^2 \left(\frac{1}{1^2} - \frac{1}{2^2} \right)$$

Where $E_0 = 13.6 \text{ eV}$, and Z (an integer ≥ 2) is the atomic number of the atom. This simplifies to,

$$E_{K\alpha} = (10.2 \text{ eV})(Z-1)^2$$

Further refinements can be made by taking into account more of the quantum numbers describing the states from which the electrons transition to / from, such as the angular momentum and spin, as well as selection rules describing which transitions are allowed.

4.4. SCANNING ELECTRON MICROSCOPY (SEM)

The scanning electron microscope is a type of electron microscope that images the sample surface by scanning it with a high-energy beam of electrons in a raster scan pattern. The SEM is a microscope that uses electrons instead of light to form an image. The electrons interact with the atoms that make up the sample producing signals that contain information about the sample's surface topography, composition and other properties such as electrical conductivity. The scanning electron microscope has many advantages over traditional microscopes. The SEM has a large depth of field, which allows more of a specimen to be in focus at one time. The SEM also has much higher resolution (~ 1 nm), so closely spaced specimens can be magnified at much higher levels. Because the SEM uses electromagnets rather than lenses, the researcher has much more control in the degree of magnification. All of these advantages, as well as the actual strikingly clear images, make the scanning electron microscope one of the most useful instruments in research today.

In a typical SEM, an electron beam is thermionically emitted from an electron gun fitted with a tungsten filament cathode. Tungsten is normally used in thermionic electron guns because it has the highest melting point and lowest vapour pressure of all metals. The electron beam, which typically has an energy ranging from a few 100 eV to 40 keV, is produced at the top of the microscope by an electron gun. The electron beam follows a vertical path through the microscope, which is held within a vacuum. The beam passes through pairs of scanning coils or pairs of deflector plates in the electron column, typically in the final lens, which deflect the beam in the x and y axes so that it scans in a raster fashion over a rectangular area of the sample surface. Once the beam hits the sample, electrons and X-rays are ejected from the sample. Detectors collect these X-rays, backscattered electrons, and secondary electrons and convert them into a signal that is sent to a screen similar to a television screen. This produces the final image as shown in Figures 4.9 and 4.10.

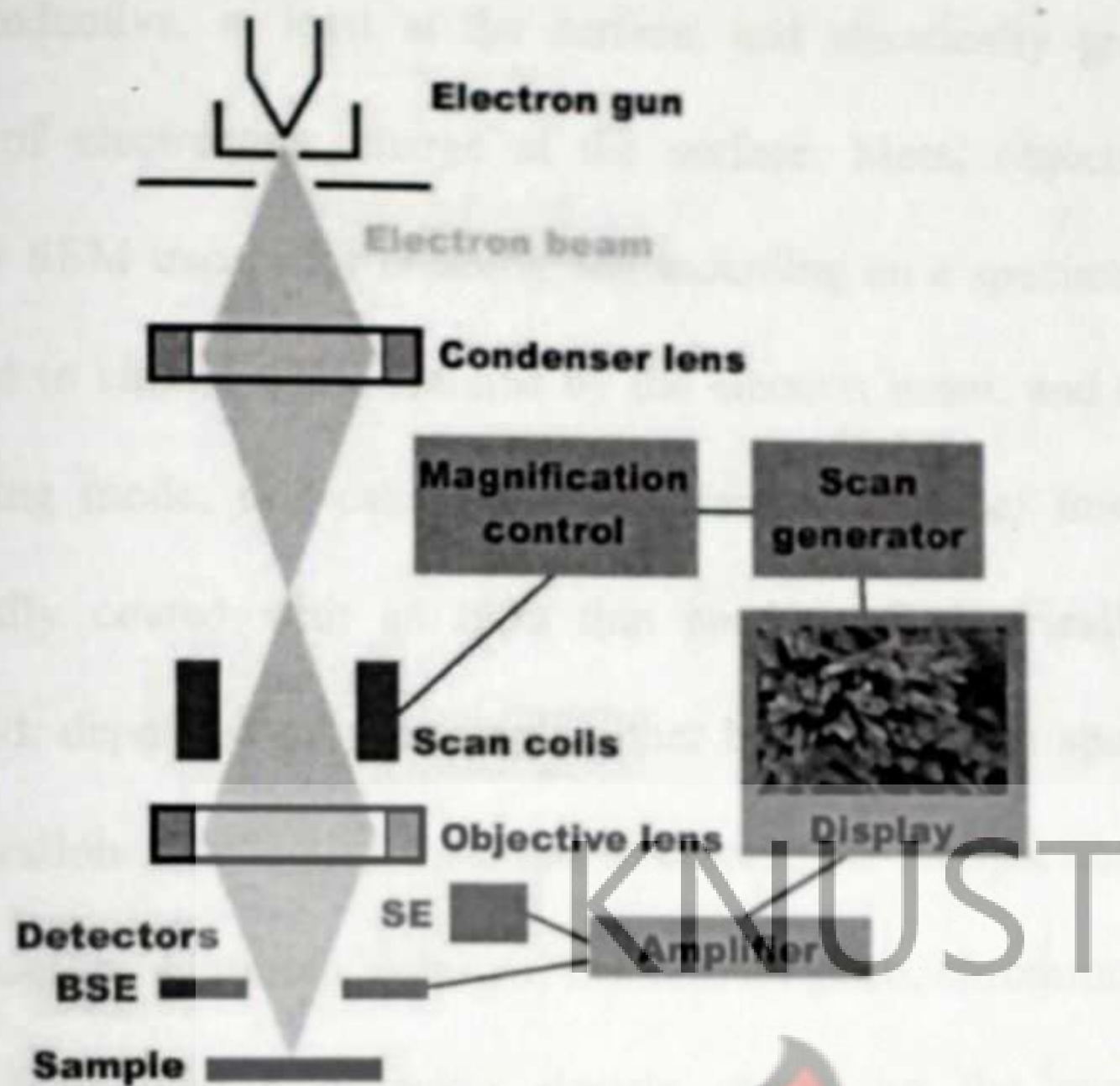


Figure 4.9: Schematic diagram of a scanning electron microscope.

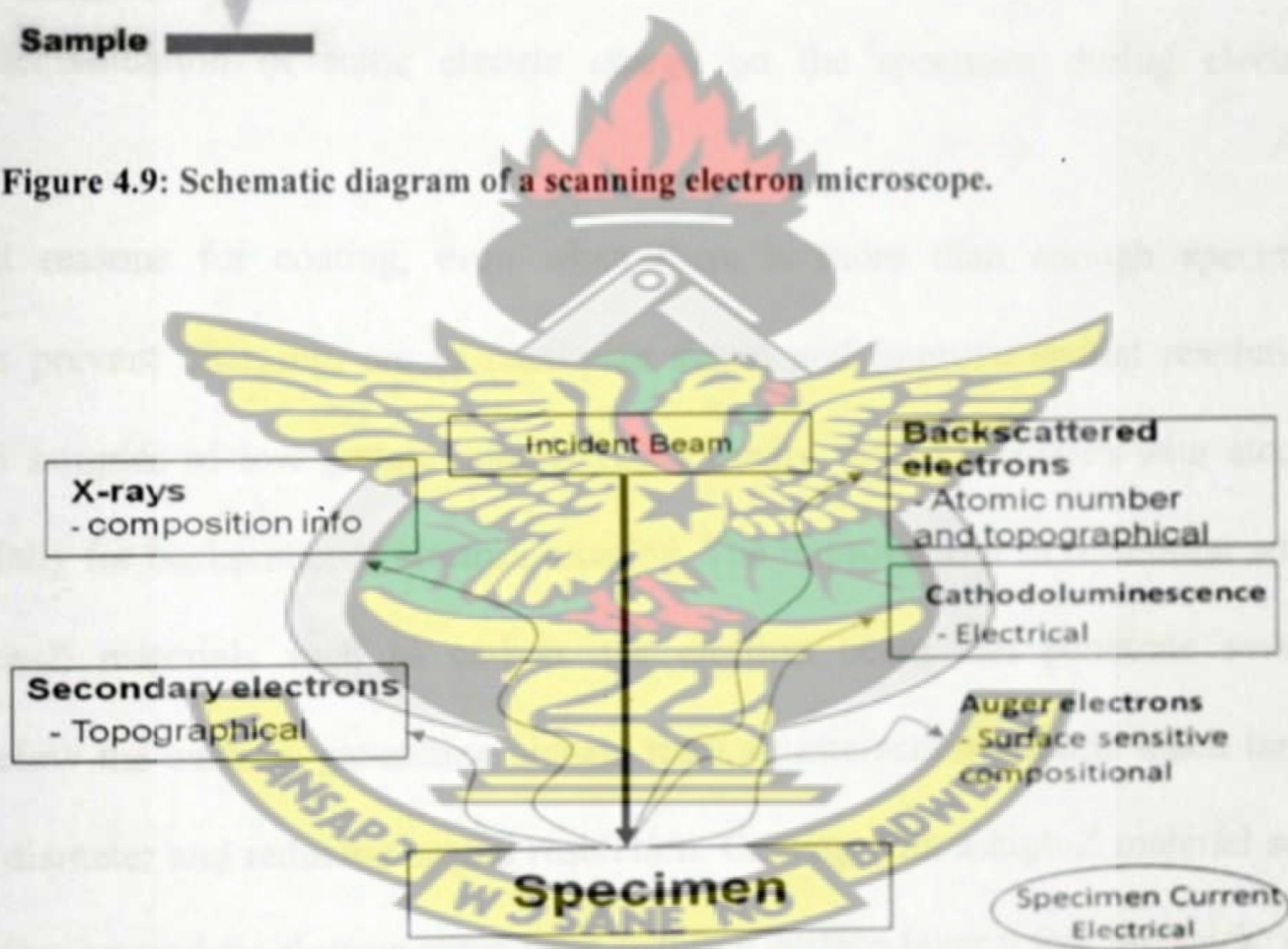


Figure 4.10: Signals produced by an electron beam incident on the specimen

All samples must also be of an appropriate size to fit in the specimen chamber and are generally mounted rigidly on a specimen holder called a specimen stub. Several models of SEM can examine any part of a 6-inch (15 cm) semiconductor wafer, and some can tilt an object of that size to 45 degrees. For conventional imaging in the SEM, specimens must be

electrically conductive, at least at the surface, and electrically grounded to prevent the accumulation of electrostatic charge at the surface. Metal objects require little special preparation for SEM except for cleaning and mounting on a specimen stub. Nonconductive specimens tend to charge when scanned by the electron beam, and especially in secondary electron imaging mode, this causes scanning faults and other image artefacts. They are therefore usually coated with an ultra thin coating of electrically-conducting material, commonly gold, deposited on the sample either by low vacuum sputter coating or by high vacuum evaporation. Conductive materials in current use for specimen coating include gold, gold/palladium alloy, platinum, osmium, iridium, tungsten, chromium and graphite. Coating prevents the accumulation of static electric charge on the specimen during electron irradiation.

Two important reasons for coating, even when there is more than enough specimen conductivity to prevent charging, are to maximize signal and improve spatial resolution, especially with samples of low atomic number (Z). Broadly, signal increases with atomic number, especially for backscattered electron imaging. The improvement in resolution arises because in low-Z materials such as carbon, the electron beam can penetrate several micrometers below the surface, generating signals from an interaction volume much larger than the beam diameter and reducing spatial resolution. Coating with a high-Z material such as gold maximizes secondary electron yield from within a surface layer a few nm thick, and suppresses secondary electrons generated at greater depths, so that the signal is predominantly derived from locations closer to the beam and closer to the specimen surface than would be the case in an uncoated, low-Z material.

CHAPTER FIVE

5. EXPERIMENTAL DETAILS

The method used to prepare or deposit a material can profoundly affect the phase composition, thermal stability, and morphology, which in turn can influence the functional behaviour of the material (Ramasamay *et al.*, 2011). One also has to keep in mind that the high sensitivity of film properties to deposition parameters can produce a multitude of undesired results; thus thin film materials must be treated with due respect and understanding (Chopra, 2004).

5.1 SUBSTRATE PREPARATION

One of the advantages of CBD is the great flexibility of substrate selection and significantly reduced manufacturing costs (Breen *et al.*, 1998), as well as the ease of application to a wide range of chalcogenide compounds (Pentia *et al.*, 2004). The main criteria for substrate selection are that the growing film will attach to the substrate and that the substrate will not dissolve in the chemical bath. Glass substrates are commonly used; microscope slides for small scale projects and glass sheets for large scale projects (Gadave and Lokhande, 1993; Varkey, 1989; Nair and Nair, 1989; Nair *et al.*, 1991; Nair *et al.*, 1998; Nair *et al.*, 2001; Grozdonov *et al.*, 1994).

The preparation of substrates is a critical aspect that can contribute to film adherence. Although thin films can be deposited by CBD on any surface, there will be certain obvious exceptions, such as substrates that are unstable in the deposition solution (this is rarely a problem in practice) or “dirty” substrates (Hodes, 2002). A clean surface is one that contains no significant amount of undesirable material (Mattox, 1978). Cleaning is defined as the removal, by physical and or chemical means, of soil that could interfere with the preparation of the desired material. Soil is matter on the surface whose chemical characteristics are

different from those being formed. The types of soils most commonly encountered are fingerprint oils, metal oxides, dirt, etc. (Beal, 1978). The nature and surface finish of the substrates are extremely important because they greatly influence the properties of films deposited on them (Chopra, 1969). It is therefore important that prior to the deposition of the semiconducting thin film the substrate, in this case, microscope glass slide is cleaned thoroughly to remove any undesirable substance from it.

In this work, the glass slides were left in a solution of Aqua Regia (3 parts HCl: 1 part HNO_3), for 24 hours to remove any grease and other contaminants. They were then washed with ethanol and rinsed with de-ionized water before use.

5.2 SYNTHESIS OF THE THIN FILMS

The starting chemicals used in the preparation of the films consisted of the following: CdCl_2 : 99 % purity, ZnCl_2 : 98 % purity, Urea: 99 % purity, and Thioacetamide: 99+ % purity, all from Sigma Aldrich (Poole, Dorset) in the United Kingdom. The samples were prepared using the method of Boyle *et al.* (2000). Aqueous solutions containing cadmium chloride (0.05 M), Zinc chloride (0.15 M), urea (5 M) and thioacetamide (1 M) were prepared. Different volumes of the solutions were mixed together in a beaker to obtain a final volume of 70 cm^3 . The pH of the solution was adjusted to 4 by drop-wise addition of 2 M HCl. A Mettler Toledo InteLab@Expert Pro pH meter with temperature compensation and glass electrodes (calibrated against standard pH 4.01, 7.00 and 9.21 buffers) was used to record the pH of the solution. The reaction mixture was stirred and maintained at a temperature of 353 K. The pretreated substrates were immersed vertically into the prepared baths.

The presence of a surface (the substrate or the walls of the reaction vessel) introduces a degree of heterogeneity that facilitates nucleation. For this reason, depositions that proceed

via the ion-by-ion process tend to occur mainly on the substrate or other surfaces, rather than involving a large amount of precipitate typical of the hydroxide mechanism. The surface can be considered a catalyst for the nucleation (Hodes, 2002). For the deposition parameters chosen, it was expected that deposition would occur via an ion-by-ion process

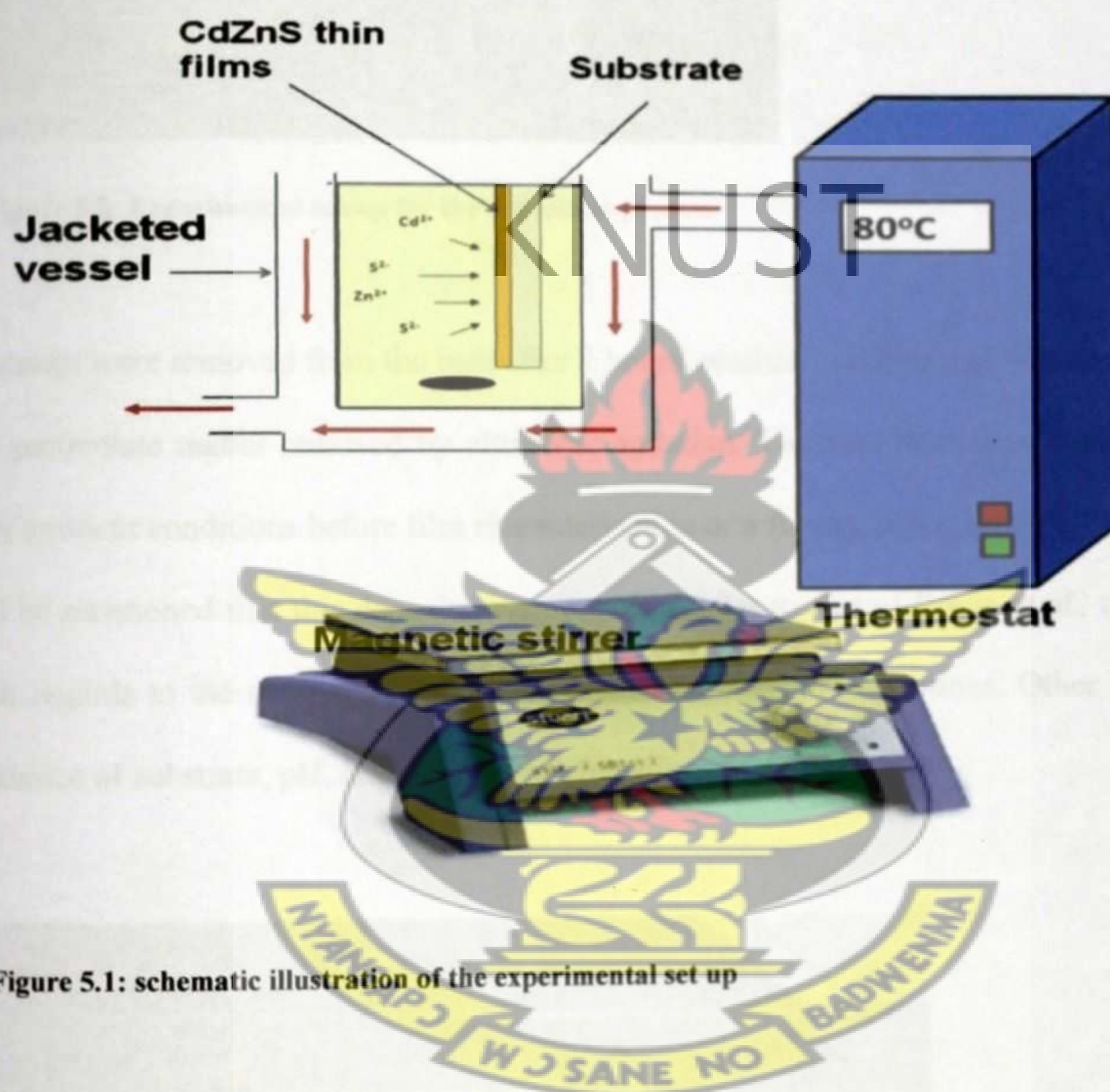


Figure 5.1: schematic illustration of the experimental set up

A schematic illustration of the experimental set up is given in Figure 5.1. It should be noted that cadmium zinc sulphide also forms homogenously in solution, and this can form a loose coating on the substrate and may prevent growth of an adherent film. For this reason, the substrate was placed vertically in the solution and continuously stirred to prevent the deposition of loosely adhering, large aggregates. With an appropriate design of the jig several samples can be prepared in a single run, as shown in the actual experimental set up in Figure 5.2.

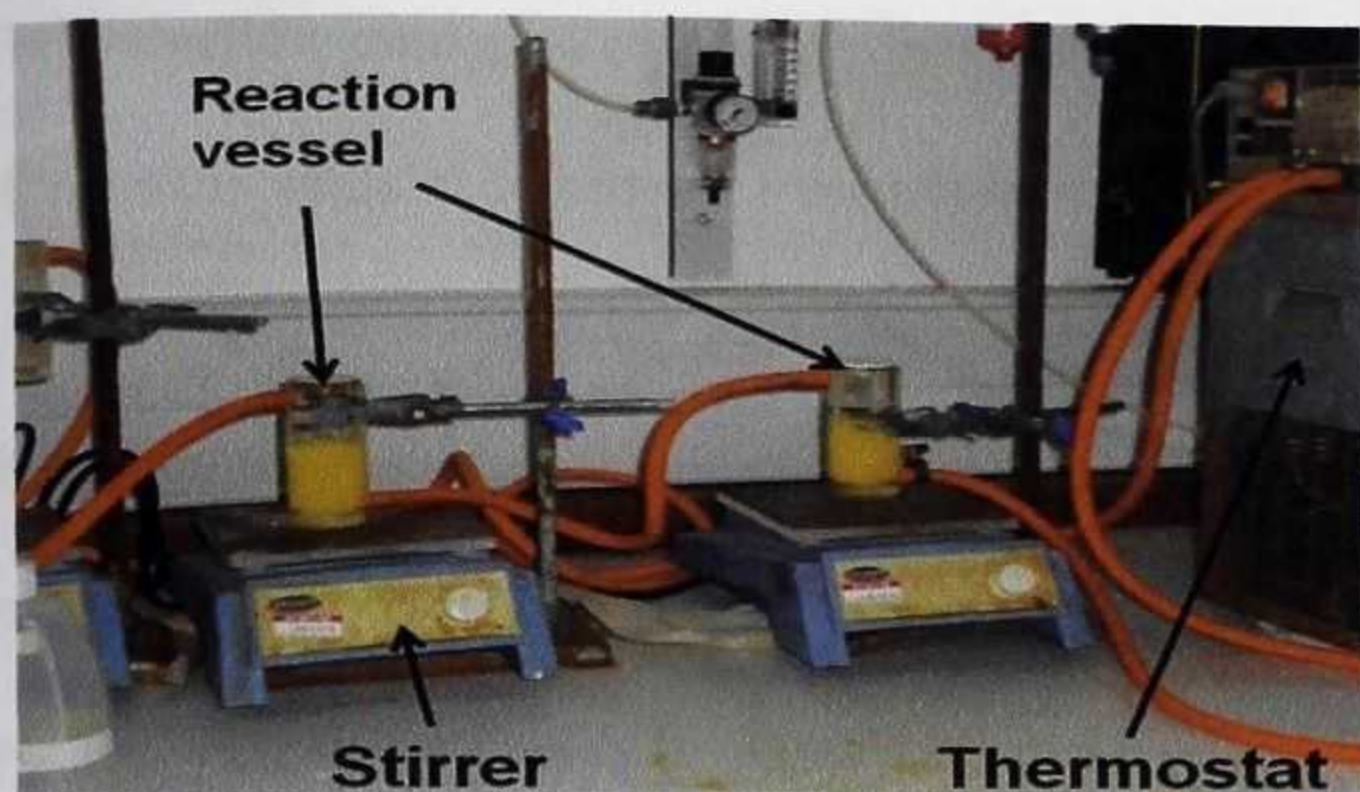


Figure 5.2: Experimental set-up for the deposition process

The substrates were removed from the bath after 2 hours, washed in de-ionised water and any adherent particulate matter removed by ultrasonic agitation. The substrates were allowed to dry under ambient conditions before film characterization or a further annealing step.

It should be mentioned that this deposition process is similar to that of Boyle *et al.*, (2000), only with regards to the choice of precursors, as well as their concentrations. Other factors such as choice of substrate, pH, and duration of annealing are different.



Figure 5.3: Pictures of as-deposited thin films.

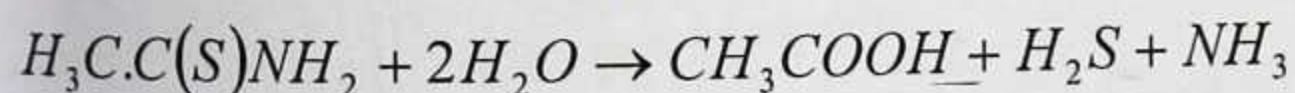
The as-deposited samples obtained by this method were smooth, uniform, adherent, pinhole free, bright yellow orange in colour and changed to pale yellow with increasing zinc content. ZnS films were white in colour and transparent as shown in Figure 5.3.

One of the major drawbacks with the CBD process is that, in the classical beaker configuration, the material yield for film formation is very low, about a few per cent, leading to an unnecessary waste in production and increased treatment cost. This is because the volume to surface ratio is very high and that only a small part of the solution is contributing to the film formation, the remaining part leading to the formation of colloids in the bulk of the solutions (Lincot *et al.*, 1999). Low yield is of concern in all industrial processes and is particularly troublesome for toxic materials such as CdS. CBD yield of CdS is often as low as 2 - 10% (Boyle *et al.*, 2000; Nair *et al.*, 2001). To avoid this problem the idea is to carry out the reaction between two plates with a small spacing filled with the solution, the plates being directly the substrates which have to be covered (Lincot *et al.*, 1999; Nair *et al.*, 2001). The interest of this configuration is that it is like a 2D configuration with no limit on the area. It can be considered as a close space configuration by analogy with existing techniques in vacuum, like close space chemical vapour transport (CSV) or close space sublimation (CSS) (Lincot *et al.*, 1999).

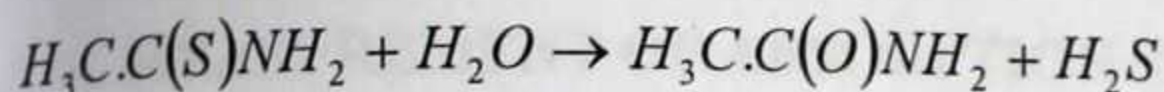
5.3 CHEMICAL EQUATIONS FOR THE DEPOSITION PROCESS

5.3.1 Decomposition of Thioacetamide

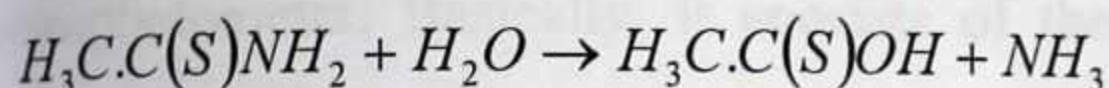
Thioacetamide has been used for a long time as an analytical reagent to precipitate metal sulphides. Thioacetamide was chosen because it can be hydrolyzed over a wide range of pH and is often used as the sulphide precursor for CBD in acidic baths.



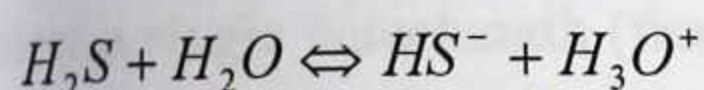
It has been shown by Peeters and Ranter (1974), that this reaction can proceed by two pathways, one in which the carbon-sulphur bond is broken first:



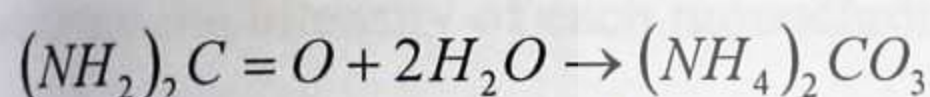
forming acetamide as an intermediate, or a pathway in which the carbon-nitrogen bond is first broken to give thioacetic acid:



This then is hydrolyzed to H_2S and acetic acid. The H_2S dissolves in water as hydrosulphide ion:



5.3.2 Hydrolysis of Urea

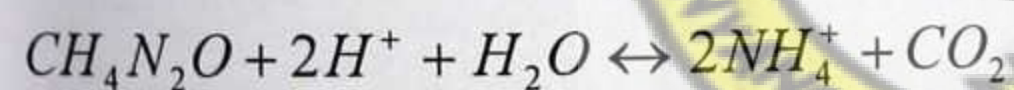
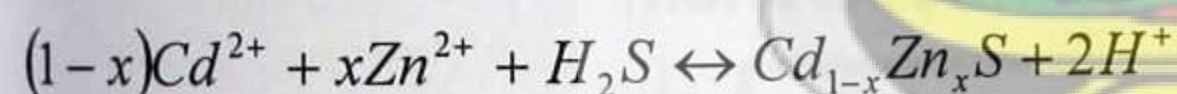


Urea is slowly hydrolyzed in water to form ammonium carbonate:



Carbonates are alkaline since they dissociate to some extent to form hydroxide ions:

The reaction process for the formation of $Cd_{1-x}Zn_xS$ may be described by the following steps:



Cadmium ions from cadmium salts, zinc ions from zinc salts and sulphide ions from thioacetamide migrate to the substrate surface and form $Cd_{1-x}Zn_xS$. Urea in the reaction solution can adjust the balance of the hydrolyzation and deposition.

5.4 MEASUREMENT OF ABSORPTION SPECTRA

Absorption spectra are usually registered by instruments known as spectrophotometers.

Figure 5.4 shows a schematic diagram with the main elements of the simplest spectrophotometer. Basically, it consists of the following components: (i) a light source (usually a deuterium lamp for the UV spectral range and a tungsten lamp for the VIS and IR spectral ranges) that is focused on the entrance to (ii) a monochromator, which is used to select a single wavelength (frequency) from all of those provided by the lamp source and to scan over a desired frequency range. (iii) a sample holder, followed by (iv) a light detector, to measure the intensity of each monochromatic beam after traversing the sample and finally (v) a computer, to display and record the absorption spectrum (Sole *et al.*, 2005).

In this work, optical absorption spectra were recorded with a Cary 5000 (ver. 1:09) UV – VIS spectrophotometer within the wavelength range of 800 – 200 nm, at 24 °C. A blank glass slide was initially scanned and used for baseline corrections.

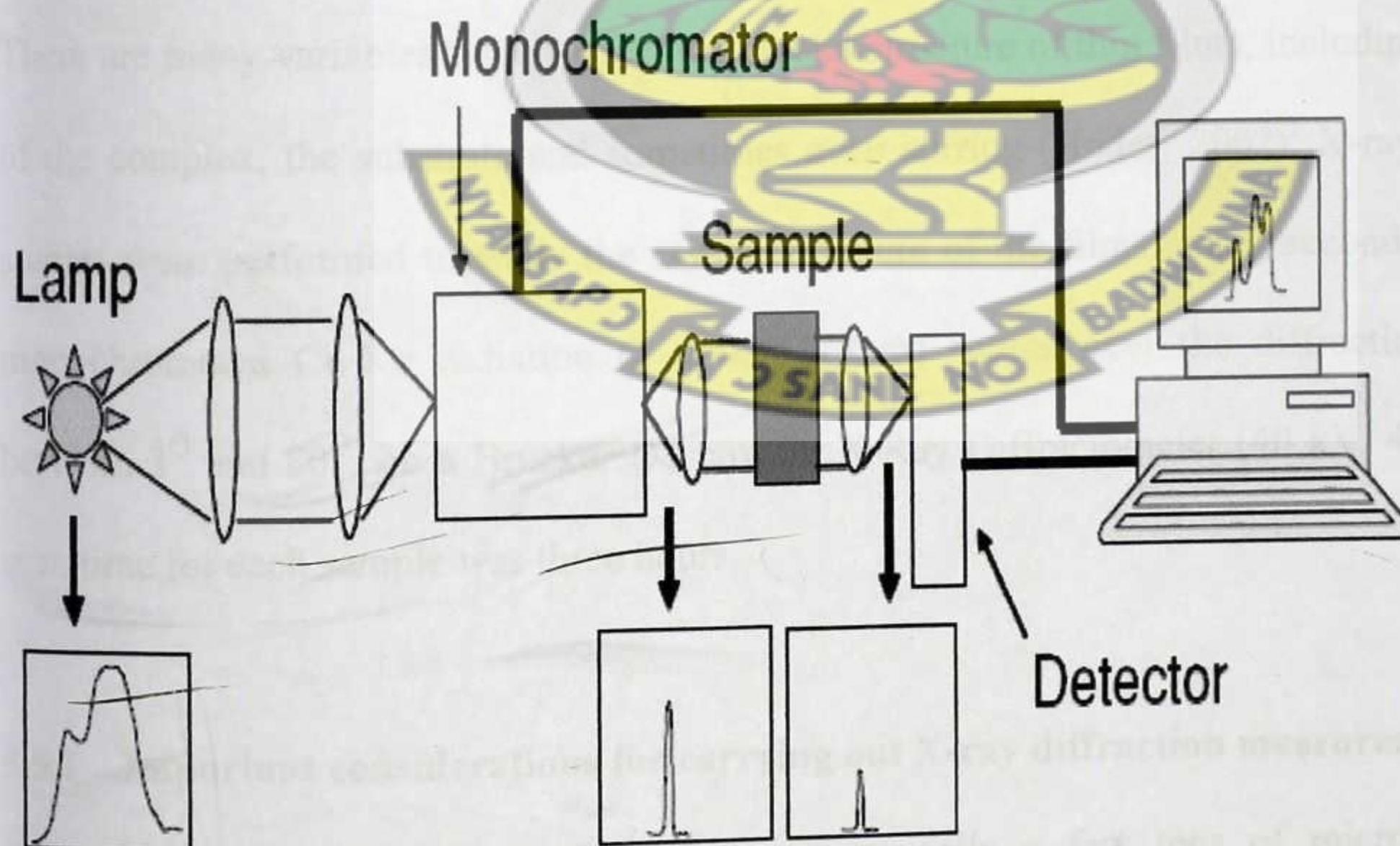


Figure 5.4 Schematic diagram of a single-beam spectrophotometer.

There are some potential problems that should be taken into account when interpreting such spectra. A spectrophotometer measures transmission (and may be, also reflection) but not absorption. What is measured as absorption is a transmission measurement that is mathematically manipulated to convert it to absorption. Absorption is usually measured as absorbance, A , which by definition is given by

$$A = \text{Log}_{10} \frac{I_0}{I}$$

where I is the intensity of the transmitted light and I_0 that of the incident light.

The transmission, T , is

$$T = \frac{I}{I_0}$$

The spectrophotometer measures the transmission and, converts the transmission into absorbance using these equations.

5.5 X-RAY DIFFRACTION MEASUREMENTS

There are many variables which affect the crystal structure of thin films, including the nature of the complex, the substrate and sometimes even stirring (Hodes, 2002). X-ray diffraction studies were performed to study the crystal structure of the films, using secondary graphite monochromated Cu-K α radiation ($\lambda = 0.15418\text{nm}$) source over the diffraction angle 2θ between 3° and 80° , on a Brucker D8 powder X-Ray Diffractometer (40 kV, 40 mA). The scan time for each sample was three hours.

5.5.1 Important considerations for carrying out X-ray diffraction measurements

The penetration depth of an X-ray beam is typically a few tens of microns. In fact, polycrystalline films in this thickness range are quite easy to deal with using a regular powder diffractometer. Below one micron, the signal from the film can be seriously obscured by the

signal from the substrate. At 100 nm, the signal from the film may be only 1% of the signal from the substrate, and that approaches the limit of sensitivity of powder diffraction (Ryan, 2001). As 10 nm thickness is reached, things only get worse. Not only is the signal a factor of ten smaller, but diffraction broadening makes the diffraction peaks wider and peak intensities drop rapidly. The depth of penetration into the sample is given by the absorption length times the sine of the incidence angle. Since most of the diffraction peaks from a typical sample material lie in the region of 20° to 100° , 2θ , incidence angles are typically in the range of $(10 - 50)^\circ$. If the sample is a thin layer, most of the X-ray beam passes through the film and is scattered by the substrate. The technique in thin-film XRD is to choose an X-ray diffraction geometry that allows you to work at very small angles of incidence, increasing the path length of the X-rays in the film and reducing the amount of X-rays that penetrate through to the substrate. An incidence angle of 6° reduces the penetration depth by a factor of 10; an incidence angle of 0.6° leads to reduction by a factor of 100 (Ryan, 2001). In this work a glancing angle of 3° was chosen. This was to ensure that the x-ray beam skims through the top layer and does not penetrate into the substrate. This was the minimum since below this angle, the resolution of the diffractometer was much reduced.



Figure 5.5: Samples loaded onto the diffractometer

Figure 5.5 shows the samples loaded onto the diffractometer, the Brucker D8 X-ray diffractometer can take a maximum of nine samples. The samples must be flat and of correct height, that is it should not extend above the loading tray. If the sample height is incorrect the surface of the sample will not coincide with the machine's (the goniometer) axis of rotation.

If the scan proceeds too quickly, the diffraction pattern would be obscured by a lot of unwanted signals (noise). To prevent this from occurring, the following two parameters must be chosen carefully; step size – this is how far the machine travels before it sends data to the computer, and counting time – the time which the machine takes to execute a step.

For this scan the following machine settings were used

- Scan Type CONTINUOUS
- Scan Mode $\theta / 2\theta$
- Step Size $0.05^\circ 2\theta$
- Scan Range 3 to $80^\circ 2\theta$
- Counting Time Per Step 2 seconds
- Total Analysis time per sample: 3 hours, 10 minutes

5.6 SCANNING ELECTRON MICROSCOPY MEASUREMENTS

Scanning electron microscopy (SEM) measurements were also conducted using a Philips XL30 FEG SEM. (XL 30 series), to examine the surface morphology of the films.

5.6.1 Sample preparation for SEM measurements

The thin films were cut to a size of 2.4 cm x 2.4 cm and mounted on aluminium specimen stubs with the aid of double sided adhesive carbon 'tabs'. During SEM examination, electrons can accumulate on the surface of the sample, such areas of charge repel the electron beam and appear as regions of white contrast in the sample image, with no visible detail. In

order to prevent this from occurring, the surface of the sample must be electrically conductive. This was achieved by coating the surface of the samples with carbon, using a GATAN Model 682 precision etching coating system. A conductive silver paint was also used to make a conductive track from coating on sample surface to specimen stub.

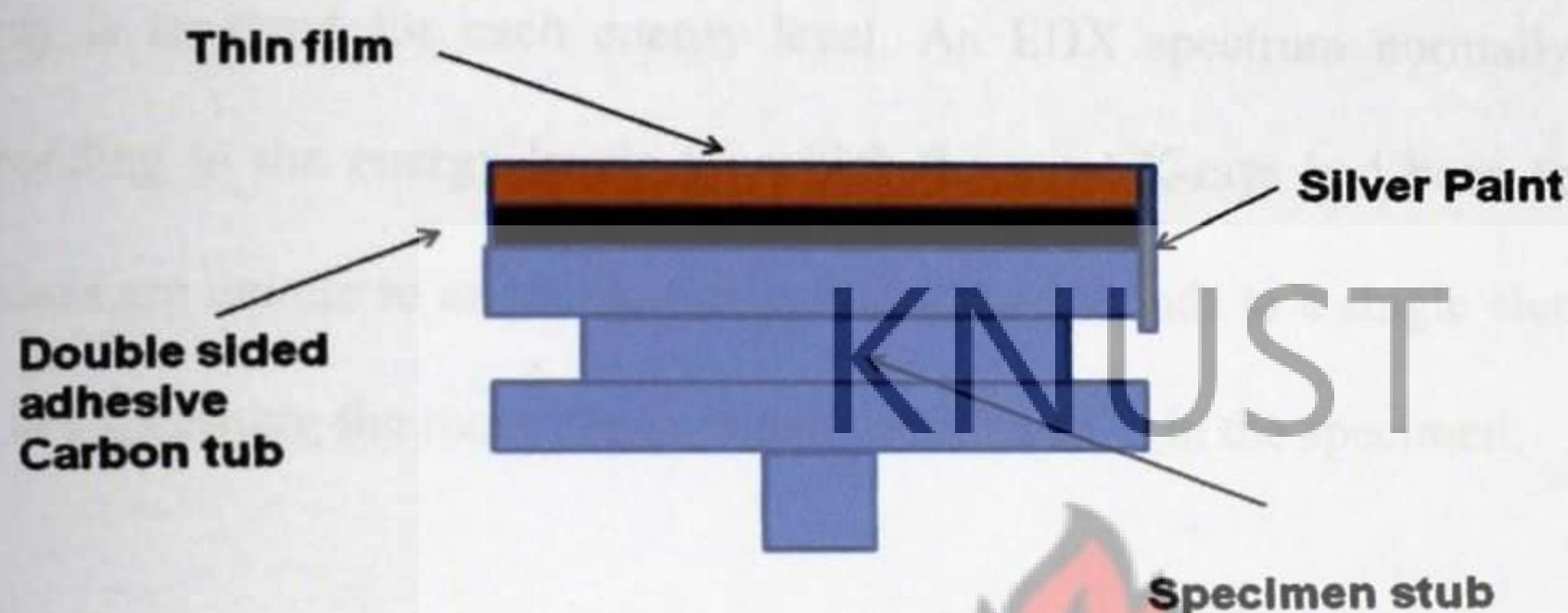


Figure 5.6: Sample mounted on specimen stub for SEM

Figure 5.6 illustrates how thin films are mounted on the specimen stub to perform SEM. When the samples have been prepared, and prior to examination in the SEM, it is very important to keep it clean. One should avoid handling the sample since grease and sweat from finger prints are volatile in the SEM, and cause 'hydrocarbon shadowing', which are dark 'shadow' areas within the image.

In the SEM, the sample was mounted on the stage inside the sample chamber. The door was shut and the chamber was evacuated to the appropriate vacuum level. The detection sequence was set to secondary electrons (SE) and an appropriate accelerating voltage was chosen on the SEM control interface. An accelerating voltage of 20 kV has been found to be most appropriate for samples containing zinc. After focusing and adjusting the stigmator, the SEM images were then recorded on a computer.

5.7 ENERGY DISPERSIVE X-RAY ANALYSIS

Energy Dispersive X-ray analysis, EDX, is a technique used for identifying the elemental composition of the specimen, or an area of interest thereof. The EDX analysis system works as an integrated feature of SEM, and cannot operate on its own without the latter. The output of an EDX analysis is an EDX spectrum. The EDX spectrum is just a plot of how frequently an X-ray is received for each energy level. An EDX spectrum normally displays peaks corresponding to the energy levels for which the most X-rays had been received. Each of these peaks are unique to an atom, and therefore corresponds to a single element. The higher a peak in a spectrum, the more concentrated the element is in the specimen.

5.8 THERMAL ANNEALING

Annealing minimizes internal defects in materials and leaves them free from internal stresses that might otherwise be present because of prior processing steps (Microsoft® Encarta® 2009). The thin films were put in a tray, placed in a corbolite furnace and heated to a temperature of 400°C, lower than the melting point of zinc (418 °C), for two hours, after which the furnace was switched off and allowed to cool to room temperature. The samples were then removed and again characterized by the same techniques.

CHAPTER SIX

6. RESULTS AND DISCUSSION

6.1 X-RAY DIFFRACTION PATTERNS OF THE THIN FILMS

Figures 6.1 to 6.7, show the x-ray diffraction patterns of the thin films. The horizontal axis of the graph is 2θ , twice the Bragg angle. The vertical axis is the intensity/ X-ray count rate, this is a function of the crystal structure and the orientation of the crystallites. The space between diffracting planes of atoms determines peak positions. The peak intensity is determined by the type of atoms in the diffracting plane.

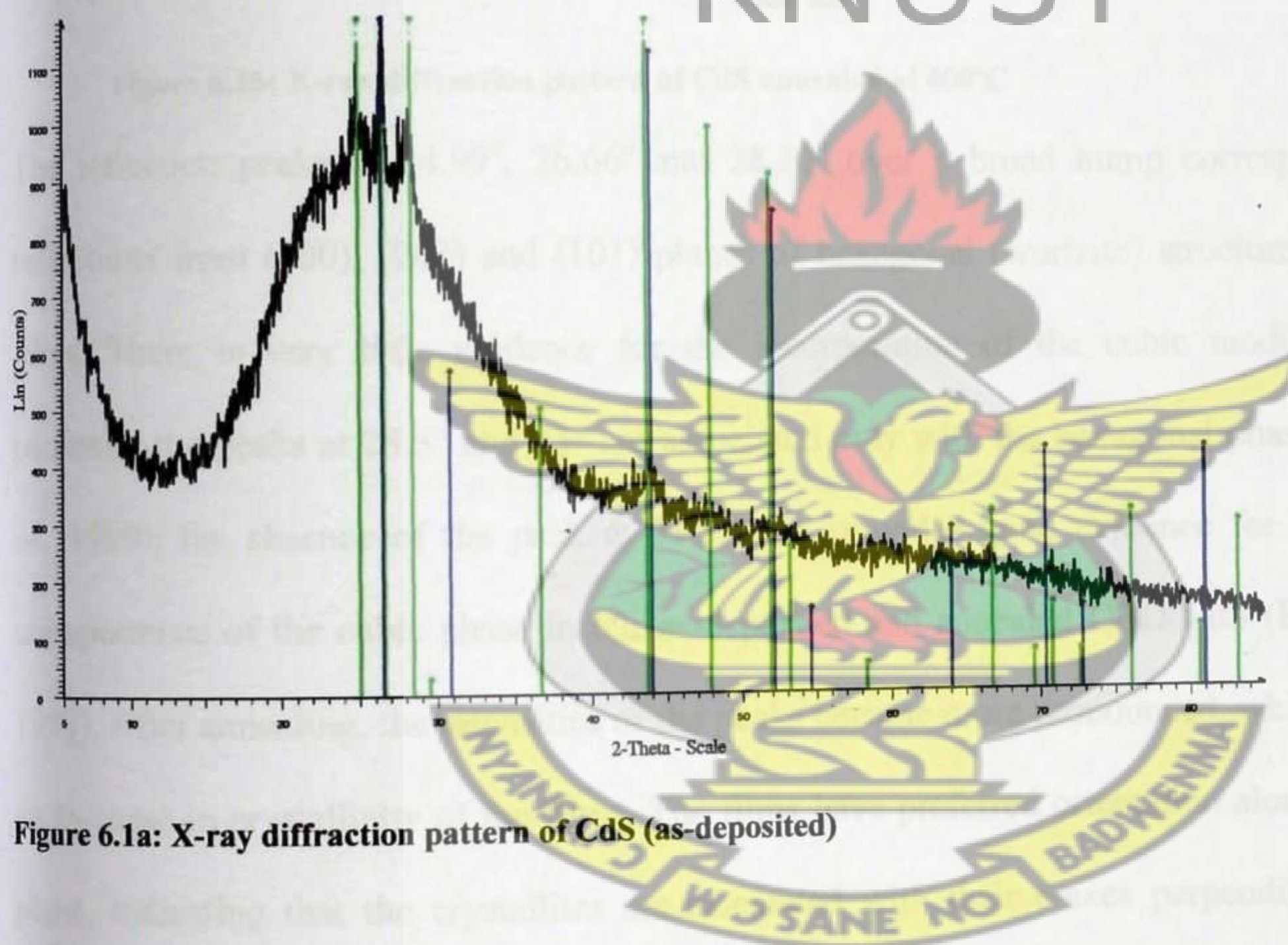


Figure 6.1a: X-ray diffraction pattern of CdS (as-deposited)

X-ray diffraction patterns of CdS thin films, before and after annealing, are shown in figure 6.1a and 6.1b. The broad hump in the range $20^\circ \leq 2\theta \leq 35^\circ$ is due to the glass substrate (Li et al., 2010). The diffraction patterns were matched with standards in the JCPDS data file, reference code, 00-001-0780.

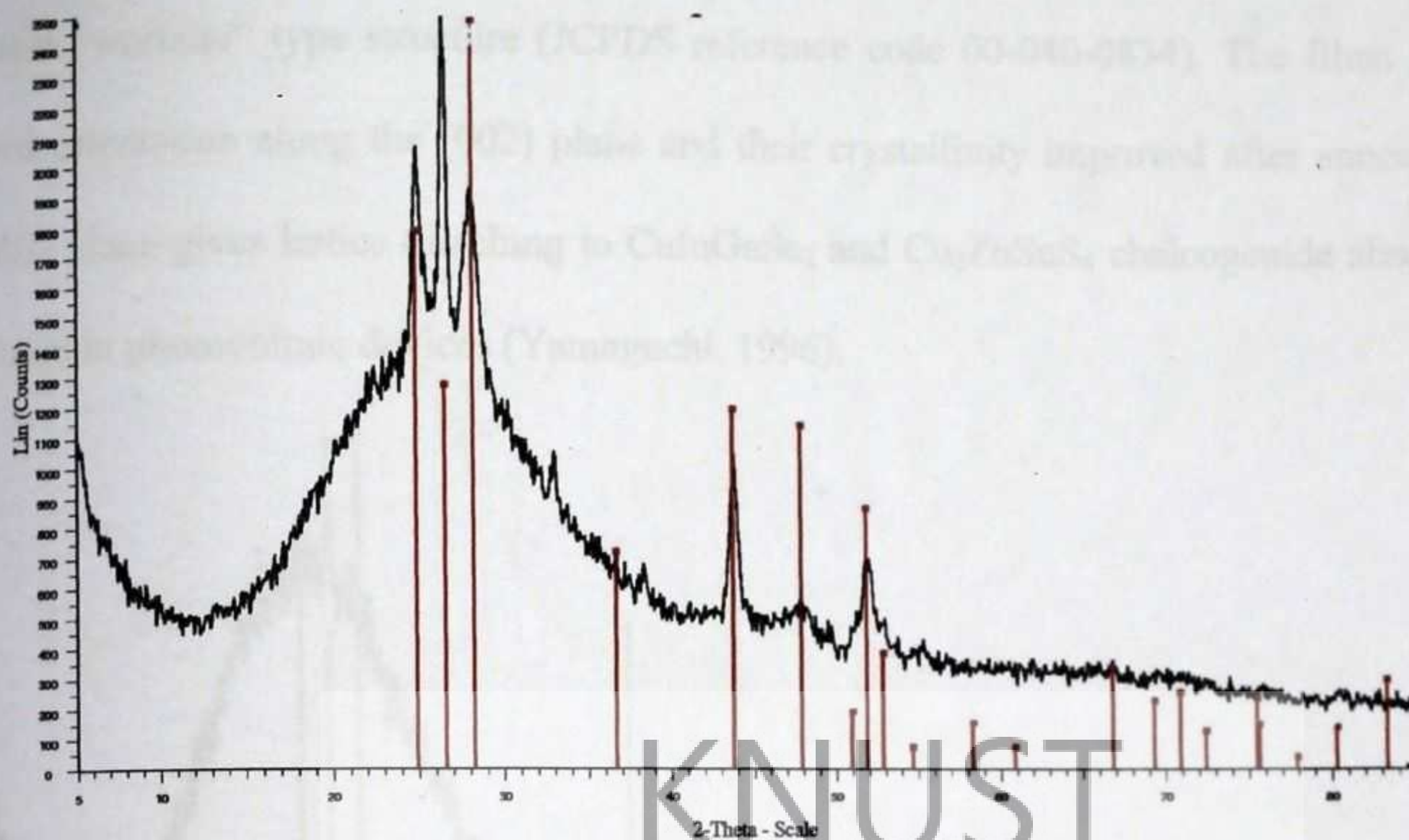


Figure 6.1b: X-ray diffraction pattern of CdS annealed at 400°C

The reflection peaks at 24.99° , 26.66° and 28.30° over a broad hump correspond to the reflections from (100), (002) and (101) planes of hexagonal (wurtzite) structured CdS thin films. There is very little evidence for the incorporation of the cubic modification. In particular the peaks at 28.3° and 53° are associated only with the hexagonal phase (Boyle *et al.*, 1999); the absence of the peak at 31.5° also provides good evidence for the relative unimportance of the cubic phase in our as-deposited and annealed CBD CdS (Boyle *et al.*, 1999). After annealing, the intensities of the peaks became more pronounced, which suggests an increase in crystallinity of the films. The films have preferred orientation along the (002) plane, indicating that the crystallites are orientated with their c-axes perpendicular to the substrate (Edamura and Muto, 1995). Such orientation is not surprising as the preferred growth direction for CdS is with the c-axis perpendicular to the substrate (Stanley, 1975). Similar observations on the preferred orientation of CBD-CdS along the (002) plane have been reported in the literature. Some authors have also made similar observations for CdS deposited by other methods such as; spray pyrolysis (Ma *et al.*, 1977), and by evaporation (Fraas and Ma, 1977). For the films with zinc composition, $x = 0.11, 0.14, 0.25$, and 0.50 , shown in figures 6.2 to 6.5, the pattern of prominent peak positions is also consistent with the

hexagonal “wurtzite” type structure (JCPDS reference code 00-040-0834). The films have preferred orientation along the (002) plane and their crystallinity improved after annealing. The (002) plane gives lattice matching to CuInGaSe_2 and $\text{Cu}_2\text{ZnSnS}_4$ chalcogenide absorber layers used in photovoltaic devices (Yamaguchi, 1996).

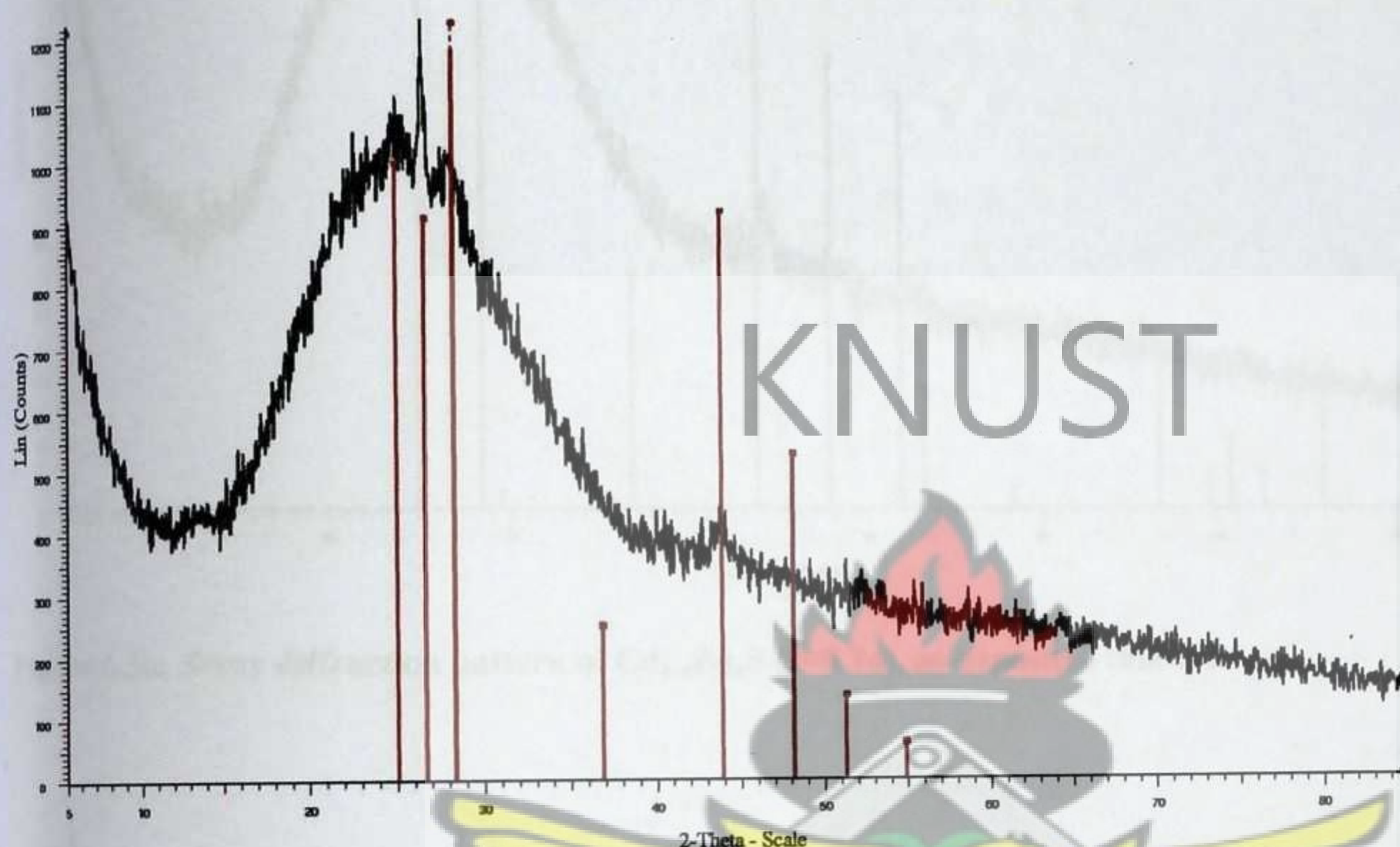


Figure 6.2a: X-ray diffraction pattern of $\text{Cd}_{1-x}\text{Zn}_x\text{S}$, ($x=0.11$) as-deposited thin film

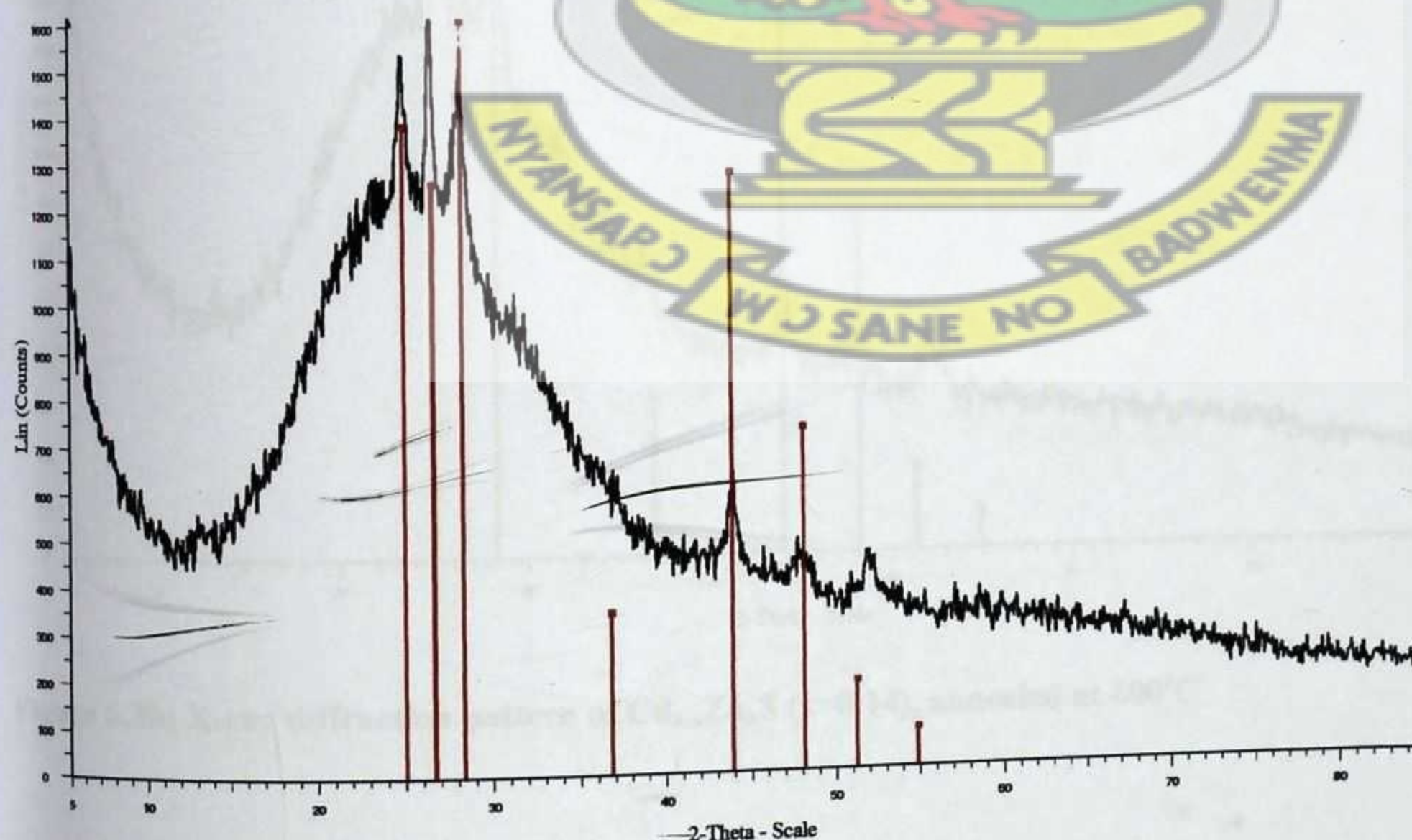


Figure 6.2b: X-ray diffraction pattern of $\text{Cd}_{1-x}\text{Zn}_x\text{S}$ ($x=0.11$), annealed at 400°C

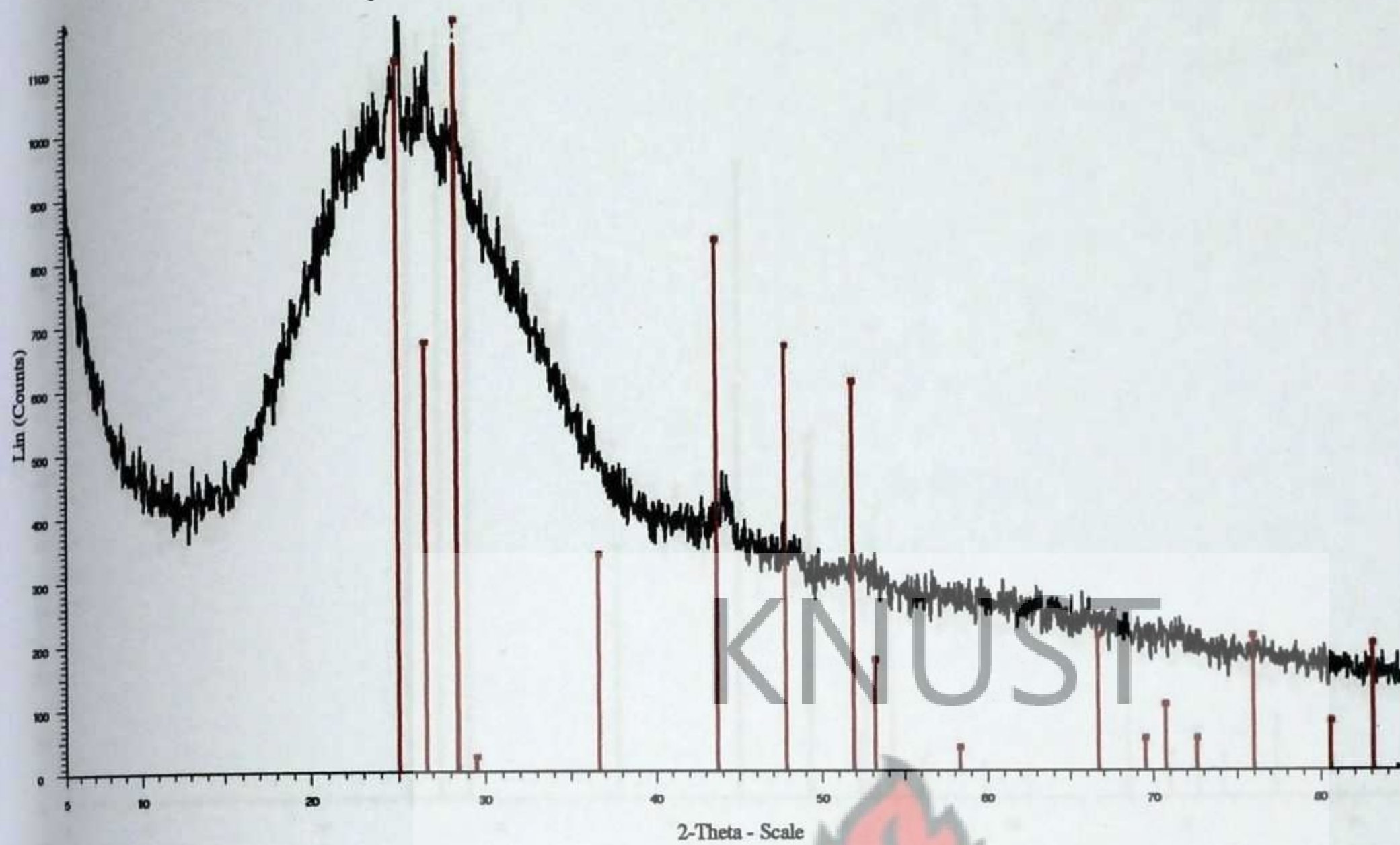


Figure 6.3a: X-ray diffraction pattern of $\text{Cd}_{1-x}\text{Zn}_x\text{S}$ ($x=0.14$), as-deposited thin film

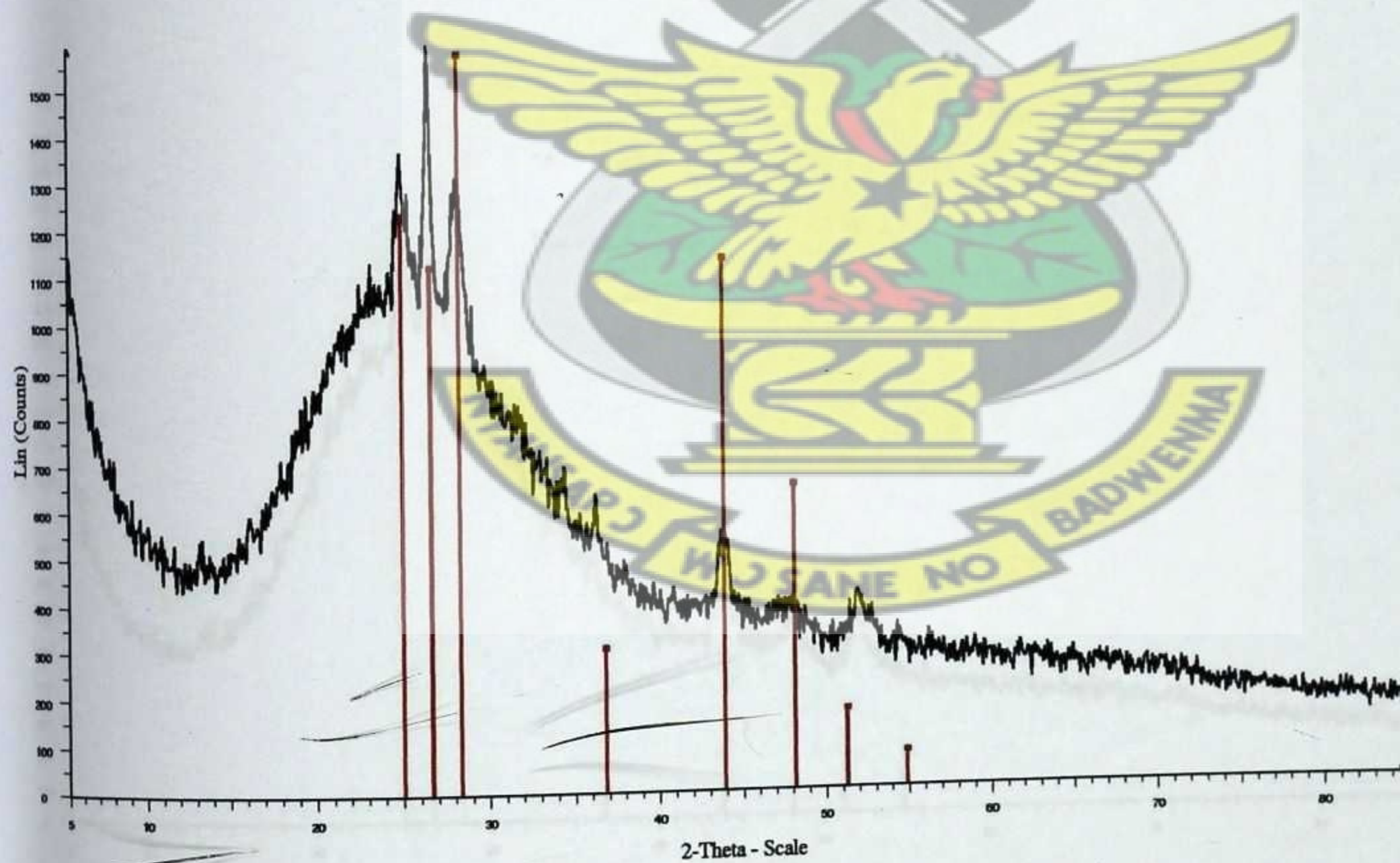


Figure 6.3b: X-ray diffraction pattern of $\text{Cd}_{1-x}\text{Zn}_x\text{S}$ ($x=0.14$), annealed at 400°C

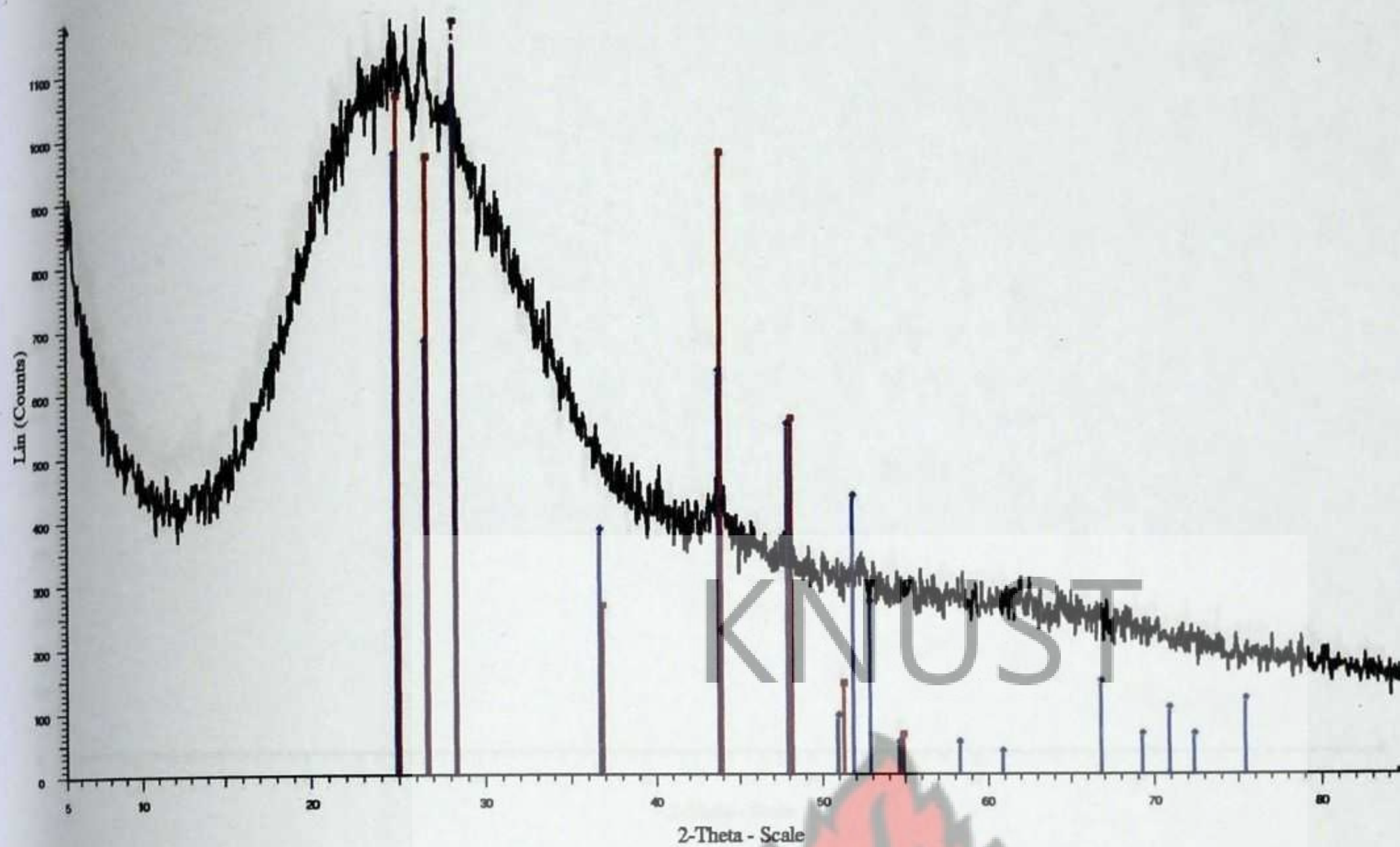


Figure 6.4a: X-ray diffraction pattern of $\text{Cd}_{1-x}\text{Zn}_x\text{S}$ ($x=0.25$), as-deposited thin film

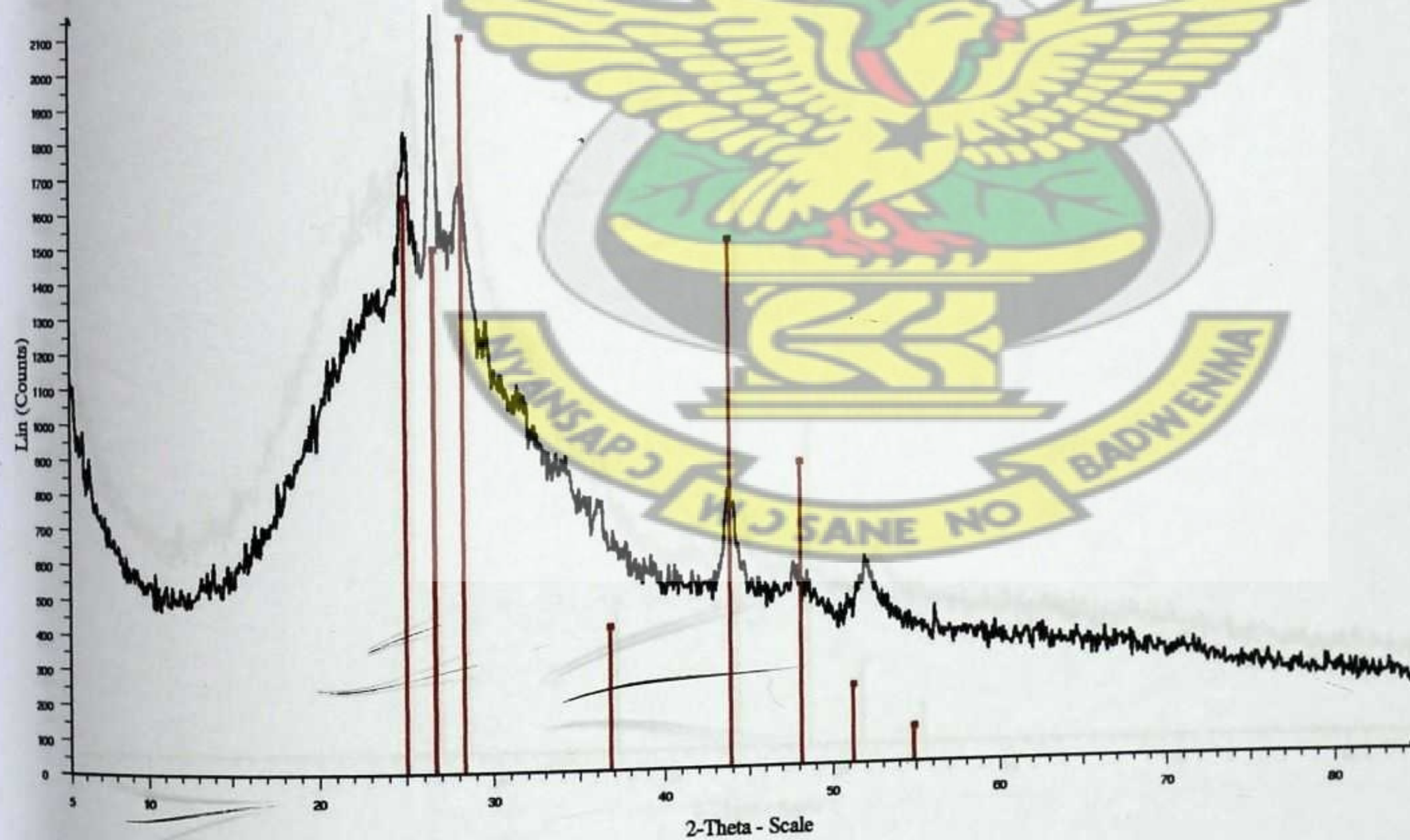


Figure 6.4b: X-ray diffraction pattern of $\text{Cd}_{1-x}\text{Zn}_x\text{S}$ ($x=0.25$), annealed at 400°C

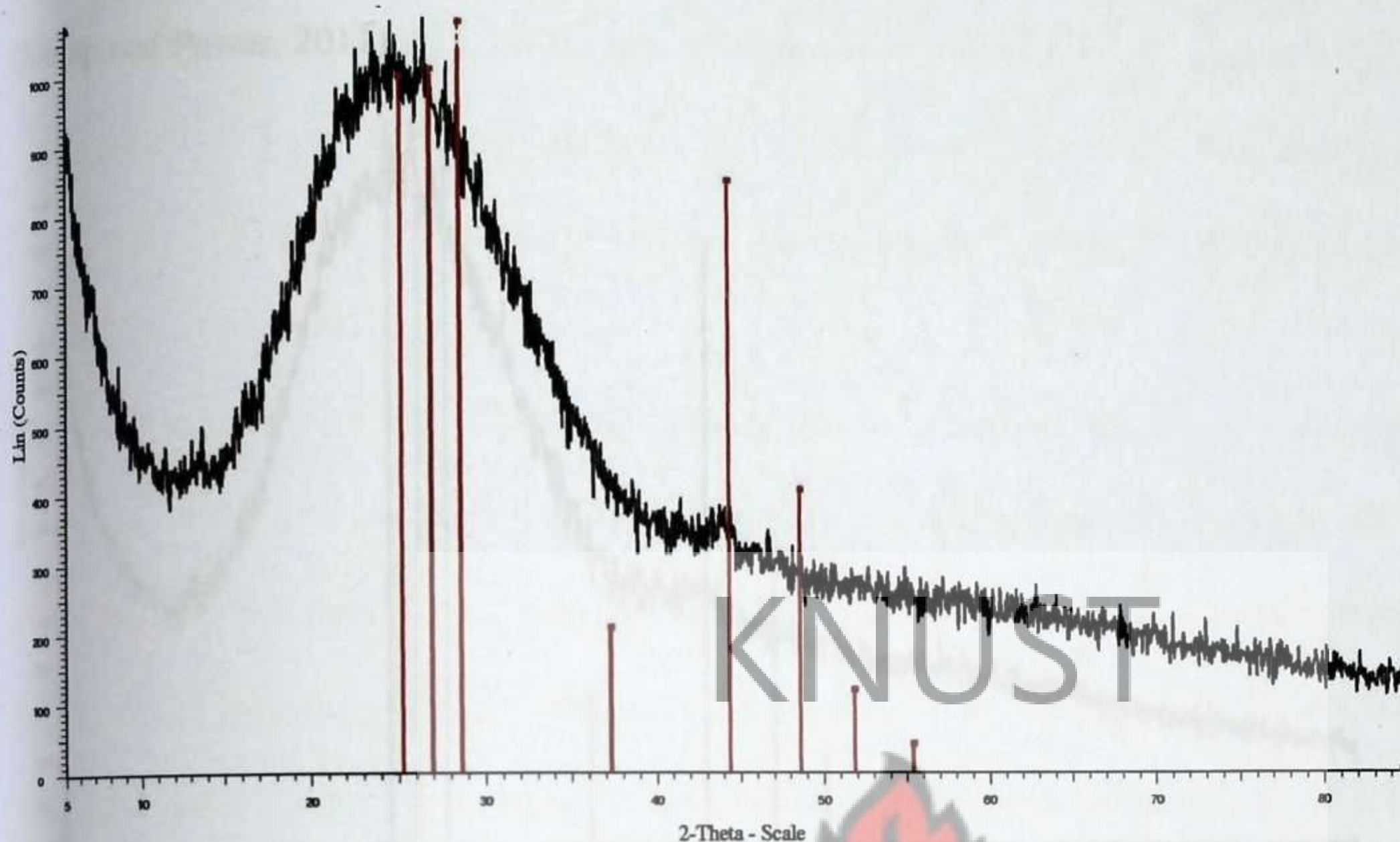


Figure 6.5a: X-ray diffraction pattern of $\text{Cd}_{1-x}\text{Zn}_x\text{S}$ ($x = 0.50$), as-deposited thin film

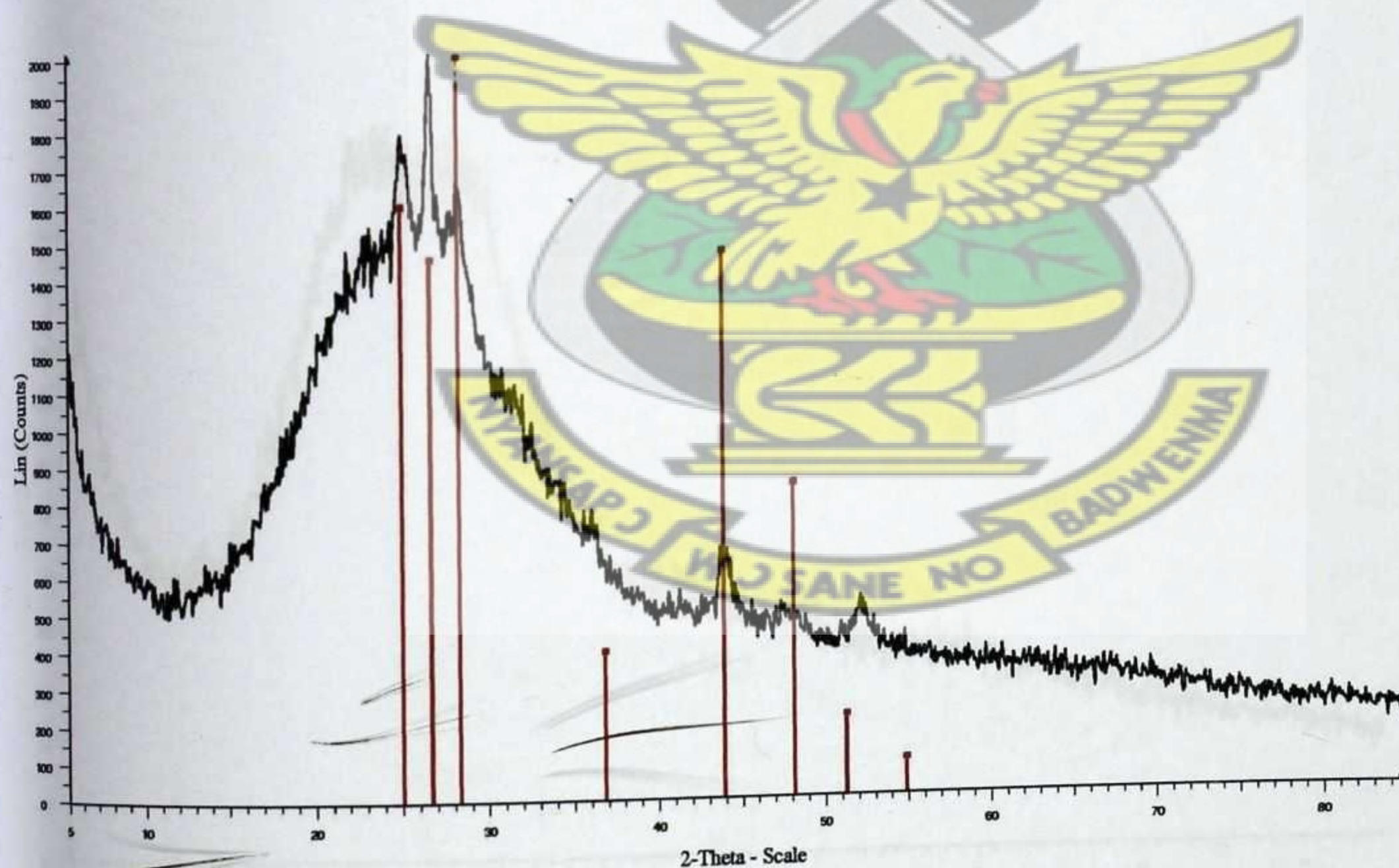


Figure 6.5b: X-ray diffraction pattern of $\text{Cd}_{1-x}\text{Zn}_x\text{S}$ ($x = 0.50$), annealed at 400°C

It can also be observed from the diffraction patterns that, as the zinc content increases, the peak intensity decreases and for $x \geq 0.25$, no discernable peaks are observed in the as-

deposited samples, suggesting that, the as-deposited films have near amorphous character (Sanap and Pawar, 2011).

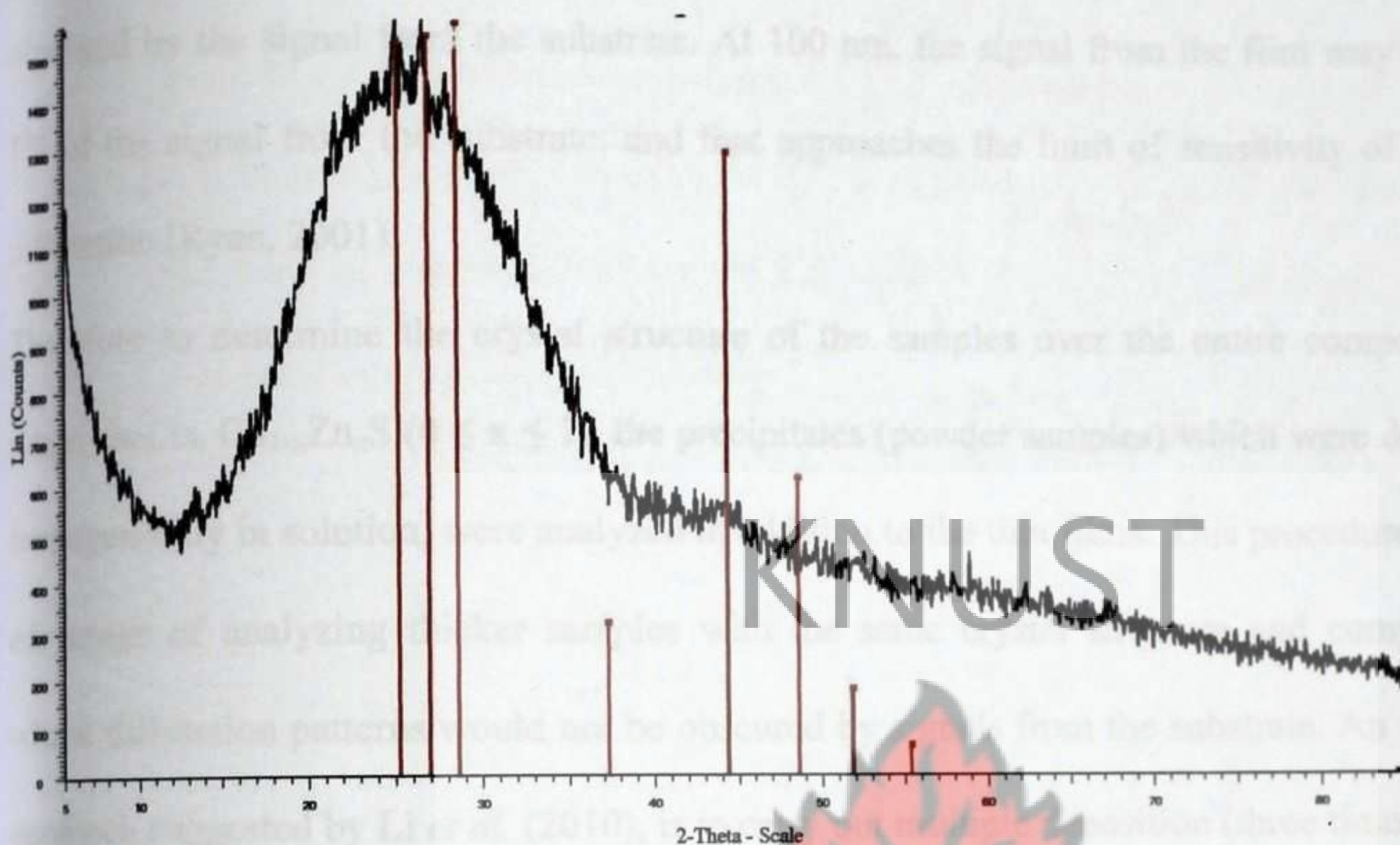


Figure 6.6: X-ray diffraction pattern of $\text{Cd}_{1-x}\text{Zn}_x\text{S}$ ($x = 0.75$), annealed 400°C

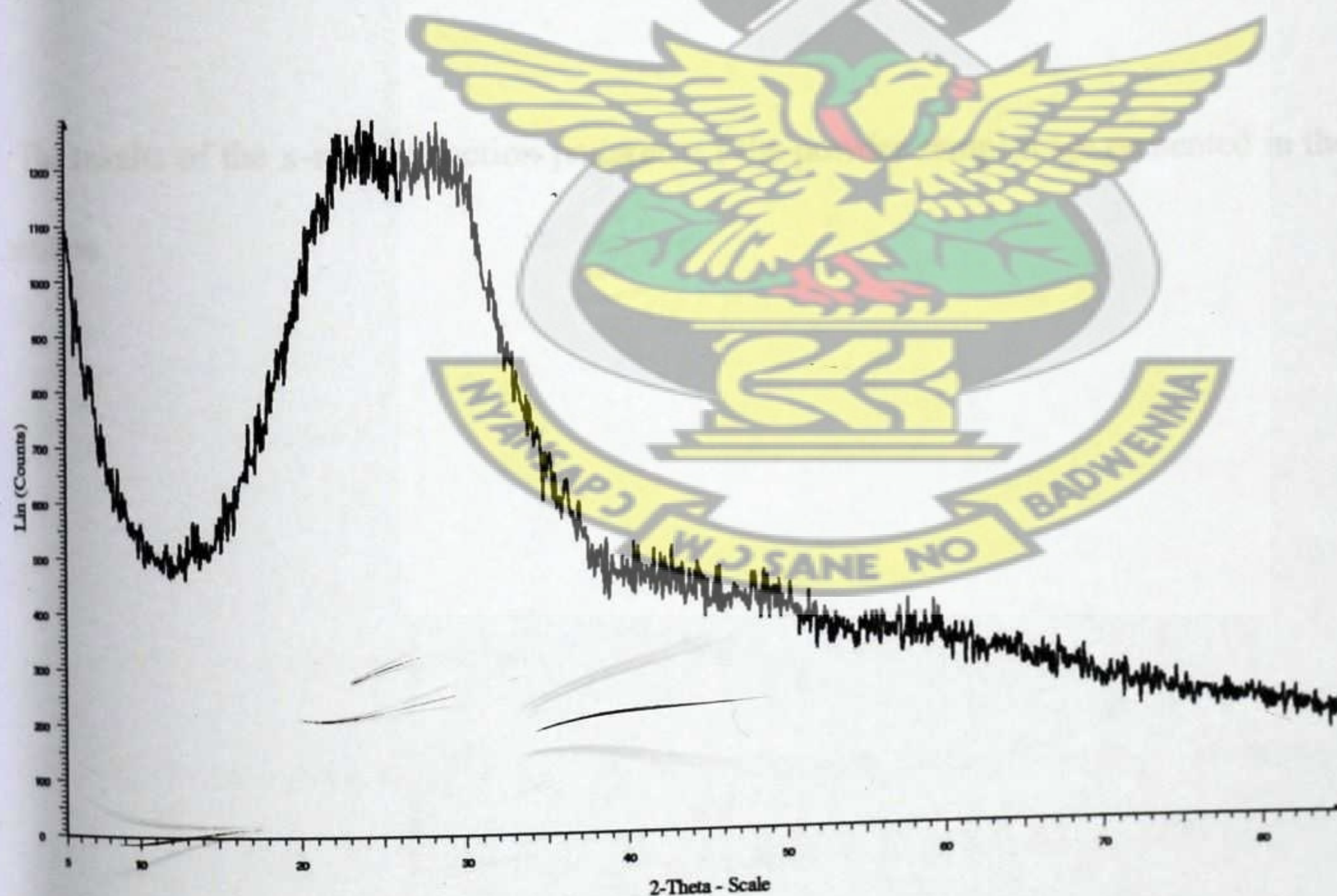


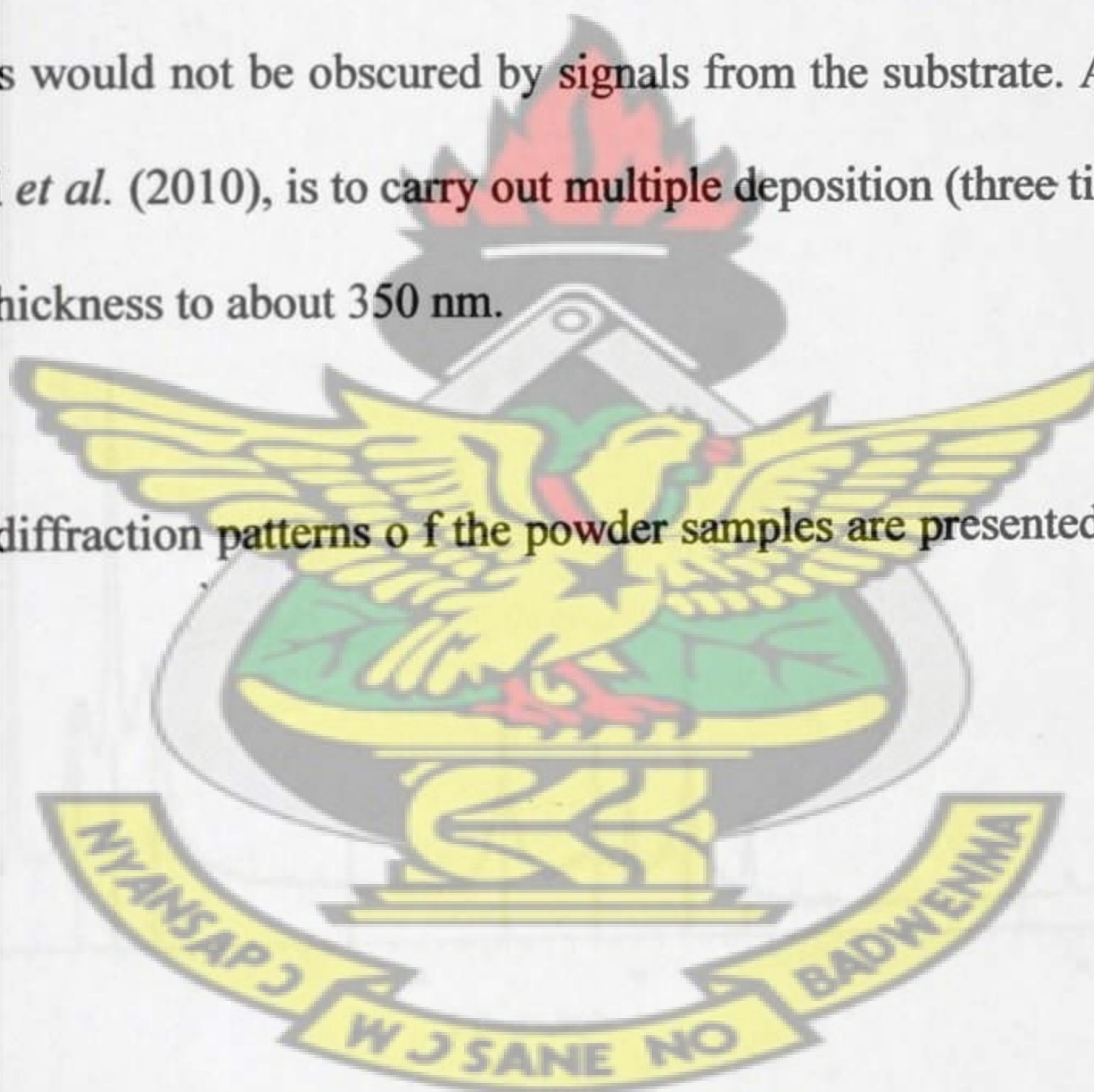
Figure 6.7: X-ray diffraction pattern of ZnS annealed at 400°C

From figures 6.6 and 6.7, the x-ray peaks in the diffraction pattern of the film with Zn composition, $x = 0.75$ after annealing were weak whilst that for ZnS did not show any peak

even after annealing. This could be due to the fact that the films with composition $x \geq 0.75$ are very thin (about 100 nm). Below one micron, the signal from the film can be seriously obscured by the signal from the substrate. At 100 nm, the signal from the film may be only 1% of the signal from the substrate, and that approaches the limit of sensitivity of powder diffraction (Ryan, 2001).

Therefore to determine the crystal structure of the samples over the entire compositional range, that is, $\text{Cd}_{1-x}\text{Zn}_x\text{S}$ ($0 \leq x \leq 1$), the precipitates (powder samples) which were deposited homogeneously in solution, were analyzed in addition to the thin films. This procedure has the advantage of analyzing thicker samples with the same crystal structure and composition, whose diffraction patterns would not be obscured by signals from the substrate. An alternate approach suggested by Li *et al.* (2010), is to carry out multiple deposition (three times) on the thin film to increase the thickness to about 350 nm.

The results of the x-ray diffraction patterns of the powder samples are presented in the next section.



6.2. X-RAY DIFFRACTION PATTERNS OF THE POWDER SAMPLES (PRECIPITATES)

Figure 6.8a shows the XRD diffraction pattern of CdS as-deposited powder samples. It can be observed that the precipitates are not affected by background noise from the substrate. Just as with the thin films, the diffraction patterns correspond to the hexagonal (wurtzite) structure, with preferred orientation along the (002) plane.

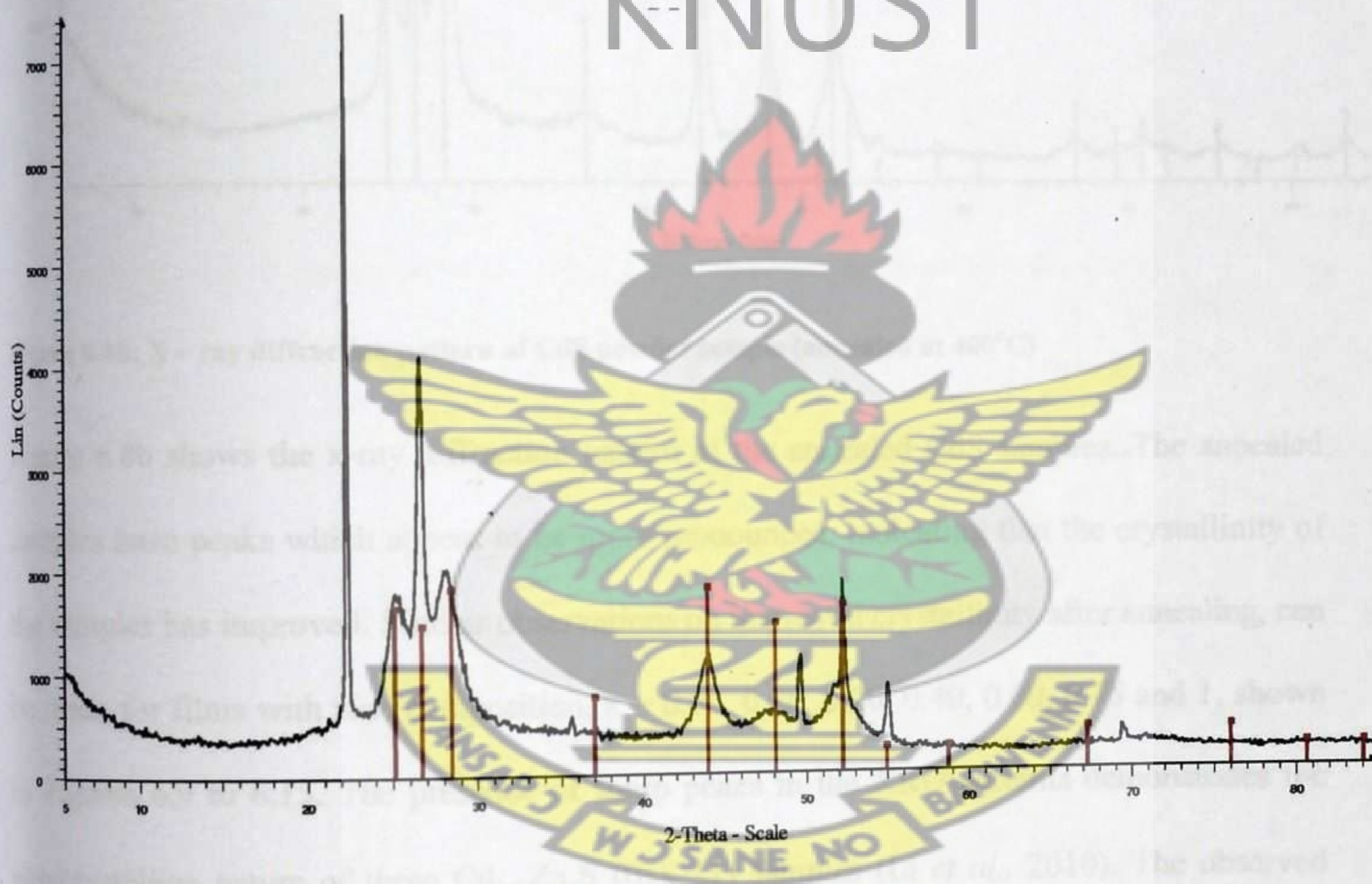


Figure 6.8a: X – ray diffraction pattern of CdS powder sample (as deposited)

A highly intense peak at $2\theta = 22^\circ$ can be observed in Figure 6.8a, and it disappears after annealing, as shown in Figure 6.8b. Similar observations can be made for all the other samples. This peak could be as a result of impurities in the as-deposited samples.

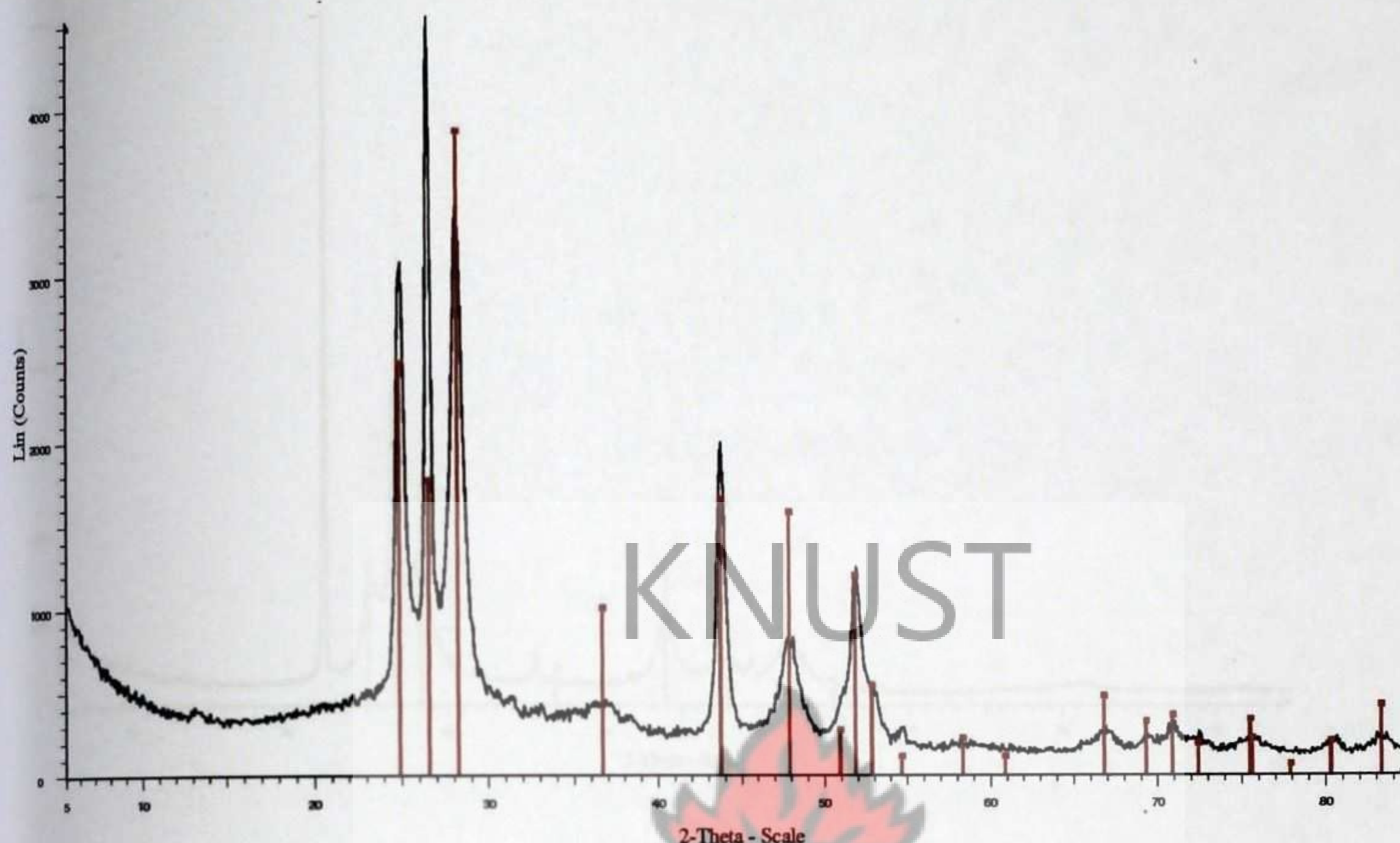


Figure 6.8b: X – ray diffraction pattern of CdS powder sample (annealed at 400°C)

Figure 6.8b shows the x-ray diffraction pattern of the annealed CdS samples. The annealed samples have peaks which appear to be more pronounced, indicating that the crystallinity of the samples has improved. Similar observations on improved crystallinity after annealing, can be made for films with zinc composition, $x = 0.06, 0.14, 0.20, 0.40, 0.60, 0.75$ and 1, shown in Figures 6.9 to 6.15. The presence of sharp peaks in the XRD patterns demonstrates the polycrystalline nature of these $\text{Cd}_{1-x}\text{Zn}_x\text{S}$ ($0 \leq x \leq 1$) samples (Li *et al.*, 2010). The observed small peak at $2\theta = 54.90^\circ$ position, correspond to the (004) plane of the hexagonal phase (Gutiérrez Lazos *et al.*, 2008; JCPDS reference code 00-040-0834).

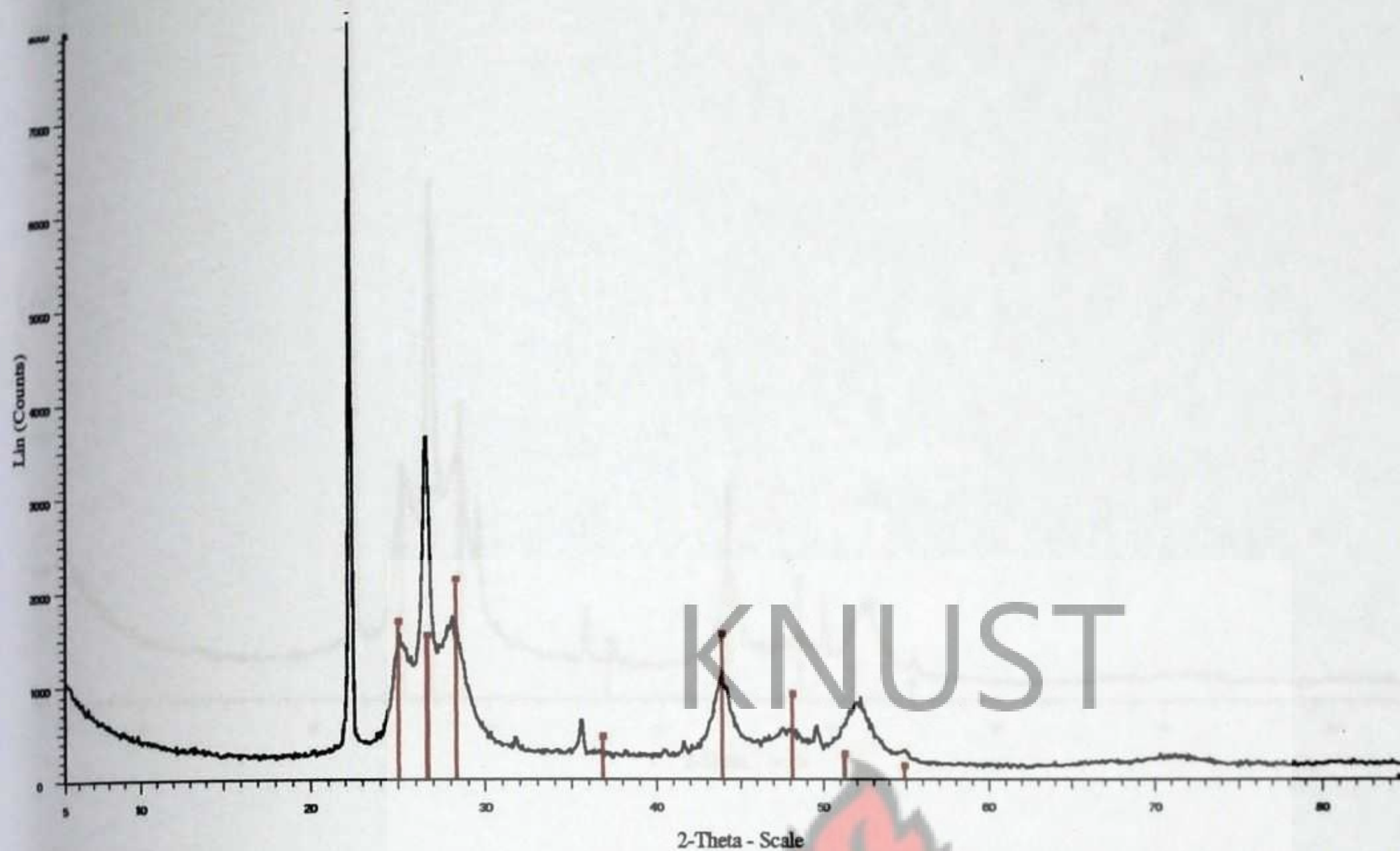


Figure 6.9a: X – ray diffraction pattern of $\text{Cd}_{1-x}\text{Zn}_x\text{S}$ ($x = 0.06$) powder sample (as-deposited)

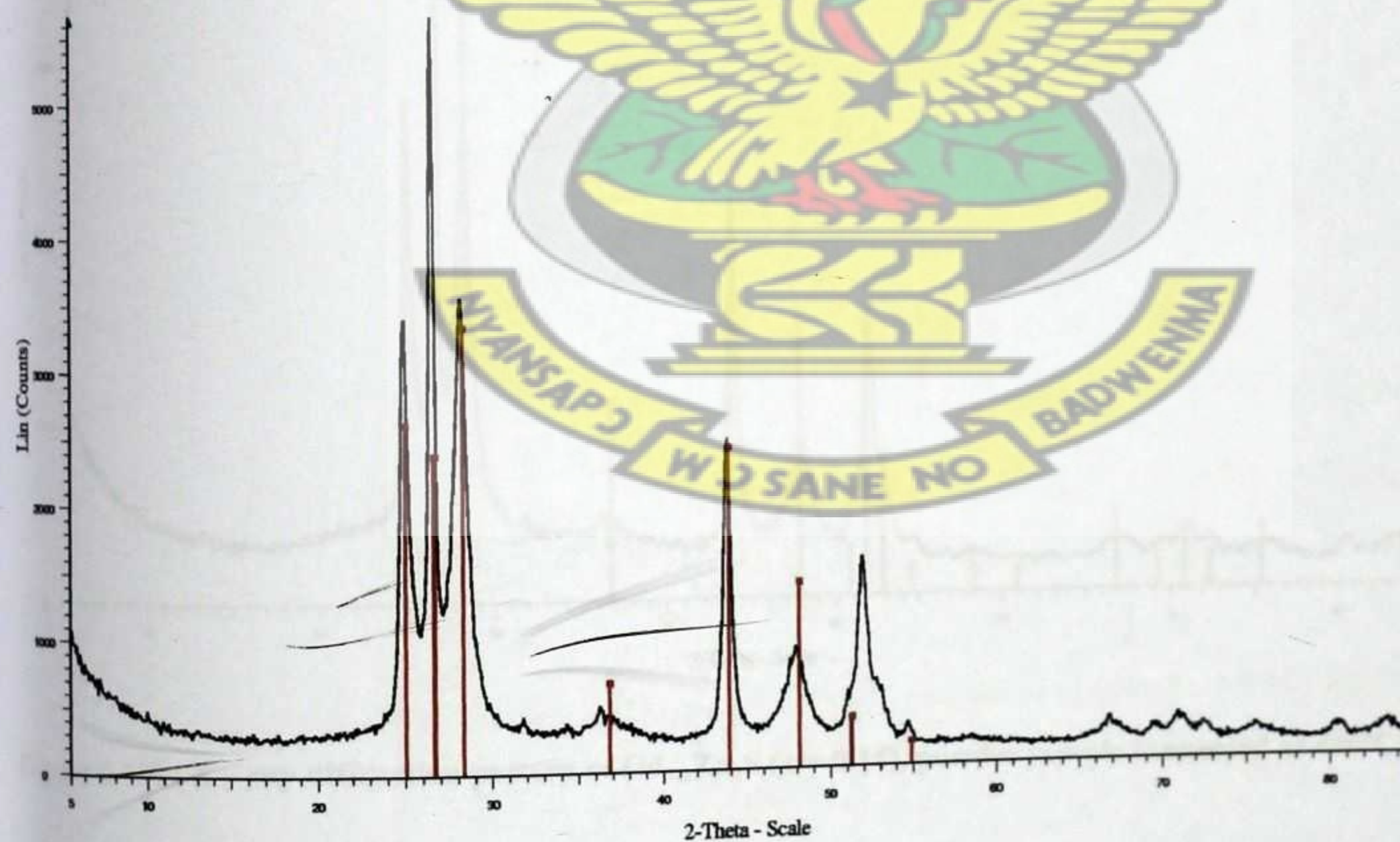


Figure 6.9b: X – ray diffraction pattern of $\text{Cd}_{1-x}\text{Zn}_x\text{S}$ ($x = 0.06$), powder sample (annealed at 400°C)

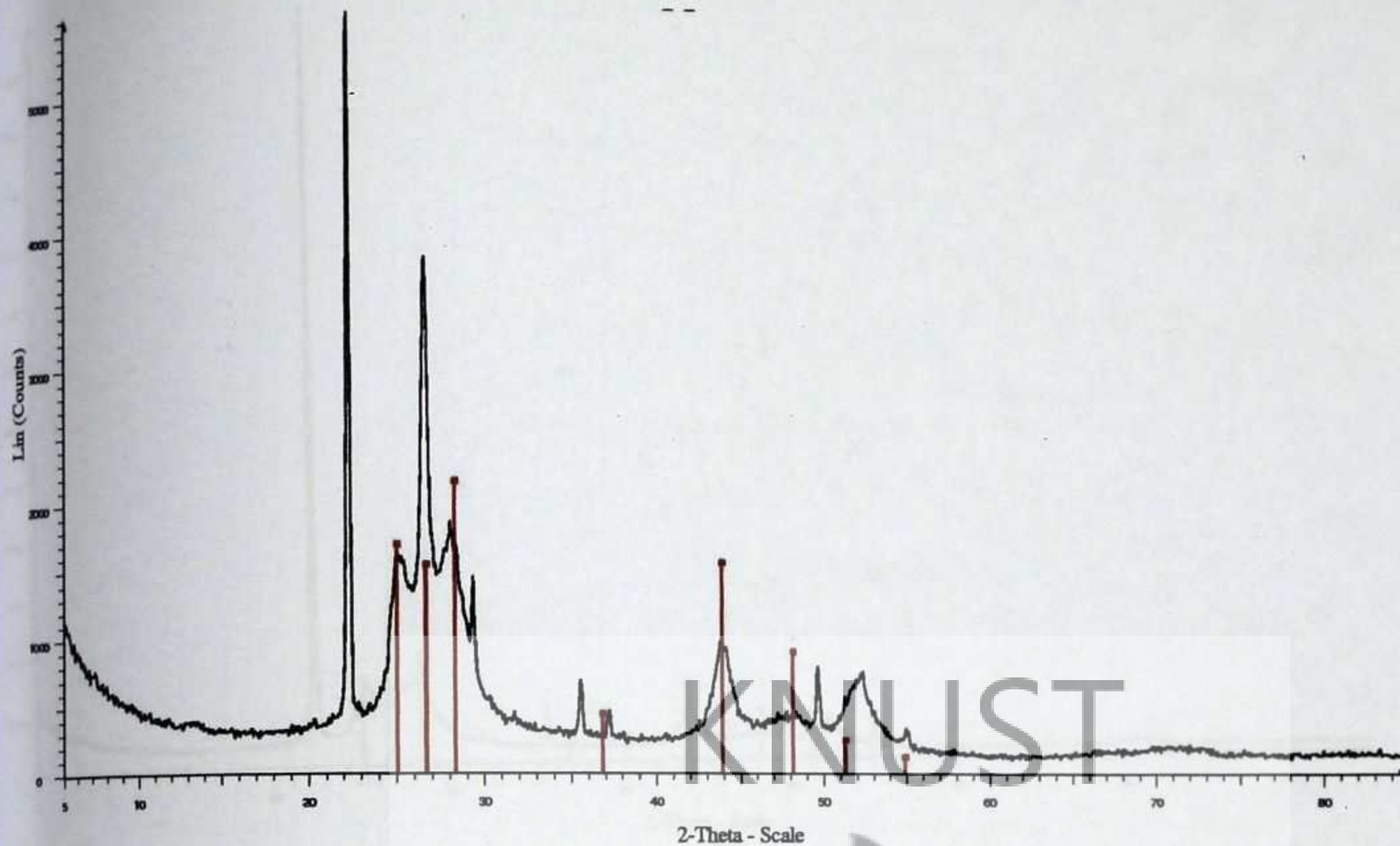


Figure 6.10a: X – ray diffraction pattern of $\text{Cd}_{1-x}\text{Zn}_x\text{S}$ ($x = 0.14$) powder sample (as-deposited)

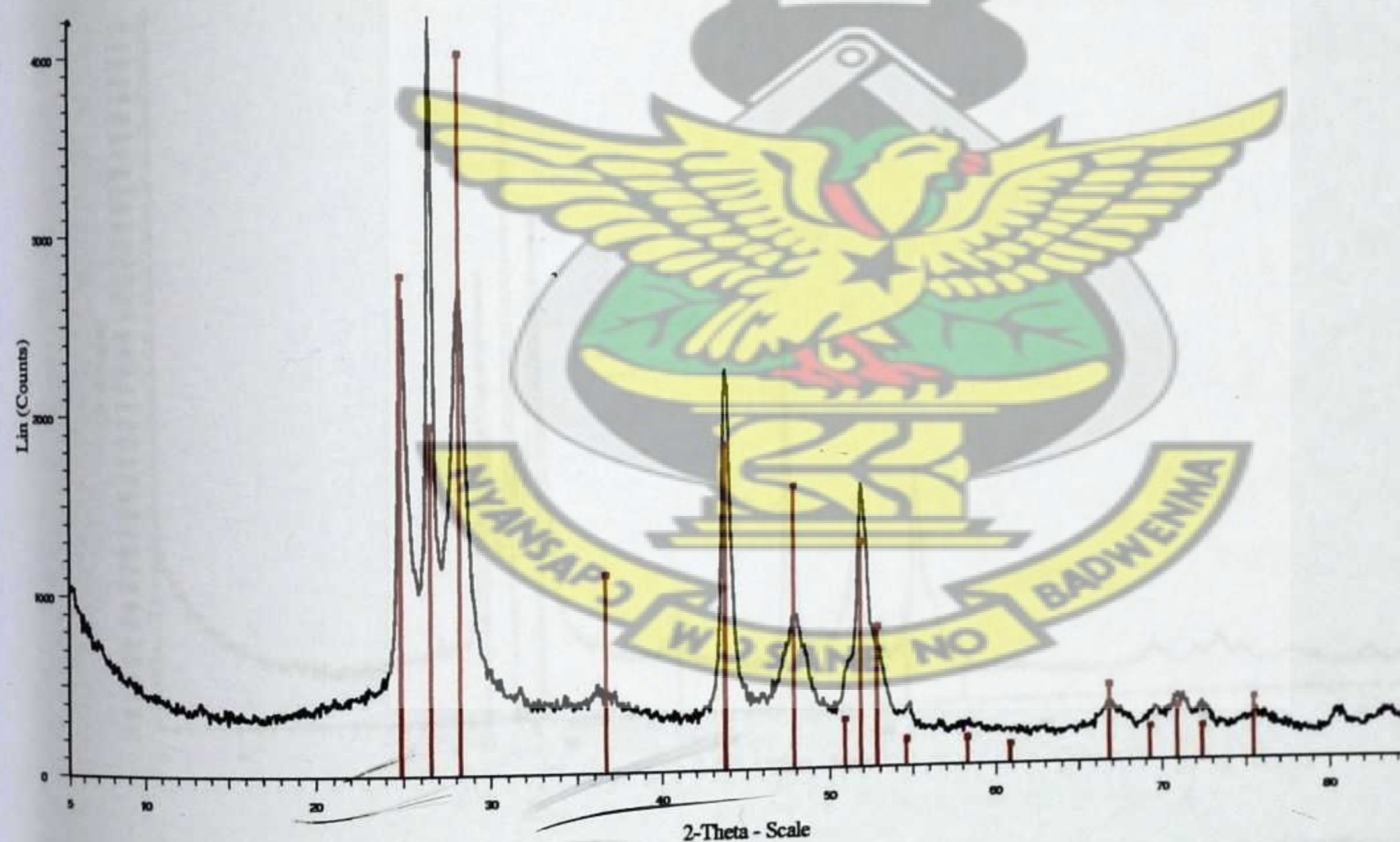


Figure 6.10b: X – ray diffraction pattern of $\text{Cd}_{1-x}\text{Zn}_x\text{S}$ ($x = 0.14$), powder sample (annealed at 400°C)

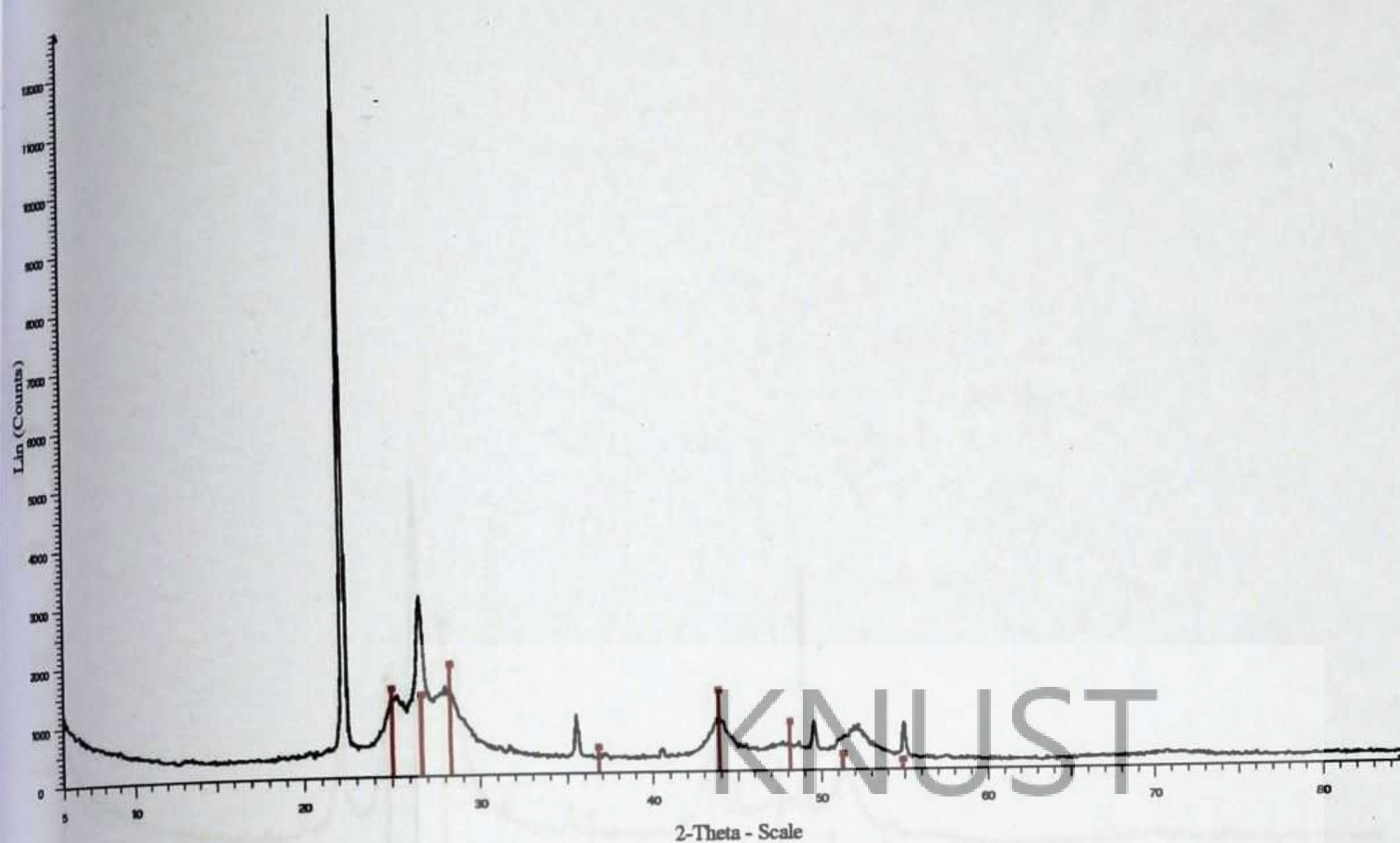


Figure 6.11a: X – ray diffraction pattern of $\text{Cd}_{1-x}\text{Zn}_x\text{S}$ ($x = 0.20$), powder sample (as-deposited)

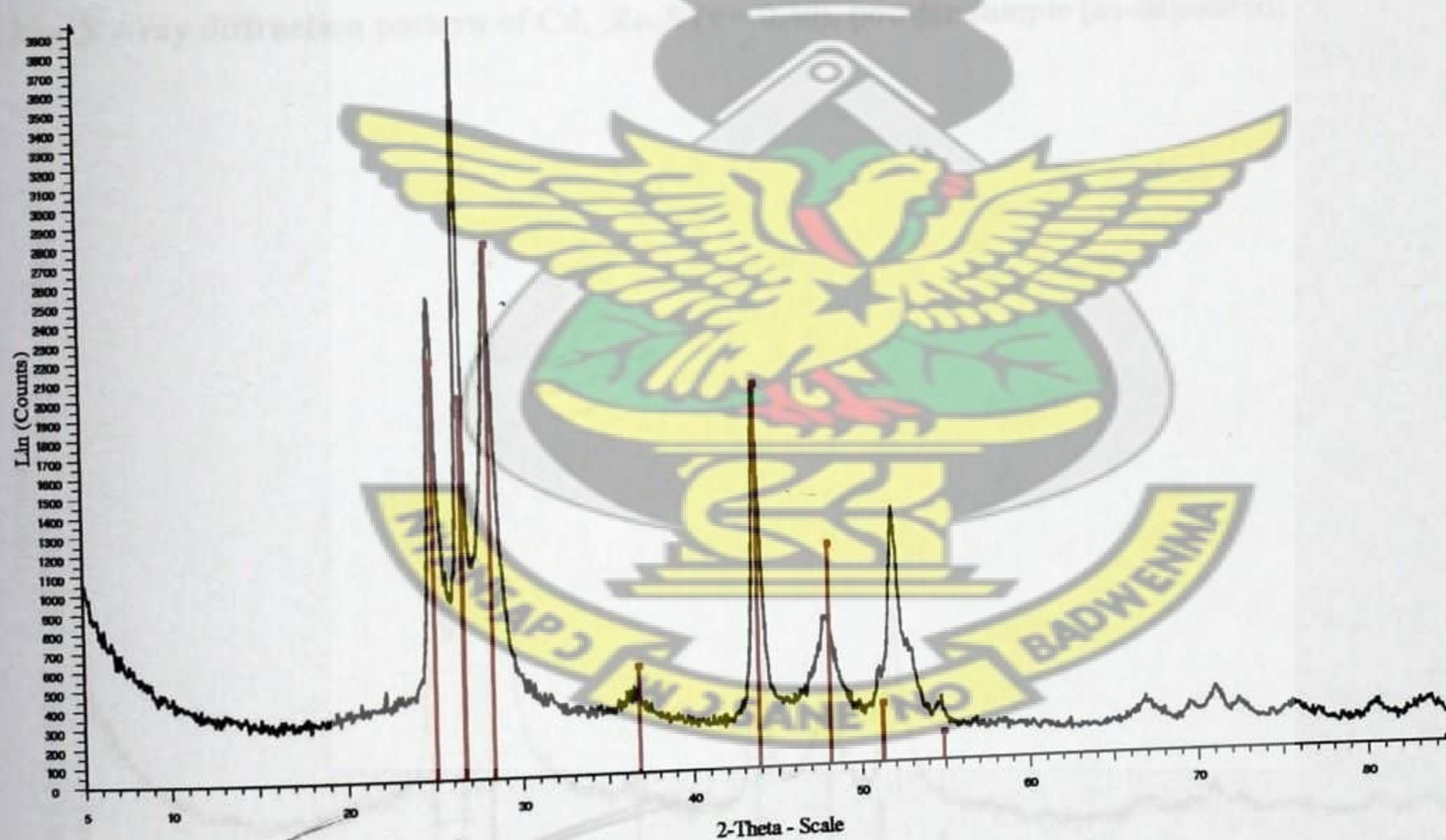


Figure 6.11b: X – ray diffraction pattern of $\text{Cd}_{1-x}\text{Zn}_x\text{S}$ ($x = 0.20$), powder sample (annealed at 400°C)

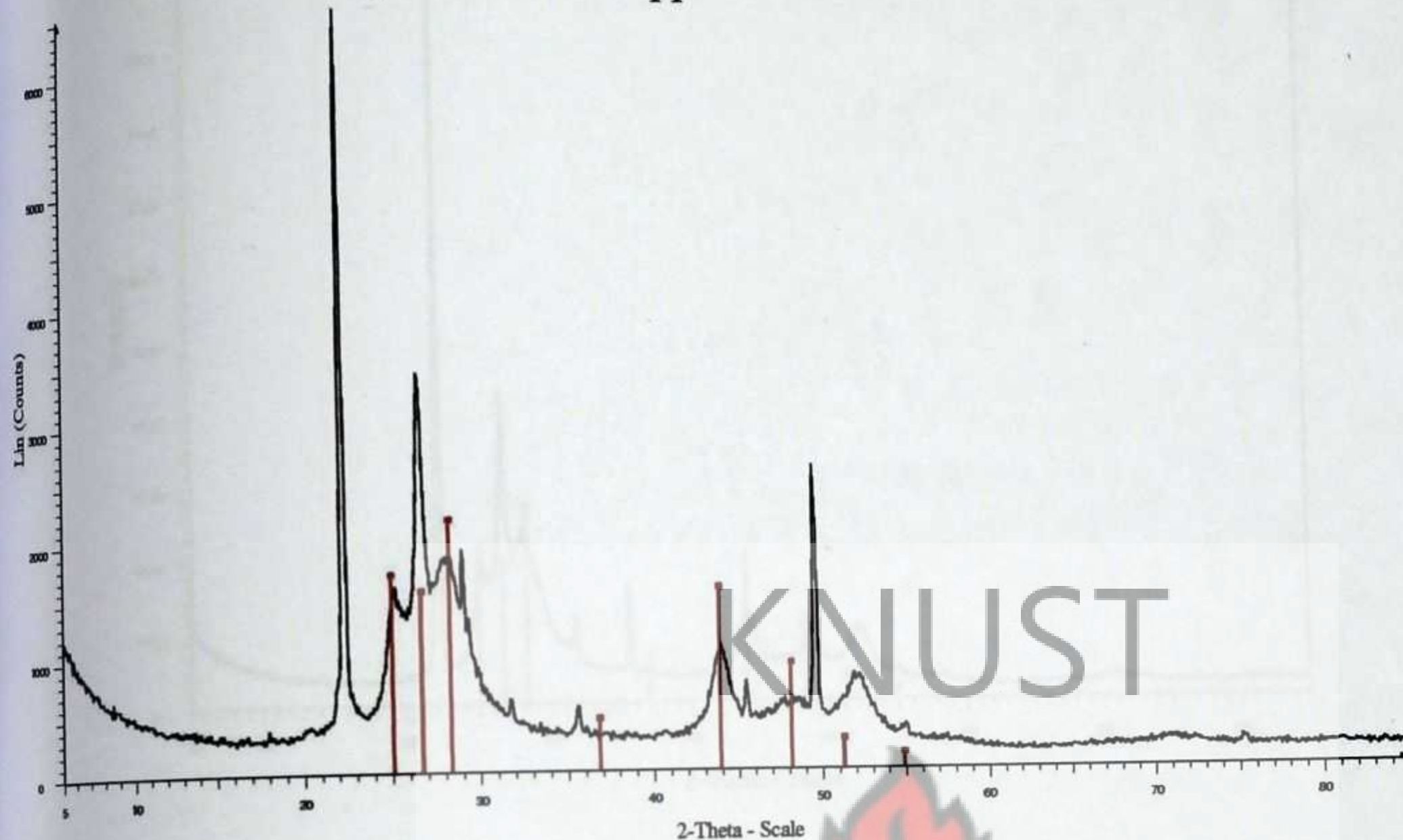


Figure 6.12a: X – ray diffraction pattern of $\text{Cd}_{1-x}\text{Zn}_x\text{S}$ ($x = 0.40$), powder sample (as-deposited)

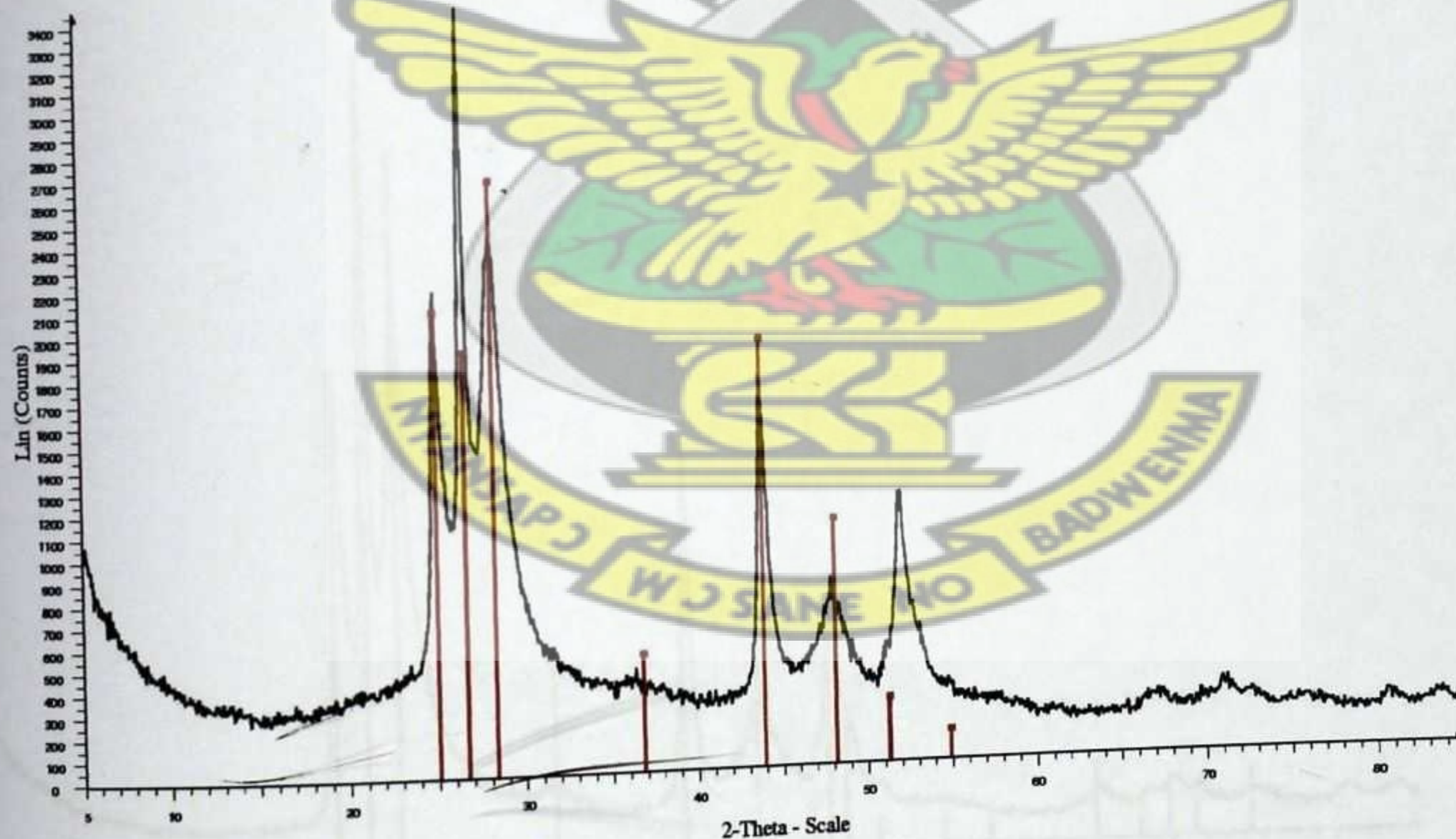


Figure 6.12b: X – ray diffraction pattern of $\text{Cd}_{1-x}\text{Zn}_x\text{S}$ ($x = 0.40$), powder sample (annealed at 400°C)

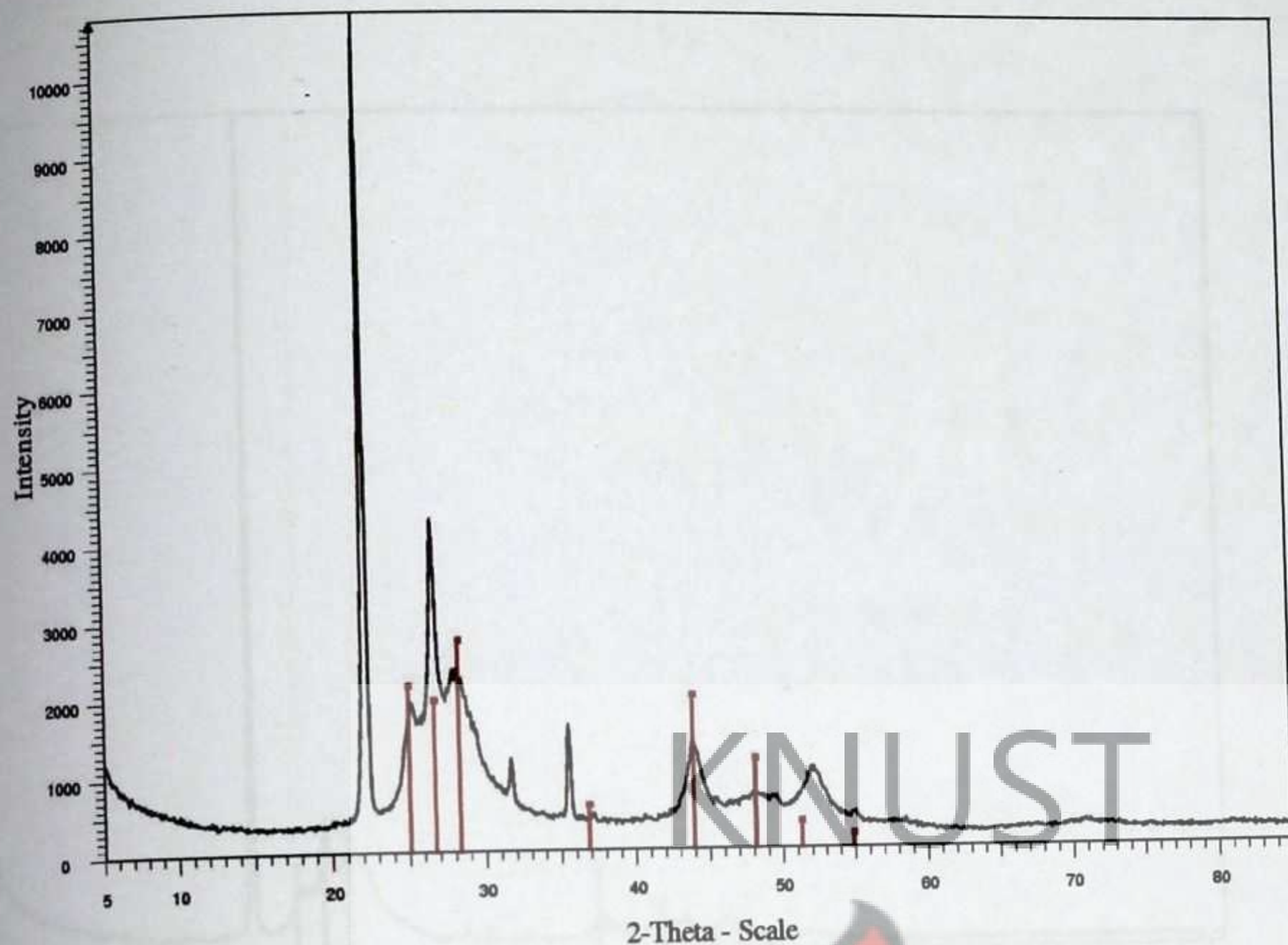


Figure 6.13a: X – ray diffraction pattern of $\text{Cd}_{1-x}\text{Zn}_x\text{S}$ ($x = 0.60$), powder sample (as-deposited)

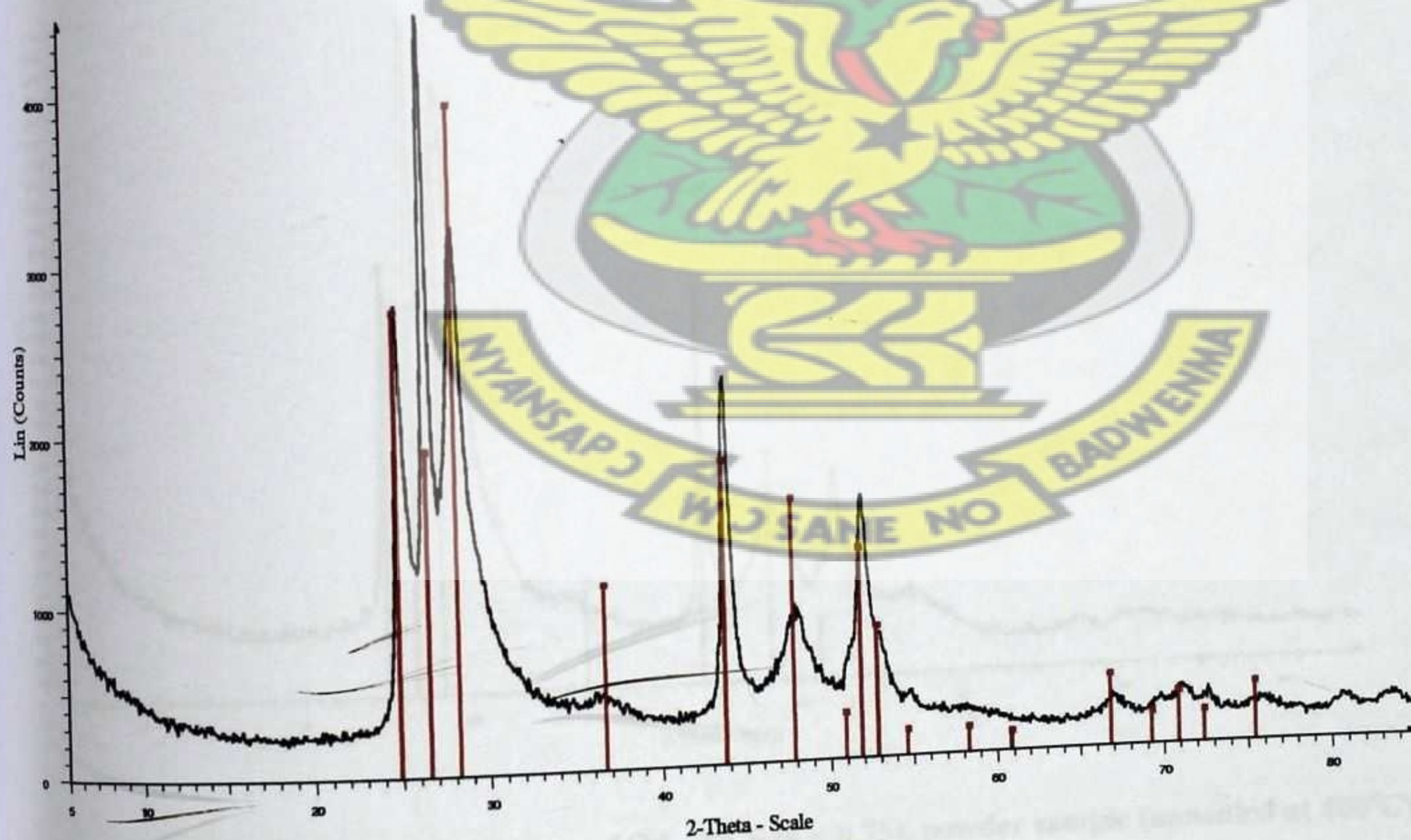


Figure 6.13b: X – ray diffraction pattern of $\text{Cd}_{1-x}\text{Zn}_x\text{S}$ ($x = 0.60$), powder sample (annealed at 400°C)

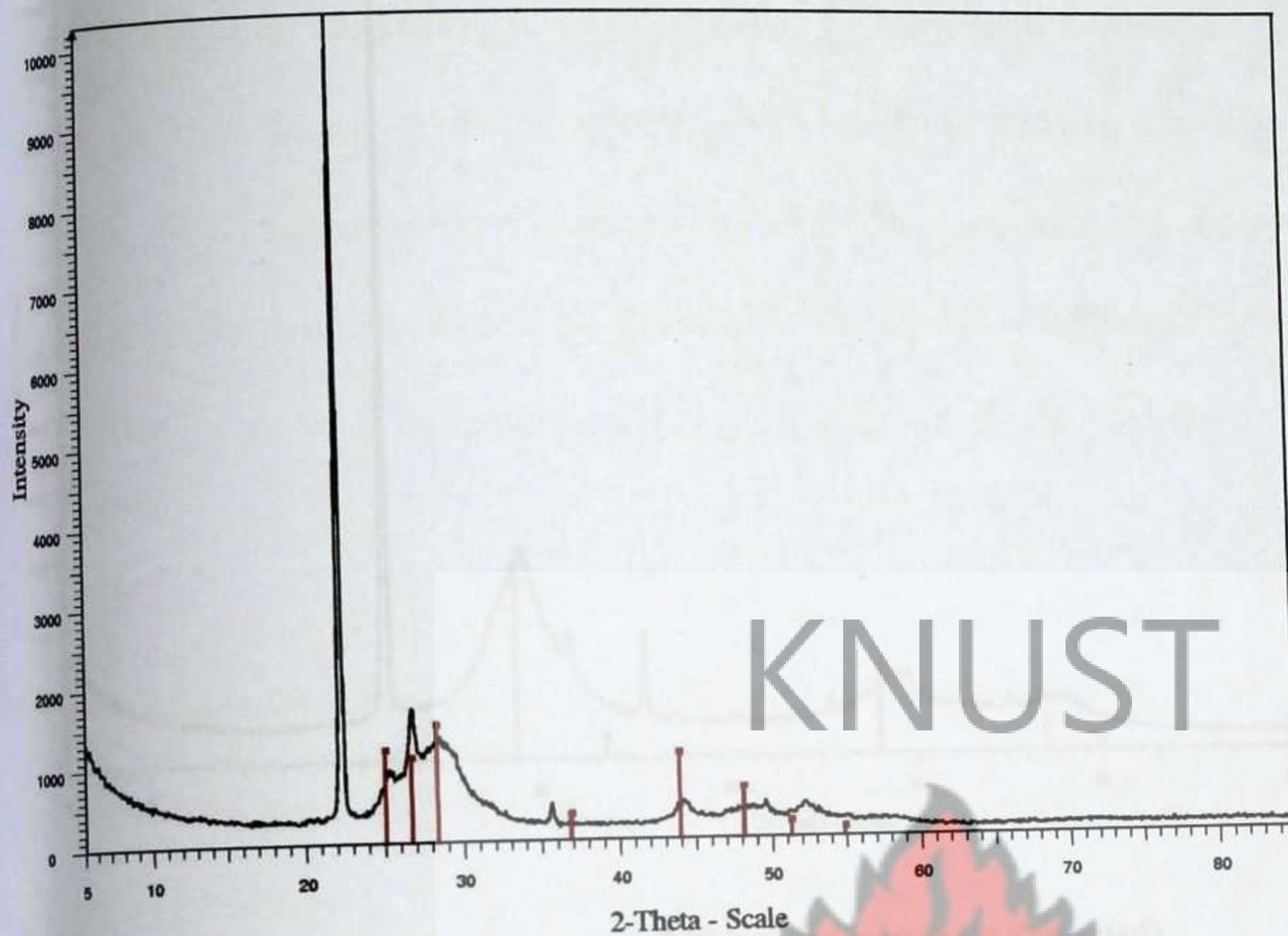


Figure 6.14a: X – ray diffraction pattern of $\text{Cd}_{1-x}\text{Zn}_x\text{S}$ ($x = 0.75$), powder sample (as-deposited)

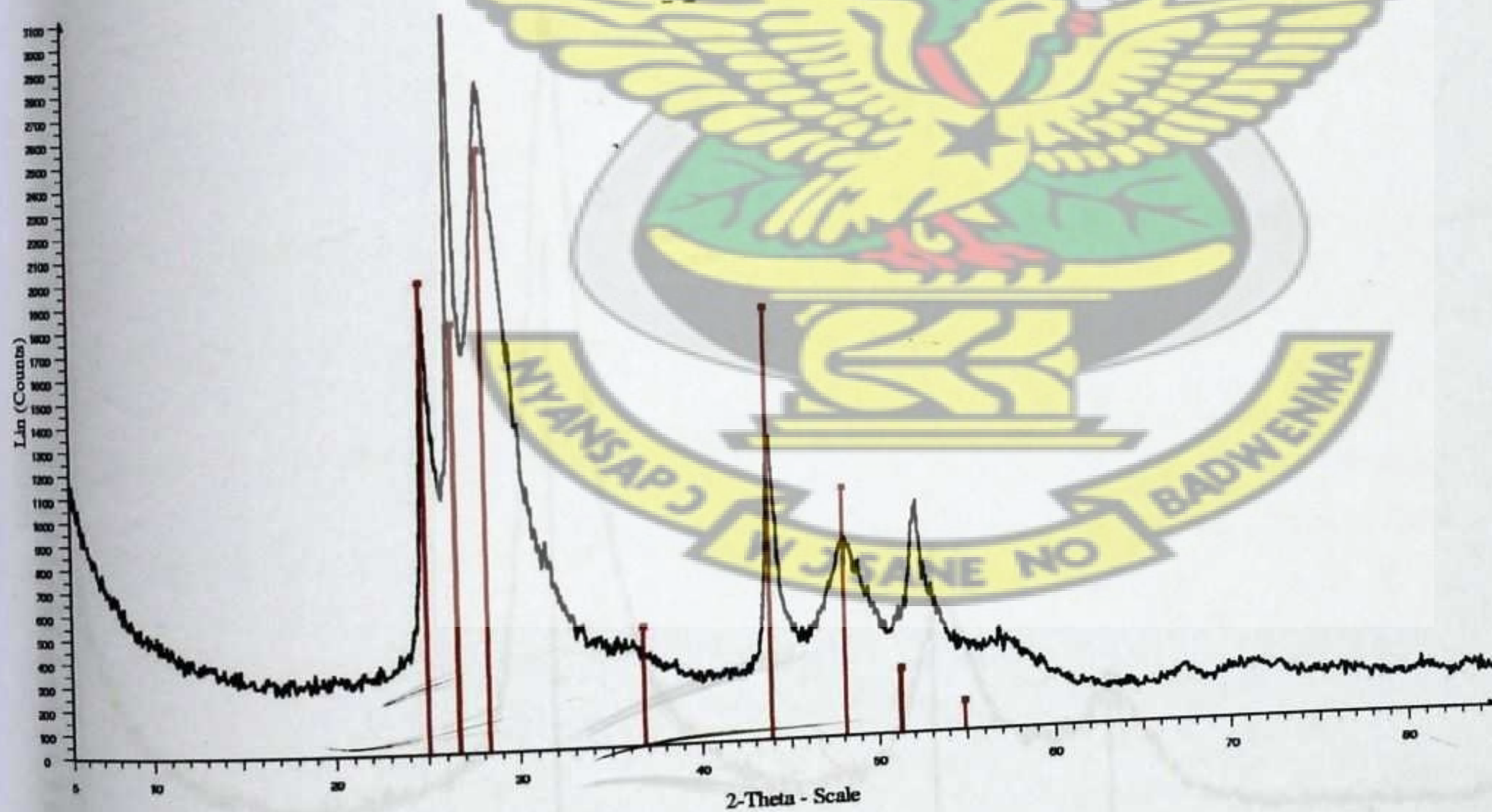


Figure 6.14b: X – ray diffraction pattern of $\text{Cd}_{1-x}\text{Zn}_x\text{S}$ ($x = 0.75$), powder sample (annealed at 400°C)

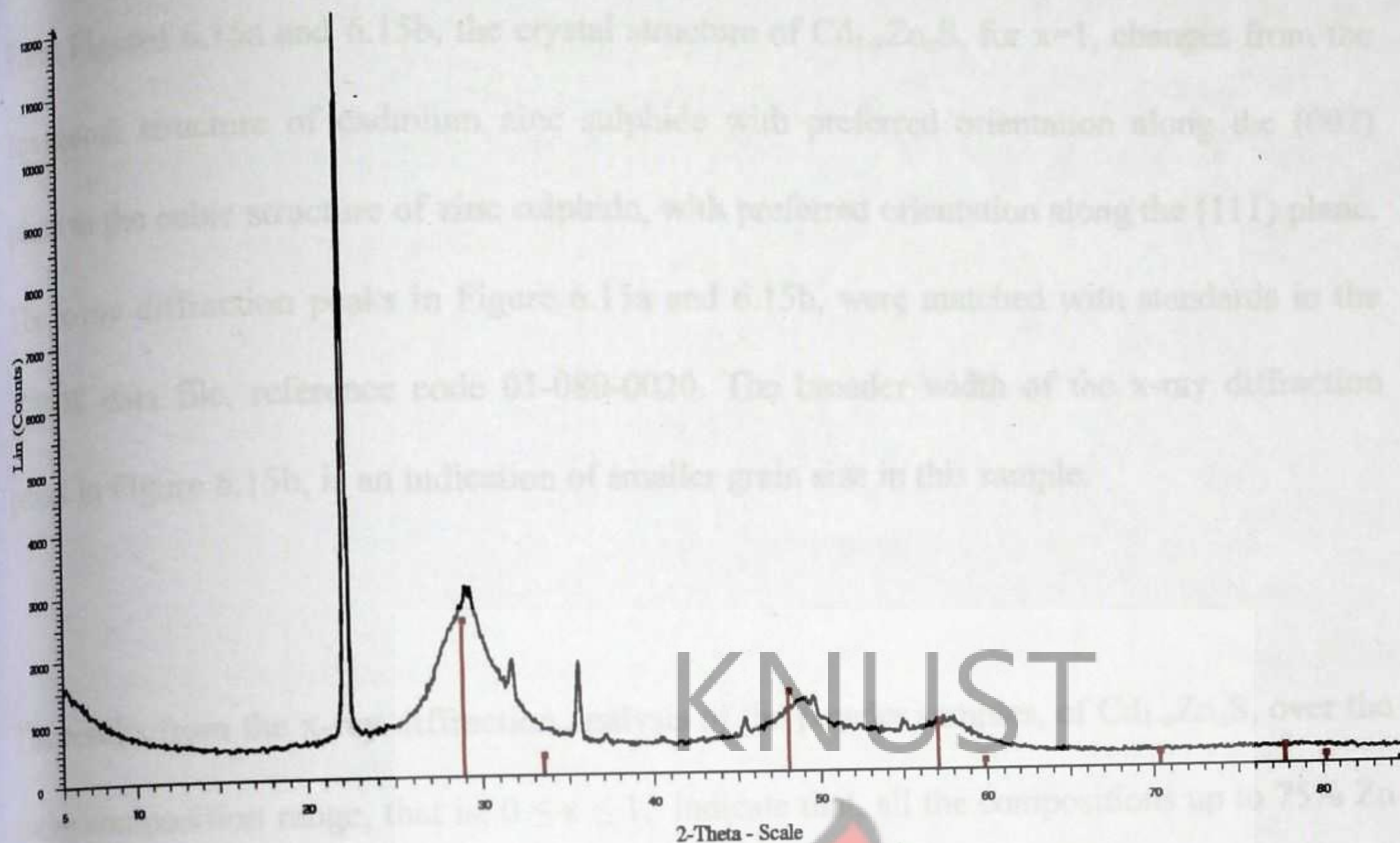


Figure 6.15a: X – ray diffraction pattern of ZnS powder sample (as-deposited)

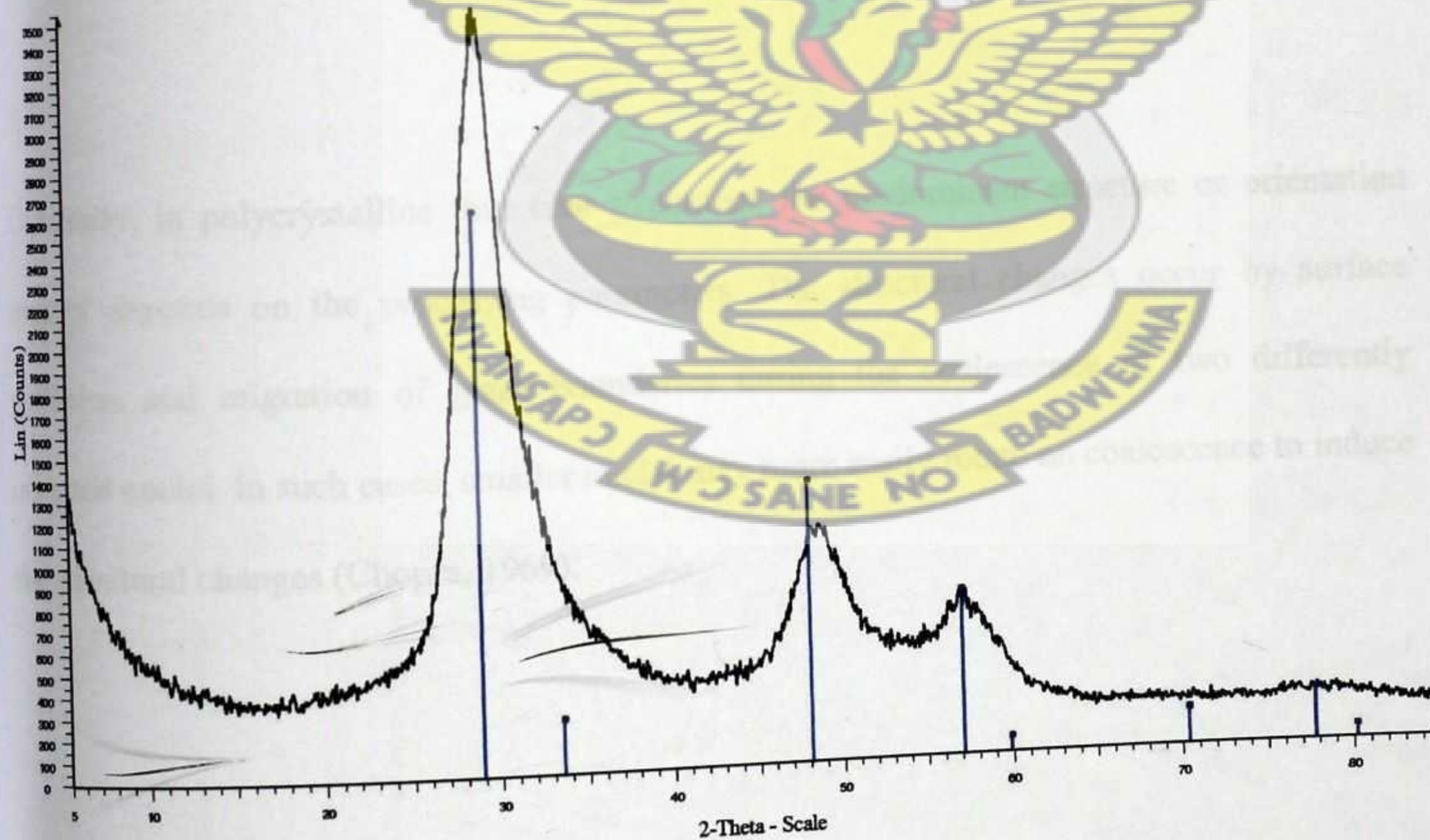


Figure 6.15b: X – ray diffraction pattern of ZnS powder sample (annealed at 400°C)

From Figures 6.15a and 6.15b, the crystal structure of $\text{Cd}_{1-x}\text{Zn}_x\text{S}$, for $x=1$, changes from the hexagonal structure of cadmium zinc sulphide with preferred orientation along the (002) plane to the cubic structure of zinc sulphide, with preferred orientation along the (111) plane. The x-ray diffraction peaks in Figure 6.15a and 6.15b, were matched with standards in the JCPDS data file, reference code 01-080-0020. The broader width of the x-ray diffraction peaks in Figure 6.15b, is an indication of smaller grain size in this sample.

The results from the x-ray diffraction analysis of the powder samples, of $\text{Cd}_{1-x}\text{Zn}_x\text{S}$, over the entire composition range, that is, $0 \leq x \leq 1$, indicate that, all the compositions up to 75% Zn have wurtzite structure, while ZnS has the spalerite structure. These observations compare favourably well with reports by Cherin *et al.* (1970), discussed in section 2.3.3, as well as that of several authors, discussed in the literature review.

Generally, in polycrystalline thin film structures, the predominant structure or orientation mainly depends on the processing parameters. The structural changes occur by surface diffusion and migration of grain boundaries during the coalescence of two differently oriented nuclei. In such cases, smaller nuclei may more easily rotate on coalescence to induce the structural changes (Chopra, 1969).

6.3 GRAIN SIZE

The average grain size (D) has been obtained from the XRD patterns using the Scherrer (1918), formula which is given as:

$$D = \frac{K\lambda}{\beta \cos \theta}$$

where,

K = constant dependent on crystallite shape, and in the absence of detailed shape information,

$K = 0.9$ is a good approximation (Klug and Alexander, 1974; Cullity, 1978)

λ = wavelength of X-ray used (1.542\AA),

β = FWHM (full width at half max) or integral breadth of the preferred x-ray diffraction peak

θ = Bragg's angle.

The average grain size of the as deposited samples varied from 12 nm for CdS to 8 nm for ZnS. After annealing at 400°C for two hours the grain size for CdS did not change however, the grain size for ZnS reduced to 4 nm. A similar grain size for ZnS has been reported by Sanap and Pawar (2011).

The D value calculated for (hkl) peak should be understood as mean crystallite size in the direction that is perpendicular to the (hkl) plane (Hodes, 2002).

6.4. VARIATION OF LATTICE PARAMETERS WITH ZINC ION CONCENTRATION

From the XRD patterns, it can be observed that the diffraction angle of (002) plane shifts towards higher angle with an increase in Zn content which means that the lattice parameter of the unit cell decreases (Gaewdang and Wongcharoen, 2007).

The lattice parameter, d , which is the spacing between the crystal planes has been plotted as a function of zinc ion concentration for the (002) plane, where d , was determined from the Bragg diffraction law as follows:

$$2d_{002} \sin \theta = \lambda$$

In the Brucker D8 diffractometer, the wavelength, λ is fixed (1.5402 Å), hence knowing 2θ , corresponding to the peak position of the 002 plane for each zinc alloy concentration, the lattice parameter, d , can be determined as;

$$d_{002} = \frac{1.5402 \text{ Å}}{2 \sin \theta}$$

The variation of lattice parameter, d , with increasing zinc mole ratio in the thin films, is shown in Figure 6.16

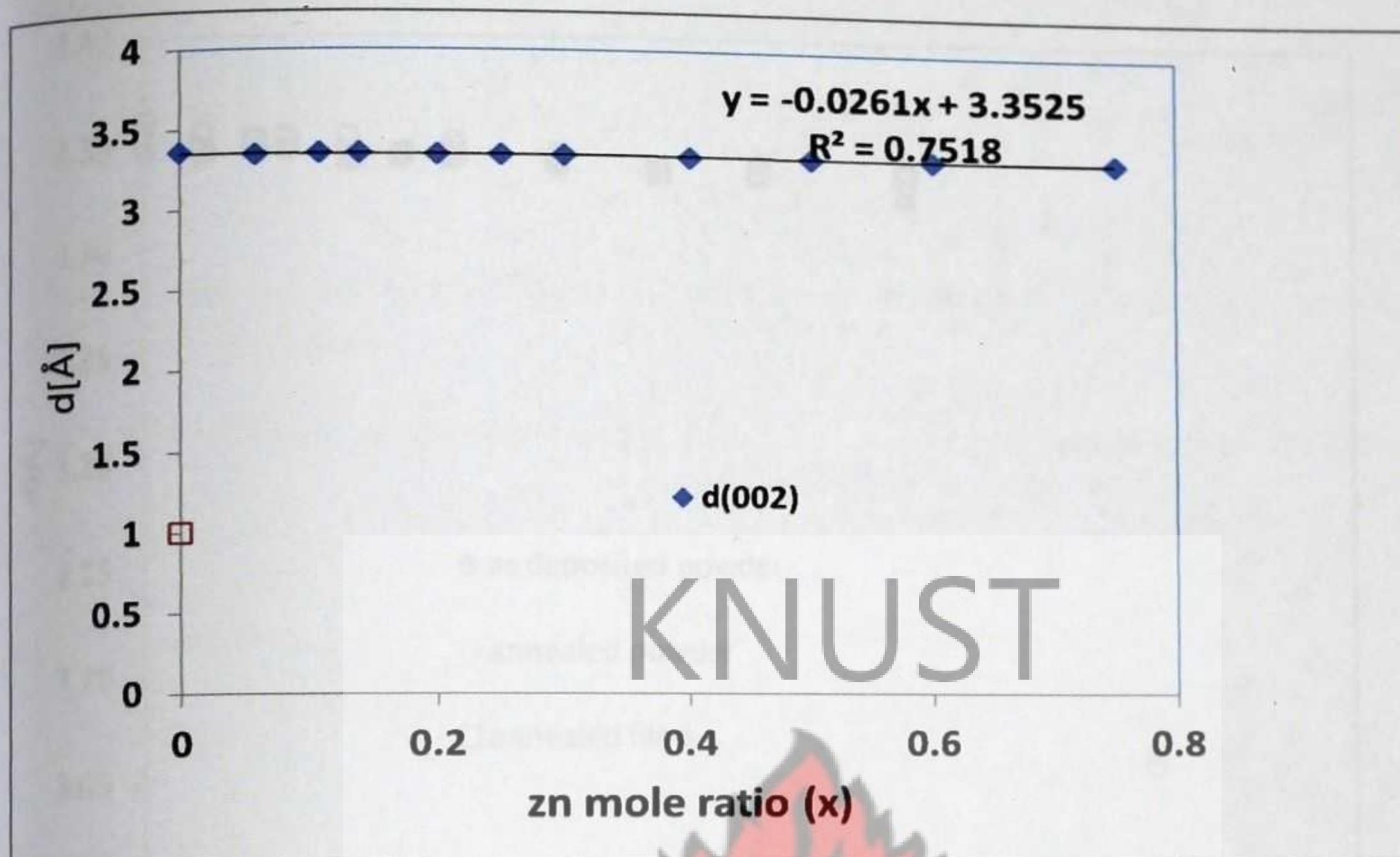


Figure 6.16 : Variation of lattice parameter, d , with increasing zinc ion concentration

From Figure 6.16, the lattice parameter, d , varies linearly with zinc ion concentration (x), from 3.36 Å to 3.337 Å for $0 \leq x \leq 0.75$. This linear variation can be explained on the basis of Vergard's law; The law states that the crystallographic parameters of a continuous substitutional solid solution vary linearly with concentration at constant temperature when the nature of the bonding is similar in the constituent phases (Vergard, 1921; Vergard, 1928).

A similar observation can be made with the powder samples as shown in Figure 6.17.

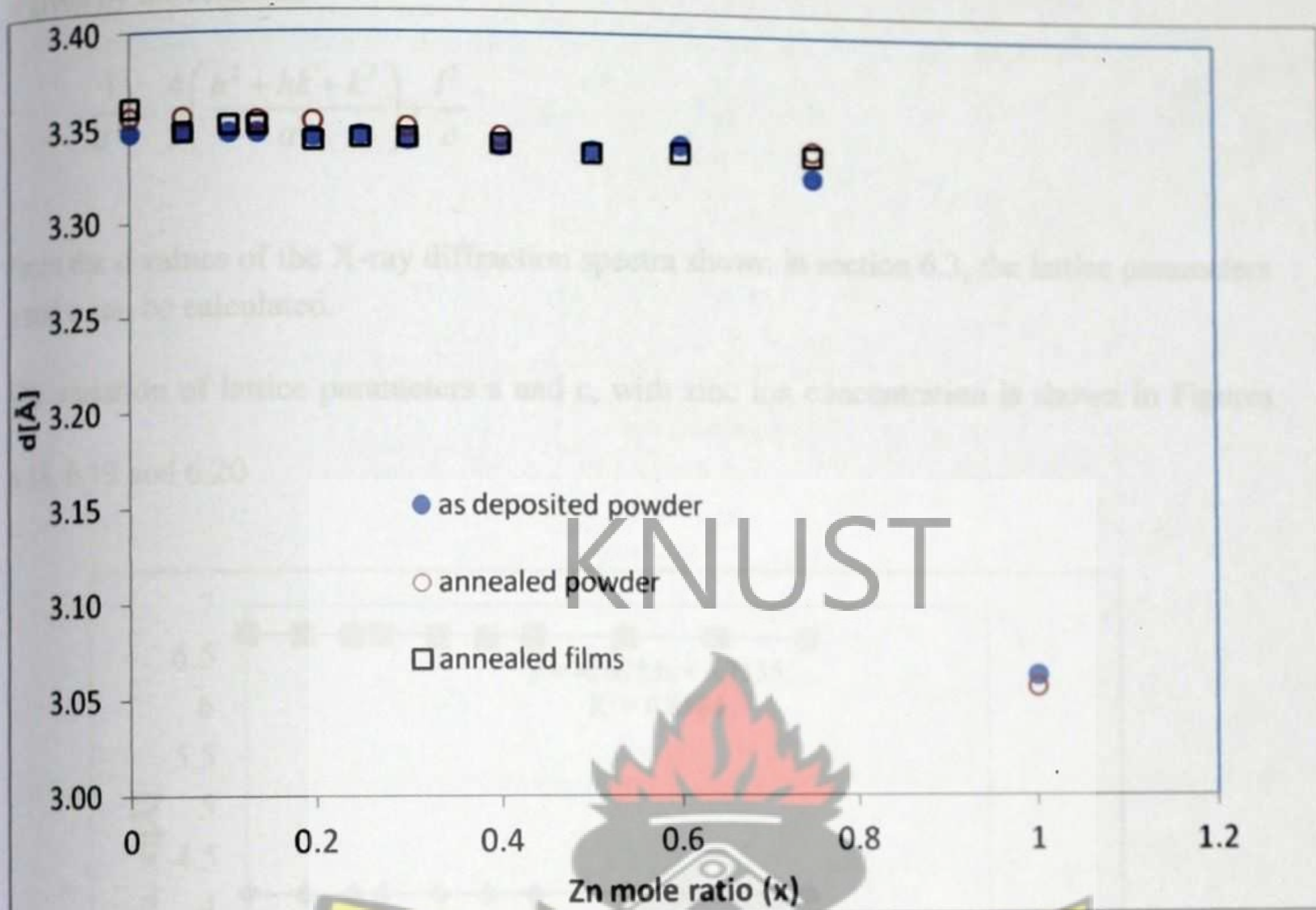


Figure 6.17: Variation of lattice parameter, d , with zinc ion concentration for thin films and powder samples.

It can be observed from Figure 6.17, that both thin films and powder samples show almost the same variation of the lattice parameter, d , with zinc ion composition, suggesting that the powder samples and thin films have similar composition and crystal structure. The abrupt change in d , for $x = 1$, is as a result of the change in crystal structure from the hexagonal structure of CdZnS with preferred orientation along the (002) plane to the cubic structure of ZnS with preferred orientation along the (111) plane.

The relation between the d-spacing and lattice parameters a and c for the hexagonal structure is given by the relation:

$$\frac{1}{d^2} = \frac{4}{3} \left(\frac{h^2 + hk + k^2}{a^2} \right) + \frac{l^2}{c^2}$$

From the d values of the X-ray diffraction spectra shown in section 6.3, the lattice parameters a and c can be calculated.

The variation of lattice parameters a and c , with zinc ion concentration is shown in Figures 6.18, 6.19 and 6.20

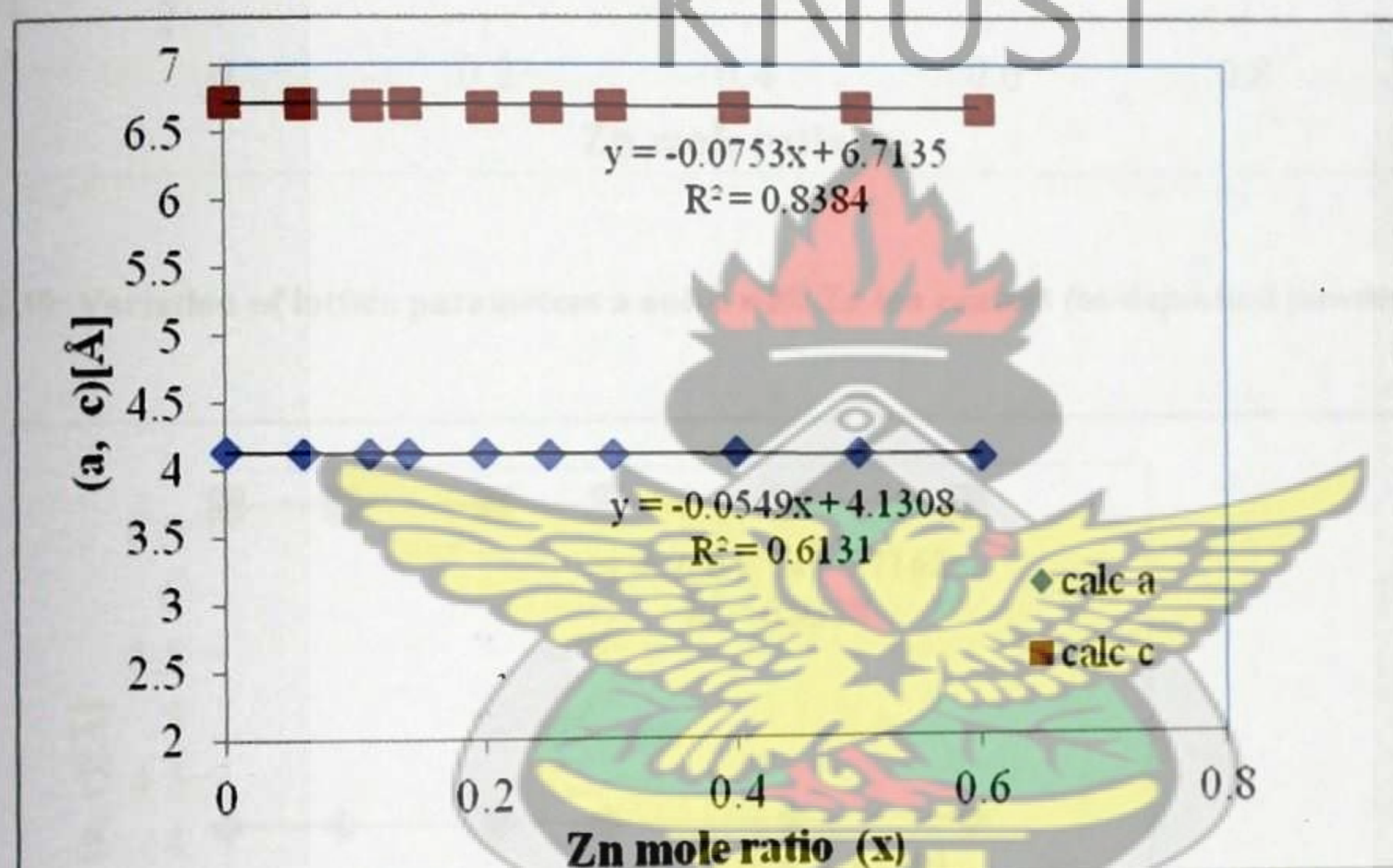


Figure 6.18: Variation of lattice parameters a and c with Zn ion content (annealed thin films).

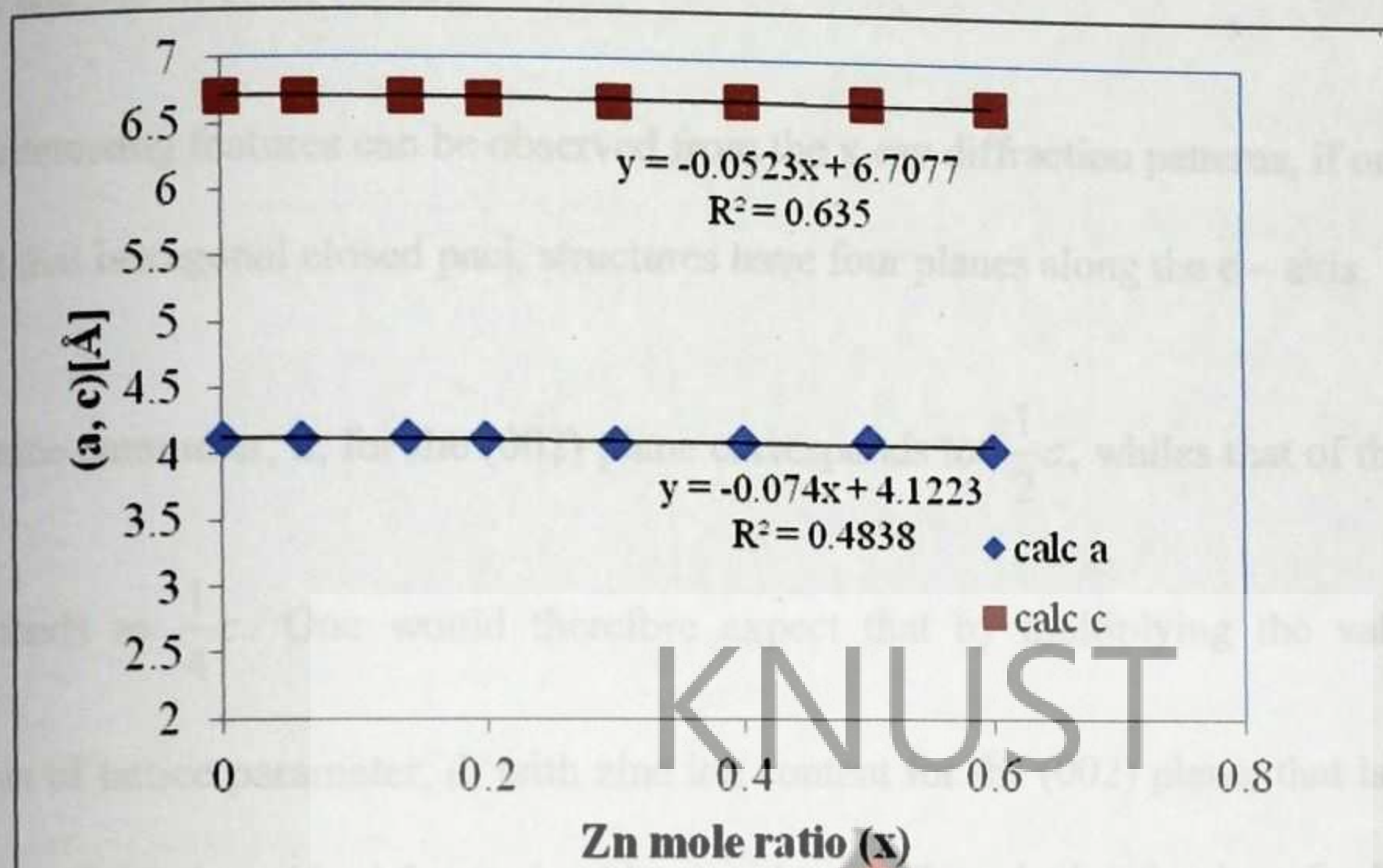


Figure 6.19: Variation of lattice parameters a and c with Zn ion content (as-deposited powder samples).

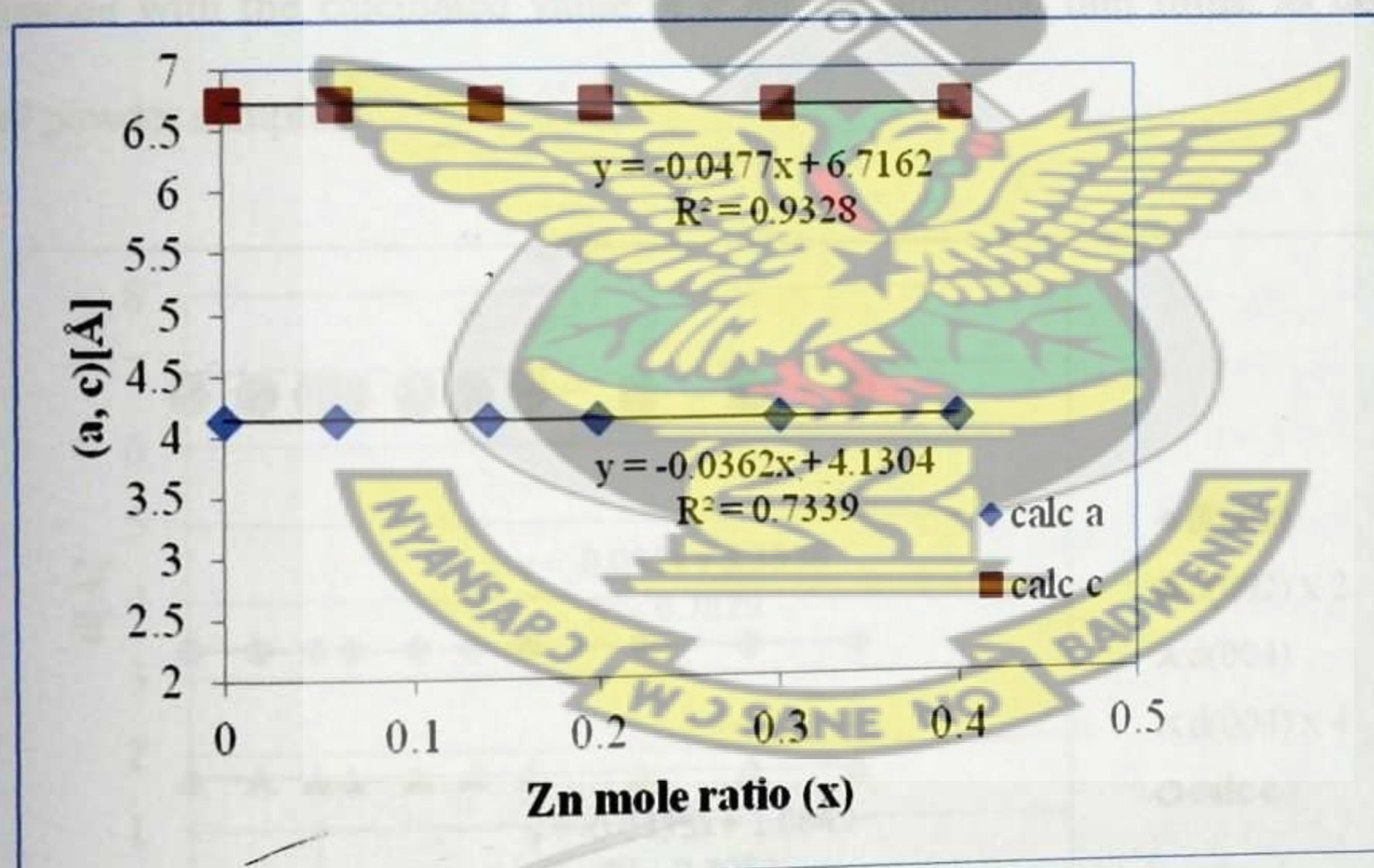


Figure 6.20: Variation of lattice parameters a and c with Zn ion content (annealed powder samples).

From Figures 6.18 to 6.20, the lattice parameters a and c , decreased with increasing Zn content. Similar variations in lattice parameters a and c with increasing zinc content, have

been reported by Morris and Vanderveen (1992), Kane *et al.* (1966), Burton and Hench (1976), and Mbow *et al.* (1982).

Some interesting features can be observed from the x-ray diffraction patterns, if one considers the fact that hexagonal closed pack structures have four planes along the c – axis.

The lattice parameter, d , for the (002) plane corresponds to $\frac{1}{2}c$, while that of the 004 plane corresponds to $\frac{1}{4}c$. One would therefore expect that by multiplying the values for the variation of lattice parameter, d , with zinc ion content for the (002) plane, that is, (d_{002}) by 2 and for the 004 plane (d_{004}) by 4, should coincide with the calculated value of c (calc c). This relation can be observed in Figures 6.18, 6.19, and 6.20 where the values for $d_{002} \times 2$ and $d_{004} \times 4$, coincide with the calculated value of c for the annealed thin films, as deposited and annealed powder samples.

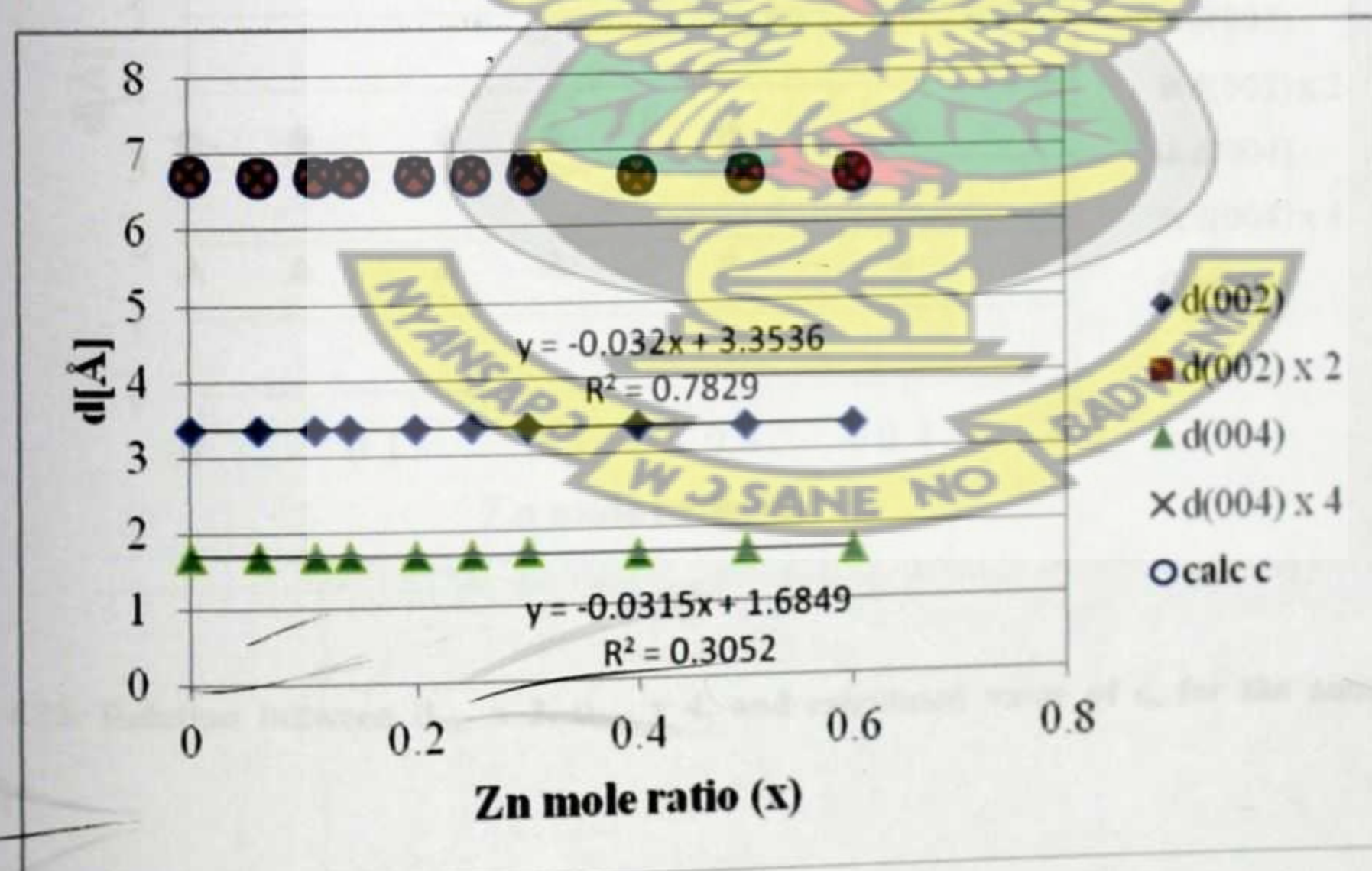


Figure 6.21: Relation between $d_{002} \times 2$, $d_{004} \times 4$, and calculated value of c , for the annealed thin films

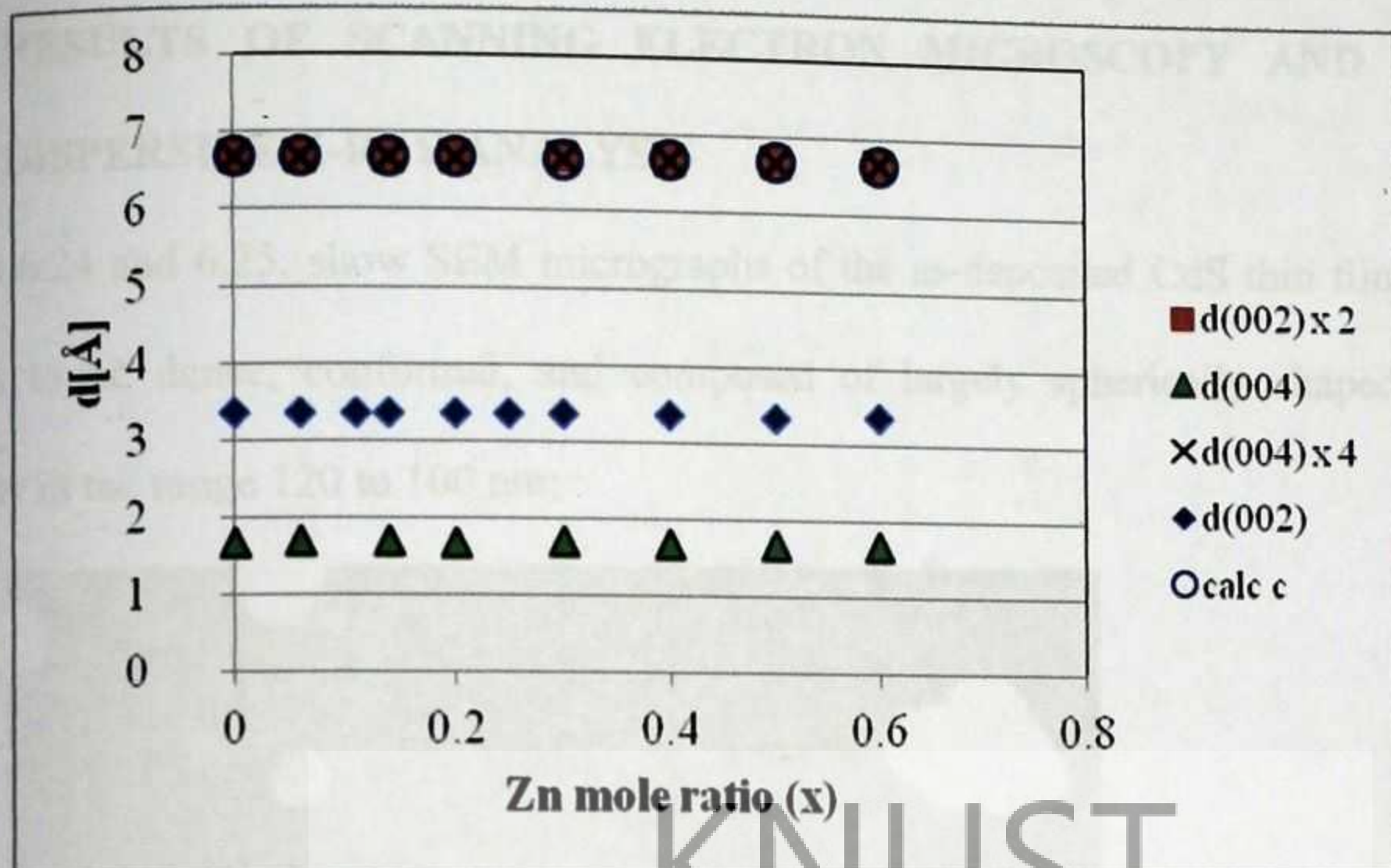


Figure 6.22: Relation between $d_{002} \times 2$, $d_{004} \times 4$, and calculated value of c , for the as-deposited powder samples

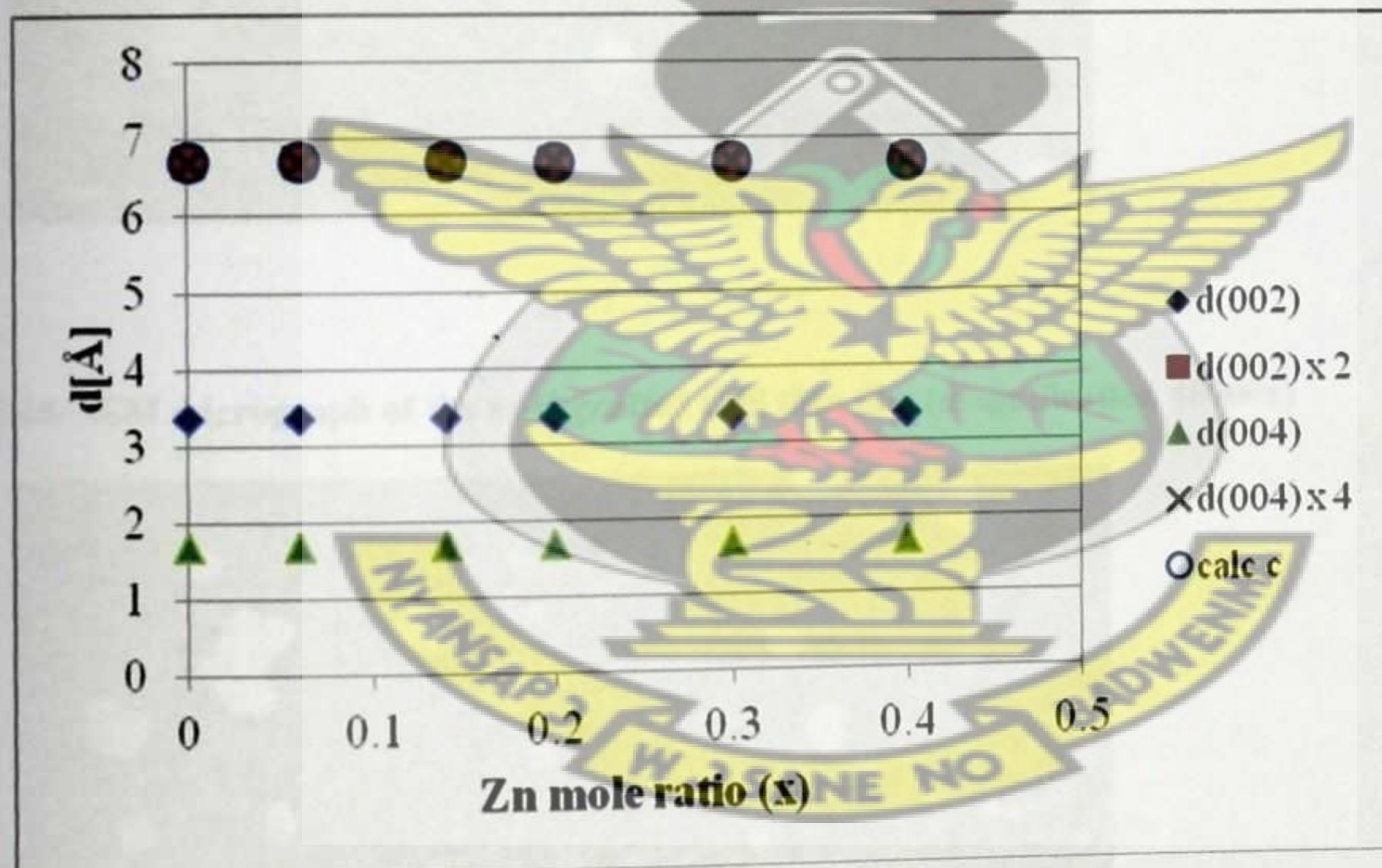


Figure 6.23: Relation between $d_{002} \times 2$, $d_{004} \times 4$, and calculated value of c , for the annealed powder samples

6.5. RESULTS OF SCANNING ELECTRON MICROSCOPY AND ENERGY DISPERSIVE X-RAY ANALYSIS

Figures 6.24 and 6.25, show SEM micrographs of the as-deposited CdS thin film. The film appears to be dense, conformal, and composed of largely spherically shaped grains of diameter in the range 120 to 100 nm;

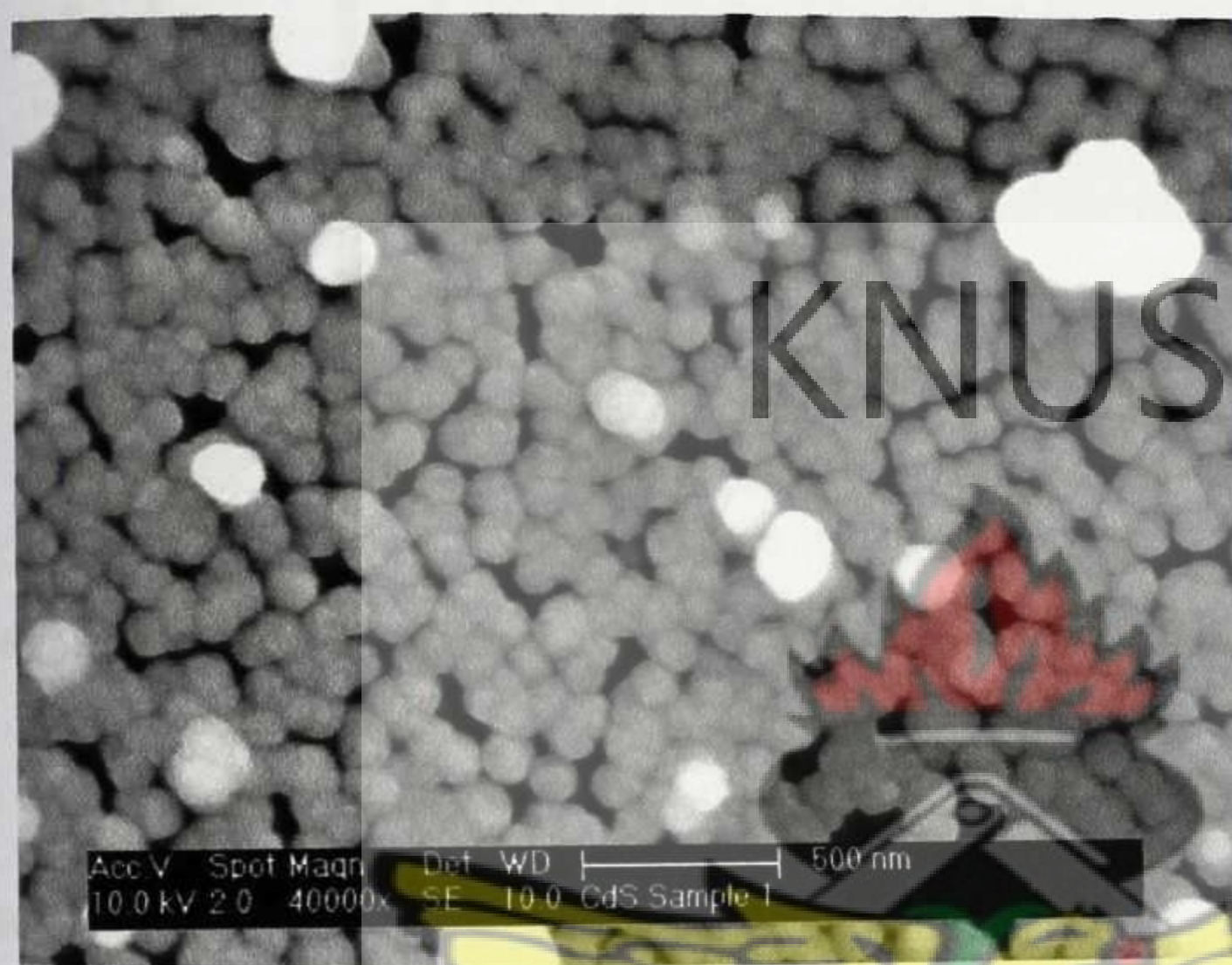


Figure 6.24: SEM micrograph of the as-deposited CdS thin film (magnification 40000x)

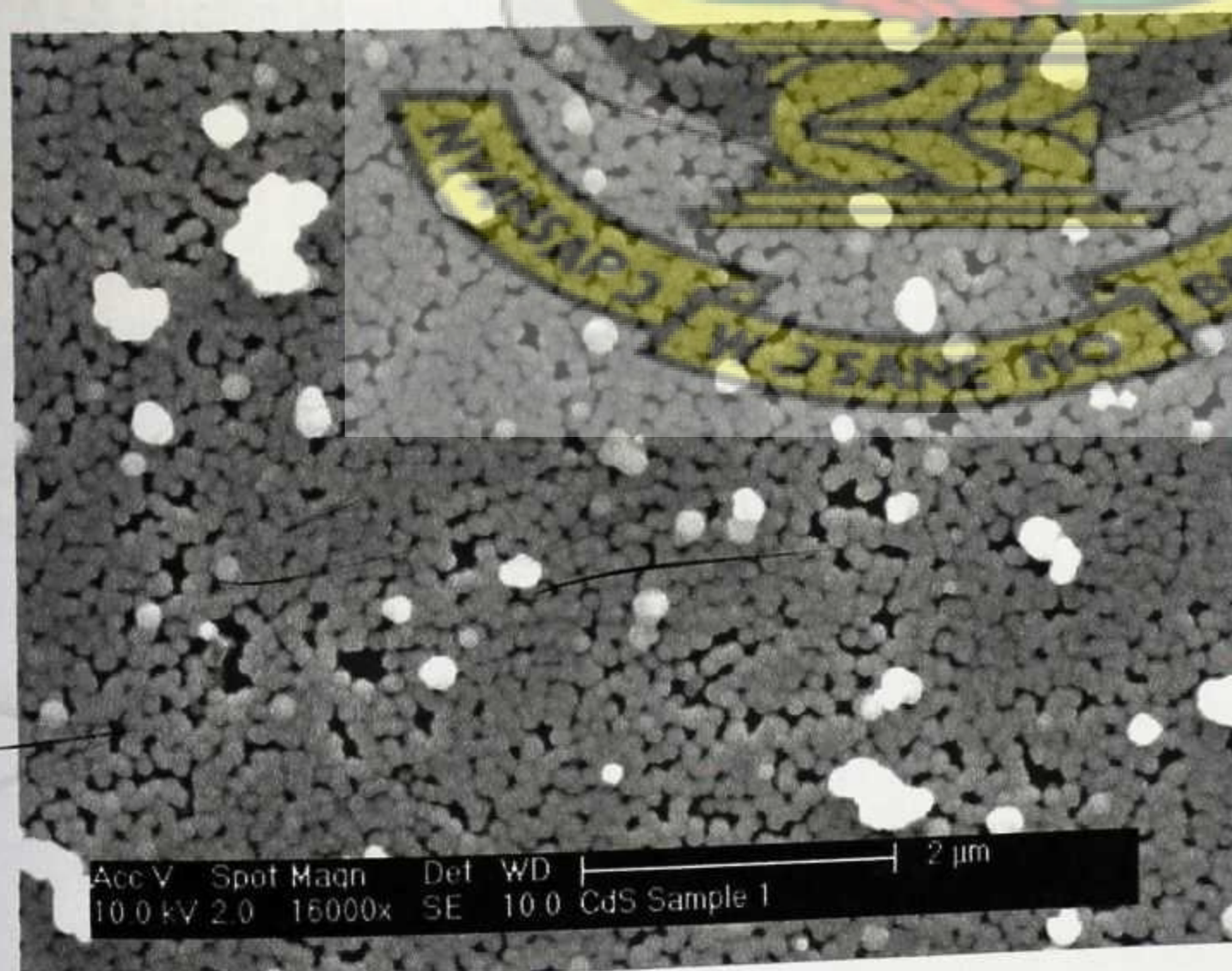


Figure 6.25: SEM micrograph of the as-deposited CdS thin film (magnification 16000x)

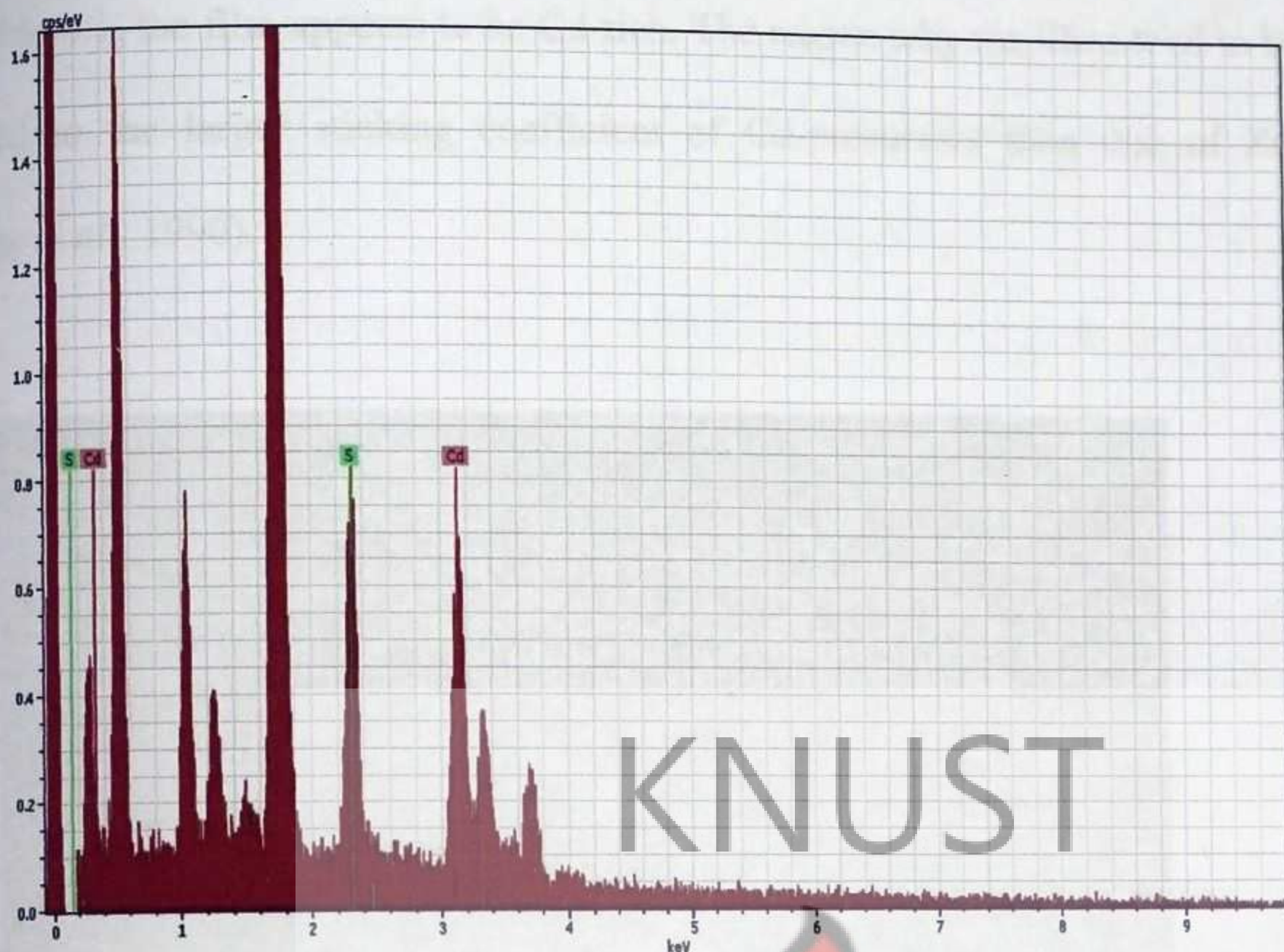


Figure 6.26: EDX spectrum of the as-deposited CdS thin film

Figure 6.26 shows the EDX spectrum of the as-deposited CdS thin film and table 6.1 gives the relative elemental ratios of Cd and S.

Table 6.1: Summary of the EDX results for the as-deposited CdS thin film

Bruker AXS Microanalysis GmbH, Germany			29/09/2011	
Quantax				
Element	series	[wt.-%]	[norm. wt.-%]	[norm. at.-%]
Cadmium	L-series	62.66319	83.55541	59.17384
Sulphur	K-series	12.33278	16.44459	40.82616
Sum:		74.99598	100	100

From table 6.1, the film appears to be Cd-rich. The reason why the films tend to be Cd-rich is attributed to the larger sticking coefficient of Cd-precursors than that of Zn-precursors (Yamaga *et al.*, 1990).

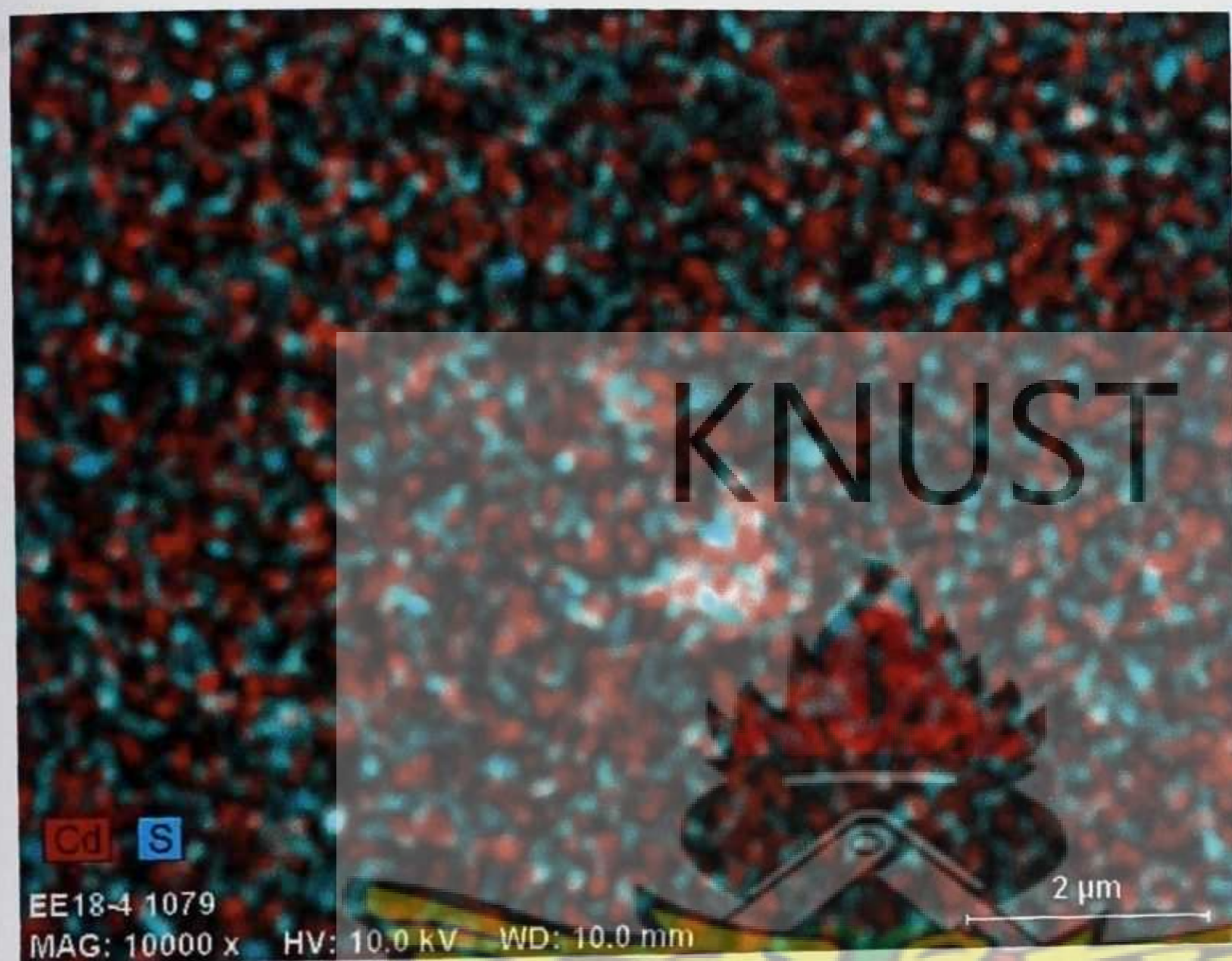


Figure 6.27: EDX elemental mapping of the as-deposited CdS Thin film

The EDX elemental mapping of the as-deposited CdS thin film is shown in Figure 6.27. From the Figure, the film appears to be uniform and homogenous. It is worth noting that most of the available literature on the chemical bath deposition of cadmium sulphide, suggests that the depositions were carried out in bath compositions with pH greater than 9, where the hydroxide concentration is high. For bath compositions with pH less than 9, powdery, non adherent substandard films were predicted to form (Chopra *et al.*, 1982). Thus, the success of depositing well adherent, uniform and homogenous high quality CdS thin films from bath compositions with pH as low as 4, is a little surprising in that CdS deposition has in general been associated with baths which are supersaturated with respect to hydroxy-cadmium species (O'Brien and Saeed, 1996). In this context we believe that the overall CBD process

has been driven towards an ion-by-ion mechanism of the type thought to predominate for CdS (Boyle *et al.*, 2000). The SEM micrographs of the as-deposited $\text{Cd}_{0.86}\text{Zn}_{0.14}\text{S}$ thin films are shown in the Figures 6.28, 6.29 and 6.30. The micrographs show a homogeneous film, without cracks, less pin holes and well packed, highly adhered globular crystallites on the glass substrates.



Figure 6.28: SEM micrograph of the as-deposited $\text{Cd}_{0.86}\text{Zn}_{0.14}\text{S}$ thin film (magnification 12800x)

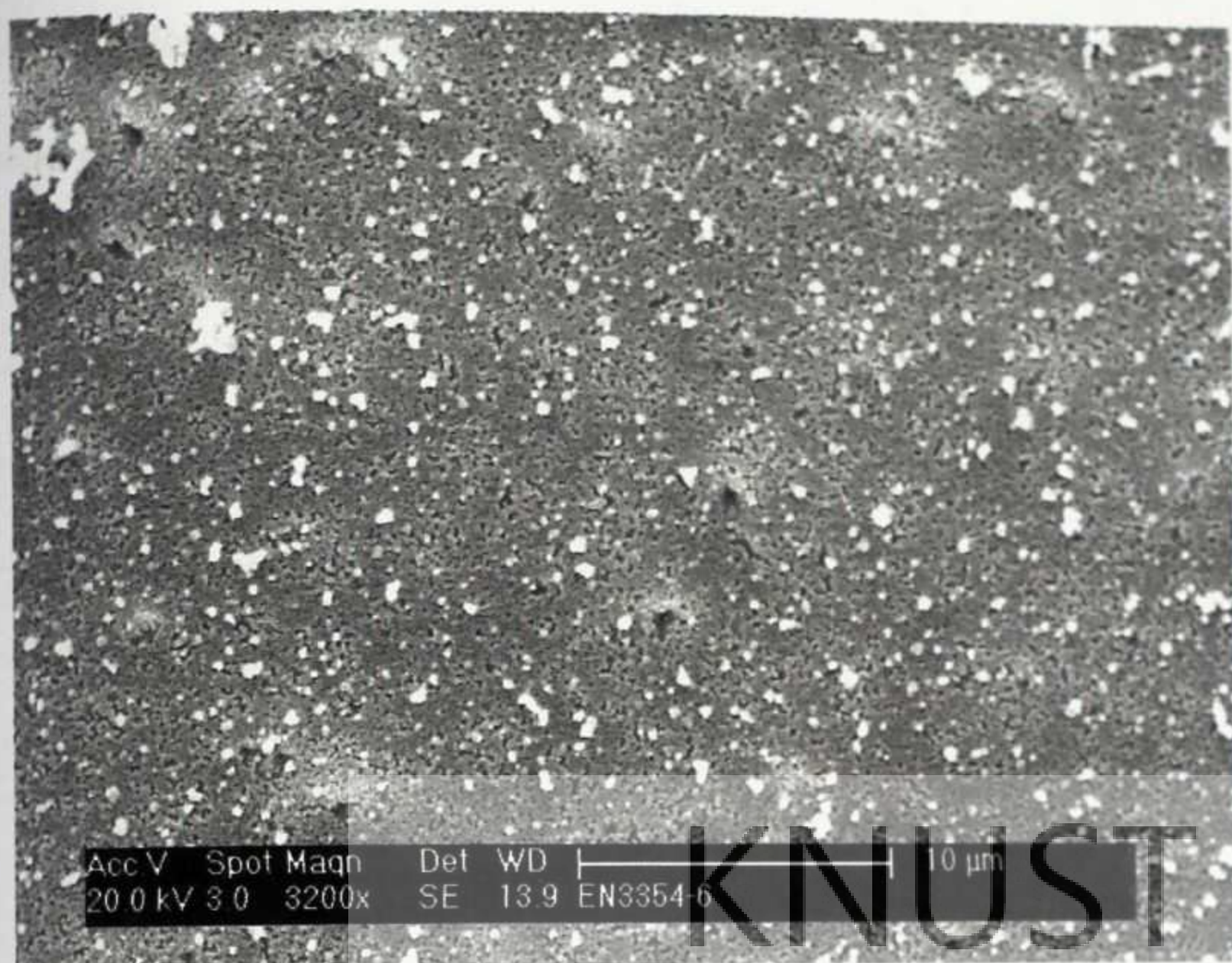


Figure 6.29: SEM micrograph of the as-deposited $\text{Cd}_{0.86}\text{Zn}_{0.14}\text{S}$ thin film (magnification 3200x)

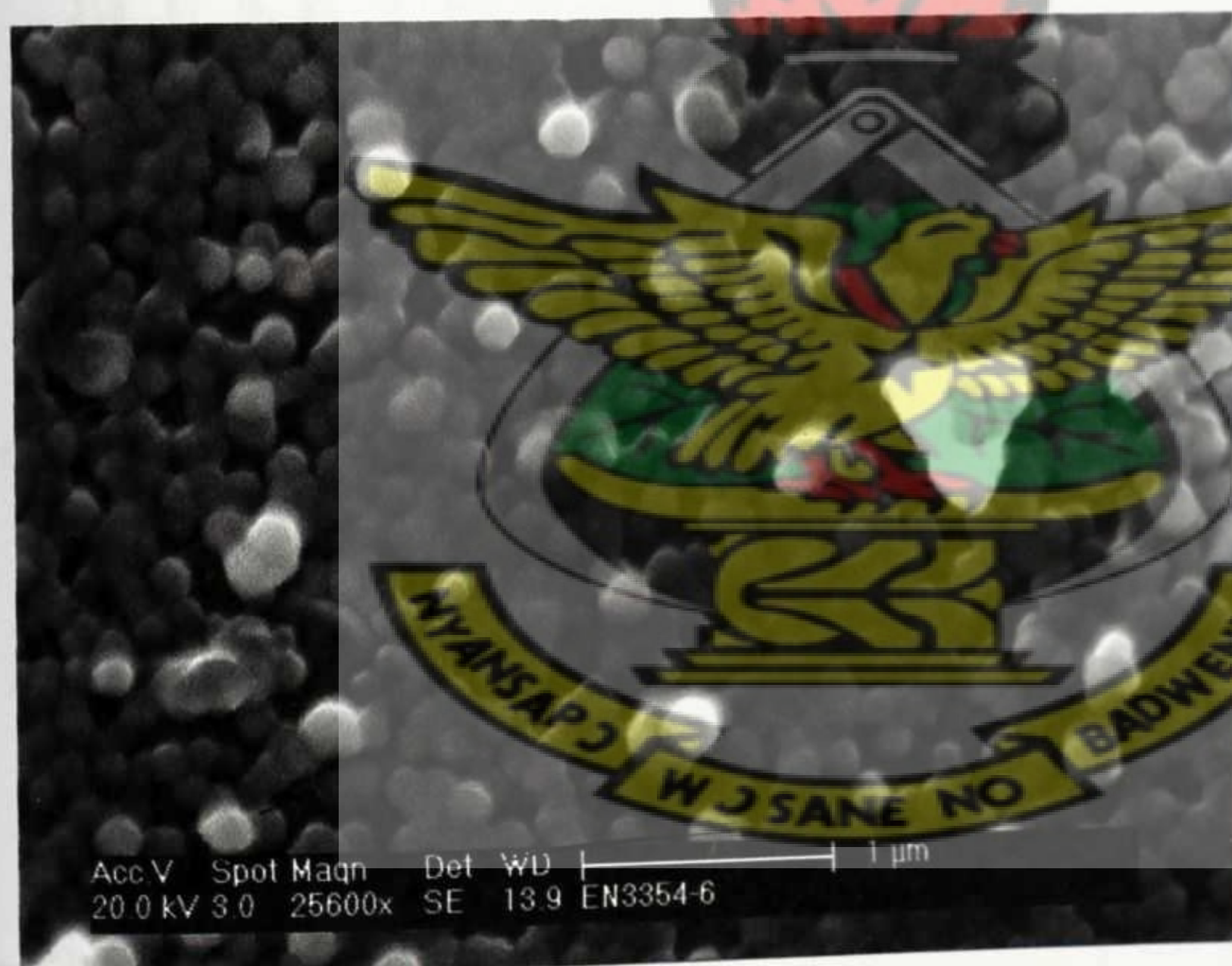


Figure 6.30: SEM micrograph of the as-deposited $\text{Cd}_{0.86}\text{Zn}_{0.14}\text{S}$ thin film (magnification 25600x)

EDX spectrum and line scan of the as-deposited $\text{Cd}_{0.86}\text{Zn}_{0.14}\text{S}$ thin film is shown in Figure 6.31 and 6.32. The film is consistent with the formation of the ternary compound on silica glass slide. The presence of the large amount of impurities such as silicon, oxygen,

magnesium, calcium and aluminum are suspected to be as a result of the microscope glass slide used as the substrate. These substances are the elemental composition of microscope glass slides, as given in appendix B.

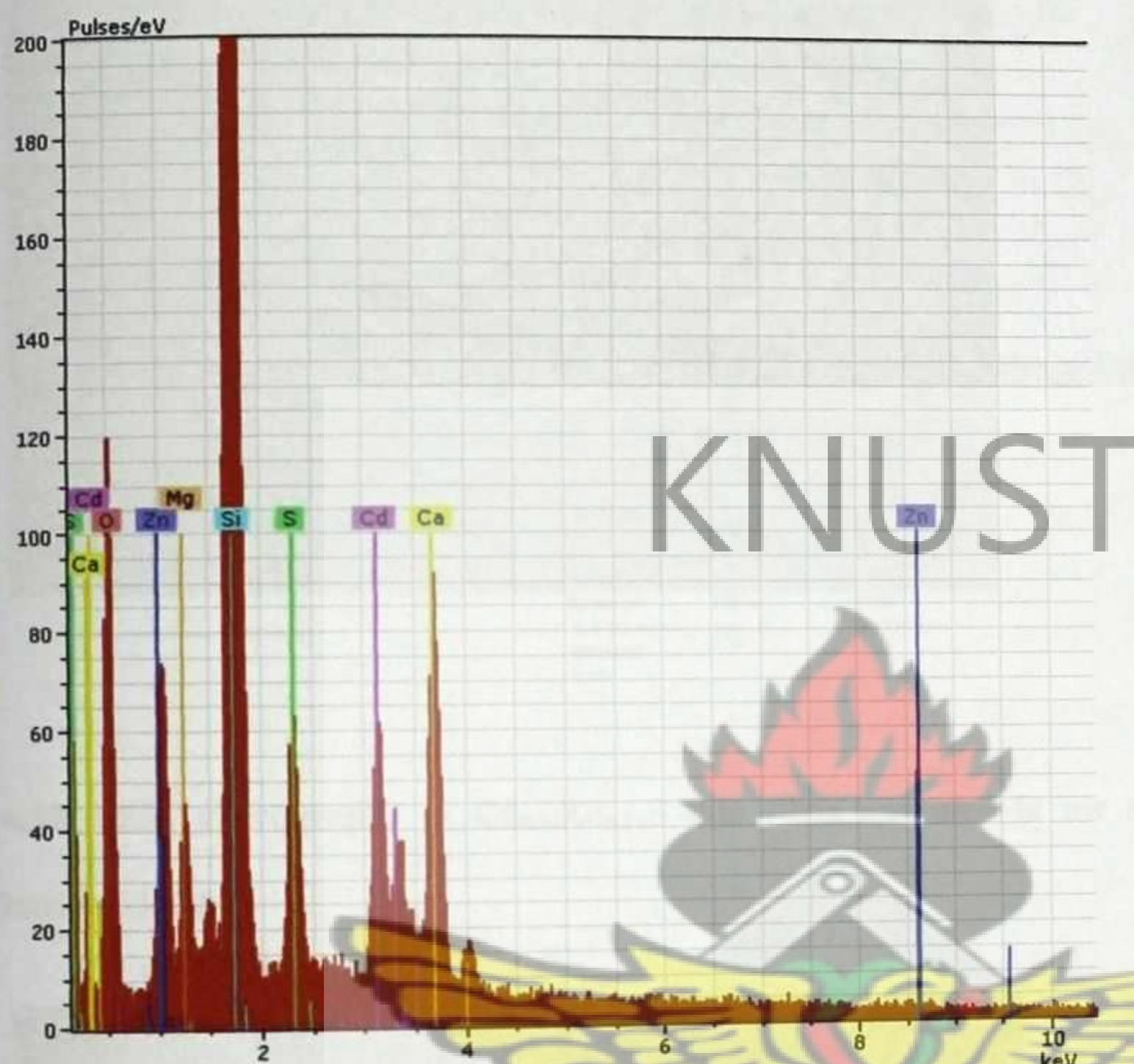


Figure 6.31: EDX spectrum of the as-deposited $\text{Cd}_{0.86}\text{Zn}_{0.14}\text{S}$ thin film

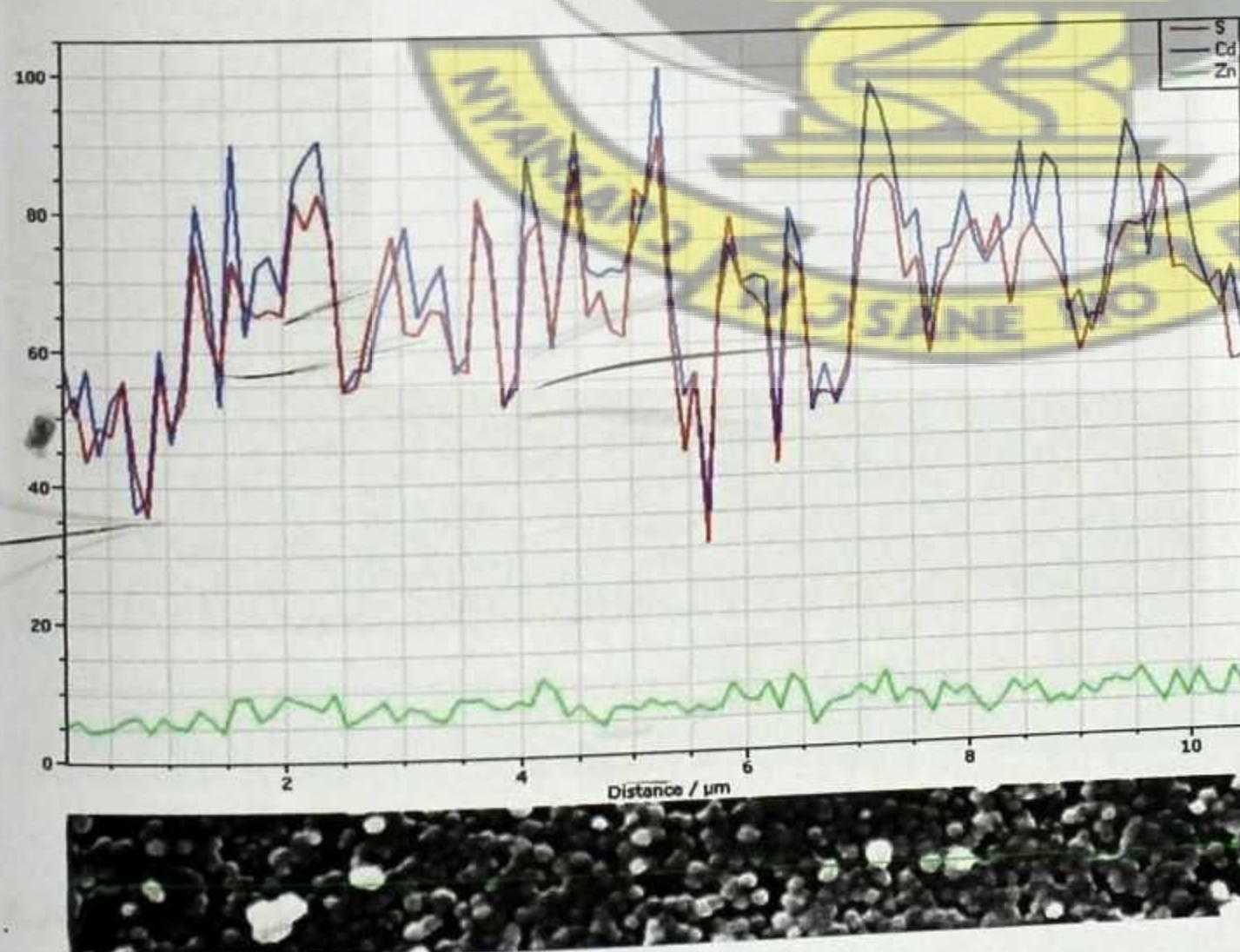


Figure 6.32: EDX line scan of the as-deposited $\text{Cd}_{0.86}\text{Zn}_{0.14}\text{S}$ thin film

Figures 6.33 and 6.34, shows the SEM micrographs of $\text{Cd}_{0.86}\text{Zn}_{0.14}\text{S}$ thin films annealed in air at 400°C for two hours



Figure 6.33: SEM micrographs of $\text{Cd}_{0.86}\text{Zn}_{0.14}\text{S}$ thin films annealed in air at 400°C for two hours (magnification 33000x)

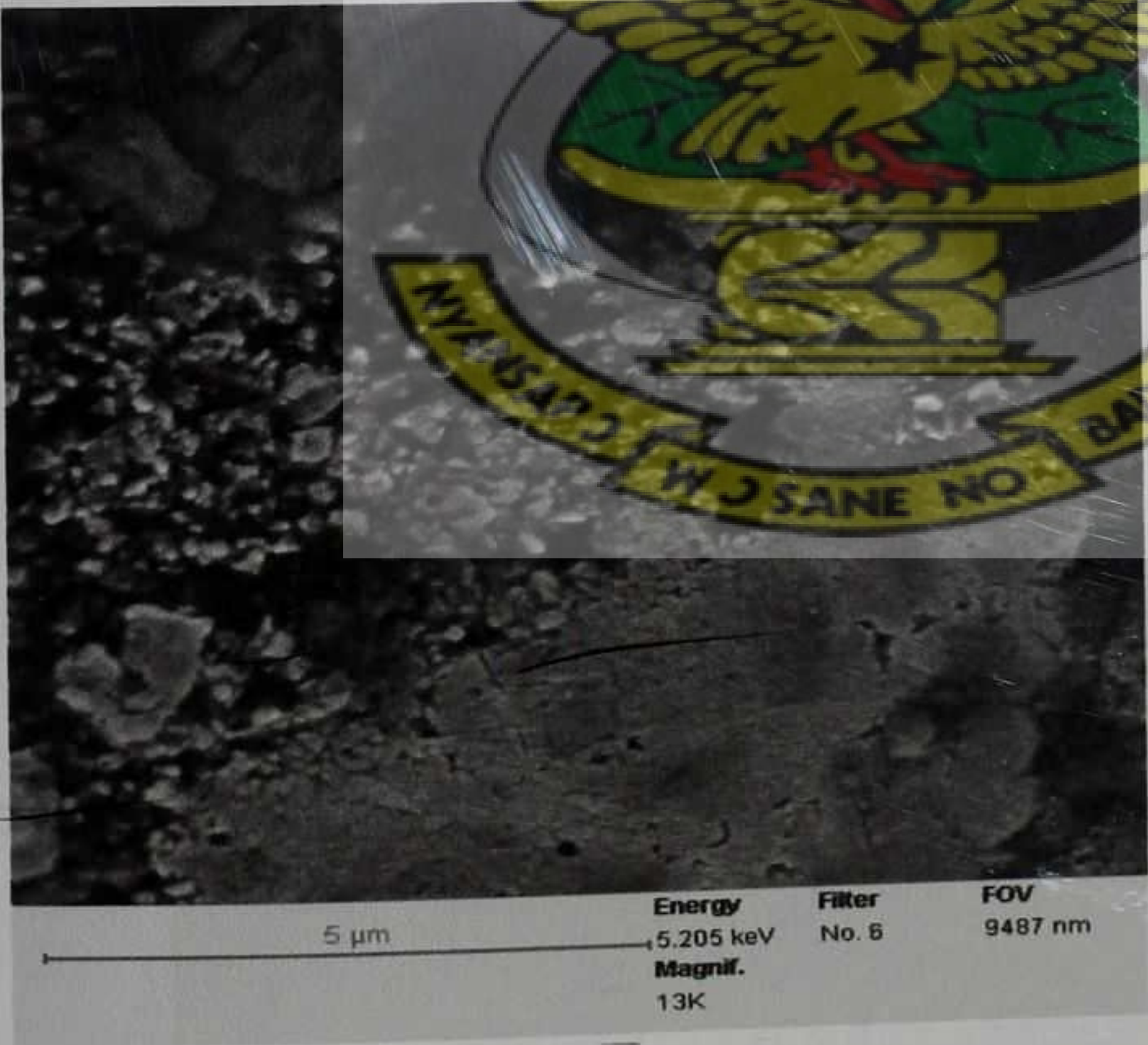


Figure 6.34: SEM micrographs of $\text{Cd}_{0.86}\text{Zn}_{0.14}\text{S}$ thin films annealed in air at 400°C for two hours (magnification 13000x)

Figures 6.33 and 6.34, shows the SEM micrographs of $\text{Cd}_{0.86}\text{Zn}_{0.14}\text{S}$ thin films annealed in air at 400°C for two hours



Figure 6.33: SEM micrographs of $\text{Cd}_{0.86}\text{Zn}_{0.14}\text{S}$ thin films annealed in air at 400°C for two hours (magnification 33000x)

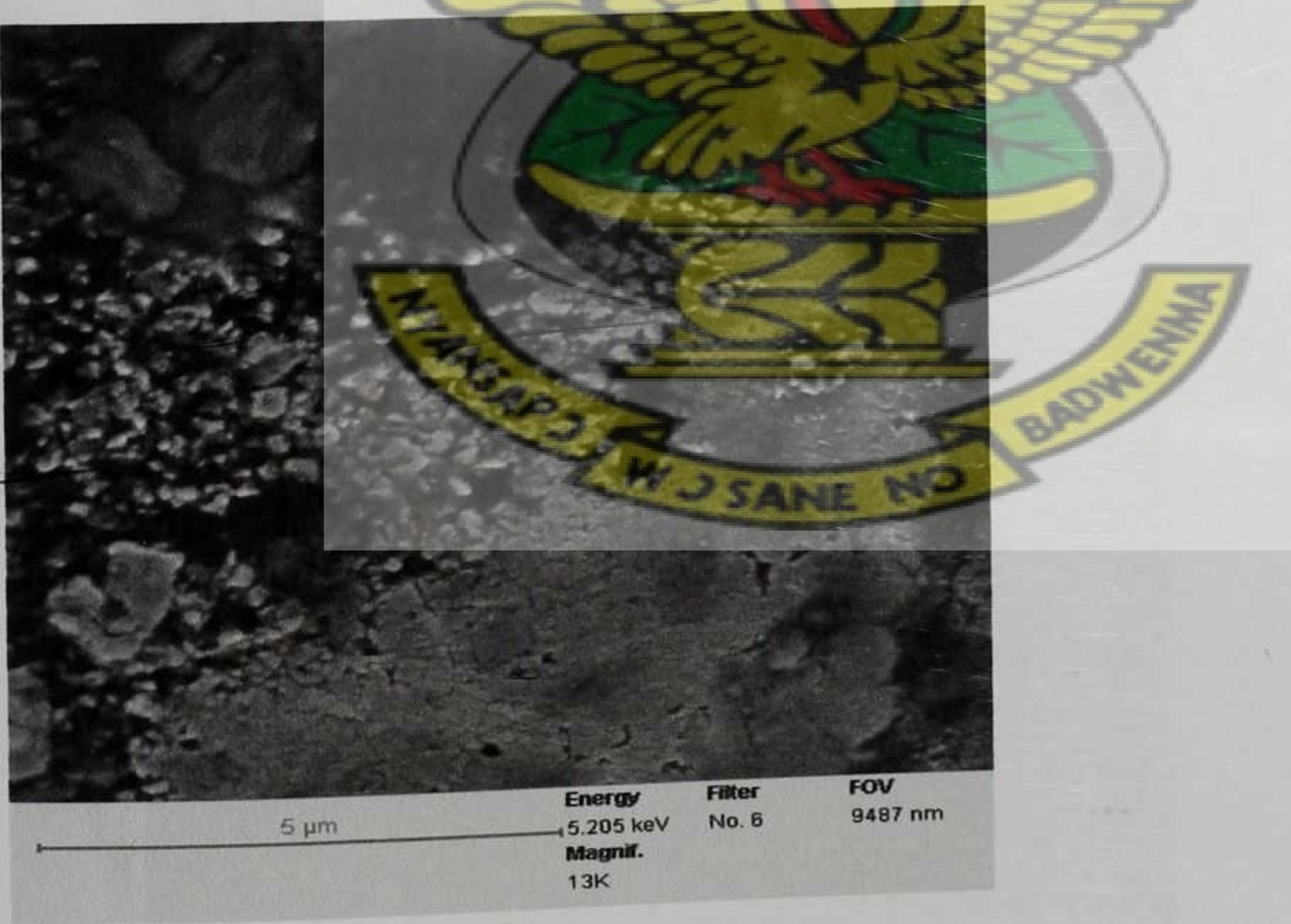


Figure 6.34: SEM micrographs of $\text{Cd}_{0.86}\text{Zn}_{0.14}\text{S}$ thin films annealed in air at 400°C for two hours (magnification 13000x)

The sharp jagged edges of the grains shown in the SEM micrographs of Figures 6.33 and 6.34 are characteristic signatures of crystals. This implies that the crystallinity of the sample improved after annealing in air at 400°C for two hours.

From Figures 6.35 and 6.36, SEM micrographs of the as-deposited ZnS thin films shows the presence of uniform and crack-free surface morphologies characterized by well-interconnected globular crystallites.



Figure 6.35: SEM micrograph of the as-deposited ZnS thin film (magnification 12708x)



Figure 6.36: SEM micrograph of as-deposited ZnS thin films (magnification 50830x)

Figure 6.36, shows an enlarged SEM micrograph of the as-deposited ZnS film shown in Figure 6.35. The films appear to be dense and composed of largely irregular shaped grains of diameter in the range 300 to 500 nm. These large grains are comprised of smaller spherical grains of 80 to 100 nm diameters.

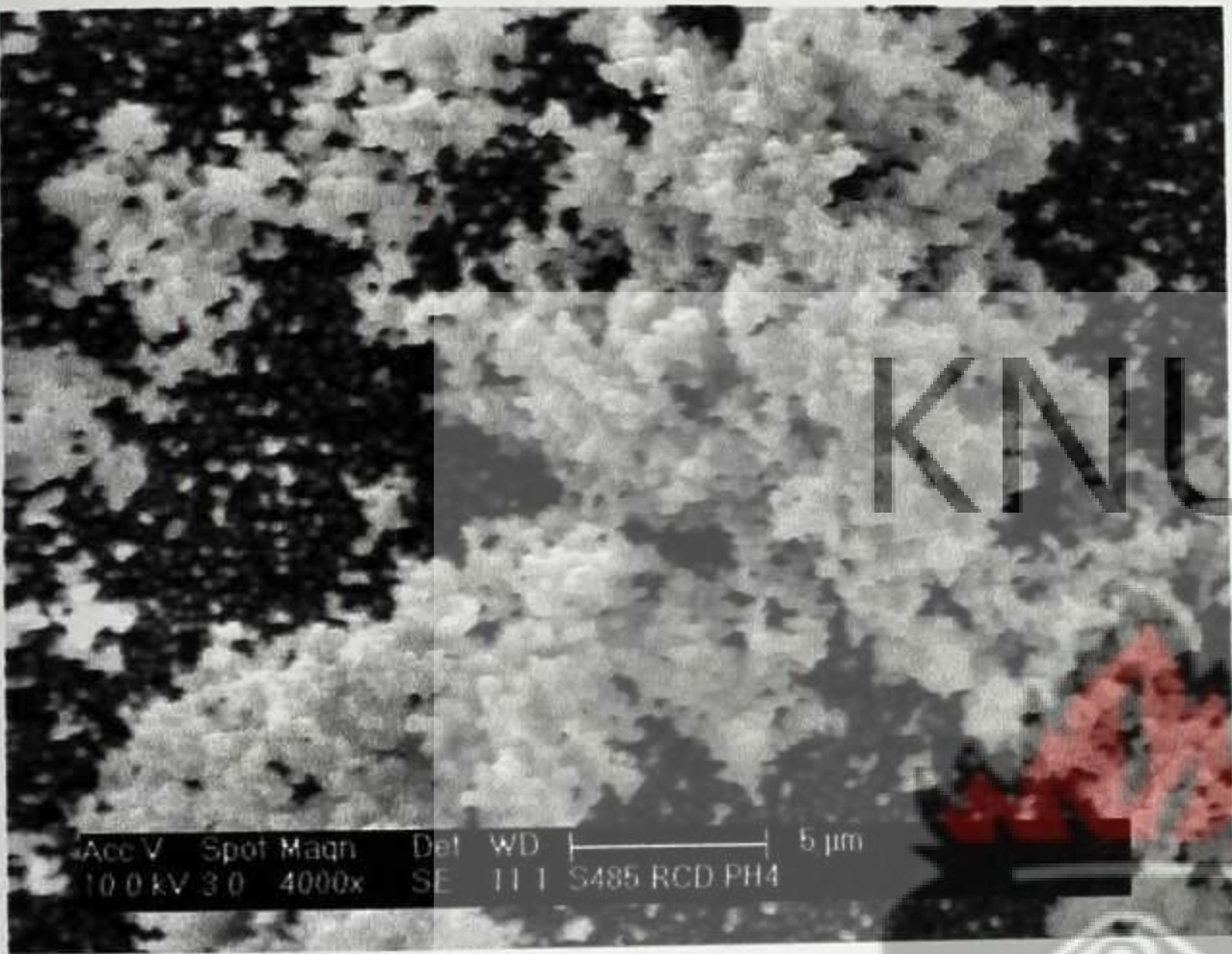


Figure 6.37: SEM micrograph showing some nano size structures on the as-deposited ZnS thin film (magnification 4000x).

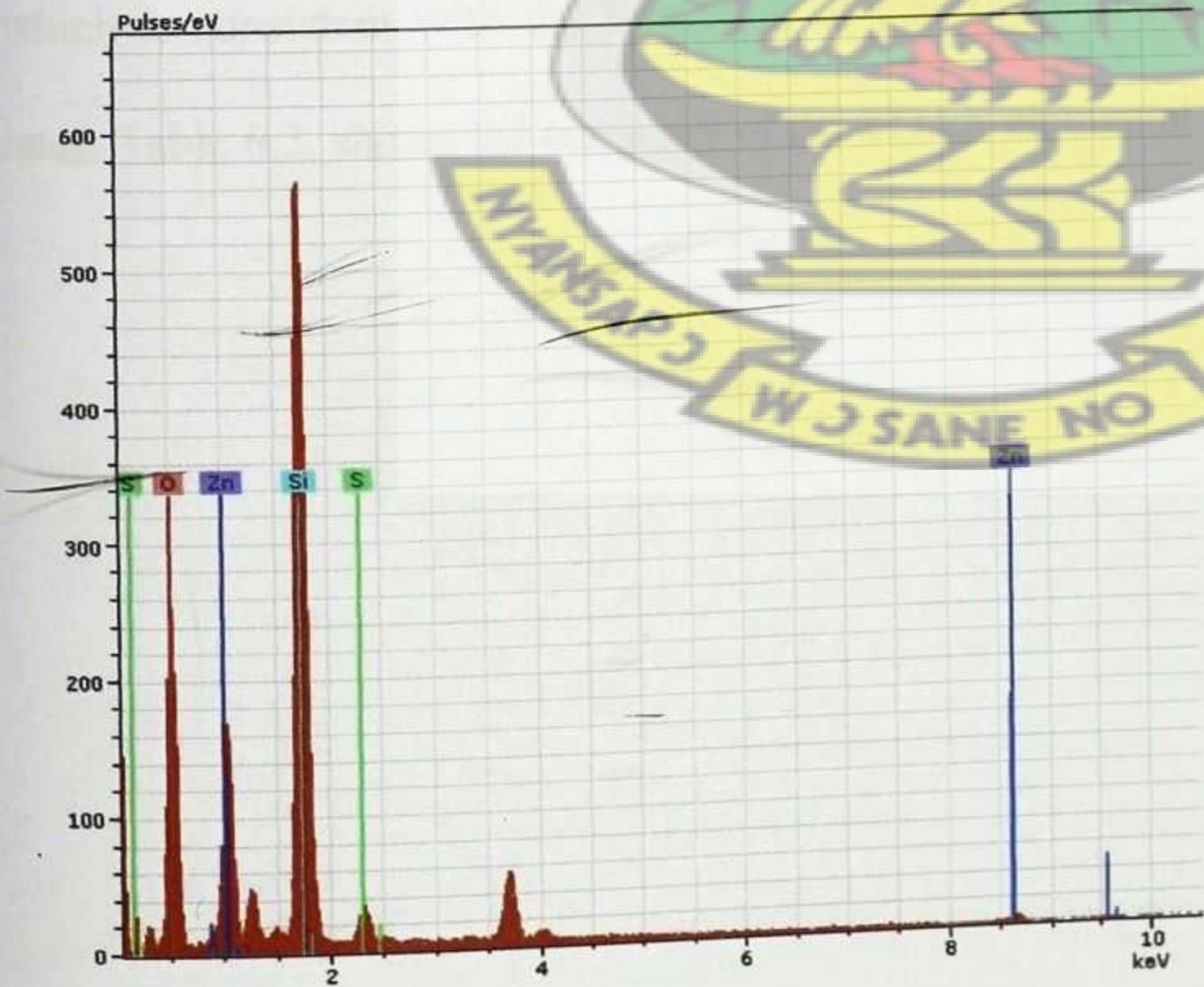


Figure 6.38: EDX spectrum of the as-deposited ZnS thin films

LIBRARY
KWAME NKRUMAH
UNIVERSITY OF SCIENCE & TECHNOLOGY
KUMASI

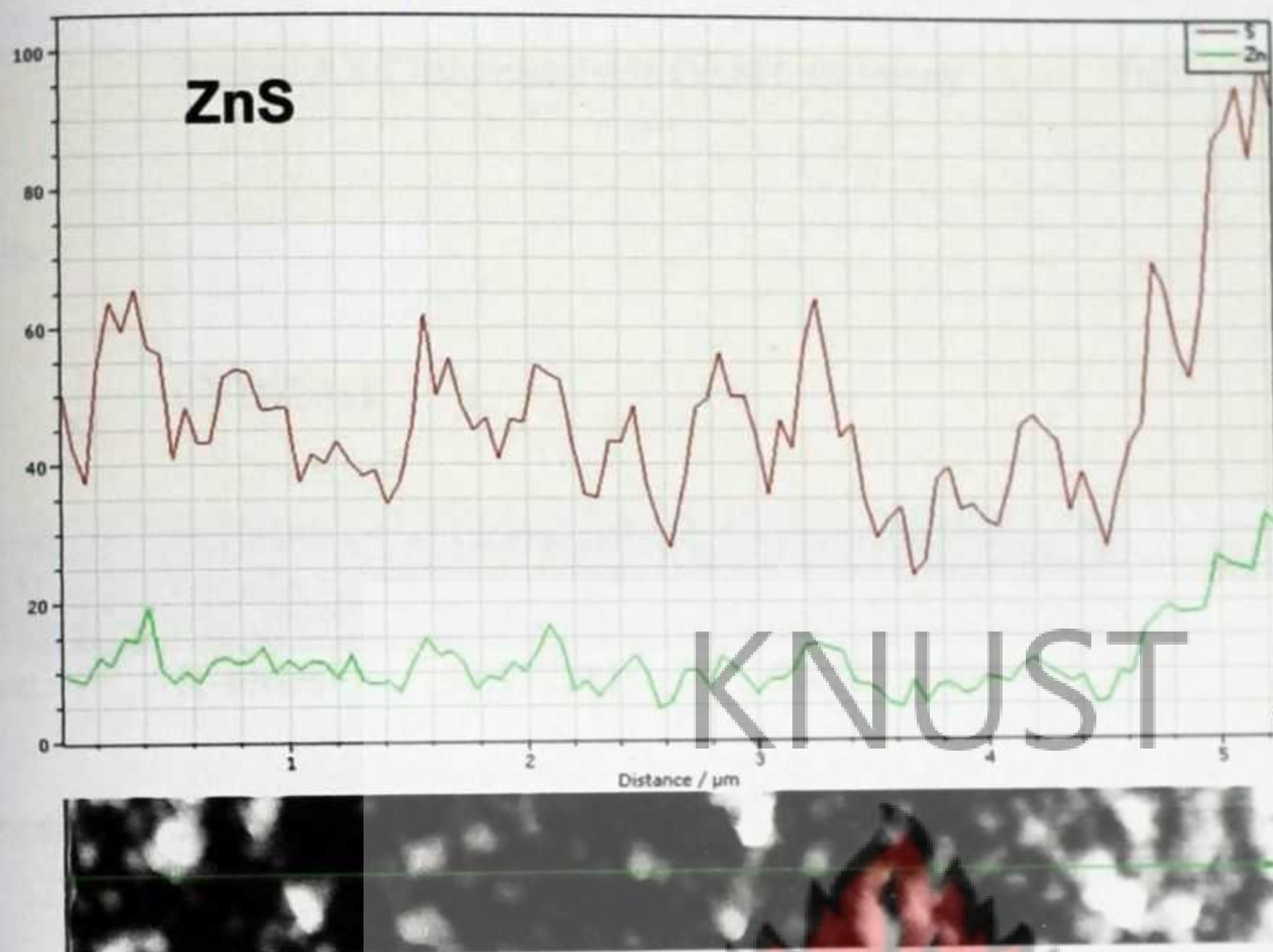


Figure 6.39: EDX line scan of the as-deposited ZnS thin films

Figures 6.38 and 6.39 show the EDX spectrum and line scan of the as-deposited ZnS thin film which is consistent with the formation of thin films of ZnS deposited on silica glass substrates. Table 6.2, shows the summary of the EDAX elemental analysis.

Table 6.2: EDAX elemental analysis results for the as-deposited ZnS thin film


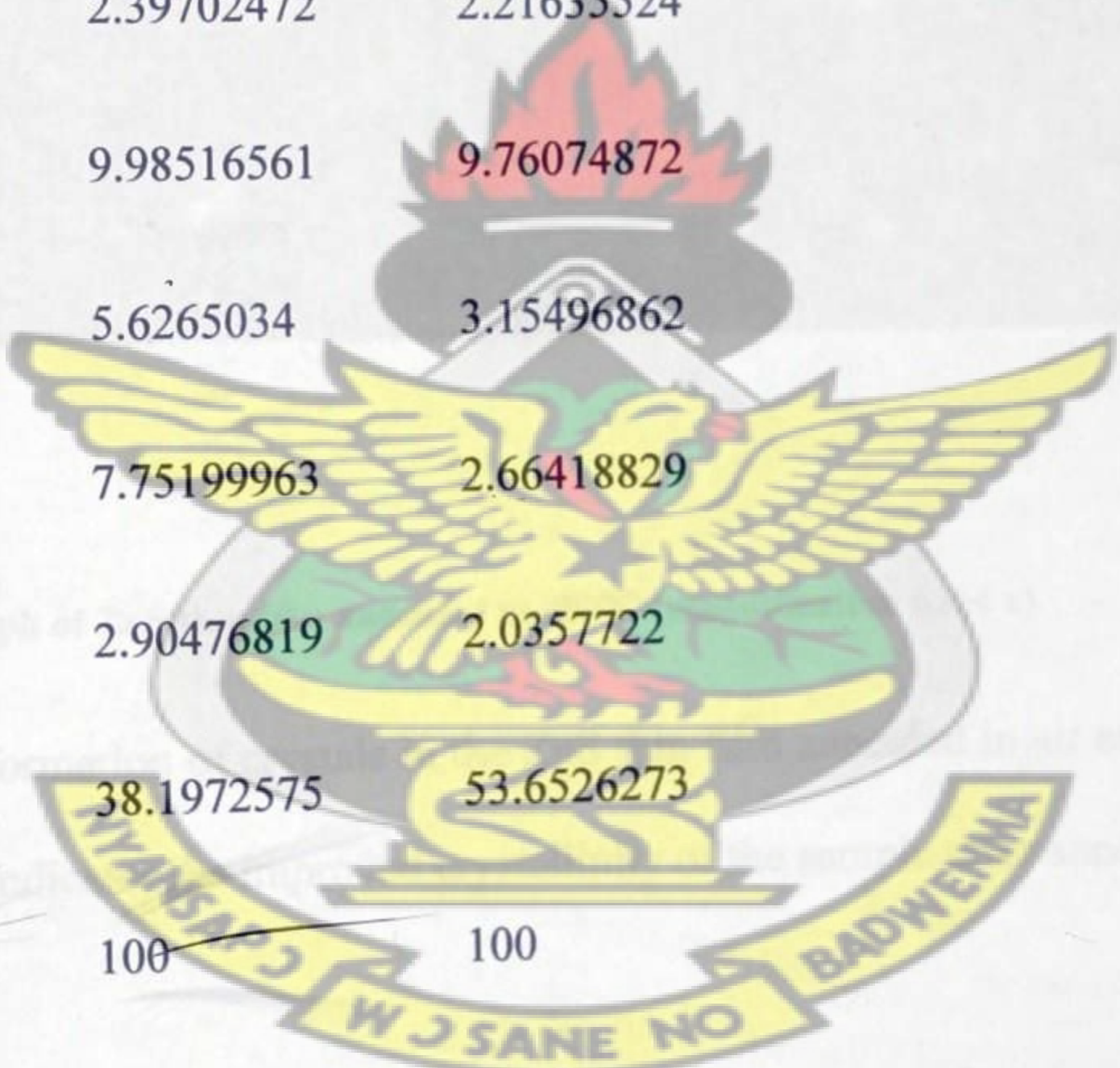
Bruker AXS Microanalysis GmbH, Germany				02/11/2011
Results				
Date:	02/11/2011			
Element	Series	[norm. wt.-%]	[norm. at.-%]	
Silicon	K-series	33.137281	26.5153396	
Magnesium	K-series	2.39702472	2.21635524	
Sodium	K-series	9.98516561	9.76074872	
Calcium	K-series	5.6265034	3.15496862	
Zinc	K-series	7.75199963	2.66418829	
Sulphur	K-series	2.90476819	2.0357722	
Oxygen	K-series	38.1972575	53.6526273	
Sum:		100	100	



Figure 6.40: SEM micrograph of ZnS thin film annealed at 400°C (magnification 6354 x)

Figure 6.40, shows the formation of crystals in the ZnS thin film annealed in air at 400°C for two hours. This clearly indicates the improved crystallinity of the sample after annealing

6.6. RESULTS OF THE OPTICAL ABSORPTION SPECTRA

The optical properties, like other properties of thin films, show profound sensitivity on the film microstructure. Since the various deposition parameters affect the microstructure, we expect, and indeed observe strong dependence of the optical properties of ultra thin films on the deposition conditions. Any changes in the electronic structure of the material would be reflected in its optical behaviour (Chopra, 1969). The most direct and perhaps the simplest method for probing the band structure of semiconductors is to measure the absorption spectrum (Pankove, 1975). In order to determine the optical band gap of the films, the absorbance spectra of the films were recorded. Figure 6.41, shows the optical absorption spectrum for $\text{Cd}_{1-x}\text{Zn}_x\text{S}$, ($0 \leq x \leq 1$), as-deposited thin films.

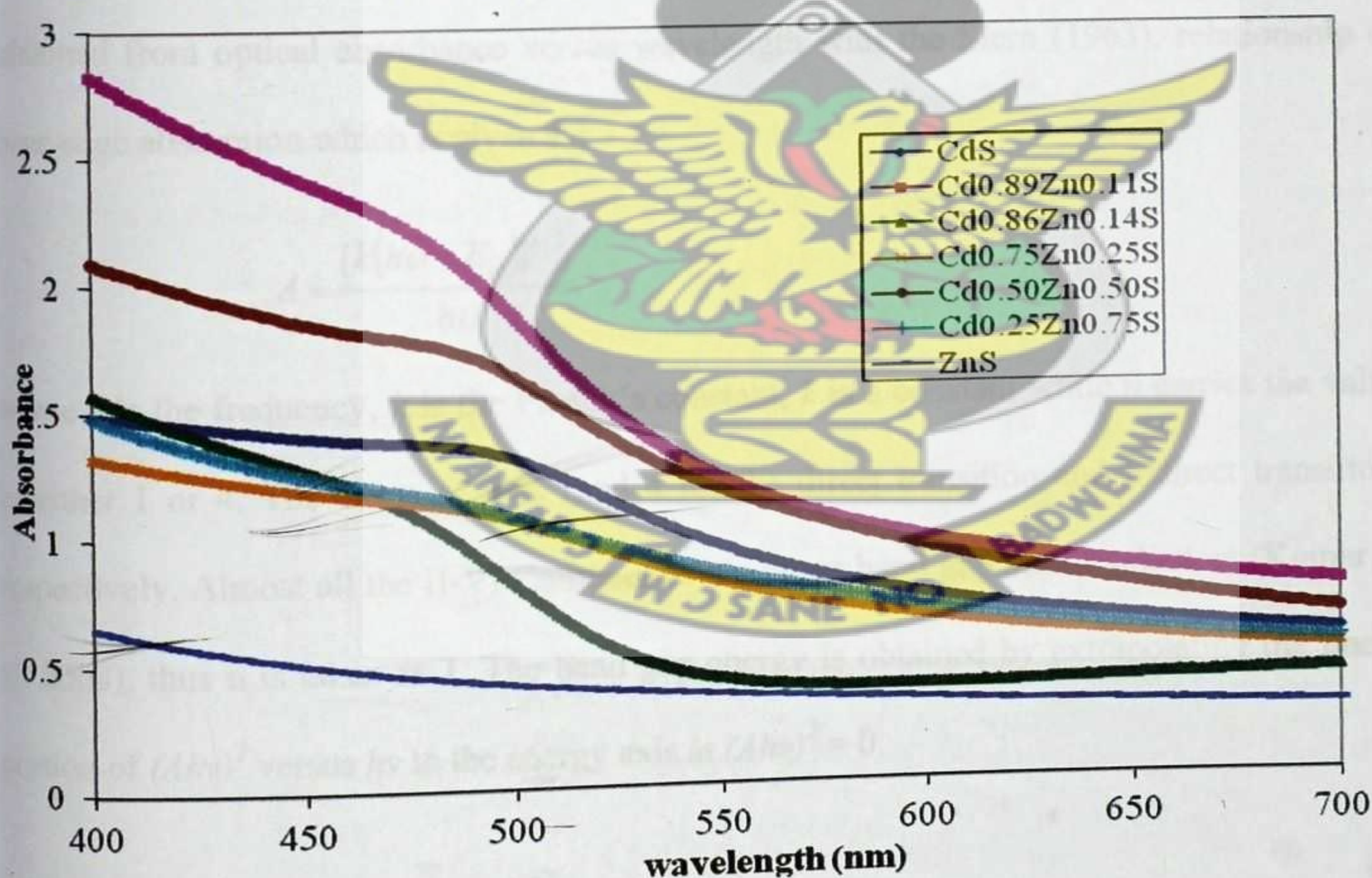


Figure 6.41: A plot of absorbance versus wavelength for $\text{Cd}_{1-x}\text{Zn}_x\text{S}$, ($0 \leq x \leq 1$), as-deposited thin films.

The vertical axis is the absorbance and the horizontal axis is the wavelength of the photons. Although the absorbance was measured within the wavelength range of 200 nm to 900 nm, this axis has been formatted to show the absorbance within the visible range, that is, the wavelength range of between 400 nm to 700 nm. This is because the band gap of the $\text{Cd}_{1-x}\text{Zn}_x\text{S}$, ($0 \leq x \leq 1$), thin films lies within this range. It can be observed from Figure 6.41, that the fundamental absorption edge of the thin films shifts towards smaller wavelengths with increasing zinc content. This shift indicates an increase of the optical band gap which may result from a decrease in grain sizes of the samples (Ezema et al, 2006).

6.7 DETERMINATION OF THE OPTICAL BAND GAP

The band gap energy and transition type was derived from mathematical treatment of data obtained from optical absorbance versus wavelength with the Stern (1963), relationship of near-edge absorption which is given as;

$$A = \frac{[k(h\nu - E_g)]^{n/2}}{h\nu}$$

where ν is the frequency, h is the Planck's constant, k is a constant while n carries the value of either 1 or 4. The value of n is 1 and 4 for the direct transition and indirect transition, respectively. Almost all the II-VI Compounds are direct band gap semiconductors (Kumar et al, 2008), thus n is taken as 1. The band gap energy is obtained by extrapolating the linear portion of $(Ah\nu)^2$ versus $h\nu$ to the energy axis at $(Ah\nu)^2 = 0$.

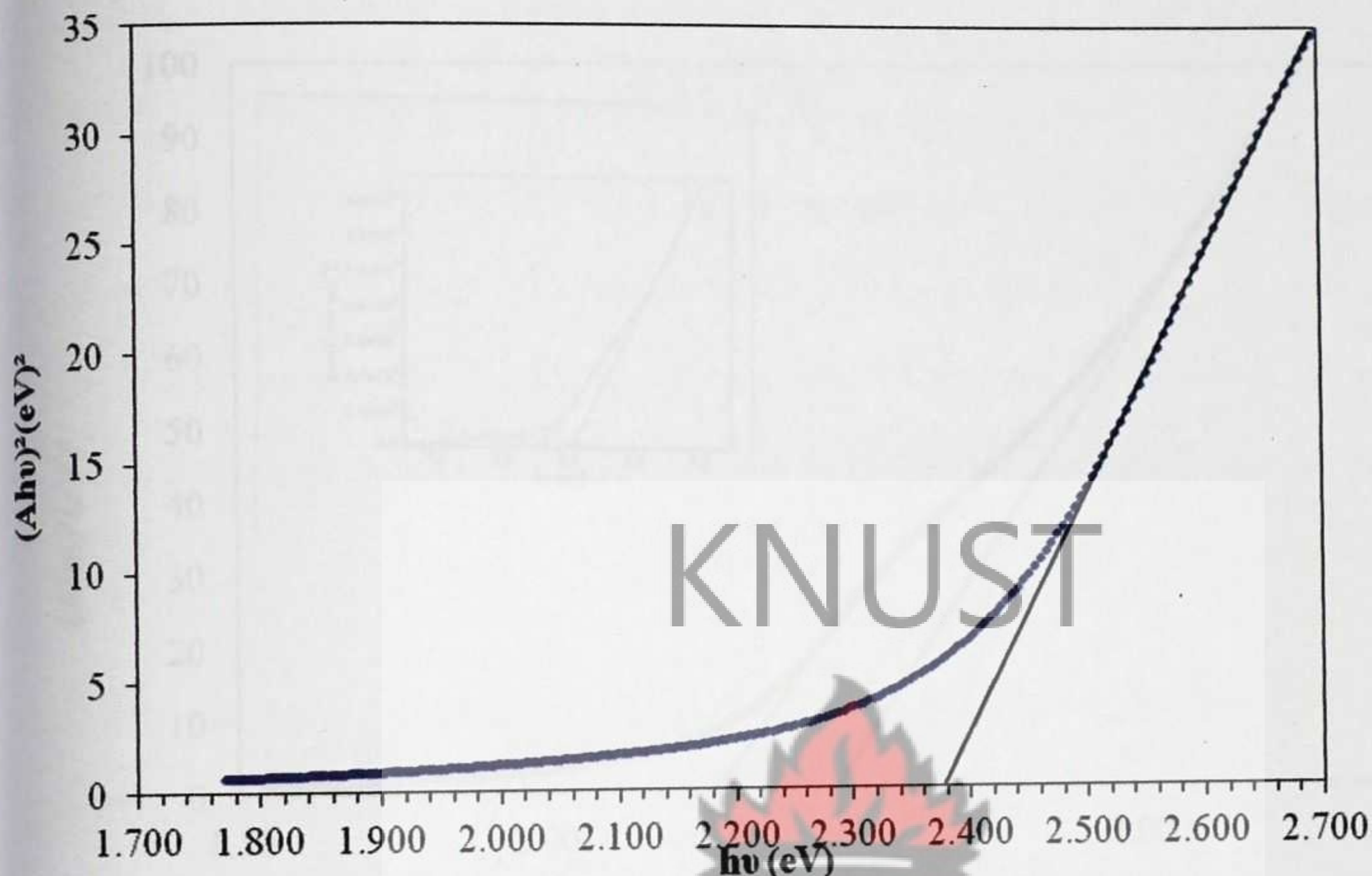


Figure 6.42: A graph of $(Ah\nu)^2$ plotted as a function of the photon energy, $h\nu$, for CdS thin film. Extrapolation of best fit line between $(Ah\nu)^2$ and $h\nu$ to intercept the $h\nu$ axis at $(Ah\nu)^2 = 0$ gives the band gap.

Figure 6.42, gives the band gap of the as-deposited CdS thin film. The value obtained for the Band gap is 2.38 eV. This value is close to the literature value of 2.42 eV (Boakye and Nusenu, 1996). The slightly lower band gap obtained in Figure 6.42, could be attributed to the presence of defect states in the band gap. It is well known that the energy band gap of a semiconductor is affected by the residual strain, defects, charged impurities, disorder at the grain boundaries, and also particle size confinement (Ramasamy, 2011).

Figure 6.43 shows a plot of $(Ah\nu)^2$ versus $h\nu$ for $\text{Cd}_{0.89}\text{Zn}_{0.11}\text{S}$.

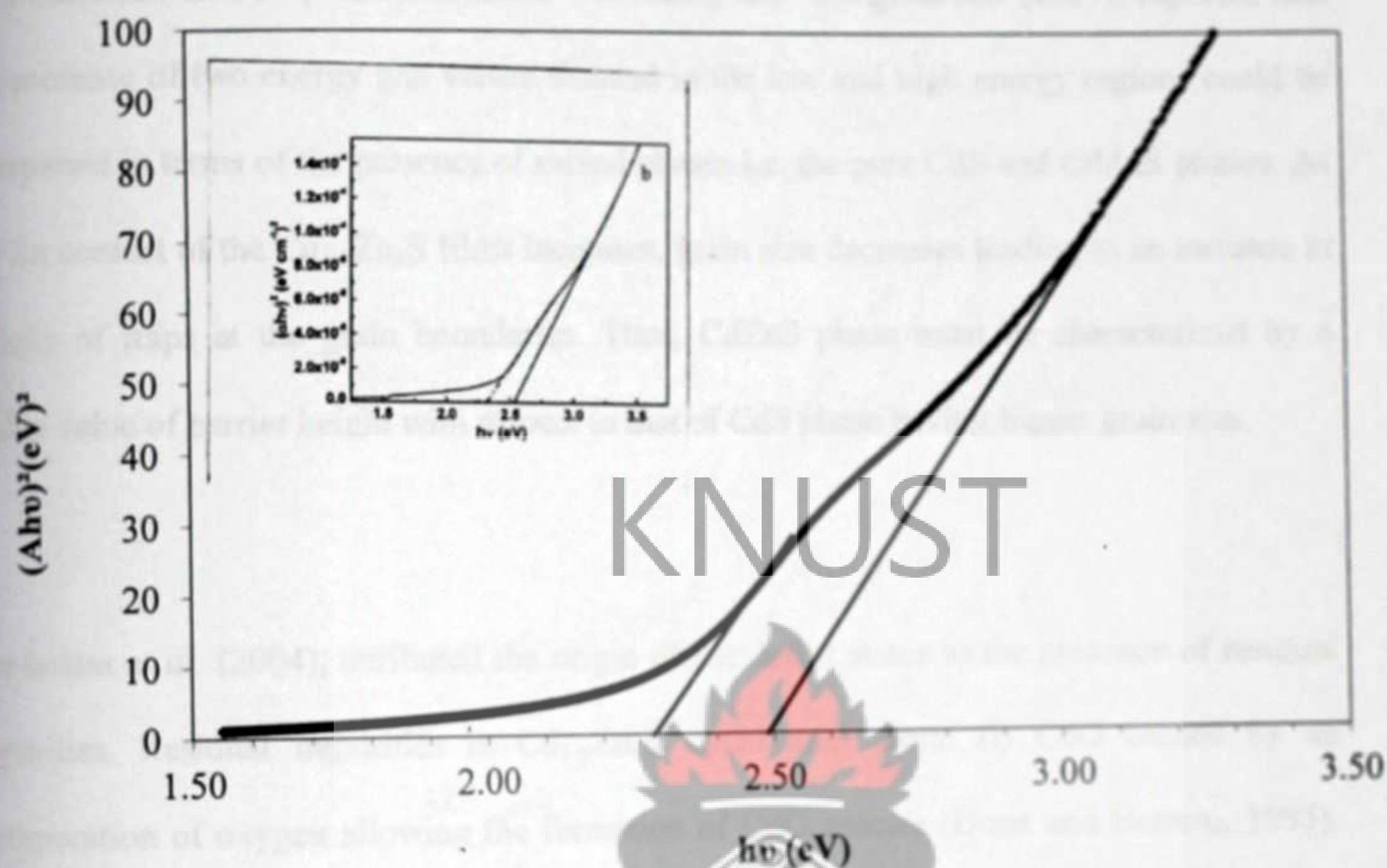


Figure 6.43: A graph of $(Ah\nu)^2$ plotted as a function of the photon energy, $h\nu$, $\text{Cd}_{0.89}\text{Zn}_{0.11}\text{S}$ thin film. Extrapolation of best fit line between $(Ah\nu)^2$ and $h\nu$ to intercept the $h\nu$ axis at $(Ah\nu)^2 = 0$ gives the band gap. (Inset: band gap and defect state by Fan *et al.* (2007))

From Figure 6.43, the extrapolations of the curves to the energy axis for zero absorption show the presence of two energy gaps; a lower one at 2.30 eV, which could be due to the presence of a defect state, and a higher one at 2.49 eV, which could be the actual band gap of the material. A similar observation on the presence of two band gaps, one being a defect state associated with CdS, has been reported by Fan *et al.* (2007), who reported a defect state at 2.32 eV (as shown in the inset of Figure 6.43).

Several authors have given various interpretations to the origin of the defect states associated with cadmium zinc sulphide thin films. Gaewdang and Wongcharoen (2007), reported that the presence of two energy gap values situated in the low and high energy regions could be interpreted in terms of the presence of mixed phases i.e. the pure CdS and CdZnS phases. As the Zn content of the $\text{Cd}_{1-x}\text{Zn}_x\text{S}$ films increases, grain size decreases leading to an increase in density of traps at the grain boundaries. Thus, CdZnS phase must be characterized by a higher value of barrier height with respect to that of CdS phase having bigger grain size.

KNUST

Khefachaa *et al.* (2004), attributed the origin of the defect states to the presence of residual impurities. Residual impurities in $\text{Cd}_{1-x}\text{Zn}_x\text{S}$ could arise from: (i) CdO caused by an incorporation of oxygen allowing the formation of CdO species (Dona and Herrero, 1995). The CdO impurities behave as donors and correspond to an energy level located at $[E_c - E_D]$ below the bottom of the conduction band, E_c (Nanda *et al.*, 1998). (ii) An excess of cadmium, which possibly occupy interstitial sites. They behave as deep acceptors.

Sebastian and Narvaez (1996), have attributed the origin of these defect states to the presence of deep acceptor centres related to Cd and Zn vacancies, and shallow donor levels due to S vacancies in the films.

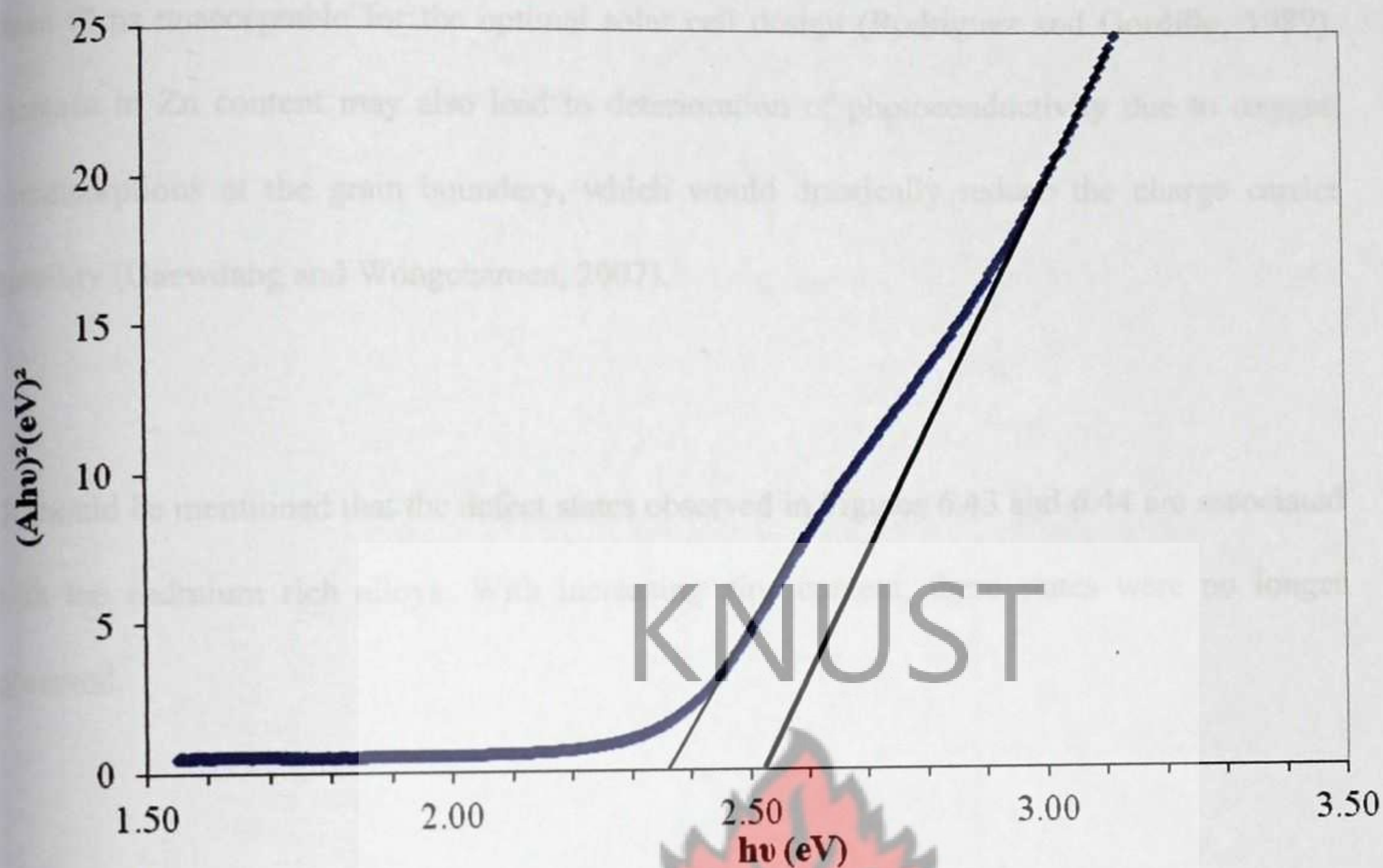


Figure 6.44: A graph of $(Ah\nu)^2$ plotted as a function of the photon energy, $h\nu$, $\text{Cd}_{0.86}\text{Zn}_{0.14}\text{S}$ thin film. Extrapolation of the best fit line between $(Ah\nu)^2$ and $h\nu$, to intercept the $h\nu$ axis at $(Ah\nu)^2 = 0$ gives the band gap.

Figure 6.44, shows a plot of $(Ah\nu)^2$ versus $h\nu$ for $\text{Cd}_{0.86}\text{Zn}_{0.14}\text{S}$. The extrapolations of the curves to the energy axis for zero absorption indicate a band gap of 2.53 eV with a defect state at 2.36 eV.

The band gaps of $\text{Cd}_{1-x}\text{Zn}_x\text{S}$ thin films, with $0 \leq x \leq 0.14$, are very important for solar cell applications. According to Domens *et al.* (1980), the physical properties of the ternary CdZnS layers are less acceptable than those of CdS , particularly when x exceeds 0.15. This is a limiting value for the CdZnS layers used for the preparation of efficient photocells. In most cases, for Zn compositions greater than 10% the resistivity exceeds $100 \Omega\text{-cm}$, thus, making

these films unacceptable for the optimal solar cell design (Rodriguez and Gordillo, 1989). Increase in Zn content may also lead to deterioration of photoconductivity due to oxygen chemisorptions at the grain boundary, which would drastically reduce the charge carrier mobility (Gaewdang and Wongcharoen, 2007).

It should be mentioned that the defect states observed in Figures 6.43 and 6.44 are associated with the cadmium rich alloys. With increasing zinc content, these states were no longer observed.

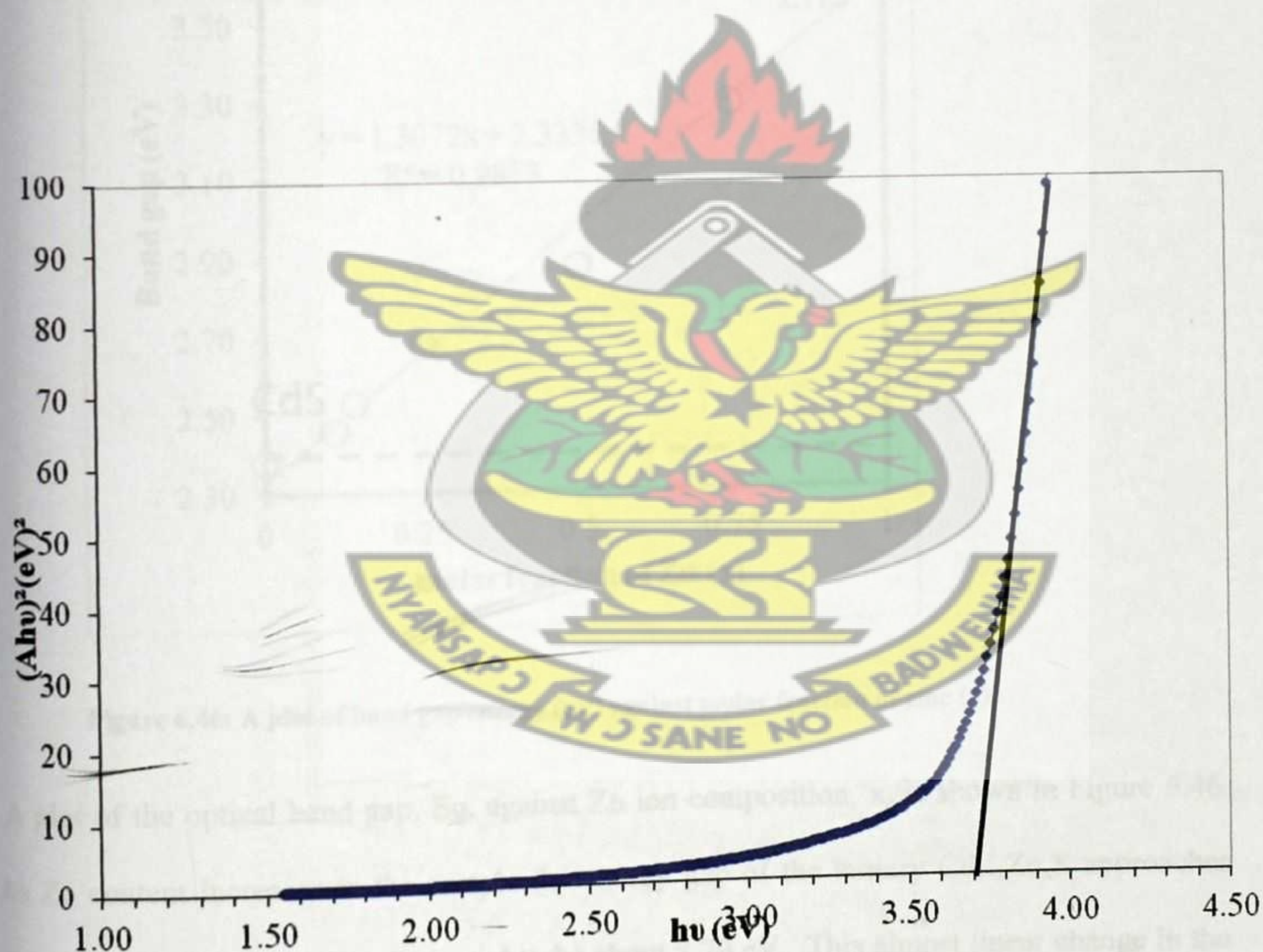


Figure 6.45: A graph of $(Ah\nu)^2$ plotted as a function of the photon energy, $h\nu$, for ZnS thin film. Extrapolation of best fit line between $(Ah\nu)^2$ and $h\nu$ to intercept the $h\nu$ axis at $(Ah\nu)^2 = 0$ gives the band gap.

From Figure 6.45, the band gap for ZnS is 3.70 eV. This is consistent with other published results such as, Ubale *et al.* (2001), who reported band gap values of between 3.68 to 4.10 eV, for thin films of ZnS, 3.6 eV, 3.68 eV and 3.7 to 3.8 eV, reported by Yamaguchi *et al.* (1999), Biswas (1986), and Ndukwe (1996,) using the conventional chemical bath deposition technique.

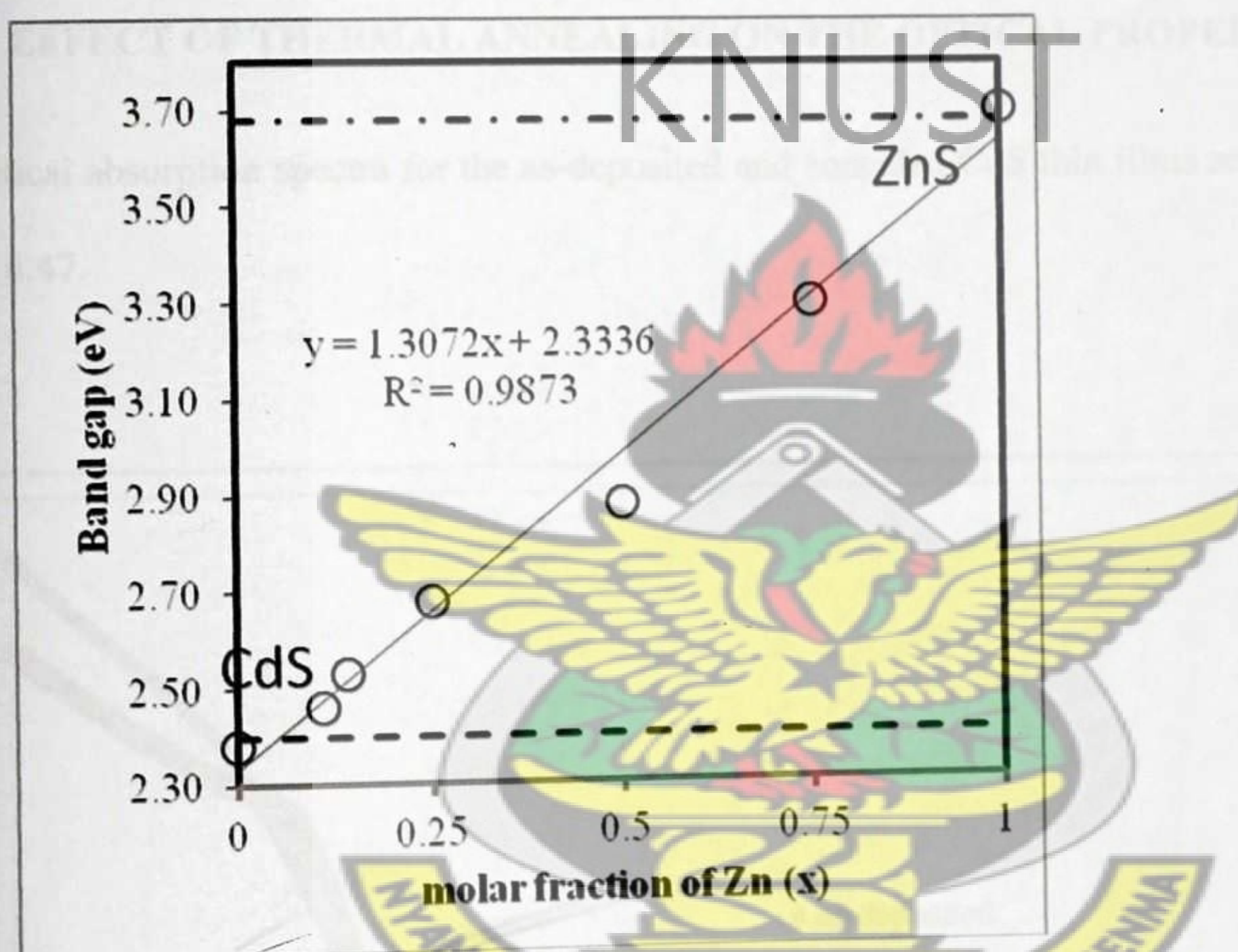


Figure 6.46: A plot of band gap energy (eV) against molar fraction of zinc (x)

A plot of the optical band gap, E_g , against Zn ion composition, x , is shown in Figure 6.46. As Zn content increases in the sample the energy gap of the ternary $\text{Cd}_{1-x}\text{Zn}_x\text{S}$ approaches that of the binary ZnS which is quoted to be about 3.70 eV. This almost linear change in the band gap of CdS by addition of Zn shows formation of a continuous series of solid solutions. Thus, the energy band gap of $\text{Cd}_{1-x}\text{Zn}_x\text{S}$ can be controlled in the range of the binary band gaps. The band gap increase with Zn concentration makes $\text{Cd}_{1-x}\text{Zn}_x\text{S}$ suitable material for

application as a buffer layer in Copper-Indium-Gallium-Selenide (CIGS) based solar cells, rather than CdS, since the higher band gap (> 2.40 eV) for CdZnS will allow more short-wavelength photons to reach the absorber layer and generate photocurrent. For best solar cell efficiency, the synthesis of a $\text{Cd}_{1-x}\text{Zn}_x\text{S}$ thin film with low zinc concentration is necessary because a higher zinc concentration leads to a high resistive material (Oktik, 1982).

6.8. EFFECT OF THERMAL ANNEALING ON THE OPTICAL PROPERTIES

The optical absorption spectra for the as-deposited and annealed CdS thin films are shown in Figure 6.47.

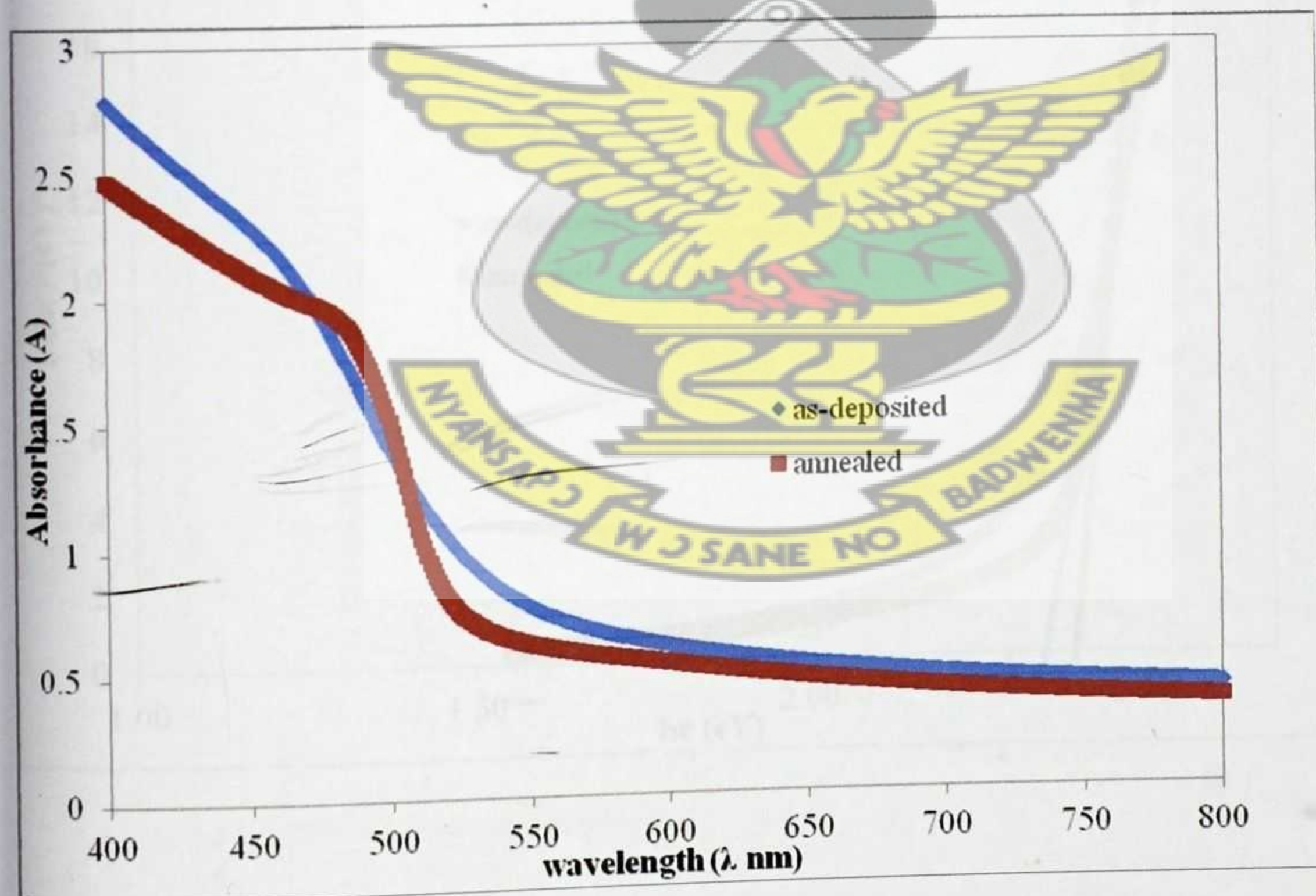


Figure 6.47: Optical absorption spectra of the as-deposited and annealed CdS thin film

From Figure 6.47, the annealed thin film has slightly lower absorbance values than the as-deposited film. This is because, annealing the samples could lead to minimizing structural imperfections in the prepared thin films resulting in fewer defect states within the band gap available for electron transitions, hence, the lower absorbance values. The sharp increase in the fundamental absorption edge in the annealed sample is also an indication of improved crystallinity. The improved crystallinity after annealing is also supported by the data obtained from XRD and SEM investigations. Similar observations on the slightly lower absorbance readings of the annealed thin films were made for all the samples.

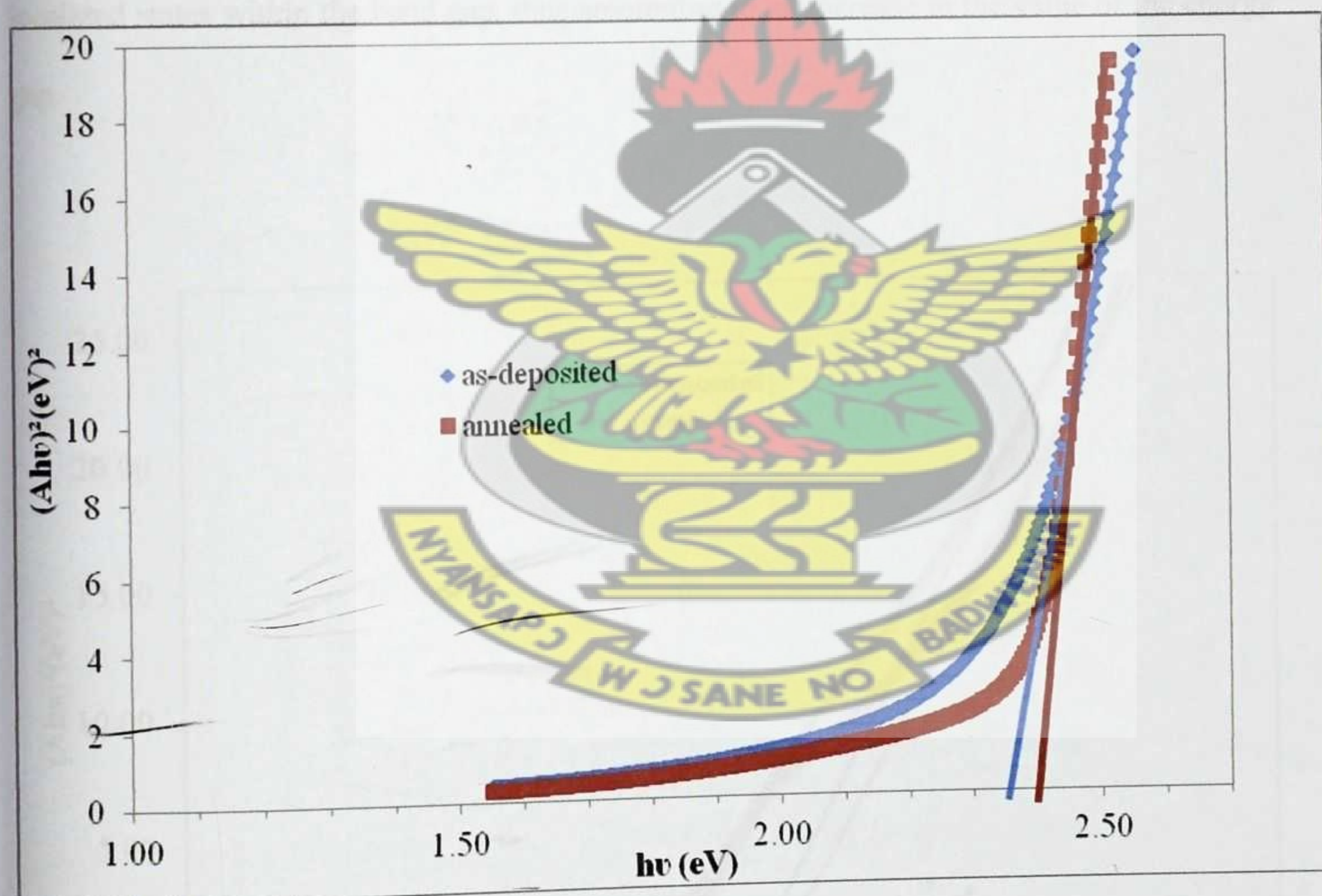


Figure 6.48: Band gap of CdS thin film, before and after annealing at 400°C

Form Figure 6.48, the band gap of CdS increased after annealing from 2.38 eV to 2.40 eV.

The temperature-dependent parameters that affect the band gap are reorganization of the film, change in the crystallite size of the film and self-oxidation (Ezugwu *et al.*, 2009). During thermal annealing, the unsaturated defects are gradually annealed out (Hasegawa *et al.*, 1978), producing large numbers of saturated bonds. The reduction in the number of unsaturated defects decreases the density of localized states in the band structure, and consequently increases the optical band gap (Dongol, 2002). Davis and Mott (1979) explained that the presence of high density of localized states in the band structure is responsible for the lower energy band gap. Annealing leads to improving the order of the atoms constituting the prepared thin films. This will result in a decrease in the number of localized states within the band gap, thus amounting to an increase in the value of the energy gap.

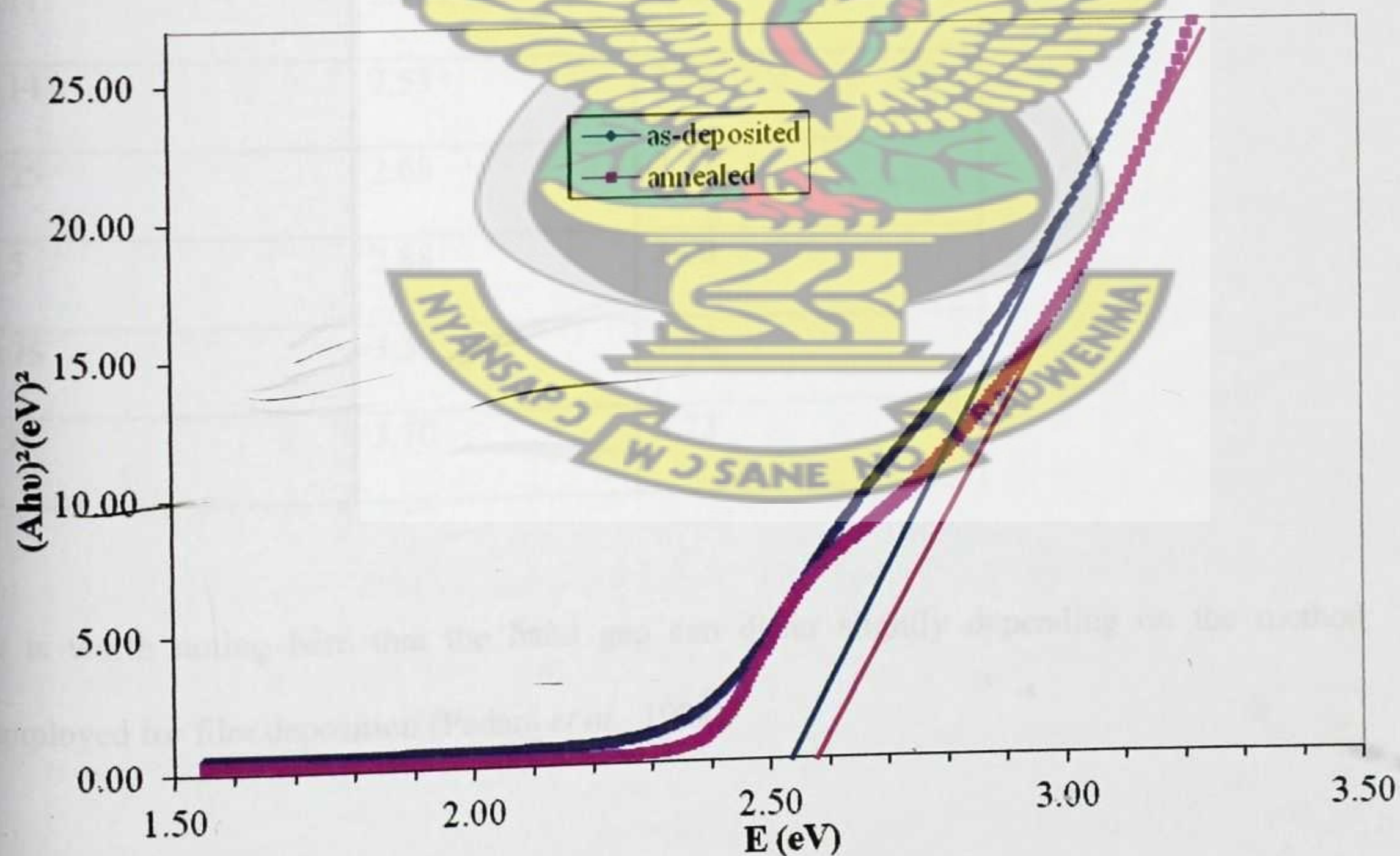


Figure 6.49: Band gap of $\text{Cd}_{0.86}\text{Zn}_{0.14}\text{S}$ before and after annealing at 400°C

Figure 6.49, shows the band gap of $\text{Cd}_{0.86}\text{Zn}_{0.14}\text{S}$ thin film before and after annealing. It can be observed that the defect state in the as-deposited sample still remained after annealing the sample in air at 400°C for two hours.

All the samples showed an increase in the band gap after annealing in air at 400°C , for two hours. Table 6.3 gives a summary of this result.

Table 6.3: Summary of variation in band gap with increasing zinc ion content for $\text{Cd}_{1-x}\text{Zn}_x\text{S}$ thin films for the as-deposited and annealed samples

Zinc ion content (x)	Band Gap (eV)	
	As-deposited	Annealed at 400°C
0	2.38	2.40
0.11	2.46	2.49
0.14	2.53	2.55
0.25	2.68	2.71
0.5	2.88	3.00
0.75	3.30	3.32
1.0	3.70	3.73

It is worth noting here that the band gap can differ slightly depending on the method employed for film deposition (Padam *et al.*, 1988).

CHAPTER SEVEN

7. CONCLUSIONS AND RECOMMENDATIONS

7.1. CONCLUSIONS

Cadmium zinc sulphide thin films with the required composition were successfully deposited from chemical baths containing zinc chloride, cadmium chloride, urea and thioacetamide at modestly acid pH values. The $\text{Cd}_{1-x}\text{Zn}_x\text{S}$ films obtained by this method were smooth, uniform, adherent, pinhole free, bright yellow orange in colour and changed to pale yellow with increasing zinc content. ZnS films were white in colour and transparent. The composition of the deposit, crystal structure and morphology were studied using Powder X-Ray diffraction (XRD) and Scanning electron microscopy (SEM). Elemental analysis was carried out using Energy Dispersive X-ray analysis (EDAX), and Optical Absorption spectroscopy was used to investigate the optical properties. The films were annealed in air at 400°C for two hours, and the effect of thermal annealing on the crystal structure morphology and optical properties were also studied. SEM micrographs of the as-deposited thin films showed the presence of uniform and crack-free surface morphologies characterized by well-interconnected globular crystallites. The annealed samples showed the presence of sharp jagged edge grains which are characteristic signatures of crystals. This implies that the crystallinity of the sample improved after annealing in air at 400°C for two hours. EDX analysis confirmed the film to be consistent with the formation of the ternary compound on silica glass slide. X-ray diffraction analysis of the thin films and precipitates of $\text{Cd}_{1-x}\text{Zn}_x\text{S}$, over the entire composition range, that is, $0 \leq x \leq 1$, showed that, all the compositions up to 75% Zn were wurtzite structure, with preferred orientation along the (002) plane, indicating that the crystallites are orientated with their c-axes perpendicular to the substrate. Pure ZnS had the sphalerite structure with preferred orientation along the (111) plane. The annealed samples have peaks which appear to be more pronounced, indicating that the crystallinity of

the samples had improved. The crystal size measured from the half width of the XRD peak varied from 12 nm (CdS) to 9 nm (ZnS). The lattice parameters a, c and d, decreased linearly with increasing Zn content, and showed very good agreement with Vegard's law.

The fundamental absorption edge of the as-deposited $\text{Cd}_{1-x}\text{Zn}_x\text{S}$ thin films, showed a blue shift with an increase in zinc ion content. The band gap, calculated from optical absorption spectroscopy, varied almost linearly with composition between that of CdS (2.38 eV) and ZnS (3.70) for the as-deposited samples while the annealed samples varied from CdS (2.40 eV) to ZnS (3.73 eV). The increase in band gap after thermal annealing is an indication of improved crystallinity in the sample. This almost linear change in the band gap of CdS by addition of Zn shows formation of a continuous series of solid solutions. The band gap increase with Zn concentration makes $\text{Cd}_{1-x}\text{Zn}_x\text{S}$ suitable material for application as a buffer layer in Copper-Indium-Gallium-Selenide (CIGS) based solar cells, rather than CdS, since the higher band gap (> 2.40 eV) for CdZnS will allow more short-wavelength photons to reach the absorber layer and generate photocurrent.

7.2. RECOMMENDATIONS

The methods employed in this work are standard techniques and any future work must be an improvement over them. It will be desirable in the future to include; electrical resistivity as a function of temperature, photoluminescence and photoconductivity measurements. These will complement the optical absorption measurements and help give more details on the trap states. It will be of interest to carry out Hall Effect measurements to determine the type of carrier, mobility, and charge carrier concentration. The effects of thermal annealing in hydrogen, and doping with indium on the electrical properties of the thin films, are areas worth investigating. It is important to investigate the possibility of oxide insertion during the

synthesis process, using highly sensitive elemental analysis techniques, such as X-ray photoelectron spectroscopy.

These further investigations are necessary for determining the right conditions which provide for optimum device performance, and also help tailor the physical properties of the material to suit the application for which it is intended

KNUST



REFERENCES

1. Al Bassan, A. A., (1999). Photoconductivity and defect levels in $\text{Zn}_x\text{Cd}_{1-x}\text{Se}$ with ($x = 0.5, 0.55$) crystals, *Solar Energy Mater. Sol. Cells* 57, pp 323-329.
2. AbuShama, J. R. Noufi, S. Johnston, S. Ward, and X. Wu, (2005). 'Improved Performance in CuInSe_2 and Surface Modified CuGaSe_2 Solar Cells', 31st IEEE, PVSC, pp. 299-302.
3. Adachi, S. Cited in Singh, J. and Shimakawa, K., (2003). Advances in Amorphous Semiconductors, CRC Press, New York, pp 56
4. Afzaal, M. and O'Brien, P., (2006). Recent developments in II-VI and III – VI semiconductors and their applications in solar cells, *J. Mater. Chem.*, 16, pp 1597 - 1602
5. Al Kuhaimi, S.A. and Tulbah, Z., (2000). Structural, compositional, optical and electrical properties of solution grown $\text{Zn}_x\text{Cd}_{1-x}\text{S}$ films, *J. Electrochem. Soc.*, 147, p 214.
6. Allen, E. T. Crenshaw, J. L. and Merwin, H. E. Cited In Hodes, G., (2002). Chemical Solution Deposition of Semiconductor Films. Marcel Dekker Inc. New York, pp.2-3.
7. American Council for an Energy-Efficient Economy (ACEEE), report, 2009. Semiconductor Technologies: The Potential to Revolutionize U.S. Energy Productivity, Web site: <http://aceee.org/pubs/e094.htm>. (Accessed 3/11/2010)
8. Anderson B. L. and Anderson R. L. (2005). Fundamentals of Semiconductor Devices, McGraw Hill, New York, ISBN 0-07-236977-9, pp 3-17

9. Anderson, F. Cited In Mahajan, S. and Sree Harsha, K. S. (1999). Principles of Growth and Processing of Semiconductors, WCB/McGraw Hill, ISBN 0-07-039605-1 New York, USA, pp 12
10. Asogwa, P. U., (2010). Variation Of Optical Properties With Post Deposition Annealing In Chemically Deposited CdZns Thin Films. *Chalcogenide Letters*, 7, 8, pp. 501 – 508
11. Barrett, C. S. and Massalski, T. B. (1966). Structure of Metals, Pergamon Press, New York, Third Edition, p. 243
12. Barrett, C. S. and Massalski, T. B. (1980). Structure of Metals, Pergamon Press, New York, Third (Revised) Edition pp. 238 - 239
13. Balkanski, M. and Wallis, R.F., (2000). Semiconductor Physics and Applications. Oxford University Press, Oxford, pp 1-2, 18-19, 68-69.
14. Beal, S. E., (1978). Cleaning and Surface Preparation, *Thin Solid Films*, 53, p97.
15. Bhattacharjee, B. Mandal, S.K. Chakrabarti, K. Ganguli, D. and Chaudhuri, S., (2002). Optical properties of $\text{Cd}_{1-x}\text{Zn}_x\text{S}$ nanocrystallites in sol-gel silica matrix. *J. Appl. Phys.* 35, p 2636.
16. Bloch, F. Cited In Mahajan, S. and Sree Harsha, K. S. (1999). Principles of Growth and Processing of Semiconductors, WCB/McGraw Hill, ISBN 0-07-039605-1 New York, USA, pp 12
17. Biswas, S. Pramanik, S. P. Basu, P. K. (1986). *Mater. Lett. (Netherlands)* 4 ,2, pp 81-84.

18. Boakye F., and Nusenu D., (1996). The Energy Band Gap of cadmium sulphide, *Solid State Communications*, 102, 4, pp 323-326
19. Bode, D. E. (1966). Versatile Solar control characteristics of chemically deposited PbS-Cu_xS thin film combinations, *Physics of Thin Films*, vol. 3, Academic Press, New York, p 275.
20. Borse, S.V. Chavhan, S.D. and Sharma, R., (2007). Growth, structural and optical properties of Cd_{1-x}Zn_xS alloy thin films grown by solution growth technique (SGT), *J. Alloys Compd.*, 436, pp 407-414
21. Bouroushian, M. Loizos, Z. Spyrellis, N. and Maurin, G. Cited In Chavhan, S.D., Senthilarasu, S. and Soo-Hyoung Lee, (2008). Annealing effect on the structural and optical properties of a Cd_{1-x}Zn_xS thin film for photovoltaic applications, *Applied Surface Science*, 254, pp 4539-4545
22. Boyle, D. S. O'Brien, P. Otway, D. J. and Robbe, O. (1999). Novel approach to the deposition of CdS by chemical bath deposition: the deposition of crystalline thin films of CdS from acidic baths. *J. Mater. Chem.* 9, pp725-729
23. Boyle, D. S. Robbe, O. Halliday, D. P. Heinrich, M. R. Bayer, A. O'Brien, P. Otway D. J. and Potter, M. D. G., (2000). A novel method for the synthesis of the ternary thin film semiconductor cadmium zinc sulphide from acidic chemical baths, *J. Mater. Chem.*, 10 pp 2439 - 2441
24. Breen, M. L. Woodward IV, J. T. Scharz, D. K. and Apblett, A. W., (1998). Direct evidence for an ion-by-ion deposition mechanism in solution growth of CdS thin films, *Chemistry of Materials*, 10, pp 710-717

25. Bube R. H. Cited In Hodes, G., (2002). Chemical Solution Deposition of Semiconductor Films. Marcel Dekker Inc. New York, pp.2-3
26. Burton L. C. and Hench T. L. Cited In Morris, G. C. and Vanderveen, R., (1992). Electrodeposited cadmium zinc sulphide films for solar cells, *Solar Energy Materials and Solar Cells*, 26, pp 217-228
27. Chavhan, S.D. Senthilarasu, S. and Soo-Hyoung Lee, (2008). Annealing effect on the structural and optical properties of a $\text{Cd}_{1-x}\text{Zn}_x\text{S}$ thin film for photovoltaic applications. *Applied Surface Science*, 254, pp 4539-4545
28. Cherin, P. Lind, E. K. and Davis, E. A., (1970). The Preparation and Crystallography of Cadmium Zinc Sulfide Solid Solutions, *J. Electrochem. Soc.: Solid State Science*, 4,20, pp 233-236
29. Chopra, K.L., (1969). Thin Film Deposition Technology, McGraw Hill; New York, pp. 55-68.
30. Chopra, K.I. and Kaur. I., (1983). Thin Film Device Applications. Plenum, New York, pp 48-49
31. Chopra, K. L. Kainthla, R. C. Pandya, D. K. and Thakoor, A. P., (1982). Chemical solution deposition of inorganic films. In: Hass, G. (Editor) Physics of Thin Films, Academic Press, New York, pp 167 – 235
32. Chopra, K. L. Paulson, P. D. and Dutta V., (2004). Thin-Film Solar Cells: An Overview, *Prog. Photovolt. Res. Appl.*, 12 pp 69–92
33. Chu, T. L. Chu, S. S. Britt, J. Ferekides, C. and Wu, C. Q., (1991), *J. Appl. Phys.*, 70, p 2688.

34. Cody, G. D., (1984). Semiconductors and Semimetals, Academic Press, New York, 21, pp11- 14
35. Cohen, M. H. Fritzsche, H. and Ovshinski, S.R., (1969). Simple band model for amorphous semiconductor alloys, *Physical Review Letters*, 22, pp 1065 – 1072
36. Colinge, J. P. and Colinge, C. A., (2002). Physics of Semiconductor Devices, Kluwer Academic Publishers, New York, ISBN 0-306-47622-3, pp 1-7
37. Cullity, B. D. Cited In Holzwarth, U. and Gibson, N., (2011). The Scherrer equation versus the 'Debye-Scherrer equation, In *Nature Nanotechnology*, Vol. 6, Macmillan Publishers Limited, p 534
38. Dimroth, F., (2006). High-efficiency solar cells from III-V compound Semiconductors, *phys. stat. sol. (c)*, 3, 3, pp373–379
39. Domens, P. Cadene, M. and Cohens, G. W., (1980). Physical Properties of $\text{Cd}_{1-x}\text{Zn}_x\text{S}$ Thin Films Prepared by Thermal Evaporation of the Solid Solution, *phys. stat. sol. (a)*, 50, p 201
40. Doña, J. M. and Herrero, J. (1994). Process and film characterization of chemical-bath-deposited ZnS thin films, *J. Electrochem. Soc.* 141, 1, pp 205-210.
41. Doña, J. M and Herrero, J. Cited In Khefacha, Z. Benzarti, Z. Mnari, M. Dachraoui, M., (2004). Electrical and optical properties of $\text{Cd}_{1-x}\text{Zn}_x\text{S}$ ($0 \leq x \leq 0.18$) grown by chemical bath deposition, *Journal of Crystal Growth*, 260, pp 400–409
42. Dongol, M. (2002). Optical Absorption and Structural Properties of as-deposited and Thermally Annealed As-Te-Ga Thin Films, *Egypt. J. Sol.*, 25, 1, pp 33
43. Dunlap, W.C., (1961). Recent Developments in Semiconductors, *J.Chem. Educ.*, 5, 38, pp 238-241.

44. Dzhafarov, T.D. Ongul, F., and Karabay, I., (2006). Formation of CdZnS thin films by Zn diffusion. *J. Appl. Phys.* 39, p 3221.
45. Edamura, T. and Muto, J., (1995). Electrodeposition of zinc cadmium sulphide thin films from acidic aqueous electrolyte solution at room temperature, *Journal of Material Science Letters*, 14, pp 889-891
46. Edelson, V.(2007). Concentration Crisis, *In Brown Alumni Magazine*, July/August
47. Electronics (2010) Encyclopedia Britannica. *Encyclopedia Britannica Deluxe Edition*. Chicago
48. Emerson-Reynolds J. Cited In Hodes, G., (2002). Chemical Solution Deposition of Semiconductor Films. Marcel Dekker Inc. New York, pp 2-3.
49. Ezema, F. I., Ekwealor, A. B. C. And Osuji, R. U., (2006). Effect Of Thermal Annealing On The Band Gap And Optical Properties Of Chemical Bath Deposited ZnSe Thin Films. *Turk J Phys*, 30, pp157 – 163
50. Ezugwu, S. C. Ezema, F. I. Osuji, R. U. Asogwa, P. U. Ezekoye, B. A., Ekwealor A. B. C. Chigbo, C. Anusuya, M. and Mahaboob Beevi, M., Quoted by Asogwa, P.U., (2011). Band Gap Shift and Optical Characterization of Pva-Capped PbO Thin Films: Effect of Thermal Annealing. *Chalcogenide Letters*, 8, 3, p p163 – 170
51. Fan, D. Thomas, P. J. and O'Brien, P., (2007). Deposition of CdS and ZnS thin films at the water/toluene interface, *J. Mater. Chem*, 17, pp 1381–1386
52. Fraas L. M., and Ma Y. Y. Cited In Danaher W. J., Lyons L. E., and Morris G. C., (1985) Some Properties of Thin Films of Chemically Deposited Cadmium Sulphide, *Solar Energy Materials*, 12, pp137-148

53. Froment, M. and Lincot, D., (1995). Phase formation processes in solution at the atomic level : metal chalcogenide semiconductors. *Electrochimica Acta*, 40, pp 1293-1303
54. Gaewdang, T. Wongcharoen, N., (2007). Optical and Electrical Properties of Chemical Bath Co-Deposited CdS-ZnS Thin Films. Proceedings of ISES Solar World Congress: Solar Energy and Human Settlement, p1
55. Gadave, K.M. and Lokhande, C.D., (1993). Formation of Cu_xS films through a chemical bath deposition process, *Thin Solid Films*, 229, pp 1-4.
56. Gaga, S. Evans, D. Hodapp, M. Sovensen, H. Jamison, D. and Kranse B., (1981). Optoelectronics/Fiber-Optics Applications Manual, Second Edition, Hewlett Packard Optoelectronics Division, pp1-2
57. Gellings, P.J. and Bouwmeester, H. J. M., (1997). The CRC Handbook of Solid State Electrochemistry, CRC Press, New York, ISBN-10: 0849389569, p 84.
58. Gilbert, B. Frazer, B. H. Zhang, H. Huang, F. Banfield, J. F. Haskel, D. Lang, J. C. Srajer, G. De Stasio, G. Quoted by Nasra, B. T., Kamouna, N. Kanzari, M. Bennaceur, R., (2006). Effect of pH on the properties of ZnS thin films grown by chemical bath deposition. *Journal of Thin Solid Films*, 500, pp 4 – 8
59. Gorer, S. Albu-Yaron, A. and Hodes, G. Cited In Hodes, G., (2002). Chemical Solution Deposition of Semiconductor Films. Marcel Dekker Inc. New York, pp.2-3.
60. Gorer, S. and Hodes, G., (1994). Quantum size effects in the study of chemical solution deposition mechanisms of semiconductor films, *Journal of Physical Chemistry*, 98, pp 5338-5346.

61. Grozdanov, I. Barlingay, C.K. Dey, S.K. Ristov, M. and Najdoski, M., (1994). Experimental study of the copper thiosulfate system with respect to thin-film deposition. *Thin Solid Films*, 250, pp 67-71
62. Gutierrez Lazos, C. D. Rosendo, E. Juarez, H. Garcia Salgado, G. Diaz, T. Rubin Falfan, M. Oliva, A. I. Quintana, P. Aguilar, D. H. Cauich, W. Ortega, M. and Matsumoto, Y., (2008). Hexagonal Phase of CdS Thin Films Obtained by Oscillating Chemical Bath, *Journal of the Electrochemical Society*, 155, 2, pp 158 - 162
63. Hasegawa, S. Yazalci, S. and Shimizu, T. Quoted by Dongol, M., (2002). Optical Absorption and Structural Properties of as-deposited and Thermally Annealed As-Te-Ga Thin Films, *Egypt. J. Sol.*, 25, 1, p 33
64. Hoff, A. M. and Ruzyllo, J. (2006). Electronics and Photonics, the electrochemical society interface, p 36
65. Hodes, G., (2002). Chemical Solution Deposition of Semiconductor Films. Marcel Dekker Inc. New York, pp.3-6.
66. Hodes, G. and Calzaferri G., (2002). Chemical solution deposition of silver halide films. *Advanced Functional Materials*, 12, pp 501 – 505
67. Hodes, G. and Albu-Yaron, A. Cited In Hodes, G., (2002). Chemical Solution Deposition of Semiconductor Films. Marcel Dekker Inc. New York, pp.2-3.
68. Hodes, G. Albu-Yaron, A. Decker, F. and Motisuke, P. Cited In Hodes, G., (2002). Chemical Solution Deposition of Semiconductor Films. Marcel Dekker Inc. New York, pp.2-3
69. <http://prism.mit.edu/xray>

70. Jagodzinski, H. Cited In Boakye, F. and Nusenu, D., (1996). The Energy Band Gap of cadmium sulphide, *Solid State Communications*, 102, 4, pp 323-326
71. JCPDS data file, reference code: 00-001-0780
72. JCPDS data file, reference code: 00-040-0834
73. JCPDS data file, reference code: 01-080-0020
74. Kainthla, R.C., Pandya, D. K. and Chopra, K. L., (1980). Solution growth of CdSe and PbSe films. *Journal of the Electrochemical Society*, 127, pp 277-283
75. Kane, W. M. Spratt, J. P. Hershinger, L. W. and Khan, I. H. Cited In Morris, G. C. and Vanderveen, R., (1992). Electrodeposited cadmium zinc sulphide films for solar cells, *Solar Energy Materials and Solar Cells*, 26, pp 217-228
76. Kaur, I. Pandya, D. K. and Chopra, K. L., (1980). Growth kinetics and polymorphism of chemically deposited CdS films. *Journal of the Electrochemical Society*, 127, pp 943 – 948
77. Khefacha, Z. Benzarti, Z. Mnari, M. Dachraoui, M., (2004). Electrical and optical properties of $\text{Cd}_{1-x}\text{Zn}_x\text{S}$ ($0 \leq x \leq 0.18$) grown by chemical bath deposition, *Journal of Crystal Growth*, 260, pp 400–409
78. Kittel, C., (2005). Introduction to Solid State Physics, Eighth Edition. John Wiley & Sons, Inc. New York, p.577
79. Klug, H. P., and Alexander, L.-E. Cited In Holzwarth, U. and Gibson, N., (2011). The Scherrer equation versus the 'Debye–Scherrer equation, In Nature Nanotechnology, Vol. 6, Macmillan Publishers Limited, p 534

80. Korvink, J.G. and Greiner, A., (2002). Semiconductors for Micro and Nanosystem Technology, WILEY-VCH Verlag GmbH, Weinheim, ISBN 3-527-30257-3, pp 15 - 16
81. Kronig, D. L. and Penney, W. G. Cited In Mahajan S. and Sree Harsha, K. S., (1999). Principles of Growth and Processing of Semiconductors, WCB/McGraw Hill, New York, USA, ISBN 0-07-039605-1, pp 12
82. Kumar, S. Bhaskarjyoti, B. and Kalita, P. K., (2009). Growth and Optical Properties of Chemical Bath Deposited $\text{Cd}_{0.7}\text{Zn}_{0.3}\text{S}$ Nanoparticles, In: Giri, P. K. Goswami, D. K. Perumal, A. and Chattopadhyay, A. (Editors), International conference on advanced nanomaterials and nanotechnology, ICANN, American Institute of Physics, 978-0-7354-0825, pp 70 – 75
83. Kumar, V., Singh, V., Sharma, S.K. and Sharma, T.P., (1998). Structural and Optical Properties of Sintered CdZnS Films. *Optical Materials*, 11, pp29-34
84. Lalena, J.N., Cleary, D.A., Carpenter, E.E. and Dean, N.F., (2008). Inorganic Materials Synthesis and Fabrication, John Wiley & Sons Inc., ISBN 978-0-471-74004-9, pp 114-115.
85. Laukaitish, G. Lindroos, S. Tamulevicius, S. Leskela, M. and Rackaitis, M., (2000). *Appl. Surf. Sci.* 161 pp 396.
86. Li, S.S., (2006). Semiconductor Physical Electronics, Second Edition, Springer, New York, pp.246-253
87. Li, Z. Q. Shi, J. H. Liu, Q. Q. Wang, Z. A., Sun, Z. and Huang, S. M. (2010). Effect of $[\text{Zn}]/[\text{S}]$ ratios on the properties of chemical bath deposited zinc sulfide thin films, *Applied Surface Science* 257 pp122–126

88. Lincot, D. Froment, M. and Cachet, H., (1999). Chemical deposition of chalcogenide thin films from solution. *Advances in Electrochemical Science and engineering*, 6, pp 165-235.
89. Lincot, D. and Ortega Borges, R., (1992). Chemical Bath Deposition of cadmium sulphide thin films. In situ growth and structural studies by combined microbalance and electrochemical impedance techniques. *Journal of the electrochemical society*, 139 pp 1880 - 1889
90. Liebig, J. (1835). Cited In Hodes, G., (2002). Chemical Solution Deposition of Semiconductor Films, Marcel Dekker Inc. New York, pp.2-3.
91. Liu, Q. Mao, G., (2009). Comparison of CdS and ZnS thin films prepared by chemical bath deposition, *Surface Review and Letters*, 16, 3, pp 469 -474
92. Ma, Y. Y. Fahrenbruch, A. L. and Bube, R. H. Cited In Danaher, W. J. Lyons, L. E., and Morris, G. C., (1985). Some Properties of Thin Films of Chemically Deposited Cadmium Sulphide, *Solar Energy Materials*, 12, pp137-148
93. Marshall, J. M. and Owen, A. E., (1971). Drift mobility studies in vitreous arsenic triselenide, *Philosophical Magazine*, 24, pp 1281 – 1290.
94. Mattox, D. M., (1978). Surface Cleaning in Thin Film Technology, *Thin Solid Films*, 1, 53, p 81.
95. Madan, A. and Shaw, M. P., (1988). The Physics and application of Amorphous Semiconductors, Academic Press Inc. London, ISBN 0-12-464960-2, pp 1-5
96. Mahajan, S. and Sree Harsha, K. S., (1999). Principles of Growth and Processing of Semiconductors, WCB/McGraw Hill, ISBN 0-07-039605-1 New York, USA, pp 6 –

97. Mbow, C. M. Laplaze, D. and Cachard, A . Cited In Morris, G. C. and Vanderveen, R., (1992). Electrodeposited cadmium zinc sulphide films for solar cells, *Solar Energy Materials and Solar Cells*, 26, pp 217-228
98. McPeak M. P. (2010). Chemical Bath Deposition of Semiconductor Thin Films & Nanostructures in Novel Microreactors, PhD Thesis, Drexel University, p1
99. Meng, C. Sun, Y. Wu, J. Chen, X. Dai, N., (2010). Acidic chemical bath deposition of $Cd_{1-x}Zn_xS$ thin films, Proc. of SPIE, Vol. 7658, 76583B
100. Microsoft Encarta ® 2009
101. Morigaki, K., (1999). Physics of Amorphous Semiconductor, Imperial College Press, London, pp 1 -11, 67
102. Morris, G. C. and Vanderveen, R., (1992). Electrodeposited cadmium zinc sulphide films for solar cells, *Solar Energy Materials and Solar Cells*, 26, pp 217-228
103. Mott, N.F., (1967). Electrons in disordered structures, *Advances in Physics*, p 16
104. Mott, N.F. and Davis, E.A. Cited In Singh, J. and Shimakawa, K., (2003). Advances in Amorphous Semiconductors, CRC Press, New York, pp 56 - 63
105. Nadeem, M. Y. and Ahmed, W., (2000). Optical Properties of ZnS Thin Films, *Turk J Phy*, 24, pp 651 - 659.
106. Nadeem, .M.Y, Ahmed, W. and Wasiq, M.F., (2005). ZnS Thin Films – An Overview . *J of Research (science)*, 16, p105
107. Nanda, K. K. Sarangi, S.N. Mohanty, S. and Sahu, S.N. Cited In Khefacha, Z. Benzarti, Z. Mnari, M. and Dachraoui, M., (2004). Electrical and optical properties of $Cd_{1-x}Zn_xS$ ($0 \leq x \leq 0.18$) grown by chemical bath deposition, *Journal of Crystal Growth*, 260, pp 400–409

108. Nair, M.T.S. and Nair, P.K., (1989). Chemical bath deposition of Cu_xS thin films and their prospective large area applications. *Semiconductor Science and Technology*, **4**, pp 191-199.
109. Nair, P.K., Ocampo, A. Fernandez, A.M. and Nair, M.T.S., (1990). Solar control characteristics of chemically deposited lead sulphide coatings. *Solar Energy Materials*, **20**, pp 235-243
110. Nair, P.K., Garcia, V.M. Fernandez, A.M. Ruiz, H.S. and Nair, M.T.S., (1991). Optimization of chemically deposited Cu_xS solar control coatings. *Journal of Physics D: Applied Physics*, **24**, pp 441-449
111. Nair, M.T.S. Guerrero, L. and Nair, P. K. (1998). Conversion of chemically deposited CuS thin films to $\text{Cu}_{1.8}\text{S}$ and $\text{Cu}_{1.96}\text{S}$ by annealing. *Semiconductor Science and Technology*, **13** pp 1164-1169
112. Nair, P.K. Cardoso, J. Gomez-Daza, O. and Nair, M.T.S., (2001). Polyethersulfone foils as stable transparent substrates for conductive copper sulphide thin film coatings, *Thin Solid Films*, **401**, pp 243-250
113. Nasr, B. T. Kamoun, N. Kanzari, M. and Bennaceur, R., (2006). Effect of pH on the Properties of ZnS thin films grown by Chemical Bath, *Thin Solid Films*, **500**, pp 4 -8
114. National Renewable Energy Laboratory, Annual Report No. ADJ13063012, 9/05/01 to 9/04/02. Processing Materials, Devices and Diagnostics For Thin Film Photovoltaics: Fundamental And Manufacturability Issues, p 2
115. Neamen, D.A., (2003). Semiconductor Physics and Devices, Basic Principles, Third Edition, pp 144-145.
116. Ndukwe I. C., (1996). Solution growth Characterisation and applications of zinc sulphide thin films, *Solar energy Materials and Solar Cells*, **40**, pp 123-131

117. O'Brien, P. and McAleese, J., (1998). Developing an understanding of the processes controlling the chemical bath deposition of ZnS and CdS. *Journal of Materials Chemistry*, 8, pp. 2309-2314
118. O'Brien, P. and Saeed, T., (1996). Deposition and characterization of cadmium sulfide thin films by chemical bath deposition. *Journal of Crystal Growth*, 158, pp 497-504
119. Ohring, M., (1992). The Materials Science of Thin Films, Academic Press, San Diego. pp. 195-199, 336-339.
120. Overhof, H. and Thomas, P. Cited In Singh, J. and Shimakawa, K., (2003). Advances in Amorphous Semiconductors, CRC Press, New York, pp 56 - 63
121. Oktik, S. Russell, G. J. and Woods, J., (1982). Single-crystal $\text{Zn}_x\text{Cd}_{1-x}\text{S}/\text{Cu}_2\text{S}$ photovoltaic cells, *Solar Cells*, 5, pp231-241
122. Ortega-Borges, R. Lincot, D. and Vedel, J., (1992). Proc. 11th E. C. Photovoltaic Solar Energy Conf., Harwood Academic Publishers, Switzerland, p 862.
123. Ortega-Lopez, M. Vigil-Galan, O. Cruz-Gandarilla, F. and Solorza-Feria, O., (2003). Preparation of AgInS_2 chalcopyrite thin films by chemical spray pyrolysis, *Materials Research Bulletin*, 38, 55-61.
124. Oztas, M. and Bedir, M., (2001). Some Properties of $\text{Cd}_{1-x}\text{Zn}_x\text{S}$ and $\text{Cd}_{1-x}\text{Zn}_x\text{S}(\text{In})$ Thin Films Prepared by Pyrolytic Spray Technique. *Journal of Applied Sciences*, 4, pp 534-537.
125. Padam, G.K., Malhotra, G.L. and Rao, S.U.M., (1988). Studies on solution grown thin films of $\text{Zn}_x\text{Cd}_{1-x}\text{S}$, *J. Appl. Phys.*, 63, pp 770.

126. Padam, G.K and Rao, S.U.M., (1986). Preparation and characterization of chemically deposited CuInS_2 thin films, *Sol. Ener. Mater.* 13, pp 297-305.
127. Pankove, J. L., (1975). Optical processes in semiconductors, Dover Publications Inc., New York, ISBN: 0486602753, pp 34 - 36
128. Pawar , S. M. Pawar, B. S. Kim, J. H. Oh-Shim, J. Lokhande, C. D., (2011). Recent status of chemical bath deposited metal chalcogenide and metal oxide thin films, *Current Applied Physics* 11 pp 117- 161
129. Pawar, S.H. Tamhanker, S.P. and Lokhande, C.D., (1986). Studies on electrochemical photovoltaic cells formed with thin film Bi_2CdS_4 Photoelectrodes, *Sol. Ener. Mater.* 14, pp 71-77.
130. Peeters, O. de Ranter, C. J. Cited In Hodes, G., (2002). Chemical Solution Deposition of Semiconductor Films. Marcel Dekker Inc. New York, pp.2-3
131. Pentia, E. V. Draghici, G. Sarau, B. Mereu, L. Pintilie, L. Sava, F. and Popescu, M., (2004). Structural , electrical, and photoelectrical properties of $\text{Cd}_x\text{Pb}_{1-x}\text{S}$ thin films prepared by chemical bath deposition, *Journal of the Electrochemical Society*, 151, pp 729 - 733
132. Petterson, J. D. and Bailey, B. C., (2005). Solid-State Physics: Introduction to the Theory, Springer Berlin Heidelberg, New York, ISBN-10 3-540-24115-9, pp 293-294, 113, 637.
133. Pillai, S. O. (2005). Solid State Physics, New Age International (P) Ltd., New Delhi, ISBN(10): 81-224-1682-9, p 87
134. Poole, C.P.Jr., (2004). Encyclopedic Dictionary of Condensed Matter Physics, 1, p. 66, 440, 1391.

135. Prem Kumar, T. Rajasekar, S. Saravanakumar, S. Joseph, P. S. and Sankaranarayanan, K., (2010). Microscopic and Optical Characterization of $\text{Cd}_{0.8}\text{Zn}_{0.2}\text{S}$ Thin Film. *Journal of Advanced Microscopy Research*, 5, pp 123–128
136. Puscher, C. Cited In Hodes, G., (2002). Chemical Solution Deposition of Semiconductor Films. Marcel Dekker Inc. New York, pp.2-3.
137. Ramasamy, K. Malik, M. A. Helliwell, M. Raftery, J. and O'Brien, P., (2011). Thio- and Dithio-Biuret Precursors for Zinc Sulfide, Cadmium Sulfide, and Zinc Cadmium Sulphide Thin Films, *Chem. Mater.* 23, pp 1471–1481
138. Repins, I. Contreras, M. A. Egaas, B. DeHart, C. Scharf, J. Perkins, C.L. To, B. Noufi, R., (2008). 19.9%-efficient $\text{ZnO}/\text{CdS}/\text{CuInGaSe}_2$ solar cell with 81.2% fill factor, *Prog. Photovolt: Res. Appl.* 16, pp 235-239
139. Rieke, P.C. and Bentjen S. B., (1993). Deposition of cadmium sulfide films by decomposition of thiourea in basic solutions, *Chemistry of Materials*, 5, pp. 43-53
140. Rodriguez, J. A. and Gordillo, G., (1989). Study of Electrical Properties in $\text{Zn}_x\text{Cd}_{1-x}\text{S}$ Thin Films, *Solar Energy Materials*, 19, pp 421-431
141. Rosenheim, G. Stadler, W. Mayer, V. J. Cited In Hodes, G., (2002). Chemical Solution Deposition of Semiconductor Films. Marcel Dekker Inc. New York, pp.2-3.
142. Ryan T. (2001). The Development of Instrumentation for Thin-Film X-ray ~~Diffraction~~, *Journal of Chemical education*, 78, 5, pp 613-614
143. Sanap, V. B. and Pawar, B. H. (2011). Study of chemical bath deposited Nanocrystalline CdZnS thin films, *Journal of Optoelectronics and Biomedical Materials*, 3, 2, pp 39-43
144. Sapoval, B. and Herman, C., (1995). Physics of Semiconductors, Springer-Verlag, New York, Inc. ISBN 0-387-94024-3, pp 1- 6

145. Sebastian, P. J. and Narvaez, J., (1996). Photosensitive ZnCdS nano particles in a CdS matrix formed by high temperature sintering of ZnS and CdCl₂ in argon, *Thin Solid Films*, 287, pp 130-133
146. Shandalov, M. and Golan Y., (2004). Microstructure and morphology evolution in chemical solution deposited semiconductor films: 2. PbSe on As face of GaAs(111). *The European Physical Journal – Applied Physics*, 28, pp 51 -57
147. Shandalov, M., and Golan Y., (2003). Microstructure and morphology evolution in chemical solution deposited PbSe films on GaAs(100). *The European Physical Journal – Applied Physics*, 24, pp 13 -20
148. Schwartz, K., (1993). *The Physics of Optical Recording*; Springer Verlag, Berlin, pp 190
149. Scherrer, P, and Nachrichten, G. Cited In Patterson, A. L., (1939). The Scherrer Formula for X-Ray Particle Size Determination, *Physical Review*, 15, p 978
150. Shur, M., (1996). *Introduction to Electronic Devices*, John Wiley & Sons, Inc. New York, ISBN 0-471-10348-9, pp 61 - 74
151. Singh, J., (2003). *Electronic and Optoelectronic Properties of Semiconductor Structures*, Cambridge University Press; New York, pp 51-52.
152. Singh, J., (2006). *Optical Properties of Condensed Matter and Applications*, John Wiley and Sons, Ltd. pp.2-4.
153. Singh, J. and Shimakawa, K., (2003). *Advances in Amorphous Semiconductors*, CRC Press, New York, pp 56 - 63
154. Sole, J. G., Bausa, L. E. and Jaque, D., (2005). *An Introduction to the Optical Spectroscopy of Inorganic Solids*, John Wiley & Sons Ltd., England, pp 11-12

155. Sólyom, J., (2008). Fundamentals of the Physics of Solids: Electronic Properties, Volume II, Springer, New York, pp 89-195
156. Song, J. Li, S. S. Yoon, S. Kim, W. K. Kim, J. Chen, J. Craciun, V. Anderson, T.J. Crisalle, O. D. and Ren, F., (2005). Growth and Characterization of CdZnS Thin Film Buffer Layers by Chemical Bath Deposition, IEEE, pp 449-451. Web site: <http://ieeexplore.ieee.org/stamp/stamp.jsp?arnumber=01488166>. Accessed 29/03/2012
157. Stanley, A. G. Cited In Danaher, W. J. Lyons L. E. and Morris, G. C., (1985). Some Properties of Thin Films of Chemically Deposited Cadmium Sulphide, *Solar Energy Materials*, 12, pp137-148
158. Stern, F. Cited In Anuar, K. Tan, W. T. Jelas, M. Ho, S. M. and Gwee, S. Y., (2010). Effects of Deposition Period on the Properties of FeS₂ Thin Films by Chemical Bath Deposition Method, *Thammasat Int. J. Sc. Tech.*, 15, 2, p 64
159. Tan, W.C., (2006). Optical Properties of Amorphous Selenium Films, M.Sc Thesis, University of Saskatchewan, pp 12 - 46.
160. Tauc, J., (1974). *Amorphous and Liquid Semiconductors*, Plenum: New York, p. 159.
161. Ubale, A. U., Sangawar, V. S. and Kulkarni, D. K., (2007). Size dependent optical characteristics of chemically deposited nanostructured ZnS thin films. *Bull. Mater. Sci.*, 30, 2, pp 147-151
162. Varkey, A. J., (1989). Chemical bath deposition of Cu_xS thin films using ethylenediaminetetraacetic acid (EDTA) as complexing agent. *Solar Energy Materials*, 19, pp 275-420
163. Vergard, L. Cited In Denton, A. R. and Ashcroft, N. W., (1991). Vergard's Law, *Physical Review A (Atomic, Molecular, and Optical Physics)*, 43, 6, pp 3161 - 3164

164. Venables, J.A., (2003). Introduction to Surface and Thin Film Processes, Cambridge University Press, Cambridge, pp 5-60.
165. Vipin, K. Sharma, M.K. Gaur, J. Sharma, T.P., (2008). Polycrystalline Zns Thin Films By screen Printing Method And Its Characterization, *J chalcogenide Letters* 5, 11 pp 289- 291
166. Wilson, A. H., (1931). The theory of electronic semi-conductors, *Proc. R. Soc. Lond.*, A133, pp 458-491
167. Wolf, H.F., (1971). Semiconductors, John Wiley and Sons, p 22
168. Wells, A. F. (1984), Structural Inorganic Chemistry (5th ed.), Clarendon Press, Oxford, ISBN 0-19-855370-6, p46-51
169. Woon-Jo, J. and Gye-Choon, P., (2003). Structural and electrical properties of CuGaS₂ thin films by electron beam evaporation, *Solar Energy Materials and Solar Cells*, 75, pp 93-100.
170. Wikipedia.org/wiki/Characterization
171. Wikipedia.org/wiki/materials_science
172. Yacobi, B. G., (2004). Semiconductor Materials an Introduction to Basic Principles, Kluwer Academic Publishers, New York, pp 1-3, 154-157, 107.
173. Yamaga, S. Yoshikawa, A. and Kasai, H., (1990). Growth and Properties of Zn_{1-x}Cd_xS films on GaAs Pressure MOVPE, *Journal of Crystal Growth*, 99, pp 432-436
174. Yamaguchi, T. Yamamoto, Y. Tanaka, T. and Yoshida, A., (1996). Preparation and characterization of (Cd,Zn)S thin films by chemical bath deposition for photovoltaic devices, *Thin Solid Films*. 516, pp 343-344

175. Yokogawa, T., Ishikawa, T., Merz, J.L. and Taguchi, T., (1994). Spectroscopic characterization of band discontinuities in free standing CdZnS/ZnS strained layer superlattice, *Appl. Phys.* 75, pp 2189.
176. Yu, S. H. and Yoshimura M., (2002). Fabrication of powders and thin films of various nickel sulphides by soft solution-processing routes. *Advanced Functional Materials*, 12, pp 277 -285
177. Wu, X. Keane, J. Dhere, R. Hart, C. D. Duda, A. Gessert, T. Asher, S. Levi, D. and Sheldon, P., (2001). 16.5%-efficient CdS/CdTe polycrystalline thin-film solar cell, Proceedings of the 17th European Photovoltaic Solar Conference, Munich, Germany. 995, pp 22-26
178. Zachreisen, W. H. Cited In Madan, A. and Shaw, M. P., (1988). The Physics and application of Amorphous Semiconductors, Academic Press Inc. London, ISBN 0-12-464960-2, p 2
179. Zhou, J. Wu, X. Teeter, G. To, B. Yan, Y. Dhere, R. G., and Gessert, T. A., (2004) CBD-Cd_{1-x}Zn_xS thin films and their application in CdTe solar cells, *phys. stat. sol.* 241, 3, pp775-778

APPENDIX

1.Reference code: 00-001-0780

Mineral name: Greenockite
PDF index name: Cadmium Sulfide

Empirical formula: CdS
Chemical formula: CdS

Crystallographic parameters

Crystal system: Hexagonal
Space group: P63mc
Space group number: 186

a (Å): 4.1420
b (Å): 4.1420
c (Å): 6.7240
Alpha (°): 90.0000
Beta (°): 90.0000
Gamma (°): 120.0000

Measured density (g/cm³): 4.82
Volume of cell (10⁶ pm³): 99.90
Z: 2.00

RIR: -

Status, subfiles and quality

Status: Marked as deleted by ICDD
Subfiles: Inorganic
Mineral
Quality: Blank (B)

Comments

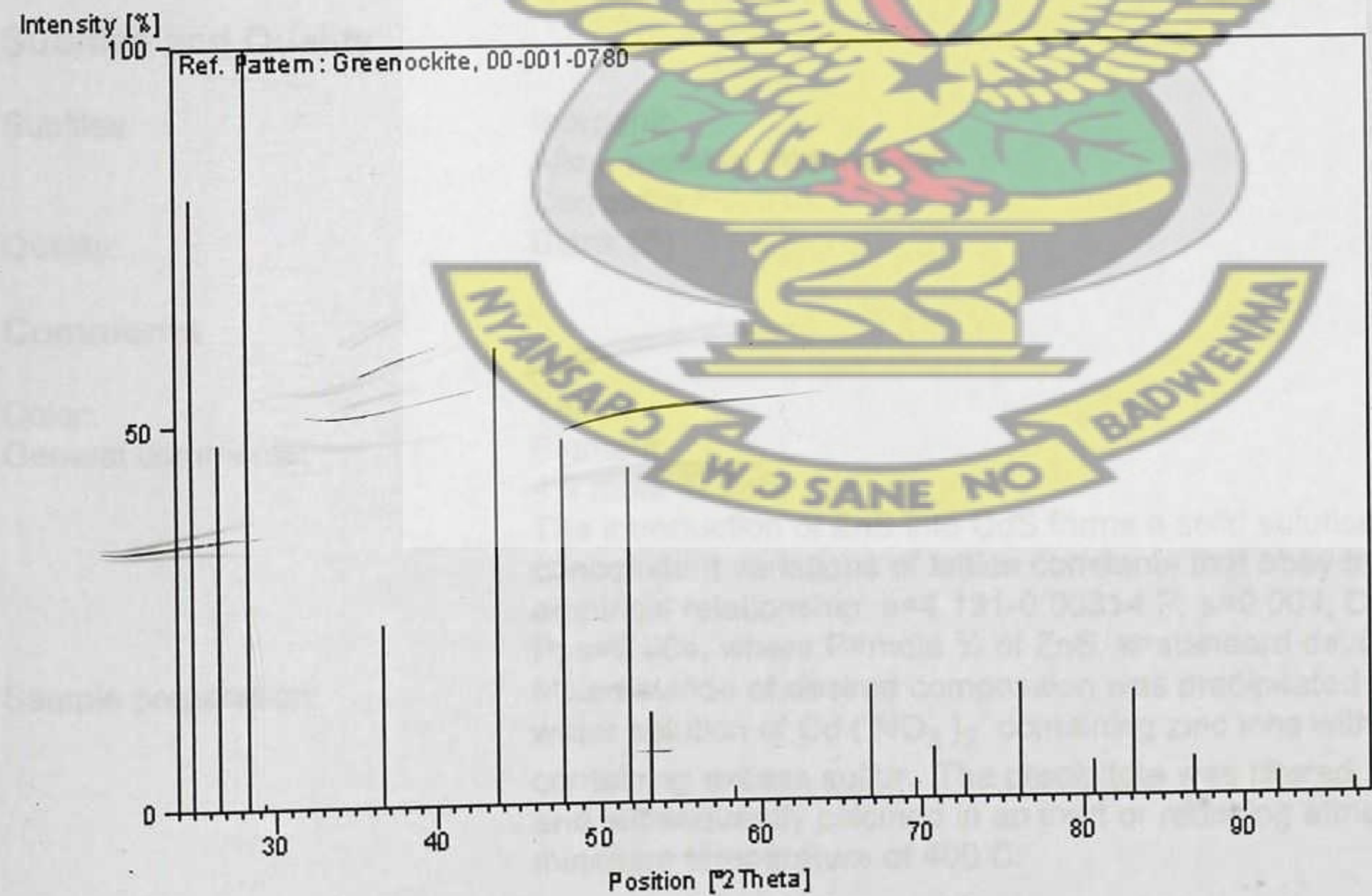
Deleted by: Deleted by NBS card 6-0314.
Color: Yellow to orange
Optical data: B=2.506, Q=2.529, Sign=+
Melting point: 780

Primary reference: New Jersey Zinc Co., Palmerton, PA, USA., *Private Communication*
Optical data: *Dana's System of Mineralogy, 7th Ed.*
Unit cell: *Dana's System of Mineralogy, 7th Ed.*

Peak list

No.	h	k	l	d [Å]	2Theta[deg]	I [%]
1	1	0	0	3.56000	24.993	80.0
2	0	0	2	3.35000	26.587	48.0
3	1	0	1	3.14000	28.401	100.0
4				3.03000	29.455	1.0
5	1	0	2	2.45000	36.650	24.0
6	1	1	0	2.07000	43.694	60.0
7	1	0	3	1.90000	47.835	48.0
8	1	1	2	1.76000	51.911	44.0
9	2	0	1	1.72000	53.212	12.0
10	2	0	2	1.58000	58.357	2.0
11	2	0	3	1.40000	66.763	15.0
12	2	1	0	1.35000	69.583	3.0
13	2	1	1	1.33000	70.785	7.0
14	1	1	4	1.30000	72.675	3.0
15	2	1	2	1.25000	76.084	15.0
16	3	0	0	1.19000	80.678	5.0
17	2	1	3	1.16000	83.219	14.0
18	0	0	6	1.12000	86.907	5.0
19	1	0	6	1.07000	92.094	3.0
20	2	2	0	1.03000	96.811	2.0

Stick Pattern



2. Reference code: 00-040-0834

PDF index name: Cadmium Zinc Sulfide

Empirical formula: $\text{Cd}_{9.51}\text{S}_{10}\text{Zn}_{0.49}$

Chemical formula: $\text{Cd}_{9.51}\text{Zn}_{0.49}\text{S}_{10}$

Crystallographic parameters

Crystal system: Hexagonal

Space group: P63mc

Space group number: 186

a (Å): 4.1120

b (Å): 4.1120

c (Å): 6.6860

Alpha (°): 90.0000

Beta (°): 90.0000

Gamma (°): 120.0000

Volume of cell (10^6 pm^3): 97.90

Z: 0.20

RIR:

Subfiles and Quality

Subfiles: Inorganic
Alloy, metal or intermetallic

Quality: Corrosion

Blank (B)

Comments

Color: Yellow

General comments: Pigment.

4.9 mole % ZnS.

Sample preparation:

The introduction of ZnS into CdS forms a solid solution with concomitant variations of lattice constants that obey the following empirical relationship: $a=4.131-0.00314 P$; $s=0.003$, $C_0=6.713-0.00458 P$; $s=0.004$, where P =mole % of ZnS, s =standard deviation. Mixed sulfide of desired composition was precipitated by reaction of water solution of $\text{Cd}(\text{NO}_3)_2$ containing zinc ions with solution of BaS containing excess sulfur. The precipitate was filtered, dried and ground and subsequently calcined in an inert or reducing atmosphere at a minimum temperature of 400 C.

Primary reference: Huckle, W., Swigert, G., Wiberley, S., *Ind. Chem. Prod. Res. Develop.*, **5**, 362, (1966)

Peak list

No.	h	k	l	d [Å]	2Theta[deg]	I [%]
1	1	0	0	3.56000	24.993	78.0
2	0	0	2	3.34000	26.668	71.0
3	1	0	1	3.15000	28.309	100.0
4	1	0	2	2.44000	36.806	19.0
5	1	1	0	2.06000	43.917	72.0
6	1	0	3	1.88800	48.158	41.0
7	2	0	0	1.78000	51.285	10.0
8	0	0	4	1.67100	54.901	4.0
9	3	1	3	0.90500	116.676	8.0
10	1	0	8	0.81390	142.322	8.0
11	3	0	6	0.81270	142.822	8.0
12				0.79600	150.802	6.0
13	2	1	7	0.77900	162.858	4.0

Stick Pattern

